A XENOLITH-BASED LITHOSPHERIC TRANSECT OF THE SLAVE CRATON, N.W.T., CANADA

MATHER, KATHLEEN,ANN

A XENOLITH-BASED LITHOSPHERIC TRANSECT OF THE SLAVE CRATON, N.W.T., CANADA

VOLUME I : TEXT

Kathy Mather

A thesis submitted in partial fulfilment of the requirements for the degree of Doctor of Philosophy at Durham University

Department of Earth Sciences

Durham University

May 2012

ABSTRACT

During the last decade, the Canadian Slave craton has emerged as an important global diamond resource. Recent work on the sub-continental lithospheric mantle (SCLM) beneath this craton has yielded tantalising suggestions about its structure and composition that are of interest to the diamond mining effort. Geochemical studies of xenoliths, sulphides, diamond inclusions and mineral separates, together with teleseismic and magnetotelluric interpretations have indicated that the Slave SCLM has a unique stratified structure. This consists of a highly depleted mantle layer above ~110 km, most pronounced in the central Slave region, with a relatively 'fertile' layer of mantle beneath that extends to the base of the lithosphere. As diamond mining and exploration in the Slave craton matures, more samples are available for study, allowing testing of earlier models and refinements on existing geotherm estimates.

This PhD provides new silicate major and trace element compositions, thermobarometry and rhenium-osmium (Re-Os) isotope data for two new suites of peridotite xenoliths from Slave craton kimberlites (Artemisia and Diavik), as well as new Re-Os data for existing suites from Gahcho Kué (Kopylova and Caro, 2004). Major element data from all localities are used to calculate new geotherms for the Slave Craton, using the method outlined by McKenzie et al (2005) and expanded by Mather et al. (2011). The average mineral compositions, rare-earth elements, Mg#, and Rhenium-depletion ages (T_{RD}) for individual xenoliths from all localities are plotted on these new geotherms. The resulting patterns of T_{RD} with depth are used to evaluate the suggestion that the Slave lithosphere is stratified in age as well as composition.

Finally, all kimberlite localities studied are used as 'pseudo-boreholes' to create a 2-dimensional linear transect from NNW-SSE through the Slave SCLM. The lithospheric stratigraphy illustrated by this transect is used to comment on the apparent layered nature of the continental lithosphere beneath the Slave province and explore which, if either, of the two main craton formation hypotheses were operating during its genesis.

DECLARATION

I declare that this thesis, which I submit for the degree of Doctor of Philosophy at Durham University, is my own work and not substantially the same as any which has previously been submitted at this or any other university.

Kathleen Mather

Durham University

May 2012

ACKNOWLEDGEMENTS

I would like to gratefully thank;

- The Geological Survey of Canada and NCIET Durham University, for funding.
- The Geological Society of London, for the Joseph Burr Tyrell award.
- Steven Creighton at the Saskatchewan Research Council, for EMP analyses.
- John Watson at the OU, for XRF analyses on challenging samples.
- Simon Jackson, for guidance and patience teaching me LA-ICP-MS methods.
- Geoff Nowell, for help and advice on using the Triton.
- Chris Ottley, for showing me how to use the Element, and offering assistance on that most frustrating of machines, the High-Pressure Asher.
- Simon Dixon and Iain Neill, for proof reading endless drafts.

- and -

- Dr Matthews and the staff nurses at University Hospital North Durham, for getting me back to fighting fitness.

-x-

When I think of all the people who are responsible for hauling this thesis into being (hauling really is the appropriate verb) the list is very long. It would be impossible to do

them all credit. However, some have contributed more than others, and I would like to thank them personally here.

Without Graham, this thesis would almost certainly be very different. Enthusiasm in the student is encouraged by attention and interest in the part of the supervisor, and Graham has liberally dished out both. With his hugely busy schedule and even when he jetted off halfway through my PhD to become some Canadian Big Cheese; I have still been able to sit and wax lyrical in his office in a way that many other supervisors would not tolerate, while he listened and responded without ever making me feel that I was wasting his time.

Bruce has oscillated between 'good cop' and 'bad cop' during the course of this PhD, usually related to the proximity of deadlines and the state of my health. He was usually the supervisor that brought things back down to Earth, made me remember that I was working to a deadline, and that this project wasn't all about blue-sky research. His contribution has been invaluable to getting me finished on time, and (relatively) within budget.

However, neither of my 'official' supervisors put up with as much as poor Chris Dale. While Graham was upstairs in his office merrily signing bits of paper, Chris was downstairs in the lab attempting to teach me Re-Os chemistry, bravely soldiering on through my endless moaning and complaining and (I imagine) strongly resisting the urge to suggest I drink a beaker-full of conc. HCl. Cheers Chris.

Academically, this thesis has benefitted from discussions with the many leaders in the field that I have been lucky enough to meet and be inspired by over the past four years. Dan McKenzie, Dave Snyder, Herman Grütter and many others have given me the privilege of

their time and helped me gain a broader understanding of the subject, which has helped focus and consolidate this work.

Emotionally, I doubt I could have gotten through the PhD without Izzy, Claire, Iona, Sarah, Kirstie and the rest of my year group; as well as those in the years above (for their sage advice) and below (for their infectious naïve enthusiasm… I'm looking at you, Pete). Claire for brightening up the (long) lab day, nattering while the n^{th} column was dripping through, and Izzy for rolling eyes with me on the open plan and supplying a shoulder to cry on. Sarah for letting me sleep at her house when I left my keys in Sainsbury's (again), Iona for long reminiscing conversations about Cambridge, and Kirstie for looking after me and understanding when my health took a turn for the worse.

This thesis is dedicated to my Mum and Dad. Mum, this is the culmination of all your hard work, keeping me on the right path for 26 years, picking me up when I fell down, and always being there to listen. Dad, this is your thanks for always encouraging me to follow my heart and not the money.

Iain – you can stop doing my washing up now.

TABLE OF CONTENTS

1 INTRODUCTION

1.1 RATIONALE AND THESIS OUTLINE

Cratons are fragments of the ancient Earth. Characterised by thick (> 200 km), cold lithospheric roots, they have acted as geodynamic 'shields' for over 2.5 billion years; protecting the crust above from reworking and destruction on the turbulent surface of our planet (Jordan, 1975).

Studying the crust in these cratonic regions is crucial for understanding the nature of the Archean Earth and the birth of the continents, but the lithospheric roots beneath are also academically and economically important. They are our only known source of ultra-high pressure carbon in the form of diamond, and they contain a variety of enigmatic geochemical features related to their extreme depletion (Boyd, 1989).

This thesis focuses on the lithospheric mantle portion of the cratons, the rocks themselves and the way in which we study them. Samples of the lithospheric mantle in cratonic regions are brought to the surface as xenoliths and xenocrysts within kimberlite magma. Historically, the study of kimberlite-borne xenoliths is associated with Southern Africa, but in the last two decades Northern Canada, and specifically the Slave craton, has emerged as a global diamond resource; the mining efforts in this remote region liberating abundant (but often small) xenolith samples for study.

1.1.1 Craton Formation and the Slave

The Slave craton is a key region for examining craton formation and evolution. Initial work (Pearson et al., 1998; Kopylova et al., 1998; Griffin, 1998) suggested that the lithosphere was uniquely stratified; the shallow lithosphere (< 110 – 140 km) being 'ultra-depleted', defined by an increased Mg# in olivine (Mg/(Mg+Fe)), an abundance of low calcium, high chromium 'G10' or 'harzburgitic' garnets (Sobolev et al., 1973; Dawson and Stephens, 1975; Grütter et al., 2004), and a smaller population of lherzolites. This 'ultra-depleted' layer was also postulated to be visible on initial teleseismic studies of the central Slave craton (Bostock, 1997), and in later Magnetotelluric measurements (Jones, 2001). The lithosphere deeper than ~140 km is purported to be more 'fertile'; with lower olivine Mg#s and a higher lherzolite/harzburgite ratio.

The stratified nature of the lithosphere in this region has meant that it is a well-worn battleground for proponents of the different mechanisms for craton formation, for which there are two main endmember hypotheses:

1) The anomalous thickness and depletion evident in cratonic roots is the residue of abnormally high volumes of melting during the Archean; specifically in plume-type environments where ambient mantle temperatures were over 300° hotter than modern-day mantle (Griffin et al., 2003)

2) The anomalous thickness and depletion in cratonic roots is the result of high degrees of melting at an Archean spreading ridge coupled with stacking and

potentially re-melting of this depleted lithosphere (Helmdstaedt and Schulze, 1980) in Archean subduction zones (Pearson and Wittig, 2008).

Briefly, advocates of the 'plume melting' hypothesis (1) cite the stratification of the lithosphere beneath the central Slave as evidence for varied amounts of melting; the shallow, ultra depleted lithosphere formed by melting at an Archean ridge, but the anomalous thicknesses observed (> 140 km), and the more fertile nature of the deeper lithosphere to be due to underplating by mantle plume melting processes. The main defence of this hypothesis is the presence of diamond inclusions of ultradeep paragenesis (Davies et al., 2004) and bulk major element arguments that suggest melting at pressures greater than 5 GPa.

In contrast, the 'subduction stacking' hypothesis (2) suggests that the clear stratification in the Slave lithosphere is evidence for fossil subduction, and that the increased fertility of the deeper layer is the result of re-working and infiltration of metasomatic melts during the long history of the craton.

The main issue with using the Slave craton as the proving ground for these hypotheses is that — unlike the Kaapvaal craton — the Slave kimberlites are very remote, making sample acquisition time-consuming and expensive. The majority of published data are on small (< 5 cm diameter) micro-xenoliths and xenocrysts, and there are a number of kimberlite localities of interest to academia (but not the diamond mining industry) that have not been rigorously examined.

1.1.2 A xenolith-based lithospheric transect

This thesis aims to consolidate the existing work on the Slave craton with new geochemical data from macroxenoliths (> 5 cm) from four kimberlite pipes. These pipes form a NNE-SSW linear transect across the Slave craton (Figure 1.1) and as such can be used as data points on a 'lithospheric transect', where geochemical and age information from individual xenoliths is plotted against depth.

This transect will answer the following questions;

1) *What is the nature and age of the Slave craton lithosphere in the far North?*
2) *How old is the 'ultra-depleted' layer of the central Slave?*
3) *How did the Slave craton form?*
4) *How has the Slave craton evolved through time?*

To address these issues, this thesis first examines the method by which equilibrium pressures and temperatures from peridotite xenoliths and xenocrysts are used to estimate the palaeogeothermal gradient in cratonic regions. Lithospheric thicknesses are also estimated using this method. This study critically examines the established procedure for obtaining palaeogeotherms from xenolith pressure – temperature (P–T) data and compares it to a numerical palaeogeotherm fitting program. The data used in this contribution comes from kimberlite localities worldwide, namely Bultfontein, Finsch and Gibeon in Southern Africa and Somerset Island in Canada. These kimberlites were chosen (rather than those within the Slave craton) as the datasets and localities are well-constrained. This study shows that a numerical, objective fitting method produces more precise and less-biased

geotherm estimates from peridotite xenolith data than the established, qualitative method. This study further shows that errors and variation in the thermobarometer combinations used to calculate the individual P–T estimates have relatively little effect on the geotherm, but these can have a major effect on the relative depth estimates of individual xenoliths.

The next chapter (3) deals with these uncertainties in depth estimates, and provides an algorithm for choosing the most appropriate depth estimate for use in lithospheric stratigraphy, which is crucial for the remaining chapters.

These following chapters use this new geotherm-fitting method and depth estimation algorithm and are focussed solely on xenoliths from the Slave craton kimberlites. A variety of geochemical and petrographic methods were used for each locality (with details summarised in each chapter) but a common theme of whole-rock Re-Os isotope[1] and X-ray flourescence (XRF) analyses, together with electron microprobe (EMP) and laser-ablation inductively-coupled plasma mass spectrometry (LA-ICP-MS) mineral analyses is present throughout the thesis, with the overall aim of constructing an age-depth profile across the Slave craton lithosphere.

Chapter 4 explores the lithosphere sampled by the Artemisia kimberlite in the far north of the Slave craton. This locality is an un-mined and as yet un-studied kimberlite in terms of peridotite xenoliths, which were obtained by fieldwork during the summer of 2009. The samples from this locality elucidate the evolution of the Slave craton in the far North. The

[1] The robustness of the Re-Os system for dating cratonic peridotites is well established (Pearson et al., 2002; Rudnick and Walker, 2009). The fundamental assumption is that, since cratonic lithosphere is highly refractory and the result of high degrees of melting, all Re has been removed in the melt fraction. This removes the parent of the isotopic decay system (^{187}Re) such the ratio of daughter to stable ($^{187}Os/^{188}Os$) in the peridotite xenolith samples is fixed at the time of melt depletion, which is assumed to be the craton formation event. These 'Re-depletion' ages (T_{RD}) are therefore minima, but still commonly yield Archean ages > 2.5 Ga (Pearson et al., 2002).

age distribution of the samples indicates massive lithospheric alteration during the Proterozoic, possibly associated with the Mackenzie igneous event. Various possibilities for the unique T_{RD} distribution are explored in an attempt to reconcile the surface geology, teleseismic and new magnetotelluric data with the geochemistry and age of the peridotite xenoliths. This data is compared with age data from the previously characterised Jericho kimberlite, making up the first 'leg' of the lithospheric transect from North to South.

Chapter 5 is a more traditional petrological and geochemical examination of xenoliths from the Central Slave lithosphere. Using a combination of new macroxenolith and clinopyroxene xenocryst samples, and a newly-collated dataset including all published xenolith and diamond inclusion data, the nature of the 'ultra-depleted' layer is characterized in detail, and sheds light on the suggestion that the lithosphere in this region youngs with depth. The age distribution for the xenoliths in this region is compared with that from Jericho and Artemisia, thus extending the lithospheric transect into the central Slave.

Chapter 6 is a synthesis of the T_{RD} and geochemical data presented in the previous chapters which, combined with published and un-published teleseismic and magnetotelluric profiles and new age data are presented from peridotite xenoliths from the Southern Slave (Gahcho Kué; Kopylova and Caro, 2002), completes the lithospheric transect from north to south and allows examination of the questions posed at the beginning of this section.

Chapter 7 presents the conclusions of the thesis as a whole.

1.2 AUTHOR CONTRIBUTIONS

Where chapters include co-authors, their contributions are outlined here.

1.2.1 Chapter 2

This paper has been published in its presented form in Lithos. *(doi:10.1016/j.lithos.2011.04.003) A reprint of this paper is included in the appendix.*

I collated all datasets from published sources, utilised and suggested modifications to the program to calculate the geotherms and wrote the manuscript, passing it to co-authors for comments and review. This review altered only the layout and structure of the contribution and not the primary geological conclusions.

Co-author contributions:

Graham Pearson instigated the project as an extension of the preliminary work that I had completed during the first year of my PhD research. He provided helpful feedback on the manuscript iterations.

Dan McKenzie is the author of the *FITPLOT* program and provided helpful initial advice on its usage. He altered the main program as the project progressed to accommodate required

changes as dictated by me. He provided helpful comments on the final draft of the manuscript

Bruce Kjarsgaard provided feedback on early versions of draft manuscripts and helped with acquisition of the DeBeers dataset.

Keith Priestley provided the S-wave geotherms for the final part of the paper.

1.2.2 Chapter 4

I performed the Re-Os wet chemistry on the Artemisia samples, 80% of the LA-ICP-MS garnet analyses, and all xenolith EMP garnet analyses. Xenocryst garnet was picked from concentrate by me. I wrote the manuscript in the whole and performed all geochemical data analysis and modelling, and directed the main focus of the study.

Co-author contributions:

Graham Pearson: negotiated the field logistics and undertook the fieldwork to collect the xenolith samples. He also provided the nucleus of the project idea as PhD supervisor and provided useful feedback on the manuscript drafts.

Bruce Kjarsgaard: also provided field logistics and collected xenolith samples. He also obtained the xenocryst samples from Stornoway diamonds, and provided helpful comments on the final versions of the manuscript.

Alan Jones: provided the magnetotelluric profile featured in the final section of the chapter.

Chris Dale: instructed me in Re-Os clean laboratory methods

Simon Jackson: provided key advice and training in LA-ICP-MS methods and analysed 20% of the xenocryst garnets via LA-ICP-MS.

Gordon Irvine: performed the Re-Os analyses on the Jericho xenoliths.

Maya Kopylova: provided the Jericho xenolith samples.

1.2.3 Chapter 5

I performed the Re-Os, EMP and LA-ICP-MS analyses and wrote the manuscript as a whole, passing it to Bruce Kjarsgaard and Graham Pearson for review, which did not alter the main geological conclusions.

Co-author contributions:

Bruce Kjarsgaard, as second supervisor, conceived the project and provided helpful feedback on manuscript drafts.

Graham Pearson co-conceived the project and provided guidance with initial EMP analysis problems at Birkbeck. He provided helpful feedback on manuscript drafts and helped in formatting the Mg#-depth plots.

Chris Dale instructed me in Re-Os clean laboratory methods

2 CONSTRAINTS ON THE DEPTH AND THERMAL HISTORY OF CRATONIC LITHOSPHERE FROM PERIDOTITE XENOLITHS, XENOCRYSTS AND SEISMOLOGY

This chapter has been published in full in *Lithos:* 125, pp 729 – 742

2.1 INTRODUCTION

The estimation of palaeogeotherms from mantle xenolith pressure – temperature (P–T) data has been an integral part of studying the ancient roots of continents for over 30 years (Boyd, 1973). While thermobarometry methods have steadily evolved and have been subject to intense scrutiny (e.g., Brey & Köhler, 1990; Finnerty & Boyd, 1984; Nimis and Grütter, 2009), the most commonly-used method for estimating mantle palaeogeotherms from these P–T data has remained the same (Pollack & Chapman, 1977). This is surprising in the light of improved understanding of the thermal properties of the lithospheric mantle (e.g., Hofmeister, 1999; Jaupart et al., 1998), and advancing computational techniques. There have been multiple efforts to formulate more accurate palaeogeotherms (e.g. McKenzie and Bickle, 1988; McKenzie et al., 2005; Michaut et al., 2007; Rudnick and Nyblade, 1999; Russell et al., 2001) but these are often specific to particular localities and datasets, and have not been widely adopted. In this contribution, we compare the extensively-used Pollack and Chapman (1977; PC77) formulation that is usually fitted to data in a qualitative manner, with a modern, numerical palaeogeotherm fitting program, *FITPLOT* (McKenzie and Bickle, 1988; McKenzie et al., 2005) that can be applied to P–T data from a variety of localities. In this way, we aim to show the limitations of the PC77 approach, as commonly used by petrologists, and highlight the advantages of using more quantitative fitting methods to estimate palaeogeotherms from peridotite xenolith data.

We show how these more quantitative fits allow objective evaluation of different models for regional lithosphere evolution, using a specific case study. In addition, the quantitative nature of the fitting method we adopt allows an evaluation of the relative accuracy and precision of palaeogeotherms derived from single-cpx xenocryst chemical data versus those derived from multi-phase peridotite xenoliths.

We also compare seismically-obtained geotherm parameterizations (c.f. Priestley and McKenzie, 2006) to those made using peridotite xenolith thermobarometry, to evaluate alternate methods of obtaining lithosphere thickness and thermal properties.

2.2 MANTLE PALAEOGEOTHERMS

Mantle palaeogeotherms derived from peridotite xenolith thermobarometry can be used to directly estimate information about the properties of the lithosphere at the time of eruption of the kimberlite, such as lithospheric thickness and thermal state. A geotherm is a description of the changing temperature of the Earth between the surface and the convecting mantle interior. Temperature increases fairly rapidly with depth within the crust; then reduces to a more linear gradient increase in the lithospheric mantle. The mantle lithosphere — where the Rayleigh number is much less than critical and therefore heat is transported by conduction— moves rigidly with respect to the crust above and is known as the Mechanical Boundary Layer (MBL; McKenzie and Bickle, 1988). As the geotherm curve approaches the ambient temperature of the asthenosphere, the gradient increases until it is parallel with the asthenospheric isentrope. The region in which this occurs has a Rayleigh number close to critical and is known as the Thermal Boundary Layer (TBL). Within this layer, heat is transported by both conduction and convection. The base of both these different regions of heat-flow (MBL, TBL) can be used to define different types of lithosphere. In this study we use the general term "lithospheric thickness", to be consistent with common terminology used in mantle geotherm studies. This "lithospheric thickness" is the depth where the projection of the MBL (i.e. conductive) geotherm intersects the isentrope; this value falling within the TBL (see: Michaut et al.,

2009, their Fig. 1). As pointed out by Rudnick and Nyblade (1999), any geotherm which does not meet the isentrope cannot be an accurate description of the way in which heat is conducted between the asthenosphere (represented by the isentrope) and the surface of the Earth.

Many of the PC77 palaeogeotherms that appear to fit peridotite xenolith P–T datasets (30 – 40 mWm^{-2}) do not cross the isentrope at any point and therefore it is not possible to estimate lithospheric thickness from the intersection of the geotherm with the isentrope. In these cases, other methods must be used to assess lithosphere thickness, such as the deepest xenolith erupted (Finnerty and Boyd, 1984). It is unlikely that kimberlites sample the lithosphere in a consistent and representative manner; this is clear from the variable spread in P–T data points produced by different kimberlite localities. Therefore, it is difficult to assess the accuracy of lithosphere thicknesses estimated using this method. A further problem is that PC77 palaeogeotherms are not unique for a given P–T array because they are calculated without reference to the P–T data, and the best–fit is estimated qualitatively by eye. As a result, two PC77 palaeogeotherms, with different surface heat flow, will often appear to fit the P–T data array equally well. Together, these problems create significant uncertainty when using PC77 palaeogeotherms as a tool for investigating craton evolution and diamond potential. Despite the lack of quantitative application of the PC77 formulation by many petrologists, far-reaching conclusions are often made on the basis of evidence provided by such palaeogeotherms, regardless of the fact that they were not initially intended for this purpose.

A palaeogeotherm formulation that is calculated using P–T data, that intersects the convecting mantle isentrope, and which provides some estimate of its accuracy would improve our assessment of the properties of the lithospheric mantle obtained using

xenolith data. We aim to compare the results of such a quantitative fitting method: *FITPLOT* (McKenzie and Bickle, 1988; McKenzie et al., 2005) with those obtained using the commonly applied PC77 approach and other techniques, in order to assess its potential as a tool for evaluating the thermal evolution of cratonic regions. We evaluate the effects on resultant estimates of the lithosphere thickness and other palaeogeotherm parameters (e.g. shape, "diamond window" thickness and heat flow). We also use the ability of the *FITPLOT* technique to produce unique palaeogeotherm fits from individual P–T arrays to quantitatively investigate the effects that using a) different thermobarometer combinations, b) non-equilibrated xenoliths, and c) xenolith-and xenocryst-derived P–T estimates have on the shape of the palaeogeotherm.

2.3 METHODS

2.3.1 Xenolith and Xenocryst Suites

Data from four suites of garnet peridotite xenoliths and two suites of single-cpx xenocryst data are used. These suites were chosen based on the abundance of samples from a wide range in depth, and, for two localities, the availability of complimentary xenocryst data for comparison. Published xenolith suites used are from Finsch (Gibson et al., 2008; Lazarov et al., 2009; Skinner, 1989), Bultfontein (Boyd and Nixon, 1978; Simon et al., 2007), Somerset Island (Schmidberger and Francis, 1999; Schmidberger, 2001), and Gibeon (Boyd et al., 2004; Franz et al., 1996a; Franz et al., 1996b). In addition to these, new mineral chemical data are included in this study from Somerset Island.

We use clinopyroxene xenocrysts from Somerset Island and Bultfontein, which have been screened for peridotitic association (2.3.3.3). The Somerset Island dataset is from this study, and the Bultfontein xenocryst dataset was obtained courtesy of DeBeers.

2.3.2 Computation of the palaeogeotherm, and previous computation-based palaeogeotherm fits

We re-calculated P–T estimates from xenolith major-element data, rather than using published P–T values. Fe^{3+} content of constituent minerals was assumed to be zero. The spreadsheet 'ptexl3' was used to calculate pressures and temperatures which were then used as input data for palaeogeotherm fitting using the *FITPLOT* program.

FITPLOT, was written by McKenzie in 1988 (McKenzie and Bickle, 1988), and expanded by McKenzie et al. (2005); a more comprehensive description of the way that the geotherm is calculated can be found there. In brief, *FITPLOT* uses equations describing the thermal properties of the lithospheric mantle, together with a range of input parameters for the crust and mantle (Section 2.3.3) to iterate a series of discrete palaeogeotherms with varying Mechanical Boundary Layer (MBL) thicknesses. In this MBL, thermal conductivity varies with temperature. In the TBL, the temperature variation with depth depends on the viscosity.

Importantly, the quantitative fit to the P–T data is obtained by calculating the misfit for each of these calculated palaeogeotherms to the input P–T array, using a root mean square distribution of ΔT from the calculated palaeogeotherm line. The palaeogeotherm output by the program is that which shows the lowest misfit (ΔT) with the input P–T data. Additionally, the lithospheric thickness and other key parameters such as crustal heat flow and heat flow through the Moho are also generated as outputs by *FITPLOT*

In contrast to *FITPLOT*, the principle independent variable within PC77 palaeogeotherm formulations is the heat flow at the Earth's surface. They are curved within the crust and upper part of the lithosphere, and their gradients increase dramatically at depth, especially at low crustal heat flow values.

There are several advantages of a scheme that attempts a best-fit of P–T data to calculated geotherm parameters, such as *FITPLOT* and the approaches of Rudnick and Nyblade (1999), Russell et al. (2001) and Michaut et al. (2007), over the use of PC77 formulations. Firstly, they use more recent approximations for the thermal structure of the lithosphere, and numerical calculation methods that were not used in PC77. Particular to *FITPLOT* is the ability to produce a 'xenolith misfit' value as an output parameter; a quantitative estimate of how well the output palaeogeotherm fits the P–T array. Quantitative estimates of the fit of PC77 palaeogeotherms to available data are possible, but not normally attempted. The calculated misfit (± ΔT) can be used to provide an estimate of the precision of the palaeogeotherm fit, to infer uncertainty on other output values such as the lithospheric thickness, and also allow quantitative assessment of the similarity of palaeogeotherms from different localities.

2.3.3 Inputs

2.3.3.1 Pressure–Temperature Estimates

Nimis and Grütter (2009) have extensively discussed the accuracy of geothermometer and geobarometer combinations applicable to mantle peridotites, and suggested a best practise

that should be implemented when calculating pressures and temperatures from xenolith mineral chemical data. We test the effect of their guidelines on the resulting palaeogeotherm by comparing the shape and outputs from the *FITPLOT* palaeogeotherm fits.

We have calculated P–T estimates using the lherzolite thermobarometer combinations of Taylor (1998) and Nickel and Green (1985; hereafter TA98_NG85), and Brey and Köhler (1990; BK90_BK90). We also use the newly modified orthopyroxene–garnet harzburgite thermometer of Nimis and Grütter (2009; NG09_NG85), and the single–clinopyroxene (cpx) thermometer and barometer of Nimis and Taylor (2000; NT00_NT00) for our xenolith data. As well as providing an independent test of garnet-orthopyroxene barometry, as proposed by Bell et al. (2003), it also allows us to directly compare the precision of xenolith– and xenocryst–derived palaeogeotherms.

2.3.3.2 Errors in Pressure-Temperature Estimation

Taylor (1998) lists the errors associated with some of the commonly-used thermometers and barometers. These errors relate to the precision of the geothermometer or barometer calibration and are not necessarily correlated.

Additional, but rarely investigated uncertainties arise from counting statistics, instrumental drift and noise during electron microprobe analyses of mineral oxides. These are an external error, unrelated to internal stoichiometry of the minerals. We have taken the average standard deviation (1σ) for each oxide in each mineral measured on a modern microprobe (Cameca SX100; total peak time: cpx: 290 seconds; opx: 300 seconds; gt: 260 seconds). It is important to note that in some cases — especially where very short counting

times are used — that the standard deviations may be significantly higher than those used here. Hence, larger errors may be evident in some xenocryst-derived geotherms that largely reflect analytical protocols rather than deficiencies in the thermobarometer.

These average instrumental uncertainties are used to calculate a range of mineral compositions around the average value, yielding slightly modified mineral compositions. From these new mineral compositions, the associated P–T was calculated using the methods outlined above. Varying each oxide composition up or down by 1, 1.5 and 2 standard deviations away from the mean yields a range of different possible mineral compositions, resulting in a 'cloud' of data points in P–T space. It should be noted that these errors are correlated. Error correlations have not been taken into account in the 'xenolith misfit' values on the palaeogeotherms.

Although the above method is a simplification, it maps out the way in which uncertainties correlate in P–T space, and therefore gives a greater appreciation of the likely uncertainties relating to particular data points than simply stating the geothermobarometer calibration errors. Nonetheless, we have shown the published calibration errors (Brey and Köhler, 1990, Nickel and Green, 1985, Nimis and Taylor, 2000, Nimis and Grütter, 2009, Taylor, 1998) as lines on the palaeogeotherm plots, along with the P–T range in which the thermometers and barometers were calibrated. This allows ready identification of data points lying outside this calibration range.

From consideration of these analytical errors, we find that for the TA98_NG85, NT00_NT00 and BK90_BK90 thermobarometer combinations, the slope of the error correlation varies from low P–T samples to high P–T samples (Figure 2.2). In addition, for these thermobarometers, the magnitude of the uncertainty increases with decreasing P and T.

The exception is the NG09_NG85 combination, where analytical uncertainties result in rather uniform correlated errors of relatively constant slope (Figure 2.2).

2.3.3.3 Evaluating Equilibrium

Of particular interest with respect to defining palaeogeotherm shape is the definition by Nimis and Grütter (2009) of 'equilibrated' and 'non–equilibrated' samples (with respect to inter–mineral equilibrium) within the xenolith dataset. It is important to be certain that the P–T estimates used to estimate palaeogeotherms represent the lithosphere at the time of kimberlite eruption, and have been minimally disturbed by recent events. The degree of inter-mineral equilibrium is defined in two ways: pyroxene equilibrium is estimated from the magnitude of the variation between temperature estimates calculated using two thermometer combinations; the NT00 single-cpx thermometer and the TCa-in-opx thermometer. Garnet–pyroxene equilibrium is estimated by the magnitude of the variation between the new NG09 thermometer and the NT00 thermometer. A more extensive discussion on xenolith disequilibrium is presented by Nimis and Grütter (2009).

We use the above criteria to select and exclude xenolith samples from the dataset that are not in equilibrium, and comment on the effect that this has on the calculated palaeogeotherm shape and the degree of fit to the P–T data.

In the same way, xenocryst data were screened according to the guidelines of Nimis (1998) and Grütter (2009, their Appendix B) to select grains that are in equilibrium and of peridotite paragenesis; this resulted in the culling of 45% (Somerset) to 48% (Bultfontein) of the data.

Any samples with mosaic porphyroclastic or porphyroclastic textures (Harte, 1977), or containing metasomatic minerals such as mica or amphibole were defined as 'porphyroclastic' samples and were excluded from the 'granular' sample dataset.

The definitions of Nimis and Grütter (2009) regarding inter-mineral equilibrium were strictly obeyed. If a sample showed either pyroxene disequilibrium or garnet-pyroxene disequilibrium — or both — it was discarded from the subsequent 'equilibrium' dataset. It should be noted that the majority of samples excluded in this way showed only one type of disequilibrium (e.g. showed pyroxene, but not garnet-pyroxene, equilibrium).

2.3.3.4 Mantle Input Parameters

2.3.3.4.1 Heat Production

There has been significant discussion on the problem of accurately estimating the heat produced within the lithospheric mantle (Jaupart and Mareschal, 2007; Michaut et al., 2007; Rudnick et al., 1998; Rudnick and Nyblade, 1999). We note that Michaut et al. (2007) show that the highest probability density of geotherms modelled with realistic lithosphere thicknesses require mantle heat production to be ≤ 0.02 μWm^{-3}, and that Rudnick and Nyblade's best–fitting Kalahari geotherm has a lithospheric heat production of 0 μWm^{-3}. Rudnick et al. (1998) outline various reasons why determining lithospheric heat production from measurements of heat producing elements (HPEs) in xenoliths is essentially arbitrary. This is due to the difficulty in quantifying the effect of secondary addition of these elements (K, U, Th) to the xenolith during metasomatism and the emplacement of the host kimberlite. While heat production in the lithosphere can be varied within *FITPLOT*, we

have chosen to use Rudnick and Nyblade's best-fitting value of 0 μWm^{-3}. Therefore, when calculating the palaeogeotherm to fit to the data, *FITPLOT* assumes that the heat flux through the base of the lithosphere is the same as the heat flux through the Moho. Assuming a heat production in the lithosphere of 0 μWm^{-3} — consistent with the above studies — reduces the problem outlined by Michaut et al. (2007) of long-wavelength thermal transients in thick, cooling lithosphere. They suggest that these transients will artificially shallow xenolith–based estimates of lithospheric thickness. With no heat production in the lithospheric mantle, such transient thermal effects are minimized unless the lithosphere initial thickness is very large (> 400 km, see Michaut and Jaupart, 2007; their Fig. 6)

2.3.3.4.2 Potential Temperature

The mantle parameters outlined are considered to be broadly uniform on a global scale, and have been kept constant between different localities for consistency. We have used Tp = 1315 °C for the asthenospheric isentrope, which accounts well for the globally constant 7 km thickness of oceanic crust generated at mid-ocean ridges (McKenzie and Bickle, 1988). The error in this value can be estimated from the variation in oceanic crustal thickness worldwide, which has a standard deviation of about 1 km. This translates to a variation in potential temperature of about 13 °C (McKenzie and Priestley, 2008). On our figures, 13 °C is approximately the thickness of the isentrope line. In addition, Katsura et al. (2010) used the olivine – wadsleyite transition to estimate the mantle potential temperature and yielded almost the same value, within error (1337 ± 37 °C)

It is possible that the mantle potential temperature might be higher than the steady-state value beneath the oceans at the time of kimberlite emplacement (Mitchell, 1984; Sleep,

2003). However, the increase in temperature would have to be small; large changes would alter the nature of melting regime at the base of the lithosphere and small-volume, volatile-rich kimberlitic melts would not be produced, being swamped by larger melt fractions e.g. McKenzie and Bickle (1988).

2.3.3.5 Crustal Input Parameters

The ability to vary crustal thickness, the proportion of upper and lower crust and their heat flow properties is important for any accurate palaeogeotherm estimation. In some previous studies, the thermal properties of the crust have been identified as a significant source of uncertainty when calculating cratonic palaeogeotherms (Russell et al., 2001) and often this complexity has not been included in an effort to increase accuracy. Rudnick and Nyblade (1999) used generalised global heat production values for Archean crust in their model.

We attempt to use the best available local estimates for the structure of the crust and its heat production to obtain the most appropriate mantle palaeogeotherm.

2.3.3.5.1 Crustal Thickness

FITPLOT assumes a two-layer crust with independent heat generation parameters, rather than a model where the estimated bulk crustal heat production is distributed between layers of equal thickness (c.f; Rudnick and Nyblade, 1999). This enables us to independently modify the upper and lower crustal thicknesses to satisfy available seismic refraction studies, while keeping the total crustal thickness the same to match crustal thicknesses derived from local receiver function analyses.

The seismic structure of the crust beneath Southern Africa and the Kaapvaal craton (Finsch, Bultfontein) and the Proterozoic crust of the Rehoboth Terrane (Gibeon) are well constrained via the Kaapvaal project (James et al., 2001; Nguuri et al., 2001) as well as other large- and small-scale seismic refraction studies (Baier et al., 1983; Durrheim and Green, 1992; Green and Durrheim, 1990). For Somerset Island fewer direct studies are available (Bank et al., 2000; Darbyshire, 2003), but there are many seismic investigations of the crust in other parts of the Superior and Slave cratons that can be used to estimate crustal thickness and structure (Cook et al., 1999; Snyder, 2008).

Our crustal thickness estimates are within the range of values used in previous studies of the thermal structure of the lithosphere in these regions. Rudnick and Nyblade (1999) used a 41 km thick crust for all their geotherms, regardless of locality. Michaut and Jaupart (2007) and Michaut et al. (2007) used 35 km for crustal thickness in their modelling of the thermal structure of the cratonic lithosphere, which is similar to our values. While this is an appreciable difference in total crustal thickness (~ 6 km), our upper crustal thicknesses are similar to those used by Rudnick and Nyblade (1999). Since the upper crust produces significantly more heat than the lower crust, we suggest that this difference may not significantly affect comparisons between the palaeogeotherms

2.3.3.5.2 Heat Production

The crustal heat production values (Table 2.2) have been determined by using best estimates from both thermal modelling of the lithosphere (e.g. Michaut et al., 2007) and from combining seismic refraction studies (Baier et al., 1983; Durrheim and Green, 1992; Green and Durrheim, 1990) with laboratory estimates for seismic velocities and heat production of different crustal materials (Rudnick and Fountain, 1995; Taylor and

McLennan, 1985) to estimate compositional structure. Our chosen values are within the range of similar studies (Michaut et al., 2007; Rudnick and Nyblade, 1999).

2.4 RESULTS AND DISCUSSION

2.4.1 Comparison of palaeogeotherm shapes and resulting lithospheric thicknesses obtained using the FITPLOT, Rudnick and Nyblade (1999) and PC77 methods.

The shape of the palaeogeotherm fitted using the *FITPLOT* methodology is quite distinct from other constructions. For comparison, the TA98_NG85 xenolith P–T array from Bultfontein, with the closest-fitting PC77 palaeogeotherm (43 mWm^{-2}), the calculated *FITPLOT* output, and the best-fitting 'Kalahari' geotherm calculated by Rudnick and Nyblade (1999; RN99) are shown in Figure 2.1. In addition, although they are not directly comparable, the computed time-integrated geotherms of Michaut et al. (2009; M+09) are also plotted.

The most obvious difference between the resulting palaeogeotherm estimates is that the PC77, M+09 and RN99 formulations all indicate thicker lithosphere than the *FITPLOT* method (Table 2.1), with the PC77 estimate being 44km thicker than the *FITPLOT* estimate. The distinct shape of the *FITPLOT* palaeogeotherms is the result of 1) the ability of *FITPLOT* to model the change in temperature with depth within the TBL, which is absent in the other models, 2) the assumed absence of heat production within the lithosphere, and 3) the inclusion in the *FITPLOT* method of the term for the temperature dependence of

thermal conductivity ($k=k(T)$). A further refinement to *FITPLOT* is the possibility to include a pressure dependence for thermal conductivity. Recent experimental results have shown that thermal conductivity in mantle minerals may also vary with pressure (Osako et al., 2004). To assess the potential importance of this result we made several geotherm fits including this term and found that the resulting fits were within error of the fits made using only temperature-dependence.

In the RN99 and PC77 models, heat flow at the surface is a primary contributor to the modelled heat flow through the lithosphere, in a 'top-down' approach. In these models, surface heat flow is reduced to the amount of heat flowing through the Moho by the linear relationship proposed by Birch et al (1968) between heat flow and the vertical distribution of heat production in the crust. Jaupart and Mareschal (2007) suggested that this relationship could not account for the highly variable nature of Archean crust, and that surface heat flow reflects only shallow differences in heat production. The Birch et al. (1968) relationship is not used by *FITPLOT* to estimate heat flux at the Moho, and contributes to the distinct difference in estimated palaeogeotherm shape. This also goes some way to explain the higher surface heat flow estimated by the *FITPLOT* method, as surface heat flow is an output of the palaeogeotherm calculation and is not fixed to measured values. Surface heat flow in both the Kaapvaal and at Somerset Island estimated using *FITPLOT* is in the range 51 – 58 mWm^{-2}, which is significantly higher than that measured for Archean cratons worldwide (41 ± 11 mWm^{-2}; Rudnick et al., 1998). We attribute this difference in part to the crustal parameters that we have input, since the Moho heat flux estimated using *FITPLOT* is within the ranges used in the other approaches (Table 2.1).

Surface heat flow and mantle xenolith P–T estimates are independent primary controls for estimating the palaeogeotherm. Since the measured values of surface heat flow reflect the thermal structure of the lithosphere today, and mainly reflect the thermal state of the crust and shallow lithosphere (Jaupart and Mareschal, 2007), we consider xenolith P–T estimates as a more robust primary control with which to fit a geotherm model.

2.4.2 Constraining the geotherm using different thermobarometer combinations

The quantitative fitting of *FITPLOT* palaeogeotherms to xenolith data allows an objective assessment of the effect of different thermobarometer combinations on the palaeogeotherm shape and output parameters. Using the three different recommended thermobarometer combinations of Nimis and Grütter (2009; see: 2.3.2.2) as well as the extensively used Brey and Köhler (1990) formulation, we produce a series of P–T arrays for the Somerset Island dataset (Figure 2.2; 2.3) in order to investigate whether the palaeogeotherms calculated from these P–T arrays are significantly different. We use the Somerset Island dataset because it contains the highest number of xenolith samples and shows the widest range in depth estimates of the datasets in this study.

It has been shown previously that the absolute P–T values generated by the different thermobarometer formulations vary for any given sample (Bell et al., 2003; Brey and Köhler, 1990; Finnerty and Boyd, 1984; Nimis and Grütter, 2009). Here, our focus is to examine how these resulting differences affect the shape of the calculated geotherm and the resulting derived parameters such as lithospheric thickness and surface heat flow. We recognise that the inter-dependence of P–T calculations naturally result in correlated data

arrays in P–T space, but this effect is seen in all iteratively-calculated P–T estimates. Accepting that the data are correlated, we examine how well these arrays approximate a geotherm, using the xenolith misfit value unique to *FITPLOT*.

Similar palaeogeotherms might be expected for the NG09_NG85 and TA98_NG85 combinations since they use the same barometer, but not for the NT_NT combination which is based only on cpx composition. We observe no significant difference between palaeogeotherms calculated using the three recommended thermobarometer formulations (Figure 2.3). The Brey and Köhler (1990) formulation yields shallower lithosphere thickness estimates than the other formulations (156 km vs. 163 – 165 km); but it is still within their xenolith misfit envelopes.

Notably, the TA98_NG85 and NG09_NG85 estimates show smaller xenolith misfits, and therefore yield more precise estimates of both the thickness of the lithosphere and the diamond window compared to the single grain cpx thermobarometer (Table 2.2) and the formulation of Brey and Köhler (1990). This result quantitatively confirms the findings of Nimis and Grütter (2009), i.e. all three recommended thermobarometer combinations tested yield the same palaeogeotherm, within error; thus indicating that they produce a similar P–T array even though the individual P–T values vary.

Subsequent comparative tests will only use palaeogeotherms calculated using the TA98_NG85 thermobarometer combination, which Nimis and Grütter (2009) suggest is the most accurate.

2.4.3 Lherzolite vs. harzburgite thermometry and palaeogeotherm shape

Some mantle xenolith suites are dominated by harzburgites (Wittig et al., 2008). In these cases, the only way to obtain temperature estimates, for palaeogeotherm estimation, is to use opx-gt Fe-Mg exchange thermometry ("harzburgite thermometry"). The accuracy of these formulations has been questioned, due to the inability to account for the effects of the oxidation state of Fe^{3+} on Fe-Mg equilibrium (Canil and O'Neill, 1996; Nimis and Grütter, 2009). Differences in absolute P–T estimates using harzburgite versus lherzolite thermometry are clear, but the effect of these differences on resulting palaeogeotherms has not been quantitatively evaluated.

Here, we have calculated pressures and temperatures for a suite of lherzolite xenoliths using both harzburgite thermometry (ignoring the cpx) and lherzolite (using both cpx and opx) thermometry and compare the resulting palaeogeotherms obtained using *FITPLOT*. The suite of xenoliths from Somerset Island is again selected for this exercise due to the large dataset and large spread in P–T values.

While — as expected — there are differences in the individual xenolith P–T estimates obtained using harzburgite (NG09_NG85) or lherzolite (TA98_NG85) thermometry, there is no significant difference, outside of our estimated uncertainty, between the calculated palaeogeotherms (Table 2.2, Figure 2.3). For instance, the thickness of lithosphere in each case is the same, 163 km, and the surface heat flow only varies by 0.2 mWm^{-2}. We therefore suggest that it might be feasible to combine P–T estimates from these two thermobarometer combinations without noticeable deterioration in the shape of the palaeogeotherm. Taking

this approach would significantly increase the number of samples available for palaeogeotherm estimation at some locations (e.g. Sand et al., 2009)

We have not investigated whether combinations of other lherzolite geothermometers and barometers would show the same result with the harzburgite geothermobarometer combination of NG09_NG85.

2.4.4 'Disequilibrium' vs. 'Equilibrium' samples

Nimis and Grütter (2009) define parameters with which to distinguish xenolith samples that are not in inter-mineral equilibrium, and are therefore unsuitable for P–T estimation using formulations based on equilibrium thermodynamics. We identified and removed the P–T data points from such xenoliths from the Somerset Island and Bultfontein xenolith P–T suites. Palaeogeotherms calculated from these filtered datasets were plotted using *FITPLOT* and compared to the palaeogeotherm obtained from the full (unfiltered) dataset, which includes both equilibrium and disequilibrium samples (Figure 2.4, Table 2.3).

There is minimal difference between the resulting palaeogeotherms such that they are indistinguishable on Figure 2.4, and resulting lithospheric properties are similar (Table 2.3). Their xenolith misfit envelopes overlap, but the misfit for the filtered dataset is smaller in both cases. This indicates that samples showing inter-mineral disequilibrium contribute to the scatter on a P–T array, and that removing these samples produces a more precise palaeogeotherm estimate, and therefore more precise estimates of lithosphere thickness. We will therefore use only equilibrated samples in all further discussions.

The Somerset Island and Bultfontein datasets both have their deepest, equilibrated xenolith at 140 – 150 km. It is about this depth where the *FITPLOT* palaeogeotherms begin to differ substantially from the other palaeogeotherm estimations (Figure 2.1) and so we investigated whether a *FITPLOT* palaeogeotherm calculated from a deeper P–T array would show a similar increase in precision to that seen in the Somerset Island and Bultfontein datasets. To do this, we calculated palaeogeotherms for peridotite xenoliths from Finsch, in the Kaapvaal craton (Gibson et al., 2008; Lazarov et al., 2009). This suite contains xenoliths from > 180 km, and has been cited as a deep and unperturbed P–T array (Bell et al., 2003) and can be compared to the well-constrained Bultfontein example.

The difference between the resulting "equilibrium" palaeogeotherm and the palaeogeotherm from the full dataset was larger than that for either Somerset Island or for Bultfontein (Figure 2.5**A**). Samples that appear not to be in inter-mineral equilibrium yield systematically higher P–T than equilibrium samples at this location, and therefore excluding them from the 'equilibrium-only' dataset results in a slightly shallower palaeogeotherm (Figure 2.5**A'**). While the difference in lithosphere thickness and 'diamond-in' depth are within error in both cases, the result shows more clearly the potential effects of inter-mineral disequilibrium. Moreover, this analysis indicates that the suggestions that some Finsch peridotites may originate from depths close to 200 km (Finnerty & Boyd, 1984; Gibson et al., 2009) may be the result of inter-mineral disequilibrium.

Another obvious feature of the Finsch P–T array is that it lies at a high angle to the *FITPLOT* palaeogeotherm. Since this effect is not removed upon screening out samples showing disequilibrium, it implies that some other mechanism is responsible for the unusual nature of the P–T distribution, or that the Finsch P–T array does not approximate

to a steady-state geotherm, as assumed by the *FITPLOT* program. Other palaeogeotherm formulations (e.g. Figure 2.1) have steeper gradients than those calculated using the *FITPLOT* methodology, resulting partly from the assumption in the *FITPLOT* routine that the lithospheric mantle heat production = 0 μWm^{-3}. The steeper gradient of the Finsch array than the *FITPLOT* palaeogeotherm could thus reflect an underlying lithospheric mantle with a heat production greater than 0 μWm^{-3}. *FITPLOT* was modified to see if an increase in the heat production of the lithospheric mantle would yield a palaeogeotherm that better fits the Finsch P–T array.

We estimated the heat production beneath Finsch by averaging the K_2O contents of the clinopyroxenes that were above the quantification limit (0.04 wt%), and that were shown to be in inter-mineral equilibrium. Core compositions were used, to minimize the effect of late-stage cryptic metasomatism. We obtained an average value of 0.05 wt% K_2O for Finsch Diopside, to which we applied the approximation of Rudnick et al. (1998; their Figure 1) to obtain a lithospheric heat production of 0.05 μWm^{-3}. This value is within the range of plausible heat production values for cratonic mantle used by Michaut et al. (2007) and Rudnick and Nyblade (1999), and was used this value as an input parameter in the *FITPLOT* palaeogeotherm fitting routine.

The newly calculated palaeogeotherm fit shows a decreased xenolith misfit in comparison to the fit where lithosphere heat production = 0 μWm^{-3} (Figure 2.5***B***). The data lie along the model palaeogeotherm, instead of oblique to it. We therefore suggest that the high angle of the Finsch P–T array to the *FITPLOT* palaeogeotherm estimation might be due to locally higher mantle lithosphere heat production. However, it is very important to note the limited depth range of the Finsch array, the limitations on the input values for the palaeogeotherm calculation, and the errors on the P–T estimates themselves. We cannot

say for certain that this increased fit is due to higher heat production until samples of the shallower lithosphere become available for study. Nonetheless, there are other features of the Finsch kimberlite that support this tentative hypothesis.

Clinopyroxene from Finsch xenoliths indicate elevated K_2O (dependent on bulk composition, as well as pressure e.g., Harlow (1997), relative to other suites, and this is consistent with a more metasomatised mantle that gives higher heat production in the lithosphere beneath. Furthermore, the Finsch kimberlite host rock is an orangeite (Mitchell 1995) i.e. a Group II kimberlite (Smith et al, 1983). These magmas are systematically more enriched in incompatible trace elements than Group I kimberlites, consistent with an origin within enriched cratonic lithospheric mantle (Smith et al., 1983). Hence, the composition of the cpx and the nature of the host magma support the suggestion that the lithospheric mantle beneath Finsch was more enriched in HPE at the time of eruption, 120 Ma ago.

2.4.5 Effect of P–T array population size on the shape and precision of the palaeogeotherm.

The datasets we are using to define the palaeogeotherms are small (generally < 50 samples) and therefore filtering of datasets could potentially have significant effects on the resulting geotherm. To evaluate the sensitivity of the *FITPLOT* fitting method to sample population size, the P–T points in the Somerset Island array were given individual reference numbers. A random numbers table was used to select 20 samples for removal from the dataset (this being an average number of samples removed by any of the above data filtering tests).

This process was repeated 10 times, and we examined the resulting palaeogeotherms and xenolith misfits for any systematic effect.

The lithospheric thickness estimates from all 10 tests vary by only 6 km. The xenolith misfit value obtained is quite variable, but shows no systematic effect as a result of the removal of P–T points. Therefore we conclude that the increased precision resulting from the removal of the 'disequilibrium' xenoliths is due to the properties of those xenoliths, rather than an artefact of decreasing the number of points in the P–T array.

2.4.6 Xenolith versus Xenocryst Palaeogeotherms

In diamond exploration, mantle xenolith data is sparse and an assessment of the thermal structure of the lithosphere beneath exploration targets is usually made using single-crystal mineral compositions from xenocrysts. Peridotite-derived xenocrysts have the advantage over xenolith data in that a significant number of P–T points can be obtained quickly and inexpensively from analysis of single-grain mounts (Grütter, 2009). It has been previously demonstrated in (2.4.2) and by Nimis and Grütter (2009) that the NT_NT single-cpx thermobarometer performs well in comparison to mineral-exchange formulations when used on xenolith clinopyroxene. Xenocryst data tends to be more scattered in P–T space, and this makes it difficult to choose a best-fitting PC77 palaeogeotherm by eye. We apply quantitative palaeogeotherm fits to xenocryst data from Somerset Island and Bultfontein and compare this to the xenolith-derived, equilibrated, granular, TA98_NG85 *FITPLOT* palaeogeotherms from the same locality.

In general, the unfiltered xenocryst datasets produce much more scattered P–T arrays and palaeogeotherms with very large xenolith misfits: ΔT = 167 °C for the Somerset Island array and 157 °C for the Bultfontein array. Filtering these data (utilizing the compositional screens of Nimis, 1998, and Grütter, 2009) significantly reduces the misfit, to 66.9 °C and 97.8 °C for Somerset Island and Bultfontein, respectively. The filtered xenocryst P–T array from Somerset Island yields a palaeogeotherm (solid black line, Figure 2.6***A***) that is almost identical to that produced from the equilibrated, granular xenoliths (red dashed line, Figure 2.6***A***). In the case of the much larger Bultfontein xenocryst dataset there is a distinct difference between the palaeogeotherm derived from the filtered xenocryst P–T data (196 km lithospheric thickness) and the equilibrated, granular xenolith P–T data (181 km), that is outside the xenolith misfit envelope of the xenolith data (red shaded region, Figure 2.6***B***). This result would produce a potentially misleading estimate of the size of the "diamond-window" at Bultfontein if only the xenocryst data were used to estimate this parameter. However, these results may reflect the relatively short counting times used to obtain the large dataset in Figure 2.5***B***. Other studies of Bultfontein xenocrysts that employed the same counting times as commonly-used for xenolith-based studies (e.g. Nimis and Taylor, 2000; their Figure 8) produced a xenocryst array that is considerably less scattered in P–T space (see blue shaded region, Figure 2.5***B***).

Considering only the Somerset Island results — where counting times for clinopyroxene microprobe analysis were the same for xenolith and xenocryst — would indicate that filtering clinopyroxene xenocryst compositions considerably increases the accuracy of the single-crystal geotherm estimations, to within error of the xenolith-derived geotherm, in agreement with Grütter (2009).

2.4.7 Quantitative petrological and seismic geotherm constraints on the evolution of the pericratonic lithosphere in southern Africa

2.4.7.1 Petrological evidence

On the basis of comparisons with PC77 geotherms, Boyd et al. (2004) argued that the geotherm beneath the pericratonic Rehoboth terrane in S.W. Namibia was the same as that beneath the Kaapvaal craton, and hence that the lithosphere thickness was the same in both regions at 70 Ma, the time of eruption of the Namibia kimberlites (Spriggs, 1988). This argument has recently been extended to include all lithosphere immediately surrounding the Kaapvaal craton (Janney et al., 2010). Franz et al. (1996b), Mitchell (1984) and Bell et al. (2003) all noted the distinct departure of the off-craton Gibeon porphyroclastic samples from the main array. We investigated the quantitative basis for these hypotheses using palaeogeotherms calculated by *FITPLOT*

The exclusion of (equilibrated) porphyroclastic-textured samples from the off-craton Gibeon P–T array has a systematic and obvious effect (Figure 2.7***C***). The Gibeon porphyroclastic xenoliths cluster at higher-temperatures than their granular, un-deformed counterparts, and removing them from the dataset causes the palaeogeotherm to steepen. A palaeogeotherm calculated using only Gibeon porphyroclastic P–T estimates (shown in Figure 2.7***C***) lies just outside the error envelope of the granular-only samples. This displacement indicates that the lithosphere beneath the Gibeon kimberlite field was not in steady state at the time of kimberlite eruption (Franz et al., 1996a; Mitchell, 1984).

To evaluate the claim that the palaeogeotherms were the same beneath the Kaapvaal craton and the Proterozoic Rehoboth terrane, we compare the equilibrated, granular P–T array from the Gibeon kimberlite field (Franz et al., 1996a, Boyd et al., 2004) with that calculated from equilibrated, granular Bultfontein peridotite P–T estimates (Figure 2.7***B***). The palaeogeotherm fits yield very similar lithosphere thicknesses; 181 km *vs*. 178 km, despite the slight elevation of the Gibeon palaeogeotherm at shallow temperatures. This is due to the increased crustal thickness in the Proterozoic terrane, and implies that while crustal structure and heat production are important when calculating palaeogeotherms — as emphasised by Rudnick and Nyblade (1999) — if the palaeogeotherms are calculated using the *FITPLOT* methodology, the effects of these crustal properties only affect the shallow lithospheric mantle.

From our quantitative palaeogeotherm analysis, we concur with Boyd et al. (2004) that there was a cratonic thermal regime and similar lithospheric thicknesses beneath the Rehoboth terrane and the Kaapvaal craton in the past. However, there has been some modification to this regime prior to the emplacement of the Gibeon kimberlites, shown by the clustering of the porphyroclastic samples at high temperature. This supports the conclusions of Franz et al. (1996b) who suggested that the decoupled P–T array indicates a heating event, associated with deformation of the lower lithosphere. Franz et al. (1996b) suggest that this might be caused by initiation of a failed rifting event, which was recorded in the xenolith suite. It is unlikely that such a transient is reflected in the surface heat flow; for this to occur, the thermal anomaly would have to remain in place for longer than 1Ga to be recorded (Jaupart et al., 1998).

Equally, the systematic distribution of the equilibrated porphyroclastic samples derived from the Namibian lithosphere could be reflecting a changing thermal regime on the edge

of cratonic regions, as proposed by Lenardic and Moresi (2000). They modelled the thermal structure of the lithosphere and upper asthenosphere, taking into account the effect of plate tectonics. They suggest that advection of heat into the thermal boundary layer beneath pericratonic regions, pulled by asthenospheric convection towards postulated downwellings beneath cratons, will counterbalance vertical heat conduction such that an inflected geotherm can be maintained. This effect could be reflected in a systematic displacement of porphyroclastic (sheared) xenoliths to higher pressures and temperatures than the extension of the conductive P–T array. The Gibeon porphyroclastic xenoliths are displaced to higher temperatures than the conductive array but are not displaced to higher pressures. This would indicate that they were not sourced from a boundary region that was distinct from the conductive lithosphere, as proposed by Lenardic and Moresi (2000), and were instead heated 'in situ', as proposed by Franz et al (1996b) and Bell et al. (2003).

Franz et al (1996b) also suggest that the Gibeon harzburgitic samples represent remnants of cratonic lithosphere, perhaps due to an extension of the Kaapvaal lithosphere beneath the Rehoboth terrane. From our palaeogeotherm data of the equilibrated peridotites, we can only conclude that a cratonic thermal regime once existed. We cannot constrain whether or not the lithosphere is an extension of the Kaapvaal craton, or simply a changing thermal regime beneath the Rehoboth terrane through time. However, we note that no indications of an Archean age have been obtained from available Re-Os isotopic data (Pearson et al., 2004).

2.4.7.2 Seismic Estimates

Xenolith–derived palaeogeotherms and lithosphere thickness evaluations can be compared with estimates of lithospheric properties obtained using other methods, e.g. seismics. Southern Africa is well-defined seismically, having been the subject of the Kaapvaal Project (c.f, James et al., 2001). As a result, many estimates of the thickness of the lithosphere in this region have been published using a variety of methods including: receiver function analyses (e.g. Hansen et al., 2009; Niu et al., 2004), shear wave (V_s) inversions (e.g. Priestley and McKenzie, 2006), seismic tomography (e.g. Fouch et al., 2004) and seismic anisotropy (Yuan and Ramanowicz, 2010). In many cases, lithospheric thicknesses obtained from these methods agree well with xenolith palaeogeotherm-derived values. However, seismic receiver function analyses consistently yield shallower estimates than those obtained from xenolith palaeogeotherm data, being on the order of 150 – 160 km versus ~200 km (Bell et al., 2009; Hansen et al., 2009; this study). Yuan and Romanowicz (2010) suggested that the shallow lithosphere thickness estimates produced by receiver function analyses could be identifying an anisotropic and depleted layer that lies within the lithosphere between 0 and 150 km, rather than defining the lithosphere–asthenosphere boundary, thus removing any major conflict between seismological and petrological estimates of lithosphere thickness beneath cratons.

Improved understanding of mineral physics now allows lithospheric geotherms to be calculated from seismic data using the parameterization of shear wave velocity (Vs) as a function of depth and temperature (z, T; Priestley and McKenzie, 2006). We calculated such a "seismic geotherm" for the Gibeon locality studied above in order to try to constrain modern-day lithospheric thickness. This geotherm was plotted using $V_s = f(z, T)$ estimates

from the exact location of the Gibeon kimberlite pipes, and is shown in Figure 2.7. Temperature was estimated at 25 km intervals, and input as P–T data into *FITPLOT*. It should be noted that the parameterization of $V_s = f(z, T)$ was constrained using xenolith P–T data, and the accuracy of lithospheric thicknesses estimated using this method is 20 – 30 km.

The xenolith data from the Gibeon locality indicate a significant thermal disturbance in the lithosphere at the time of kimberlite eruption, recorded in the porphyroclastic xenoliths, as discussed above. The seismic geotherm is a reflection of the lithosphere today and therefore should reflect any large-scale changes in the lithosphere beneath Gibeon since the eruption of the kimberlite.

A notable difference is observed between the seismic and xenolith geotherms, and the resulting lithosphere thickness estimates at Gibeon (Figure 2.7***D***). The V_s geotherm is 55 km shallower, which is outside the error margin of both the xenolith palaeogeotherm (see Figure 7***B***, ***D***) and the seismic geotherm (20 – 30 km). The shallow nature of the present day lithospheric thickness under Namibia estimated from V_s data supports the hypothesis of a thermal event — recorded by the porphyroclastic samples — that caused lithospheric thinning in the peri-cratonic lithosphere to the West of the Kaapvaal craton between 70 Ma and today (Bell et al., 2003; Franz et al, 1996a; Mitchell, 1984). The mechanism behind such thinning cannot be resolved using P–T based xenolith palaeogeotherms, but may be due to the westward-migrating heating event proposed by Bell et al. (2003).

2.5 CONCLUSIONS

We have used a procedure that combines a numerical approach to modelling lithospheric heat flow with quantitative fitting of peridotite xenolith derived P–T data (McKenzie & Bickle, 1988; McKenzie et al., 2005) to generate palaeogeotherms for several well sampled kimberlites. The quantitative nature of the fitting procedure allows objective comparison of different palaeogeotherms, an aspect that is generally missing from typical xenolith-based thermobarometry studies. We demonstrate the potential of *FITPLOT* to produce accurate fits for discrete P–T arrays (2.4.1 – 2.4.7), including those derived from xenocrysts. We also show how it can be used to investigate and constrain problems related to lithosphere evolution, especially when combined with present-day seismic observations. Some of our conclusions amplify, and quantify those arrived at in earlier studies that used non-quantitative geotherm fitting techniques. We expect these conclusions to be generally applicable to other approaches if similar crust and mantle heat generation models are used.

Although different thermobarometer combinations yield differing absolute P–T estimates, for Somerset Island peridotites, the overall P–T array produced — and the subsequent palaeogeotherm calculated using *FITPLOT* — is the same regardless of these differences. This implies that P–T estimates from harzburgites (using the NG09_NG85), and lherzolites (using TA98_NG85), could be combined to increase the data density of a given xenolith P–T array and hence the accuracy of the palaeogeotherm fit. The precision of the *FITPLOT*

palaeogeotherm fit can be improved by screening the xenolith P–T data for disequilibrium samples, as defined by Nimis and Grütter (2009).

For Bultfontein, comparison of geotherms calculated using peridotite xenoliths to those using clinopyroxene xenocrysts (single crystals from disaggregated peridotite) reveals significantly different geotherms and hence lithospheric thicknesses, even after careful data filtering. At Somerset Island; the xenolith and filtered xenocryst palaeogeotherms are similar, but the much greater imprecision of the xenocryst-derived palaeogeotherm makes the significance of this result difficult to assess.

Quantitative testing of previous suggestions that the lithospheric mantle beneath the Rehoboth crustal terrane of Namibia was of equivalent thickness and thermal structure to the main Kaapvaal craton (Bell et al., 2003; Boyd et al., 2004) shows that there are very subtle differences in the shape of the palaeogeotherms, but that the estimated maximum depth of lithosphere at the time of kimberlite eruption is indistinguishable, within the limits of thermobarometry.

We have shown that it is possible to obtain P–T estimates from inversions of seismic surface wave data, and use these to fit a "present-day" geotherm for the Gibeon locality. The seismic geotherm supports the xenolith evidence for a thermal event, which is reflected at the present day by significantly thinner lithosphere. The temporal difference in geotherm constraints offered by kimberlite-derived xenoliths versus seismic observations opens up a powerful new way of studying lithospheric evolution beneath cratons.

3 PRACTICALITIES OF LITHOSPHERIC STRATIGRAPHY ANALYSIS

3.1 LITHOSPHERIC STRATIGRAPHY

The following chapters of this thesis rely, in full or in part, on the construction of lithospheric stratigraphy from xenolith data. That is, the plotting of geochemical characteristics from a particular suite of xenoliths or xenocrysts against estimated depth, with a view to comparing it with available geophysical data and/or lithospheric stratigraphy results from localities across the Slave and other cratons.

Lithospheric stratigraphy is a popular way to investigate the cratonic mantle, and various methodologies have been employed. The more well-publicised of these is the 'geochemical tomography' approach of Griffin et al. (1999a; 2004), where geochemical information from kimberlite-borne garnet xenocrysts is plotted against projected depth. For the Slave craton, these xenocryst tomography plots have been produced (Griffin et al., 1999a), as well as a number of attempts to produce a lithospheric stratigraphy from xenoliths, such as the compilations of Kopylova and Caro (2002, their Figure 13) and Heaman and Pearson (2010).

The purpose of this chapter is to explore the methodology behind lithospheric stratigraphy based on xenolith and xenocryst data, in order to come up with a systematic algorithm for producing lithospheric stratigraphy plots for the Slave craton that take into account the uncertainty in pressure–temperature (P–T) estimates (as explored in 2.3.3.2).

3.2 MAJOR LIMITATIONS TO GEOCHEMICAL LITHOSPHERIC STRATIGRAPHY METHODS

3.2.1 Uneven sampling of the lithosphere by the kimberlite, and use of xenocryst data

It is well known that kimberlites do not sample the lithosphere evenly. In many cases, large regions of the lithospheric column are 'missing' xenolith data, precluding analysis of their composition, age and other geochemical parameters. Alternatively, some regions of the lithosphere are sampled much more densely than others; it is often the case that the shallow lithosphere is more sparsely populated in terms of xenolith samples than the deeper lithosphere.

One way to counter poor lithosphere sampling in terms of xenoliths by the kimberlite is to use xenocryst data from the kimberlite deposits themselves. Xenocrysts are often the result of disaggregated peridotite xenoliths, and therefore depths where xenolith survival is low and lithosphere sampling is poor may have high concentrations of xenocryst data resulting from destroyed xenoliths (Canil, 1990). Additionally, geochemical analysis of individual xenocrysts is much more rapid than full examination of a peridotite xenolith, which makes accumulating large datasets less expensive and faster (c.f. Griffin et al., 1999a).

The caveat of xenocryst data is that it stands alone and can be severely limited in terms of the geochemical information it can yield. For example, the composition of garnet xenocrysts is often used to estimate lithology, and the abundances of each type of garnet are used to estimate the relative proportions of different lithologies in different regions in the lithosphere. The problem is that the abundance of garnet varies between different mantle lithologies; harzburgite contains significantly less garnet than lherzolite due to its much more depleted nature (Walter, 2003). Therefore using the ratio of 1:1 for garnets in different lithologies will yield false relative abundances of different minerals, when the ratio of garnets in lherzolite to harzburgite (for instance) can be of the order of 3:1 (Pearson and Wittig, 2008).

Nevertheless, garnet xenocrysts can provide major and trace element data, and an estimate of temperature of equilibration. This is unarguably useful information, and the estimated temperatures can provide a *relative* stratigraphy of the samples within the dataset. However, in many cases it is useful to be able to compare geochemical data such as these to geophysical surveys and magnetotelluric transects, and this raises the issue of relative versus *absolute* stratigraphy.

3.2.2 Relative and absolute stratigraphy.

Geophysical data applicable to mantle lithosphere studies (magnetotelluric surveys and broadband teleseismic analyses of reflectors and anisotropy) allow large-scale views of the lithosphere in a given region. The results of these studies are usually displayed against

depth. In order to compare geochemical and geophysical data, it is necessary to obtain precise and accurate depth estimates for given xenoliths or xenocrysts.

A garnet xenocryst dataset provides a suite of temperature estimates, which require projection to a geotherm in order to obtain depths for each sample. It is possible to obtain pressure estimates from the Cr content of garnet (Grütter et al., 2006), but these, again, are dependent on previously constrained mantle geotherms. It has been shown (Chapter 2; Mather et al., 2011) that geotherm estimations for cratonic mantle lithosphere can vary significantly in method of calculation, resulting in a variety of geotherm shapes. These differences can result in quite significant discrepancies between projected depth estimates. While this is immaterial for making comparisons between the xenocryst data itself, as the relative depth order of the samples will not change since all geotherms are (broadly) straight lines, it makes a substantive difference when these depth estimates are used to correlate geochemical characteristics with geophysical data. The same issue applies when using xenolith-based multiphase thermobarometer combinations to estimate P–T (and therefore depth). The main issue that needs to be addressed is; how accurate are the depth estimates that we obtain using geochemical data, and to what extent can they be compared to features at a particular depth within the lithosphere estimated using independent methods.

3.3 PRESSURE-TEMPERATURE ESTIMATES, AND OBTAINING A DEPTH ESTIMATE FOR USE IN LITHOSPHERE STRATIGRAPHY

3.3.1 Accuracy of P–T estimates

It has been established in Chapter 2 (2.3.3.2) that significant error is associated with individual multiphase iteratively-calculated P–T estimates that is independent of the errors published for the geothermometer and geobarometer calibrations themselves. This error is dependent upon the counting times used when analysing mineral compositions using the electron microprobe (EMP), with shorter counting times resulting in less accurate mineral compositions with larger oxide standard deviations. In Chapter 2, these standard deviations were used to vary the oxide composition of minerals within the xenolith, and a P–T estimate was calculated using this new mineral composition. This process was repeated for each oxide such that a 'cloud' of P–T estimates were obtained that reflected the *potential* variation in pressure and temperature of that xenolith from EMP compositional uncertainty. However, because pressure and temperature are calculated iteratively, this 'cloud' of P–T estimates obtained usually trends parallel with the geotherm, and therefore it was decided that these errors would not cause significant variation to the calculated palaeogeotherm fit.

In contrast, for lithospheric stratigraphy, these uncertainties become significant and cannot be ignored. This is because it is desirable to be able to plot depth for an individual xenolith against other geochemical characteristics, such as the Mg# of the olivine in that sample, or the age of that sample. Since the estimated equilibration pressure (and therefore the depth) of a xenolith is calculated iteratively with temperature, it is not possible to simply assign the published error on the geobarometer to the depth estimates for xenolith and xenocryst samples; it is also necessary to assign the error from the microprobe analysis and the corresponding error 'cloud', and to each of the data points in the error 'cloud' add the error in the thermobarometer. This is illustrated in Figure 3.1, and the final error in depth is shown on the Y axis of each plot for three xenolith samples, one at low P–T, one at mid P–T, and one at high P–T, since it was observed in 2.3.3.2 that the size of the P–T error cloud varies with depth.

Depth uncertainty varies from 22.5 km (high P–T BK90_BK90; abbreviations for thermobarometer combinations as Chapter 2) to 46.5 km (low P–T TA98_NG85). Lower P–T estimates are always associated with larger depth uncertainties, although for the NG09_NG85 thermobarometer combination this effect is minimal. The high error at low P–T is probably due to 1) the extrapolation of the thermobarometer expressions to lower temperatures than they were calibrated at (shown by the brown shaded regions on Figure 3.1 and 2) that in the case of BK90_BK90 and TA98_NG85 the temperature estimates are based on the clinopyroxene solvus, and at temperatures < ~900 °C the variation in temperature with composition is less well-resolved (Boyd, 1973). The magnitude of these depth variations is extremely large when compared to the estimated average thickness of the lithosphere. On the one hand, this suggests that samples must be greater than (on average) about 35 km apart in the depth stratigraphy in order to be certain that they are actually sampling different regions of lithosphere. On the other hand, it indicates that the

variation in P–T estimates for the same xenolith using different thermobarometers is, in most cases, smaller than this uncertainty and this is of benefit to lithospheric stratigraphy analysis.

However, it is still necessary to establish a method to accurately estimate a depth for a sample from multiphase P–T estimates that takes into account the variability in the estimates from respective thermobarometer combinations, which can dramatically alter the depth order of samples and, following from this, any depth-chemistry relations.

3.3.2 Which thermobarometer to use for lithospheric stratigraphy?

Debate over the most appropriate thermobarometer combination to use on peridotite xenoliths to estimate equilibration P–T has been a topic of contention for many years, and the debate is ongoing (e.g. Taylor, 1998; Nimis and Grütter, 2009; Wu and Zhao, 2011; Nimis and Grütter, *in press*). It has been shown that the individual variation in P–T estimates from different thermobarometers does not affect the shape of the geotherm produced using the *FITPLOT* method (2.4.2) even though it does cause variation in the absolute P–T estimates obtained. Whether this variation in absolute P–T causes differences in the resulting lithospheric stratigraphy estimates depends on whether the relative *depth order* of samples is the same with each thermobarometer combination. If this is not the case, then the lithospheric stratigraphies estimated using each method will differ.

Figure 3.2 shows the central Slave dataset (Chapter 5) where pressure and temperature has been estimated using three recommended thermobarometer combinations of Nimis and Grütter (2009) and the Brey and Köhler (1990) combination. An equation for the depth-

dependent uncertainty for each thermobarometer combination was estimated using a linear interpolation from the values shown on Figure 3.1.

NT00_NT00 depth error (km) = -0.129*depth (km) + 51.655

NG09_NG85 depth error (km) = -0.0241*depth (km) + 40.981

TA98_NG85 depth error (km) = -0.0926*depth (km) + 50.936

BK90_BK90 depth error (km) = -0.226*depth (km) + 53.644

These were then then applied to the respective depths estimated for each xenolith to calculate a depth uncertainty which takes into account both the variation in P–T from electron microprobe oxide uncertainty and the published error in thermobarometer calibration.

The maximum and minimum depth estimates for each sample using the various thermobarometer combinations was then obtained, and if the maximum depth estimate for a given sample *minus* its respective uncertainty yielded a deeper depth than the minimum depth sample *plus* its respective uncertainty, then that sample was discarded. In effect, this removes 'disequilibrium' samples as defined by Nimis and Grütter (2009; see: 2.4.4) since their equilibrium indicator was the amount of agreement between temperatures estimated using the Nimis and Taylor (2000) thermometer and the Brey and Kohler (1990) thermometer.

In Table 3.1 the *depth order* of samples are also shown, to illustrate the difference that using a different thermobarometer makes to lithospheric stratigraphy. The dataset was ordered by depth for each thermobarometer combination, and then assigned a depth 'position'

from 1 – 66 (n = 66). The difference in depth 'position' for each sample for the four thermobarometer combinations is shown.

The data presented in Table 3.1 indicates that there is no systematic relationship between depth order and thermobarometer combination, nor a relationship between the range in depth estimates (e.g., 156 km, 138 km, 167 km = *range* of 29 km) and the range in depth order (e.g. 1st, 7th, 15th = *range* of 14 places). This means that there is no way to adequately choose the 'best' thermobarometer for obtaining a lithospheric stratigraphy, or (as emphasised in 3.2.3) for estimating an absolute depth (to compare with geophysical observations). R^2 values for straight-line fits of depth orders for various thermobarometers indicate that the greatest agreement in depth order is between the TA98_NG85 depth estimate and the CaOpx_NG85 depth estimate ($R^2 = 0.87$), probably because these are both iteratively calculated using the same geobarometer. The lowest agreement is between the BK90_BK90 estimate and the CaOpx_NG85 estimate.

It was decided that for the purposes of lithospheric stratigraphy, an average of all available depth estimates was taken to be the most likely depth of equilibration, since there is no way to be sure which depth estimate from the four 'recommended' (Nimis and Grütter, 2009) combinations is likely to be more accurate than another. The advantage of this method over choosing a particular thermobarometer combination is that it does not artificially down-sample an available database by requiring a specific mineralogy to be able to calculate P–T and (therefore) depth. For example if the TA98_NG85 combination were to be chosen, it would mean that no harzburgitic samples could be included in the lithospheric stratigraphy analysis, and this may well have a significant effect on any depth-chemistry and depth-age relationships obtained. It would also mean that lherzolitic

samples where the garnet or orthopyroxene stoichiometry is poor (i.e. outside ± 0.02 desired value) could also not be included in the stratigraphy.

Individual P–T estimates for the central Slave craton database are shown in Figure 3.2, ordered by this average depth estimate, to illustrate the range in P–T from each sample. Only samples where the maximum and minimum depth estimates are within error of each other are shown.

3.3.3 Nickel-in-Garnet Temperatures

At some kimberlite localities, no silicate minerals except garnet are suitable/available for EMP analysis, such as in the xenoliths from the Drybones Bay kimberlite in the southwest Slave craton (Carbno and Canil, 2002). It is desirable to be able to include these localities in a lithospheric stratigraphy study, and therefore single-garnet thermometry methods are used (Ryan et al., 1996). It was outlined above that a robust palaeogeotherm fit is necessary for the accurate projection of temperature estimates to obtain depths within the lithosphere, for comparison with multiphase estimates (expressed as depths).

There is some debate on the partitioning of Ni between garnet and olivine in peridotites, and the effect that this has on temperature estimates from Ni-in-gt thermometry. Canil (1999) emphasised this, and re-calibrated the Ni-in-garnet thermometer to include the Ni content of olivine, but the usefulness of this recalibration was disputed by Griffin et al. (2004), who claimed that it artificially 'compacted' the obtained temperature range.

One way to assess the viability of the single-garnet geothermometer is to compare projected depths from Ni-in-gt temperature estimates with depths estimated from

multiphase formulations from the same xenolith. To do this; samples from the central Slave database (Chapter 5) were used to estimate Ni-in-garnet temperatures using both the empirical calibration of Ryan et al. (1996) and the olivine-calibrated version of Canil (1999). Ni content of olivine was estimated by using the maximum and minimum values of DeHoog et al. (2010; 2041 ppm, 3307 ppm) to obtain a temperature range for the Canil (1999) formulation.

These temperature estimates were projected to the central Slave palaeogeotherm (see: Figure 5.6) in order to obtain depth values that could be compared with those from the multiphase thermobarometers (Figure 3.3). The Ryan et al. (1996) values commonly underestimate temperature, but are usually closer to the average multiphase value (see: 3.3.2) more often than the Canil (1999) version, although the Canil (1999) values are closer to the multiphase average at shallower depths. Therefore, the Ryan et al. (1996) thermometer will be used to construct lithospheric stratigraphy in localities (such as Drybones Bay, Carbno and Canil, 2002) where only garnet is available, since it is commonly the case that there is a larger sampling density in the deep lithosphere, where the Ryan (1996) formulation appears to be more accurate. However, a larger depth uncertainty should be applied to these estimates, based on the average difference between the projected Ni-in-gt depth and the average multiphase depth (± 19 km). This is significantly larger than the published value for the thermometer cited by Ryan et al. (1996; ± 50 °C, approximately 9 km).

3.4 SUMMARY

- Large depth uncertainties of up to ± 20 km are common for multiphase pressure-temperature estimates where uncertainty in EMP analysis and thermobarometer calibration is taken into account.

- An investigation into the relative depth order of xenolith samples calculated using different thermobarometer combinations indicates that estimates for lithosphere stratigraphy should be obtained by taking an average of available multiphase depth estimates, provided that these values are within error of each other. This allows an absolute value to be obtained for comparison with independent data (such as geophysical observations).

- Large uncertainty is common in single-crystal Ni-in-garnet methods when compared with average multiphase depth estimates from the same sample. A large error (± 20 km) should be ascribed to single-crystal depths to account for this.

4 THE NORTHERN SLAVE LITHOSPHERE

4.1 INTRODUCTION

It is generally understood that the central Slave craton is underlain by a lithospheric mantle root which is thick, ancient, and hosts diamonds that range in age from the Archean to the Proterozoic (Griffin et al., 1999a; Aulbach et al 2004; Westerlund et al., 2006; Heaman and Pearson, 2010; Aulbach et al., 2011b). However, the lateral extent of this ancient keel is poorly known, particularly to the North.

Here, we present new bulk geochemical, geothermometeric, rare-earth element and Re-Os isotope data for a suite of peridotite xenoliths from the Artemisia kimberlite, in the Coronation Gulf kimberlite field (Figure 4.1) located in the northern part of the Slave craton, distal to the central Slave. We also use previously un-published peridotite Re-Os isotope data (Irvine, 2002) from the Jericho kimberlite (Kopylova et al., 1998; Kopylova et al., 1999; Kopylova and Russell, 2000) to compare the age structure of the lithosphere beneath the northern Slave. In this way, the Artemisia kimberlite completes a N-S transect of lithospheric mantle beneath the Slave craton, from the central Slave Lac de Gras kimberlites in the south, through the Jericho kimberlite, extending to Artemisia at its northernmost extent. This transect, when integrated with a new magnetotelluric profile through the same region, provides new insights into the > 2.5 Ga history of the Slave Cratonic lithosphere.

4.1.1 Geological Setting and Sample Acquisition

Artemisia is a small (~3 ha) diamondiferous kimberlite, erupted at ca. 616 Ma (Armstrong et al., 2012) within the Coronation Gulf kimberlite field. These kimberlites are hosted by surface rocks of the Coronation Supergroup and Wopmay Orogen, which are themselves underlain by ancient basement comprised of the Archean Yellowknife supergroup and late Archean granitoids (Bowring and Grotzinger, 1992). Multiple generations of diabase dykes and sills intrude both the Archean basement rocks and the overlying rocks of the Wopmay orogen; the Mackenzie swarm (~1.27 Ga; Fahrig and Jones, 1969; LeCheminant and Heaman, 1989) and dykes and sills of the Franklin event (0.72 Ga; Heaman et al., 1992).

Over 100 peridotite and pyroxenite xenoliths were collected from the Artemisia kimberlite during the summer of 2009. Thirty-two peridotite xenoliths from this collection were selected for analysis based on size (> 10 cm diameter) and relative freshness, since all samples collected showed variable degrees of weathering and/or alteration.

A suite of 30 peridotite xenoliths from Jericho, previously analysed for bulk major elements and mineral major and trace elements by Kopylova et al (1998, 1999) and Kopylova and Russell (2000), were obtained as powders for Re-Os and platinum-group element analysis only (Irvine, 2002).

4.1.2 Petrography of the Artemisia Sample Set

Unfortunately, extensive serpentine alteration is evident in all samples, replacing most of the primary silicates. Garnet is the only silicate mineral remaining unaltered in 19 out of 32 samples. The remainder of the sample suite had no primary silicate minerals remaining.

Both spinel-facies peridotites and garnet-facies peridotites displaying porphyroclastic to granular textures are present, analogous to the facies and textural range of peridotites found at Jericho (Kopylova et al., 1999). Detailed assessment of petrology and modal mineralogy - in particular the amount of original diopside - was precluded by the altered nature of the samples.

4.2 ANALYTICAL METHODS

Detailed information on the analytical procedures used and standard data are available in Chapter 8, and will be summarised briefly here. All methods used are well-established in the literature.

Artemisia samples were analysed for bulk composition by XRF at the Open University, UK. Electron microprobe (EMP) analyses on the Artemisia xenolith and xenocryst garnets were performed on Cameca SX100 instruments at the University of Cambridge, UK, and at the Saskatchewan Research Council, Saskatoon, Canada. Three points were analysed in the core of each crystal to produce an average composition, and one point was analysed on the rim of each crystal to assess intra-crystal variability.

Where present, primary garnet was picked from a coarse crush of the xenolith material for major and trace element analysis. In addition, 150 garnet xenocrysts (> 2.5 mm) were picked from heavy mineral concentrate prepared from the kimberlite and analysed in the same way, to supplement the xenolith garnet data. Trace element abundances in the Artemisia garnets were acquired by laser-ablation inductively coupled plasma mass spectrometry (LA-ICP-MS) at the Geological Survey of Canada. Three analyses were performed on the cores of individual garnets to produce an average composition.

Re-Os isotopes and platinum-group element systematics for both Artemisia and Jericho xenoliths (Irvine, 2002) were analysed at the Northern Centre for Isotopic and Elemental Tracing, Durham University, UK, using a high-pressure asher and isotope dilution (Ishikawa et al., 2007).

4.3 RESULTS

4.3.1 Whole-rock major elements

The Artemisia samples have elevated (10 – 12 wt%) loss-on-ignition values, reflecting their altered nature, and therefore only Al_2O_3 is used to compare the Artemisia and Jericho samples as this oxide remains relatively immobile during alteration (Pearson et al., 2004).

The very low mean and median Al_2O_3 values of the Artemisia peridotites are similar to worldwide cratonic peridotites (mean 0.98 wt%; Figure 4.2), but have a slightly larger standard deviation than those from Jericho (0.48 wt% versus 0.39 wt%), possibly reflecting the fresher nature of the Jericho sample set.

4.3.2 Xenolith and xenocryst garnet major-element compositions

Garnet compositions for Artemisia peridotites are typical of cratonic Cr-Pyropes (Dawson and Stephens, 1975) and were classified using the algorithm of Grütter et al. (2004). The samples plot exclusively along the Ca-Cr G9 'lherzolite array' (Figure 4.3; Grütter et al., 2004), in contrast with peridotites from the central Slave region (Pearson et al., 1999;

Menzies et al., 2004). Additionally, no low-Ca, high-Cr (G10) garnets are present in the xenolith suites from either Artemisia or Jericho. G10 garnets are also largely absent from the xenocryst dataset from Artemisia, except for three garnets that fall just within the G10 field. There is no distinctive difference between the distributions of xenolith-borne and xenocrystic garnet from Artemisia, with the exception of more "G12" (wehrlite) xenocryst garnets.

4.3.3 Trace-element composition of xenolith and xenocryst garnet

Artemisia xenolith garnets (Figure. 4.4) show a smaller range in Y concentration (0.58 ppm > Y > 19.50 ppm) compared to the xenocrysts (0.27 ppm > Y_9 > 34.08 ppm). Jericho xenolith garnets (Kopylova et al., 1999) have a similar Y range to all but the most depleted Artemisia xenolith garnets (2 ppm > Y > 21 ppm). 55% of the Artemisia xenocryst garnet (n = 161) analysed, and 47% of the Artemisia xenolith garnet (n = 19) plot within the 'depleted' field of Griffin et al. (1999b). In contrast, of the Jericho dataset, only 15% (n = 26) of the samples plot within this 'depleted' field, as noted by Kopylova et al. (1999).

Xenolith garnets from Artemisia display the full range in rare-earth element (REE) profiles commonly associated with cratonic Cr-Pyrope (Figure 4.5; Burgess and Harte, 1994; Stachel et al., 2004). These include harzburgitic 'sinusoidal' profiles, where mid to heavy REE concentrations (Tb-Yb) are typically less than 2x chondritic and mid-light REE values (Ce-Eu) are up to 10x chondrite (Stachel et al., 2004). No garnet REE data is available for the Jericho sample set for comparison.

The large number of Artemisia garnets analysed (n = 161) allows meaningful quantification of the distribution of REE patterns in order to assess their relative abundance within the dataset. The parameter $[Gd_n/Dy_n]_{gt} \geq 1.2$ was used to classify pattern shapes that have 'sinusoidal', harzburgitic patterns (Figure 4.5) because of the relative ease with which Dy and Gd can be measured by LA-ICP-MS. This minimises erroneous classification due to imprecise analysis. However, those patterns with $[Gd_n/Dy_n] < 1.2$ require further subdivision into 'melt-equilibrated', lherzolitic patterns (using the criteria of Stachel et al., 2004) and a third type of pattern that shows extreme depletion across the REEs (abundances at or lower than 2x chondritic) but which in general shows a gradual increase in concentration from the light to heavy REEs (Figure 4.5). This type of pattern is termed 'depleted', and is characterised by $Dy_n < 2$ and ($Dy_n > Tb_n$).

Using this classification, the Artemisia xenocryst garnet dataset (n = 161) contains 61% 'sinusoidal', 34% 'melt-equilibrated' patterns, and 15% 'depleted' patterns. The smaller xenolith garnet dataset (n = 19) is more evenly distributed, containing 37% 'sinusoidal' patterns, and 32% of both 'melt-equilibrated' and 'depleted' pattern types.

4.3.4 Rhenium & Platinum-Group Element Concentrations.

Rhenium contents in the Artemisia xenoliths are low, averaging 0.079 ppb. Osmium concentrations vary from anomalously low (for peridotites; 0.355 ppb) to high; four samples contain > 10 ppb Os. Excluding these outliers from the dataset, the average Os concentration in the Artemisia xenoliths is 3.6 ppb, similar to cratonic peridotite xenoliths worldwide (3.8 ± 2.6 ppb, Pearson et al., 2003), and higher than that for 'off-craton'

peridotite xenoliths (2.0 ± 1.1 ppb). Re concentrations in Jericho peridotites vary from 0.005 to 0.29 ppb and Os concentrations vary from 0.31 to 21.53 ppb, with a median of 3.86 ppb, within the normal cratonic range (Pearson et al., 2004). The highest Os concentrations are only observed in two of the Jericho samples (10.10 ppb and 21.53 ppb).

4.3.5 Rhenium-Osmium Isotopes

Rhenium-depletion model ages (T_{RD}) for Artemisia and Jericho peridotites are calculated by assuming that any Re present was introduced during kimberlite eruption, removing the calculated radiogenic Os and then assuming Re/Os = 0.

Gaussian mixture-modelling of the Artemisia T_{RD} ages (Sambridge and Compston, 1994; Figure 4.6, ***top***) using an age uncertainty of 0.2 Ga identifies a broad peak in the data in the Mesoproterozoic, which can be divided into two components at 1.0 ± 0.1 Ga (28% of the dataset) and 1.6 ± 0.1 Ga (56% of the dataset). There is also a poorly-defined Palaeoproterozoic component at 2.3 ± 0.1 Ga. In contrast, the same mixture modelling procedure for the Jericho T_{RD} ages produce a distribution from 0.5 to 3.1 Ga with a main peak in the Neoarchean at 2.8 ± 0.1 Ga (44%; Figure 4.6 ***(middle***) and minor peaks in the Proterozoic 2.1 ± 0.1 Ga (30%) and 1.3 ± 0.1 Ga (27%).

4.3.6 Thermobarometry

Multi-phase estimation of equilibration pressures and temperatures for the Artemisia xenoliths is precluded by the lack of primary silicate phases. Instead, only nickel-in-garnet temperatures (Ryan et al., 1996) can be obtained. There are a variety of iterations of the single-garnet Ni-thermometer, including the calibration of Canil (1999), which requires, in addition to the Ni concentration of garnet, the Ni concentration of coexisting olivine. As has been previously outlined, no fresh olivine remains in the Artemisia samples for analysis, and therefore only the version of Ryan et al. (1996) can be employed, with associated limitations as outlined in (3.3.3). Ni concentration in the Artemisia xenolith and xenocryst garnet ranges from 15 to 150 ppm, yielding an approximate Ni-in-Gt_{Ryan} temperature range of 738 to 1514°C. Projected to a Jericho palaeogeotherm (calculated using the methods outlined in Chapter 2, with data of Kopylova et al., 1998), this gives a sampling depth range of approximately 100 km (Figure 4.7).

4.3.7 Depth – chemistry relationships

Xenolith garnets from the Artemisia kimberlite can be grouped into two depth ranges, taking into account the large errors on the depth estimates. 3 samples are from relatively shallow mantle lithosphere (108, 109 and 135 (± 20) km), and are outside error from the second group of samples that range in depth from 182 – 222 (± 20) km.

4.3.7.1 Y-Zr vs. depth

The Y-Zr content of the Artemisia samples, grouped by type (depleted, ultradepleted or melt-metasomatised) is shown plotted against depth in Figure 4.8A. There is a suggestion that garnets with 'ultra-depleted' Y-Zr concentrations occur in the shallow lithosphere, but there are very few of these samples in the dataset as a whole. There is no significant difference between the depth-distributions of the depleted and non-depleted (i.e., melt metasomatised) samples.

4.3.7.2 Rare-earth Elements

REE patterns from the three shallow samples show the 'depleted' and 'sinusoidal' pattern types, with the two shallowest samples having the 'depleted' pattern and the c. 135 km sample with the sinusoidal pattern. The deeper group of samples has a range of 40 km, and therefore taking into account the large error in depth associated with projected Ni-in-Gt temperatures (± 20 km), most of these samples cannot be distinguished from each other in terms of depth. However, the shallowest of these samples (182 km) can be distinguished, outside of error, from the deepest of these samples (222 km). The 182 km sample shows a 'sinusoidal' pattern similar in shape to that seen in the 135 km sample, but with much higher mid-REE (Sm-Ho) content. The deeper xenolith shows the lherzolitic, 'melt-equilibrated' (Stachel et al., 2004) pattern type.

The xenocryst dataset, because of its much larger size, is more complex to analyse for pattern type when the large errors on P–T estimates are accounted for. Figure 4.8B shows the depth distribution of different pattern types classified using the parameters outlined in

4.3.3. The shallowest samples show 'depleted' patterns but these are not restricted only to the shallow lithosphere. There appears to be a bimodal distribution of this pattern type, with another group of samples at around 200 km. However, this is probably an artefact of the pattern classification process, since close inspection of these deeper samples (shown with grey outlining Figure 4.8B) indicates a positive gradient in the mid-heavy REEs (yielding $[Gd_n/Dy_n] < 1.2$), such that there is a 'sinusoidal' shape, but the trough is located further towards the light-REEs than in the average 'sinusoidal'-type sample. Also, in these samples the light-REEs are much more enriched than in the shallower samples, adding to their more 'sinusoidal' character than the samples at shallower levels. Ignoring this deeper group of samples, which we do not think are representative of the 'depleted' pattern type, the average depth of 'depleted'-type samples is 120 km.

The 'sinusoidal'-type patterns are represented at all levels of the lithosphere, and the average depth of this pattern type is 193 km. This average is so deep partly due to the uneven sampling of the kimberlite, which means that the deeper lithosphere is better-sampled and therefore pulls the average down slightly.

4.3.8 Depth – age relationships

Figure 4.8C shows the age-depth relationships of the Artemisia xenolith samples. From these data it is difficult to say whether any significant pattern between the age of a sample and its position in the lithospheric column is present beneath Artemisia. On the one hand, while sampling density for shallow samples is poor, all available samples from < 165 km are Palaeoproterozoic in age, whereas the deeper samples range from this age to late

Archean. However, the deeper lithosphere contains samples that are > 2.0 Ga and < 1.0 Ga, so this result is ambiguous.

4.4 DISCUSSION

4.4.1 Thickness of the Lithosphere beneath the Northern Slave Craton

Accurate estimation of the thickness of the cratonic keel beneath Artemisia using a peridotite xenolith palaeogeotherm geotherm fit, for comparison with Jericho, the central Slave, and other cratonic regions is not possible due to the lack of primary silicate minerals for calculation of equilibrium P–T. However, projecting Ni-in-garnet temperatures from Artemisia xenoliths to the peridotite palaeogeotherm from Jericho – the closest locality for which a xenolith palaeogeotherm has been obtained (Figure 4.7; data from Kopylova et al., 1998; geotherm fitted using the methods outlined in Chapter 2) indicates that Artemisia samples were derived from a depth range of 120 - 215 km. Using this approach we estimate that the lithosphere beneath Artemisia is of comparable thickness (215 km; from the projected deepest xenolith, Figure 4.7) to that at Jericho, if the palaeogeotherms are similar at both localities. Independent estimates of lithospheric thickness in this region from published seismic data (see Figure 4.7) and our new magnetotelluric data are also shown that corroborate the Ni-in-garnet data, suggesting that that the lithosphere beneath Artemisia is of equivalent thickness to that beneath Jericho and the central Slave craton.

4.4.1.1 Chemistry and age of the Northern Slave Lithosphere

A variety of geochemical data indicate that the lithosphere sampled by the Artemisia kimberlite has many geochemical characteristics typical of ancient cratons. Bulk Al_2O_3 is low, similar to worldwide cratonic values and also to the Jericho peridotites to the south (Figure 4.2). Artemisia garnet chemistry falls within the published range for Central Slave lithosphere, and although Artemisia has only 3 sub-calcic 'G10' garnets, the Cr-rich nature of the "G9" garnets is typical of cratonic garnets (Dawson and Stephens, 1975; Grütter, 2004). Garnet REE patterns also display the 'sinusoidal' signatures characteristic of cratonic mantle (e.g., Burgess and Harte, 1994; Shimizu et al., 1997) and harzburgitic garnets included in diamonds (e.g., Stachel et al., 2004). In addition, Re and Os abundances at both Artemisia and Jericho are similar to those from the Kaapvaal and other cratons worldwide (Pearson et al., 2004).

However, one striking and unusual difference between the Artemisia xenolith suite and other cratonic peridotite suites (including Jericho) is the great scarcity of Archean-age samples, with only one sample marginally older than 2.5 Ga (2.51 ± 0.2 Ga), and the majority (84%) of the dataset having Proterozoic T_{RD} ages.

Although the surficial geology directly beneath the Artemisia kimberlite (Coronation Supergroup) is of Palaeoproterozoic age, this overlies the much more ancient Slave craton basement (Bleeker, 2002). The longevity of Archean crustal rocks in other cratonic regions is commonly explained by their thick, cold cratonic roots acting as geodynamic 'shields' to destruction and re-working in mobile belts (Jordan, 1975), and therefore it is reasonable to assume that the ancient crust around the Artemisia kimberlite has been protected in the

same way since its formation in the Archean. This is in direct contrast to the predominantly Proterozoic T_{RD} ages obtained for the Artemisia peridotite xenoliths. If the T_{RD} ages represent lithosphere formation ages, then the majority of the thick lithosphere beneath the ancient crustal rocks at Artemisia has either only existed since the Mesoproterozoic, or has been replaced by equally thick and strong lithosphere that was depleted in the Mesoproterozoic. Alternatively, the peak in Re-Os ages observed could be the result of lithospheric-scale re-setting of the Os isotope system. We explore these possibilities in turn below.

4.4.2 Proterozoic depletion of the Artemisia subcontinental lithospheric mantle.

In order for the observed 1.0 - 1.5 Ga signal to represent a peak in lithospheric mantle formation, a major mantle melting event in the Palaeoproterozoic is required. This melting event would have either been the result of further melting of original cratonic lithosphere, or the formation of new lithosphere at this time.

There is evidence in the northern Slave craton crust for a pronounced, large-volume melting event during the Proterozoic at ~1.2 Ga – the Mackenzie igneous province (Fahrig and Jones, 1969; LeCheminant and Heaman, 1989; Ernst and Baragar, 1992). The Mackenzie event includes the 1.27 Ga Mackenzie dyke swarm, which is a continental-scale feature and penetrates the entirety of the Slave craton (Figure 4.1). The dyke swarm is the inferred near-surface expression of the 1.27 Ga Mackenzie plume, along with the Muskox intrusion (M; Figure 4.1) and the Coppermine flood basalts (LeCheminant and Heaman, 1989). The suggested focus of the plume is approximately 400 km northwest of Artemisia

(Ernst and Baragar, 1992; Baragar et al., 1996), making this kimberlite the most proximal to the plume focus within the Slave craton.

Large igneous provinces often occur within and around cratonic mantle lithosphere (Deccan traps, Cox and Hawkesworth, 1985; Siberian Traps, Renne and Basu, 1991), although in many cases the mechanism behind their emplacement given the thick lithosphere in cratonic regions is debated (e.g. Kent et al., 1992). Nevertheless, it is likely that the large volumes of melting during the Mackenzie igneous event had a significant influence of the on the lithospheric mantle in the region.

Dupuy et al. (1992) investigated the geochemistry of the Coppermine flood basalts, and noted that their composition suggested the interaction of more than one mantle melt component; an asthenospheric and a lithospheric component. However, melting continental lithospheric mantle, especially highly depleted Archean cratonic mantle as present beneath the Slave craton to the south, is not straightforward (e.g. Davies, 1994; White and McKenzie, 1995). However, it is possible to thin and remove cratonic lithosphere, as demonstrated beneath the North China Craton (Menzies and Xu, 1998; Gao et al, 2004), but there are many conflicting explanations for the mechanism of lithospheric thinning in this region (e.g. Menzies and Xu, 1998). One hypothesis is that the lithospheric mantle had been previously 'primed' for removal, either by addition of melts which fertilize the lithospheric mantle and make it more fusible, or by addition of water from a subducting slab.

The 1.8 Ga Wopmay orogeny (Hoffman and Bowring, 1984) is purported to have involved east-dipping subduction beneath the main bulk of the Slave craton (Cook et al., 1999). The NW-SE alignment of the kimberlites in the Slave craton means that kimberlites in the north are much closer to the leading edge of the Wopmay orogeny than those to the south, and

therefore the lithosphere that they sample might be expected to show a greater extent of modification as a result of interaction of the Wopmay slab with the Slave lithosphere.

Thus, in the same way as is suggested by some workers for the removal of the North China Cratonic lithosphere (Kusky et al., 2007), it is possible that refertilization of the cratonic lithosphere in the northern Slave by slab fluids/melts 'primed' the lithosphere for melting and removal in the northern Slave. This allows the signature of continental lithospheric melt to be recorded in the Coppermine flood basalts (Dupuy et al., 1992), and can also explain the predominantly Proterozoic mode of the T_{RD} ages recorded in the Artemisia peridotite xenolith suite, since large-volume melting as hypothesised for the Mackenzie event (> 15%, Day et al., 2008) would lead to Re-depletion and freeze the $^{187/188}Os$ ratio in the late Proterozoic.

Evidence in support of this lithosphere removal/re-formation hypothesis comes from REE element inversion of the Mackenzie dykes themselves (White and McKenzie, 1995; Figure 4.9). The REE composition of a melt is directly related to its depth of melting and volume (McKenzie and O'Nions, 1991) owing to the strong control that garnet has on the heavy REEs. The Mackenzie dyke REE compositions suggest that melting occurred between 100 and 60 km, which is consistent with a region of thinned lithosphere. Interestingly, it is evident from geophysical surveys that the lithosphere today beneath the Artemisia kimberlite is of similar thickness to that of the rest of the Slave craton (see: Figure 4.7, and references therein). In this way, it is different to the North China Craton where the lithosphere has remained thin post-removal (Menzies et al., 2007).

However, it should be noted that the volume of melt hypothesised for the Mackenzie event (90,000 km^3 for the Mackenzie Dykes, and 140,000 km^3 for the Coppermine flood basalts,

LeCheminant and Heaman, 1989; 20,000 km^3 for the Muskox intrusion, Francis, 1994) is not sufficient to represent > 20 % melting (required to deplete sub-continental lithosphere to isopycnic stability; Jordan, 1988). 20 % melting of a lithospheric column 170 km deep and with a radius of 50 km would yield ~270,000 km^3 melt. While this value is close to that for the total Mackenzie melts (250,000 km^3), it does not take into account melting of the plume material (suggested by the asthenospheric component required to explain the composition of the Coppermine flood basalts; Dupuy et al., 1992), nor any melting of the crust, which is also required by the composition of both the Muskox intrusion (Day et al., 2008) and the Coppermine flood basalts (Dupuy et al., 1992). Therefore we consider it unlikely that this mechanism is responsible for the unusual T_{RD} distribution seen at Artemisia.

4.4.3 Metasomatism of the Artemisia lithosphere

In contrast to the hypothesis outlined above, the predominant Proterozoic peak in the T_{RD} distribution at Artemisia could be the result of extensive metasomatism of the lithosphere, causing re-setting of the osmium isotope system. There are two end-members to this mechanism: 1) silicate melt overprinting and 2) sulphide addition.

4.4.3.1 Silicate melt overprinting

The first endmember, extensive percolation of silicate melt through depleted cratonic lithosphere should have a significant effect on the major and trace element geochemistry of the surrounding peridotite wall rock. The addition of fertile material will add Re to the depleted material, thereby re-setting the Os isotope system. Rudnick and Walker (2009)

suggested that re-fertilization of cratonic lithosphere by melt-rock reaction can be identified using Al_2O_3 – $^{187}Os/^{188}Os$ relations (Figure 4.10). If melt-rock reaction occurred during percolation of the Mackenzie melts through the lithosphere, a clear trend towards increasing Al_2O_3 with increasing $^{187}Os/^{188}Os$ should be observed. When simple mixing between typical depleted cratonic peridotite (Pearson et al., 2003) and a primitive Mackenzie melt, such as the keel dyke of the Muskox intrusion (Day et al., 2008) is modelled, the Artemisia peridotites do not show the expected systematic deviation to higher Al_2O_3 concentrations (Figure 4.10).

Additional evidence against large-scale silicate melt interaction with the Artemisia lithosphere is provided by the trace-element composition of xenolith-derived and xenocrystic garnets. The low Y and Zr concentrations of the Artemisia garnets (Figure 4.4) suggest that the majority (76%) have not been significantly affected by silicate melt metasomatism. This result is the opposite of what would be expected given the large volumes of melt associated with the Mackenzie event. It is possible to envisage a situation where melt moves through the lithosphere in dunitic channels (c.f. Kelemen et al., 1995), and therefore the chemical effects of melt-rock reaction are limited to the regions close to these channels. This would be reflected as a decrease in T_{RD} with re-enrichment in Y & Zr. No such correlation exists in the Artemisia dataset; samples with Proterozoic T_{RD} ages show Y concentrations from the most depleted (0.44 ppm) to the most enriched (20.07 ppm).

The available geochemical evidence suggests that large-scale re-setting of the Os isotope system by silicate melt percolation is not the process responsible for the T_{RD} distribution seen in Artemisia peridotite xenoliths.

4.4.3.2 Sulphide addition

Despite the lack of Archean T_{RD} ages, many of the geochemical characteristics of the Artemisia peridotites are similar to those recognised in cratonic lithosphere worldwide (e.g. Pearson et al., 2003). This might suggest that the mechanism to generate the unusual T_{RD} distribution at Artemisia has affected mostly the highly siderophile elements, leaving the bulk of the geochemistry of the lithosphere in this region untouched. Such a mechanism is pervasive percolation of a sulphur-saturated melt (i.e., an immiscible sulphide melt co-existing with a silicate melt) that deposits metasomatic sulphide in wall rocks, hence affecting the siderophile elements, but not the major elements.

The effect on the Os isotope system of sulphide addition can be modelled by mixing between a 2.9 Ga depleted peridotite and a range of different metasomatic sulphides, that can be simply modelled as two different endmember compositions (Figure 4.11). Sulphide A (Figure 4.11, ***top***) has a chondritic $^{187}Os/^{188}Os$ at 1.27 Ga ($\gamma Os_{1270} = 0$) to simulate the broadly chondritic Mackenzie plume magmatism (Day et al., 2008), which might be considered a significant source of metasomatic melts. Sulphide B (Figure 4.11, ***bottom***) has a highly suprachondritic composition ($\gamma Os_{1270} = 20$) to model sulphide associated with potential Mesoproterozoic subduction (e.g., Aulbach et al., 2009a).

The variation in initial depleted peridotite Os concentration, as suggested by the > 2.5 Ga samples from Jericho (0.5 – 3.5 ppb) means that addition of variable amounts of a $\gamma Os_{1270} = 0$ sulphide — associated with the Mackenzie event — can adequately explain the T_{RD} distribution at Artemisia. The suprachondritic sulphide B (Figure 4.11, ***bottom***) can adequately explain some of the data, but not the samples with extremely high Os concentrations. Between 0.01 and 0.04 wt% sulphide with $\gamma Os_{1270} = 0$ can explain the

majority of the Artemisia data, and hence this is our preferred model to explain the unusual T_{RD} distribution seen in the peridotite xenoliths from this locality, which requires some variability in the initial Os concentration in the host peridotite that is within the range observed in un-metasomatised samples from Jericho.

--

The variability of sulphur solubility in magmas with depth of ascent (e.g., Mavrogenes & O'Neill, 1999) would suggest that the shallowest samples in the Artemisia column might be associated with the least sulphide overprinting. However, as shown in Figure 4.8C, the oldest, and therefore in this context the 'least metasomatised' sample is also located in the deepest section of the lithosphere.

Additionally, the melt which brought the sulphur-saturated component must have been small-volume; otherwise it would have also perturbed the major element chemistry of the peridotite. Small volume melts are associated with extremely enriched light- REE and high field strength elements (HFSEs), and therefore the samples which show the greatest hypothesised sulphide addition might also be expected to have garnets with melt-metasomatised Y-Zr systematics and LREE enriched rare earth element patterns. This is not observed in the Artemisia dataset – the samples with highest Os (> 10 ppb; indicating maximum interaction with sulphidic metasomatic melt) all show 'depleted'-type Y-Zr systematics (Figure 4.4) and sinusoidal REE profiles (Figure 4.5). One way to explain this apparent discontinuity is that the xenoliths only sample the sulphide-metasomatised parts of the lithosphere, and the co-existing silicate melt has affected other regions of the lithosphere that have not been sampled.

In conclusion, while the sulphide overprinting hypothesis is our preferred model to explain the unusual T_{RD} distribution at Artemisia, there are aspects of this model that do not fit with the observed data.

4.4.4 Distal influences of the Mackenzie plume in the Slave craton.

If the magmatic activity at the time of the Mackenzie magmatic event was sufficient to generate a large volume of new lithospheric mantle or significantly metasomatise it, then we may expect to see evidence of this event in the lithosphere further afield. Moreover, we may expect to observe some physical differences between the lithospheric mantle in the central and the very northern Slave lithosphere.

Examining the first of these predictions, it seems likely that the lithosphere beneath the relatively proximal (~180 km SSE) Jericho kimberlite may reveal evidence of Mackenzie events. If the same modelling procedure is applied to the Jericho data (Figure 4.12), there is a significantly larger proportion of Archean un-metasomatised samples, but a proportion of the dataset, including many of the most Os enriched samples can be explained by variable addition of a 1.2 Ga sulphide. However, it should be noted that one Archean sample also contains very high Os and therefore may have been subject to infiltration by sulphide from the convecting mantle in the Archean with a chondritic Os isotope composition and low Re/Os. (~10 ppb, Figure 4.12).

The explanation for this contrast in the hypothesised effect of the Mackenzie event on the lithosphere within a relatively short distance across the northern part of the Slave craton probably lies in the shift in the flow regime of Mackenzie magmas. Ernst and Baragar

(1992) proposed that the flow regime in the Mackenzie dykes changes from vertical (i.e, trans-lithospheric) to horizontal (i.e., inter-crustal) in the region between the Artemisia and Jericho kimberlites (Figure 4.1). White and McKenzie (1995) postulate that melt flow in dyke swarms associated with large igneous events is mainly confined to the crust, and therefore if the change to horizontal flow is due to melt no longer percolating upwards through the lithosphere, and instead flowing outwards through the crust, then there should be a significant decrease in the impact on the lithospheric mantle. Mixture modelling of T_{RD} ages calculated from published peridotite Os data (Figure 4.6; Aulbach et al., 2004; Westerlund et al., 2006; Aulbach et al., 2009a) from the central Slave region, 360 km SSE of Artemisia clearly shows that the effect of Mackenzie melts lessens significantly on moving further away from the focus of vertical magma flow, with only 10% of T_{RD} ages being Proterozoic (Figure 4.6). In contrast, even at this distance, the effects of the Mackenzie event are clearly documented by a variety of chronometers in lower- and mid-crustal xenoliths (Davis, 1997) because of the strong crustal channelling of magma. It is also interesting to note that Irvine et al. (2003) suggested the influence of the Mackenzie event at Somerset Island (550 km east of the centre of the plume head), based on a small subset of peridotite samples with ~1.3 Ga T_{RD} ages.

4.4.5 Electric structure and thickness of the Northern Slave Lithosphere

Magnetotelluric (MT) measurements of the resistivity of cratonic lithosphere have become more widespread in the last decade and have the potential to distinguish between different types of continental lithosphere (e.g., Jones, 1999). Figure 4.13 shows the results of an E-W

passive magnetotelluric survey (black triangles Figure 4.1) deployed in the northern Slave lithosphere in 2004. The projected location of the Artemisia kimberlite is marked by the grey star. The results indicate that the lithosphere beneath Artemisia has substantially lower resistivity than lithosphere to the west. Differences in resistivity arise mainly from the presence of conductors within the medium being analysed, therefore the decrease in resistivity beneath Artemisia can either be interpreted as the presence of water, or another conductor such as graphite within the grain boundaries. What is clear is that the MT evidence suggests that the lithosphere directly beneath Artemisia is different to that in the surrounding region of the Slave craton, and could support either the suggestion that it was formed during the Mackenzie event, or has been dramatically altered by sulphide metasomatism.

4.5 CONCLUSIONS

Peridotite xenolith compositions from the Artemisia kimberlite suggest that the mantle lithosphere beneath the northern Slave craton is of a similar major- and trace-element composition to that of the Jericho kimberlite (Kopylova et al., 1998; Kopylova et al., 1999; Kopylova and Russell, 2000) and cratonic localities worldwide (Pearson et al., 2003).

Os isotope compositions of Jericho peridotites reveal a major component of Archean samples (up to 3.1 Ga) with minor peaks in the age distribution at 1.8 and 1.3 Ga. In striking contrast, there are no Archean ages from Artemisia peridotites, but a broad peak in T_{RD} ages at ca. 1.0 – 1.5 Ga, with an additional minor component of Palaeoproterozoic T_{RD} ages that range from 2.3 to 1.75 Ga. We examine two hypotheses for the mechanism by which this plume impact event has modified the lithosphere to generate major and trace element characteristics that are similar to cratonic mantle, yet with Os isotope compositions that bear no Archean lineage. These hypotheses are illustrated in Figure 4.14.

The thickness of the lithosphere beneath Artemisia, estimated at 616 Ma (the time of kimberlite eruption) and today (from seismic and magnetotelluric data) indicates that the lithosphere must have been thickened since eruption of the Mackenzie dykes with tholeiitic compositions, and with REE contents that indicate melting at depths of 60 – 100 km. A variety of hypotheses were explored to explain these features.

The first hypothesis posits that the Archean cratonic root beneath the Artemisia kimberlite (suggested by the presence of Archean basement rocks at the surface) was first primed by subduction of the dipping slab associated with the Wopmay orogeny, which allowed thinning of the lithosphere by impingement of the Mackenzie plume at ca. 1.26 Ga. This thinning provided a region where upwelling and melting preferentially took place, resulting in the ~500 km discontinuity between the proposed focus of the Mackenzie plume and its surface expression, represented by the Coppermine Flood basalts and the Muskox Intrusion. The effects of the plume wane to the south such that the lithosphere beneath the Jericho kimberlite has a reduced yet still significant fraction of Mackenzie age residues (27%), whereas this event caused relatively minor disturbance of the lithosphere and crust in the central region of the Slave, > 700 km south of the plume focus.

The second hypothesis, which is our preferred model, involves modelling of the addition of a ca. 1.26 Ga sulphide to the Archean lithospheric mantle beneath Artemisia and Jericho. It was shown that addition of this sulphide can explain both the T_{RD} and Os concentration of the peridotite xenolith samples. However, bulk Al_2O_3 and garnet REE evidence from the same xenoliths indicate that this sulphidic melt cannot have been associated with either large-fraction or small-fraction melt percolation.

Both hypotheses cannot explain all the available data, and although they are intriguing speculative suggestions on the processes that have affected the Slave craton in this region, more work is required to resolve which, if either, of these is correct.

5 THE AGE OF THE ULTRA-DEPLETED LAYER OF THE CENTRAL SLAVE CRATON

5.1 INTRODUCTION

It is widely accepted that the lithosphere beneath the central Slave craton is stratified (e.g. Heaman and Pearson, 2010; Aulbach et al., 2011b). This stratification is visible in broadband teleseismic analyses (Snyder et al, 2004, 2008), magnetotelluric transects (Jones et al., 2001), and in the chemical composition of garnet xenocrysts (Griffin et al., 1999a; Grütter et al., 1999), and is therefore thought to be a fundamental feature of the Slave craton in this region, relating to the mechanism by which it was formed (Aulbach et al., *in press*, and references therein)

Published work on peridotite xenoliths from the central Slave (Pearson et al., 1999; Mackenzie and Canil, 1999; Aulbach et al., 2004; Westerlund et al., 2006; Aulbach et al., 2007a; Creighton et al., 2008; Creighton et al., 2010) all examined microxenolith samples < 5 cm diameter, and current age estimates from the central Slave lithosphere are almost all from analysis of single-sulphide grains liberated from olivine crystals or from diamonds. Only six whole-rock Re-Os ages have been obtained from the central Slave region from Ekati xenoliths (Westerlund et al., 2006). The advantage of whole-rock ages is that they can be reliably compared with geochemical characteristics, such as major- and trace-element concentrations, and also with geochemically-derived estimations e.g. pressure and temperature (P–T) of equilibration. This allows insight into the age stratification of the

lithosphere in this region, as single-sulphide analyses provide very limited age – depth relations.

The purpose of this paper is to contribute new, whole-rock Re-Os isotope ages, bulk compositions, mineral major elements and garnet trace elements from a suite of 35 peridotite macroxenoliths (> 5 cm diameter) from the central Slave craton together with a suite of 250 clinopyroxene xenocryst major element compositions to supplement the xenolith data. The aim is to provide improved age versus depth resolution in the central Slave lithospheric mantle with the hope of better understanding the mechanism of formation of this lithosphere.

We will also use existing published data for xenoliths from the Central Slave region (Torrie pipe: Mackenzie and Canil 1999; Ekati pipes: Menzies et al., 2004; Westerlund et al., 2006; Diavik: Aulbach et al., 2004, Aulbach et al., 2007a; Aulbach et al., 2009a; Creighton et al., 2008; Creighton et al., 2010) in order to examine the new data, and comment on the age and composition of the 'ultra-depleted layer' (Griffin et al., 1999a) using peridotite xenolith evidence.

5.2 GEOLOGICAL SETTING

The Slave Craton is situated in the Northwest Territories and Nunavut in northern Canada. It is a relatively small craton bounded on three sides by mobile belts; the Thelon tectonic zone extends along the north-eastern side of the craton; in the west, the Wopmay orogen and Great Bear magmatic zone. The Great Slave Lake Shear Zone and Taltson magmatic zone mark the southernmost extent of the craton. Bedrock geology, as summarised by Bleeker (2002), suggests that the craton has existed as a contiguous block since amalgamation by at least ca. 2.7 - 2.9 Ga. Parts of the craton are substantially older, evidenced by the ca. 4.0 Ga Acasta gneisses, the oldest rocks yet described on Earth (Bowring and Williams, 1999).

The kimberlites in the Slave craton are distributed in a linear array (Figure 5.1), beginning at the Gahcho Kué kimberlites (Kopylova and Caro, 2002) in the south and extending north, through the central Slave region (Ekati, Diavik), until reaching the Jericho and Artemisia kimberlites in the far north. The kimberlites in the central Slave are the youngest, being Eocene in age (Kjarsgaard and Levinson, 2002), and this region is the most extensively studied, both in terms of xenoliths (Pearson et al., 1998; Aulbach et al., 2004; Menzies et al., 2004; Westerlund et al., 2006; Aulbach et al., 2007a; Aulbach et al., 2011a) and xenocrysts (Griffin et al., 1999). A number of mantle geophysical studies have also been undertaken in this region, e.g., seismic (Snyder 2008; Snyder and Bruneton, 2007)) and

magnetotelluric (Jones et al., 1999, 2001, 2003) analyses. We will use our geochemical observations to try to interpret some of the features evident in the geophysical surveys.

5.3 ANALYTICAL METHODS

5.3.1 Sample processing

Thin section billets were cut from all suitable samples on a diamond-blade bench-top saw, and the remaining sample was then crushed using a fly-press. Approximately $^1/_8 - ^1/_{16}$ of this coarse crush was then separated and powdered in an agate ball-mill for 35 – 45 minutes to ensure complete powdering of rock chips.

5.3.2 Electron Microprobe (EMP)

Minerals in the Diavik peridotites were analysed using Cameca SX100 instruments at the University of Cambridge, the Saskatchewan Research Council, and the University of Alberta, in wavelength dispersal mode. Repeat analyses on the same sample were performed at both institutions to ensure consistency of results (see 8.2.3). EMP conditions are summarised in Chapter 8.2.1.

Three points were analysed on the core of each mineral and one point on the rim, to check for homogeneity. Only core analyses where cation totals were ± 0.02 from the ideal value

were used to calculate average mineral compositions for a given sample. Example maps of probe analysis locations are shown in 8.1.2.

Mineral modes were estimated visually, since thin sections where grain sizes are relatively small (2 – 2.5 mm diameter) commonly show heterogeneous distribution of clinopyroxene and garnet, precluding modal mineral abundances by point counting. Samples with large grain sizes (> 3 mm) are not suitable for point counting since they are unrepresentative of the sample as a whole (Van der Plas and Tobi, 1965).

5.3.3 X-Ray Flourescence (XRF)

Bulk major-element analyses, including Ni and Cr were performed on fusion beads of 3 g powdered sample at the Open University, UK. All samples that it was possible to prepare a bulk analytical powder from (n = 32) were analysed.

GIT-IWG Standards G94 (Threkeld microgranite; Thompson et al., 1996), UB-N (Serpentinised peridotite; Govindaraju, 1982) and WS-E (Whin Sill dolerite; Govindaraju et al., 1994) were analysed with xenolith samples were within 2 % of accepted values (Table 8.4.1).

5.3.4 Laser-Ablation ICP-MS (LA-ICP-MS)

In-Situ LA-ICP-MS analyses were performed on garnet crystals separated from coarse crush of the xenoliths and mounted in epoxy resin pucks. A Photon Machines laser of

wavelength 193 nm was coupled to an Agilent 7700x quadrupole ICP-MS and ablated the samples with a beam diameter of 52 μm. Energy density was 7 Jcm^{-2} and the pulse repetition rate was 10 Hz. Dwell time on each sample was 120 seconds, including 45 second gas blank and 75 second ablation time. At least 3 crystals were analysed from each sample to check for variation.

Standard basaltic glass GSD-1G (Jochum et al., 2011) was used for element calibrations and garnet standard PN2 was used (Canil et al., 2003) for high-pressure garnet calibration. Standard values were within 1 % of published values for GSD-1G (Jochum et al., 2011) and 5 % of published values for PN-2 (See Table 8.5.1). CaO content was used to normalize the trace element analyses, which were processed using the software GLITTER (Longerich et al., 1996; Griffin et al., 2008) which allowed visual investigation of the analytical signal for accurate selection of good-quality measurements.

5.3.5 Separation of PGEs

Re and Os were separated from 1 g sample powder by digestion of sample in reverse Aqua Regia solution in a high-temperature asher at 300 ℃ and 100 bar for 16 hours. Osmium was separated from Re and using CCl_4 and HBr extraction, and purified via micro-distillation. Anion resin was used to separate Re from the other PGEs.

5.3.6 ICP-MS

Samples were taken up and analysed in 1.5 mL of 0.8N HNO_3 on a ThermoFinnigan *ELEMENT2* at the Northern Centre for Isotopic and Elemental Tracing (NCIET), Durham University. Average Re blank was 0.032 ppb. Methods and analytical conditions have been described in detail by Dale et al. (2009), and are visually summarised in 8.1.4.

5.3.7 Thermal-Ionisation Mass Spectrometry (TIMS)

Os was analysed as OsO^{4-} on a ThermoFinnigan *TRITON* TIMS. Samples were taken up in 0.5 μL HBr and dried onto an outgassed Pt ribbon filament and coated with 0.3 – 0.5 μL $Ba(OH)_2$ activator. Os was analysed using a dynamic measurement regime as 4 blocks of 25 ratios, resulting in 92 useable analyses (after interpolation). Measurements were taken over three analytical sessions during 2009 – 2010. Average Os blank for the Diavik suite was 1.2 pg.

TIMS Re-Os standard solution DROsS (Nowell et al., 2004) was analysed during all analytical sessions, variation is shown on Figure 8.3.1. Values measured fell within accepted ranges. Peridotite Re-Os standard GP13 was also analysed at regular intervals, with Os concentrations and isotopic ratios comparing well with previously published summaries (Pearson et al., 2004; Figure 8.3.2). In addition, a highly-depleted peridotite xenolith (MX5022) was analysed four times as an in-house standard for refractory

peridotites. The range of $^{187}Os/^{188}Os$ ratios observed for GP13 was almost identical to the range for MX5022 (0.000846 vs. 0.000854) and this level of variation appears to be inherent sample heterogeneity.

5.4 XENOLITH PETROGRAPHY

Samples were classified as harzburgitic or lherzolitic based on the amount of clinopyroxene present in thin section; samples with > 5% cpx were classified as lherzolites. Estimated mineral proportions are reported in Table 5.1. Where abundances are not available, xenoliths were too fragmentary for creation of a thin section, and mineral compositions were analysed on grain separates mounted on thin section glass. Textural terminology is after Harte (1977).

5.4.1 Coarse Peridotite

Coarse peridotite xenoliths show three types of garnet morphology. Three main types are evident; 1) crystals of a similar size and shape to the surrounding silicates, 2) rounded crystals, often with inclusions, that are occasionally much larger than the surrounding silicates, and 3) 'starry', anhedral crystals that appear to be in-filling gaps within the surrounding silicates (see Figure 5.2a, b, c).

Some coarse samples show bimodal olivine size distributions, with large crystals of olivine mantled by a narrow region of variably altered finer-grained, neoblastic olivine. Clinopyroxene is variable in proportion, but where present is often concentrated with

garnet in vein-like regions, surrounded by coarser-grained olivine and orthopyroxene (Figure 5.3)

5.4.2 Porphyroclastic Peridotite

A smaller proportion (9 of 22 samples for which thin sections were possible) of the Diavik sample set are classified as porphyroclastic. These samples show both fluidal and disrupted textures. Recrystallized/disrupted textures are most common where 'pools' of coarse grained olivine and orthopyroxene remain, surrounded by recrystallized, fine-grained olivine. These samples have not developed the full fluidal texture associated with two samples, where clear flow structures surround equally-sized porphyroclasts of olivine, orthopyroxene, clinopyroxene and garnet.

5.5 BULK MAJOR ELEMENTS

Many of the Diavik samples show extensive calcite in thin section, which is attributed to syn/post-eruption modification by the kimberlite as it commonly occurs in large cracks. However, while this effect is easy to resolve petrographically, the impact on bulk-rock major element determinations is large.

Cratonic peridotite normally shows bulk rock CaO/Al_2O_3 ratios of 1.25 or less (Pearson et al., 2003 and Pearson, *pers comm.*). Using this criterion, six of the central Slave bulk analyses (DDM#'s 164, 332, 444 and 336; MX#'s 5056 and 5054) could be considered as showing primary compositions. MgO in these samples varies from 46.5 to 48.6 wt%, within the range for normal cratonic peridotites (Pearson et al., 2003; Pearson and Wittig, 2008). Bulk Mg# varies from 89.6 to 91.5, with a mean that is slightly low, at 90.8. Al_2O_3 varies from 0.6 to 2.4 wt%, with an average at 1.5 wt%, similar to the Al_2O_3 content of the Jericho and Artemisia peridotite xenoliths (Chapter 4).

However, the limited number of samples available and the difficulty in assessing whether these measurements reflect (broadly) primary residue compositions significantly limits the conclusions that can be drawn from these data.

5.6 MINERAL MAJOR-ELEMENT CHEMISTRY

5.6.1 Olivine

There is no observable difference in chemistry (outside analytical error) between olivine neoblasts and olivine porphyroclasts in the same sample, with two samples utilized for comparison (MX5023, MX5059). Olivine Mg# ($Mg\#_{ol}$) in the Diavik samples varies from 90.5 to 92.8, within the range reported for cratonic lithosphere worldwide (Pearson and Wittig, 2008), although the average value is slightly lower. The $Mg\#_{ol}$ distribution has two peaks, at 91.18 and 92.48 (Figure 5.4; n = 24) picked out by Gaussian mixture modelling (Sambridge and Compston, 1995).

5.6.2 Orthopyroxene

Orthopyroxene compositions are similar within samples and between samples. No significant core/rim variability is observed in any element. Orthopyroxene Mg# ($Mg\#_{opx}$) varies between 91.8 and 93.1, and the magnitude of $Mg\#_{opx}$ is correlated with $Mg\#_{ol}$ (R^2 =

0.913) indicating that the phases are in equilibrium. In all cases the $Mg\#_{opx} > Mg\#_{ol}$, but this can vary from an increase of 0.27 to 1.37, very roughly correlated with $Mg\#_{ol}$.

5.6.3 Clinopyroxene

Overall, there is little systematic core/rim variation in the Diavik clinopyroxenes, except in TiO_2. On average, rim values are 167 % greater than the core value, excluding sample DDM_384 where the rim shows very high TiO_2 enrichment (1088 %), although the bulk rock TiO_2 enrichment in this rock is no more elevated than any other of those that exceed 0.05 % in the Diavik suite.

5.6.4 Garnet

No systematic core/rim enrichment in garnet is observed in the Diavik samples. Cr_2O_3 – CaO systematics (Figure 5.5) indicate only one G10-type (Dawson and Stephens, 1975; Grütter et al., 2004) composition is present in the Diavik peridotite dataset. All other samples plot within the G9 lherzolitic field despite lacking clinopyroxene in thin section. The scarcity of G10 garnet compositions in the xenolith sample suite we have analysed is anomalous when compared to published garnet data from central Slave microxenoliths and diamond inclusions with acceptable stoichiometry (Figure 5.5, grey diamonds; data from; Mackenzie and Canil, 1997; Davies et al., 2004; Klein-BenDavid et al., 2004; Menzies et al.,

2004; Westerlund et al., 2006; Aulbach et al., 2007a; Creighton et al., 2008; Donnelly, 2009; Van Rythoven and Schultze, 2009; Creighton et al., 2010).

5.7 PRESSURE-TEMPERATURE CALCULATIONS

5.7.1 Method

In order to calculate a P–T array for the central Slave craton, it was necessary to combine macroxenolith data from this contribution with previously published samples, as Mather et al. (2011) emphasise the importance of the number of samples in the P–T array for precisely constraining the geotherm.

Twenty-seven new macroxenolith P–T estimates were added to a collated database of 366 xenoliths and diamond inclusions (Mackenzie and Canil, 1997; Davies et al., 2004; Klein-BenDavid et al., 2004; Menzies et al., 2004; Westerlund et al., 2006; Aulbach et al., 2007a; Creighton et al., 2008; Donnelly, 2009; Van Rythoven and Schultze, 2009; Creighton et al., 2010) from which 258 viable P–T estimates were obtained.

Multiphase P–T estimates were calculated depending on the available mineralogy as explained in Chapter 3. Only samples with good stoichiometry for clinopyroxene, orthopyroxene and garnet were utilized, using the recommended lherzolite thermobarometer combinations of Nimis and Grütter (2010); the Taylor (1998) two-pyroxene thermometer and the garnet-orthopyroxene barometer of Nickel and Green (1985) with Al-on-M1 calculated after Carswell and Gibb (1987; TA98_NG85). If one of the

phases was missing, or had poor stoichiometry, we applied one or other of the single-clinopyroxene thermobarometer of Nimis and Taylor (2000; NT00_NT00), or a harzburgitic thermobarometer combination using either Brey and Kohler's Ca-in-orthopyroxene (Ca-in-opx) thermometer with the Nickel and Green (1985) barometer, or the relatively new Nimis and Grütter (2010) thermometer with the same Nickel and Green (1985) barometer (Ca-in-opx_NG85 and NG09_NG85, respectively). Mather et al. (2011; Chapter 2) showed that P–T estimates from these different thermobarometer combinations could be combined to form one P–T array for palaeogeotherm estimation without a significant change in the shape of the palaeogeotherm.

250 new xenocryst compositions were analysed by EMP and filtered for good stoichiometry and peridotitic affinity according to the guidelines of Nimis (1998), Read et al. (2004), and Grütter (2009), leaving 191 xenocrysts to contribute to the palaeogeotherm fit.

Palaeogeotherms were fitted as outlined in Mather et al. (2011; Chapter 2). P–T calculations were performed using ptexl2011, a modification of the ptexl3 spreadsheet of Andrei Girnis (Stachel, 2011, *pers. comm.*). Three palaeogeotherm fits were run from the collated new and published peridotitic data; 1) NT00_NT00 xenocryst only clinopyroxene P–T array, 2) NT00_NT00 xenolith clinopyroxene P–T array and 3) multiphase P–T array using a combination of lherzolitic, harzburgitic and single-clinopyroxene P–T estimates.

5.7.2 Results

Harzburgitic thermobarometry results were extremely variable, with the Nimis and Grütter (2009) thermometer yielding unreasonably high P–T estimates when compared

with the Ca-in-opx (Brey and Köhler, 1990) thermometer when coupled to the same barometer (Nickel and Green, 1985). Creighton et al. (2010) commented on the oxidation state of the central Slave mantle lithosphere and concluded that the shallower regions were more oxidised than the deeper regions. This change in oxidation state may have influenced the Fe^{2+}/Fe^{3+} systematics of the xenolith samples, altering the Fe-Mg-based thermometry estimates. For this reason, the Ca-in-opx thermometer was combined with the Nickel and Green (1985) barometer for samples lacking clinopyroxene, or good clinopyroxene analyses, as recommended by Nimis and Grütter, (2009).

The palaeogeotherm fits yield lithosphere thickness estimates that vary between 217 km and 251 km (Figure 5.6). Overall, the palaeogeotherm is 'cool', in agreement with Grütter (2009); indeed, the NT00_NT00 xenocryst P–T array indicates deeper, cooler lithosphere than the xenolith array, although this is within error. The NT00_NT00 single clinopyroxene xenolith palaeogeotherm is more precise than the xenocryst palaeogeotherm. However, based on the detailed discussion in Mather et al. (2011) we suggest that the 4 phase peridotite palaeogeotherm is the most viable, and that the base of the lithosphere is at 217 ± 15 km. This palaeogeotherm crosses the diamond-graphite boundary at 131 ± 7 km, yielding a diamond window of just under 90 km.

5.8 GARNET TRACE ELEMENTS

5.8.1 Other trace elements

Zr-Y concentrations of Diavik macroxenolith garnets are shown on Figure 5.7 and compared with existing trace element data from Westerlund et al. (2006; black triangles) and Creighton et al. (2008; white diamonds). The majority of garnets in this study (grey diamonds) plot outside the 'depleted' field of Griffin et al. (1999b), trending into the melt-metasomatism field at higher Zr and Y values. The sample with the unusual ultra-depleted rare-earth element pattern has extremely high Y given the low Zr (indicated with red arrow on Figure 5.7), in comparison with many other samples from this dataset and the published data.

5.8.2 Rare-earth Elements

Laser-ablation ICP-MS analyses of Diavik macroxenolith garnets for rare-earth elements show three main CI-chondrite normalized pattern types (Figure 5.8), similar to the Artemisia xenolith and xenocryst data (See: 4.3.3); sinusoidal, 'lherzolitic', and

ultradepleted. Sinusoidal patterns have been associated with diamond inclusions and diamond-forming fluids (Figure 5.8; Stachel et al., 2004; Klein-BenDavid and Pearson, 2009), and are relatively rare in the Diavik dataset, with only 3 samples showing this pattern. The bulk of the samples (n = 14) show the 'lherzolitic' silicate melt-equilibrated pattern (Burgess and Harte, 2004; Figure 5.8).

One sample shows a distinct rare-earth element pattern that is dissimilar to either the 'lherzolitic' or sinusoidal types. MX 5022 (Figure 5.8) shows extreme depletion (< 1x chondrite values) in the LREEs with a gradual increase from LREE to HREE. This pattern is termed 'ultradepleted', since the combination of such low abundances of the mid-light rare earths (Pr, Nd, Sm) with a positive gradient in these plots is rarely seen in cratonic xenolith garnets.

5.9 RE-OS ISOTOPES

5.9.1 Os

Os concentrations vary from 0.020 – 6.54 ppb, with an average and median concentration of 2.72 ppb and 2.74 ppb, respectively. 5 samples had very low concentrations of Os (0.02 – 0.03 ppb), with suprachondritic $^{187}Os/^{188}Os$ isotope ratios. Overall $^{187}Os/^{188}Os$ isotope compositions are between 0.1075 and 0.1491, with a median value of 0.1173 ± 0.0001. $^{187}Os/^{188}Os$ ratios were used to calculate Re-depletion model ages by assuming that Re/Os = 0 at formation, and thus that any Re present in the sample was introduced during kimberlite eruption. The Os isotope composition was corrected for the decay of this additional Re between kimberlite eruption (~55 Ma; Davies and Kjarsgaard, 1997) and today, and the resulting $^{187}Os/^{188}Os$ value projected to the O-Chondrite bulk Earth evolution line to obtain a minimum age estimate for the formation (Re-depletion) of the xenolith sample.

Two main components are visible in the Gaussian mixture-modelled T_{RD} population for the Diavik macroxenoliths (Figure 5.9). Mixture modelling follows the guidelines in Pearson et al. (2007): The bandwidth on probability density diagrams were fixed for all samples at ± 0.2 Ga (reflecting the Os isotope heterogeneity of the mantle evolution curve in the Archean) to avoid producing artificially sharp peaks. A very broad 'Proterozoic' peak is

visible in the T_{RD} distribution at 1.2 – 1.7 Ga ± 0.2 Ga (n = 16), and a sharper Archean peak at 2.6 Ga ± 0.2 Ga (n = 7), indicating that there is a significant Archean component to the Diavik macroxenolith dataset.

5.9.2 Re

Re contents of the Diavik xenoliths vary by an order of magnitude, from 0.04 ppb to 0.40 ppb. There is no relationship between Re content and $^{187}Os/^{188}Os$, ($R^2 = 0.15$, n = 29). There is no correlation between bulk rock composition and Re content; samples where $CaO/Al_2O_3 < 1.25$ show Re concentrations from 0.11 to 0.31 ppb, showing neither the extremely depleted nor highest values within the dataset.

5.10 DISCUSSION

5.10.1 Palaeogeotherm results and comparison with seismic and magnetotelluric data

Existing teleseismic estimates of lithosphere thickness in the central Slave region do not focus on defining the exact lithospheric thickness. Most such studies focus primarily on the postulated 140 km discontinuity and seismic anisotropy in the region (e.g. Snyder, 2008). However, our lithospheric thickness estimates (217 km) are within error of previous seismic and magnetotelluric geotherm estimates from the central Slave craton (190 – 210 km, Snyder, 2008; 250 ± 50 km, Bank et al., 2000; ~210 km, Jones et al., 2003), indicating that within the resolution of the techniques, there has been no significant decrease in lithospheric thickness between intense kimberlite activity at ~55 Ma and today.

5.10.2 Lithosphere compositions from xenoliths or diamond inclusions?

It has been suggested (Aulbach et al., 2011) that xenoliths are rarely pristine records of the lithosphere at the time of formation, having been altered probably multiple times during their history. However, there is a trade-off between the pristineness of a sample and the

amount of information that can be yielded from it. While diamond- and olivine-inclusions are shielded from the potential effects of metasomatism (silicate, sulphide, or otherwise), there are only relatively rare occurrences of inclusions where two or three phases are in contact. Hence, there is limited opportunity to reliably estimate P–T and obtain representative analyses of trace elements, without introducing further uncertainty by projecting calculated temperatures to estimated palaeogeotherms. For example, Aulbach et al. (2009a) use Re-Os isotope measurements from sulphide inclusions in olivine and diamond to date the ultra-depleted layer, estimating depth of equilibration using novel approaches such as temperature estimation from N aggregation state in diamond, and Al-in-olivine thermometry projected to a 38 mWm^{-2} Pollock and Chapman (1977) geotherm. Mather et al. (2011; Chapter 2) showed that these Pollock and Chapman (1977) geotherms are anomalously convex in the shallow part of the lithosphere, and cannot be relied upon to give realistic models of the thermal structure of the lithosphere. Moreover, Pearson & Wittig (in press) have recently made the case that diamond inclusion olivines have been affected by carbonatite metasomatism and only provide a narrow window on the lithospheric mantle. We contend that xenolith-derived data is more representative and can yield very valuable insights using systematic approaches. Careful identification of samples where clear metasomatism has occurred using systematic EMP and petrographic analysis can help to mediate the potentially muddling effect of metasomatism on whole-rock samples and their constituent mineral and isotopic analysis.

5.10.3 New constraints on the geochemistry and age of the Ultra-Depleted Layer from the macroxenolith database.

5.10.3.1 Major elements

The advantage of a coupled geochemical and whole-rock Re-Os isotope study on well characterized peridotite xenoliths is that ages can be combined with both multiphase P–T estimates and suggested tracers for depletion in this shallow layer (e.g. garnet major- and trace-element abundances). This approach provides robust data for rigorously assessing previous suggestions (Aulbach, *in press*; Aulbach et al., 2011, and references therein) that the 'ultra-depleted' layer in the central Slave lithosphere is also older as well as more depleted than the lithosphere below.

Chemical stratigraphy underpinned by multi-phase xenolith P–T is our chosen approach. Such measurements have their own intrinsic errors, but crucially do not rely on an accurate lithosphere geotherm for their estimation. Many thermobarometer combinations are available (see Chapter 3) from which an average P–T is calculated.

The central Slave craton xenoliths have an age distribution with a significant Archean (> 2.5 Ga) component (Figure 5.9). There are 7 xenoliths with T_{RD} ages > 2.5 Ga, the remainder of the samples are all < 2.0 Ga. These 7 samples are taken to be the Archean component of the dataset, and examined as a separate group to the younger samples (n = 20). These samples can be objectively identified as belonging to a separate component by mixture modelling (Figure 5.10).

Figure 5.10(a) shows the average P–T estimates for xenoliths older and younger than 2.5 Ga from this study. The average P–T and associated standard deviations for all samples within each age group are shown in the inset for clarity, and indicate that the older samples yield consistently shallower estimates, on average, than the younger samples. Also illustrated on Figure 5.10(b) are the $Mg\#_{ol}$ for samples in each age group. Again, the > 2.5 Ga samples have significantly higher $Mg\#_{ol}$ than those in the < 2.5 Ga age group. Both these observations indicate that the shallow lithosphere in the central Slave region is older, and also has a higher $Mg\#_{ol}$, indicating that it is more depleted than the lithosphere below.

Interestingly, there is no relationship between G10 garnet compositions and age group observed in our Diavik macroxenolith database. Griffin et al. (1999a) suggest that the Ultra Depleted Layer contains proportionally more G10 garnet than the deeper layer. It has been proposed (Canil, 1990) that harzburgitic xenoliths containing G10 garnet also contain carbonate which, upon decompression, causes destructive fracturing of the xenolith during ascent in the kimberlite. This fracturing means that few, if any macroxenoliths of this material remain, and the majority of the G10 garnet is present as xenocrysts in the kimberlite volcanic deposits. This is one way to explain the lack of significant amounts of G10 garnets visible in the Archean macroxenolith samples. In support of this, garnets in Archean microxenoliths from the central Slave analysed by Westerlund et al. (2006) show a much higher proportion of G10 garnets (100 % of samples with acceptable cation totals), indicating the prevalence of G10 garnets in smaller sized samples that are > 2.5 Ga.

Figure 5.11 shows the Ti concentrations from xenolith garnets measured via LA-ICP-MS. Also shown are the median concentrations quoted by Griffin et al. (1999a) for the shallow layer in the central region of their lithospheric survey (Griffin et al., 1999a, Figures 8 & 9). Our new data suggest that the Archean sample group have significantly lower Ti than the

younger age sample group. This is consistent with the results of Griffin et al. (1999a, 2004) for the 'ultra-depleted' layer.

5.10.3.2 Trace elements

Figure 5.12 shows the Zr, Ga and Y content of xenolith garnet from the Diavik macroxenoliths, and also includes data from 7 harzburgitic microxenoliths from the Ekati mine, the only other published coupled age and geochemical data from this region (Westerlund et al., 2006), in an effort to increase dataset size. Creighton et al. (2010) analysed an overlapping peridotite xenolith suite, and where REE patterns were available for macroxenolith samples which were analysed for T_{RD} in this study, these values were also included into the dataset. The medians and standard deviations of the different age groups are illustrated and indicate that in all cases, the younger samples have higher concentrations of REE elements than the older samples. The older samples are also within error (with the exception of Ga in the > 2.5 Ga dataset) of the Griffin et al. (1999a) median compositions for both the shallow and deeper layers, and in fact, the xenolith garnet data consistently yields more depleted compositions for the older layer than estimated by Griffin et al. (1999a), from garnet xenocrysts. This provides a clear indication that the > 2.5 Ga sample group are representative of the ultra-depleted layer, and that this layer is not entirely composed of G10-bearing garnet peridotite.

Figure 5.13 shows the garnet rare-earth element patterns from the Diavik xenoliths highlighted by their associated age group. Also shown on Figure 5.13 (as dotted lines) are the partial rare-earth element patterns from garnets from the harzburgitic microxenoliths of Westerlund et al. (2006). There is a clear relationship visible in both the macro- and micro-

xenolith garnet rare-earth element patterns where 'lherzolitic', silicate-melt equilibrated (Stachel et al., 2004) patterns are associated with < 2.5 Ga samples (blue), and sinusoidal profiles are associated with > 2.5 Ga samples.

5.10.4 Base of the Ultra Depleted Layer

Coupled P–T, trace element and whole-rock T_{RD} data suggest that the Archean samples in the central Slave (Diavik and Ekati) micro and macro-xenolith suite have extremely depleted compositions, and can be directly attributed to the shallow, 'ultra-depleted' layer postulated by Griffin et al. (1999a, based upon xenocryst data) and further discussed by Aulbach et al. (2007a, 2011a). However, this 'ultra-depleted' layer is purported to have a base at 140 – 150 km, which has been linked to a discontinuity at ~130 – 140 km visible in both broadband seismic profiles (Snyder, 1998) and a region of unusually conductive lithosphere visible in magnetotelluric surveys at ~80 – 110 km (Jones et al., 2003). The data presented here suggest that the Central Slave ancient, ultra-depleted layer extends to 180 ± 10 km, allowing for the overlap of young and old samples illustrated in Figure 5.10(a). This implies that the magnetotelluric feature and seismic discontinuities potentially indicate other feature(s), rather than the base of the ultra-depleted layer.

5.10.5 Diamond abundance and depth-dependent metasomatism

Sinusoidal rare-earth element profiles in garnets are commonly seen in analyses of garnets included in diamonds (Stachel et al., 2004; Stachel & Harris, 2008), and have been associated with the metasomatic effect of diamond-forming fluids (Klein-BenDavid & Pearson, 2009). In the central Slave craton, the prevalence of sinusoidal rare-earth element profiles within garnets from the > 2.5 Ga peridotites might suggest that many of the diamonds erupted in the central Slave could have formed in this region.

The 140 – 150 km purported base of this ultra-depleted layer has meant that these ultra-depleted diamonds formed in the very small window between the diamond-graphite boundary (Kennedy and Kennedy, 1976) at approximately 128 km (from the Central Slave multiphase geotherm, 5.7), and the bottom of the ultra- depleted layer at 140 – 150 km. However, the much deeper estimate for the thickness of the ultra-depleted layer suggested by the macroxenolith evidence presented here leaves a much larger window of ultradepleted peridotite within which diamond is stable (~ 52 km).

Interestingly, the only sample with an average multiphase P–T depth shallower than the geophysical discontinuity recognised at ~130 – 140 km is MX 5022. This is also the sample that was identified as being extremely depleted in the LREE in comparison to other samples, with a positive slope through the MREE in comparison to the negative slope seen in the other sinusoidal profiles (Figure 5.9). The lack of a sinuous form to the REE garnet profile in this sample could be evidence that this sample has not interacted with diamond-forming fluids (Klein-BenDavid & Pearson, 2009) and that the high diamond grade in the

central Slave is the result of these diamond forming fluids 'ponding' beneath the shallow 130 – 140 km discontinuity, producing an unusually diamond-rich lithospheric mantle in the lithosphere below.

5.11 CONCLUSIONS

New silicate mineral major element, whole rock Re-Os isotope, garnet trace element and P–T data from a suite of macroxenoliths from the Diavik kimberlite were combined with published data from the central Slave region (Mackenzie and Canil, 1997; Davies et al., 2004; Klein-BenDavid et al., 2004; Menzies et al., 2004; Westerlund et al., 2006; Aulbach et al., 2007a; Creighton et al., 2008; Donnelly, 2009; Van Rythoven and Schultze, 2009; Creighton et al., 2010).

From this collated database, a palaeogeotherm was calculated using the methods outlined in Mather et al. (2011; Chapter 2) which indicates that lithospheric thickness in this region is 217 ± 15 km, within the range of published seismic and magnetotelluric analyses (Bank et al., 2000; Jones et al., 2003; Snyder, 2008).

Coupled Os isotope, major- and trace-element systematics for Diavik xenoliths indicate that samples older than 2.5 Ga show highly depleted compositions that are similar to those outlined for the 'ultra-depleted' layer. However, P–T estimates from these same xenoliths indicate that these ancient and highly depleted samples come from depths up to ~170 – 180 km, which is significantly deeper than the geophysical reflectors (seismic and magnetotelluric) that have been previously ascribed as representing the base of the 'ultra-depleted' layer.

The only sample that has been erupted from a depth shallower than these reflectors (~100 – 120 km) shows a strikingly different REE profile to those ancient samples from below the reflector. Garnet REE systematics are used to suggest that the diamond forming fluids commonly cited as the cause of these sinusoidal REE profiles did not percolate above these geophysical reflectors, perhaps suggesting that they were prevented from doing so by the nature of the reflectors themselves. Alternatively, the diamond forming fluids simply froze in the lithosphere at ~ 130 km (e.g. Menzies et al., 1987).

6 SYNTHESIS: A XENOLITH-BASED LITHOSPHERIC TRANSECT

6.1 INTRODUCTION

This chapter aims to summarise the work of the thesis as a whole, in order to answer the final two questions posed in the introduction, namely;

- *How did the Slave craton form?*
- *How has the Slave craton evolved through time?*

The previous two questions:

- *What is the nature and age of the Slave craton lithosphere in the far North?*
- *How old is the 'ultra-depleted' layer of the central Slave?*

have been explored and answered in the preceding chapters, and will not be dealt with further here, although the conclusions from these individual studies will be used to contribute towards the synthesis of the data; namely a xenolith-based lithospheric transect.

6.2 FORMATION OF THE SLAVE CRATON

As outlined in section 1.1, there are two main hypotheses that are invoked for the mechanism of formation of the Slave craton lithosphere, and cratonic lithosphere in general. The aim of this project was to create a lithospheric transect that brings together observations from kimberlite localities across the craton, in order to realistically assess which mechanism might have been operating during the formation of the Slave craton. The two main hypotheses for craton formation are summarised in more detail below. However, it is important to note that these are the main endmember models, and it is very likely that some combination of these, or potentially an as-yet un-described model may instead have been operating. However, for simplicity, only the two main competing craton formation hypotheses will be outlined.

6.2.1 Plume Subcretion

Recently summarised by Aulbach (*in press*), the plume subcretion hypothesis suggests that craton formation is a two-stage process. First, a depleted portion of lithospheric mantle is created by shallow melting, either at an Archean mid-ocean ridge or in a plume–type environment. Second, abnormally hot asthenospheric mantle upwelling impinges on this

depleted keel. The upwelling plume material melts and the residue of this melting 'subcretes' (underplates) onto the base of the pre-existing lithosphere. Many arguments are used in defence of this hypothesis, and they mainly centre on the geochemical signatures of deep versus shallow melting. In particular, bulk rock FeO – MgO systematics are a key piece of evidence that are used to indicate melting at pressures > 3 – 5 GPa (100 – 150 km), precluding formation of the entire thickness of lithospheric mantle at mid-ocean ridges. Notwithstanding the difficulties in estimating bulk major element compositions from small samples of coarse-grained rocks (Pearson and Wittig, 2008), and the insensitivity to melting pressure of most bulk rock parameters versus their relative ease of being disturbed by metasomatism, this hypothesis suffers from the major caveat that large-volume melting, required to deplete residues to isopycnic stability (Jordan, 1988), is difficult to produce at depths > 100 km (White and McKenzie, 1995).

6.2.2 Subduction Accretion

The subduction accretion hypothesis requires that melting occurs in a mid-ocean ridge or subduction setting, and the great thicknesses of cratonic lithosphere are formed by 'accreting' sections of lithospheric mantle together (Helmstaedt and Schultze, 1989; Pearson and Wittig, 2008), or in a single melting event at a hot Archean ridge that produces > 150 km of depleted lithosphere (Herzberg and Rudnick, *in press*; Pearson and Wittig, *in press*). Proponents of this hypothesis argue that major element concentrations of mantle xenoliths are strongly affected by secondary metasomatism and re-introduction of mineral phases, explaining the discrepancy between predicted mineral modes for residues of > 30% melt

extraction and those observed in cratonic xenoliths, namely the presence of garnet and clinopyroxene. This alteration means that reliable determination of depth of melting from bulk major elements is not possible.

In contrast, the Mg# of cratonic xenolith olivine ($Mg\#_{ol}$) is used as the main evidence for the large volumes of melting required to deplete cratonic lithosphere occurring in the spinel stability field at an Archean ridge and being subducted to great depths to form cratonic lithosphere. The average $Mg\#_{ol}$ in cratonic peridotite is ~ 92.6 (Bernstein et al., 2006), supporting the shallow-melting hypothesis since much higher values are predicted from melting in an Archean plume-type environment due to the higher mantle temperatures compared with the Phanerozoic (Herzberg and Rudnick, *in press*.)

A weakness of this hypothesis is the mechanism by which the stacking of the lithospheric sections is accomplished. The mechanism of plate tectonics in the Archean is still highly debated by those who model these processes numerically (e.g. van Hunen and van den Berg, 2008) and those who study their crustal remnants (e.g. Bleeker, 2002). When, if, and how subduction operated in the Archean is a key parameter in this hypothesis that is as yet not fully understood.

6.3 PREDICTIONS FOR THE LITHOSPHERIC STRATIGRAPHY OF THE SLAVE CRATON

This section will explore what, if any, primary geochemical and geophysical features should be observed in the mantle lithosphere of the Slave craton if each of the examined hypothesis were correct, and acted to form the sub-continental lithospheric mantle in this region. Note that these predictions are for the *initial conditions*, and ignore the effects of any subsequent metasomatism or alteration (examined in the next section). These predictions, together with those for the effect of metasomatism on the lithosphere, will be compared to the observations noted in Chapters 4 and 5 of this thesis, as well as with those from published data sources, in an attempt to comment on the potential formation and metasomatic history of the Slave craton. Again, these are endmember scenarios, and it should be noted that it is entirely possible that a hybrid of these models, or another model entirely, might have been operating during the formation of the Slave craton.

6.3.1 Plume subcretion

The following features are predicted for the plume subcretion hypothesis (Figure 6.1):

Geochemical:

1. Shallow melting in an arc/ocean ridge/ocean plateau setting forms lithosphere with high $Mg\#_{ol}$. Deeper regions are residues of melting in a plume-type upwelling. Melt volume at depth is precluded by limited adiabatic decompression melting leading to smaller volumes of melting and lower $Mg\#_{ol}$ than would be expected from shallow plume-type melting.

2. A shallow layer that is distinct in age, and older than the layer below, owing to the different mechanisms of formation of the upper and lower layers.

Geophysical:

3. A boundary in the lithosphere which was initially at the base of the shallow-formed layer that now forms the top of the deep-formed layer. Since both layers are peridotite, this may or may not produce a seismic reflector (Snyder, 2008).

4. A deeper layer of lithosphere that has anisotropy aligned with plate motion at the time of plume upwelling (forming thick lithosphere and inducing cratonization), and a shallower layer with anisotropy that either reflects anisotropy as observed in modern-day mid-ocean ridges (Achenbach et al., 2011); or the radially outward motion of plume-formed residua. Note that the second option for the shallow layer would not produce any noticeable seismic anisotropy.

6.3.2 Subduction Accretion

The following features are predicted for the subduction accretion hypothesis (Figure 6.1):

Geochemical:

1. The presence of an eclogite layer (or layers) within the lithosphere that show evidence of being derived from subducted oceanic crustal material.

2. $Mg\#_{ol}$ should *initially* vary with depth, with the shallowest regions of each lithospheric stack having experienced the most melting, and therefore having the highest $Mg\#_{ol}$, increasing with depth until the top of the next 'layer' of subducted lithosphere. This will not be the case if the entire thickness of lithosphere was produced in one melting event at an Archean ridge, where a gradually increasing $Mg\#_{ol}$ with depth would be expected.

3. The formation of the different layers of lithosphere at different times should lead to a distinct age structure of the lithosphere that reflects the nature of the subduction stacking, unless subduction stacking happened rapidly relative to the chronological resolution of the Re-Os system for peridotite model ages: ~ 0.2 Ga (Pearson and Wittig, 2008).

Geophysical:

4. The presence of a layer (or layers) of eclogite within the lithosphere represents a significant compositional boundary, and will produce a pronounced seismic reflection (Snyder, 2008) owing to the higher density of eclogite relative to depleted peridotite.

5. If the great thickness of lithosphere is formed by subduction stacking in one direction (i.e., from one subduction zone), then the lithosphere should have a pronounced anisotropy, related to ridge flow (e.g. Achenbach et al., 2011). However, if the 'stacks' of lithosphere are formed by more than one subduction event from different directions (i.e., from more than one subduction zone) then multiple, distinct anisotropy should be seen in each layer.

6.4 METASOMATISM AND ALTERATION

The lithospheric mantle in the Slave craton has existed for over 2.8 Ga (Chapter 5), and the likelihood is that it has experienced multiple stages of metasomatism which will modify the 'base' structure of the lithosphere (as shown in Figure 6.1, and summarised above) during this time. This section aims to explore the nature of main potential metasomatic agents and their effects on the lithosphere, namely; diamond forming fluids, percolating small-fraction melts and sulphur-saturated melts. These melts and/or fluids may result in either cryptic or modal metasomatism (Dawson, 1987, Menzies et al., 1987) that may prevent clear resolution of which lithosphere formation hypothesis might apply to the Slave craton.

6.4.1 Diamond-forming fluids

The Slave craton contains an abundance of diamonds, and these are present at each kimberlite locality studied in this thesis. Therefore it is clear that the process responsible for diamond formation has operated across the craton and will potentially overprint any initial starting lithospheric stratigraphy. In Chapter 5, the effect of these diamond forming fluids was cited as being responsible for the sinusoidal garnet rare-earth element (REE)

patterns observed in the macro- and micro-xenolith samples, based on the work of Stachel et al. (2004) and Klein-BenDavid and Pearson (2009). It is prudent to note, however, that multiple theories for the effect of diamond-forming fluids on garnet, and the nature of the 'sinusoidal' REE pattern, exist (Stachel and Harris, 2008).

An exploration into the potential mechanisms of diamond formation from diamond-forming fluids is beyond the scope of this thesis. However, elucidating the nature of these fluids is important in order to assess their effect on the lithospheric mantle. The most direct way of sampling the diamond-forming fluid is by analysis of inclusions in fibrous and monocrystalline diamonds, and these studies have shown that the composition of these included fluids can vary dramatically even within a single diamond (Klein-BenDavid et al., 2004); and may involve a number of potential sources (Klein-BenDavid et al., 2010). Therefore elucidating the effect that these fluids might have on the lithospheric mantle is not straightforward. However, most diamond-forming fluids are enriched in light-REEs, K, Mg and Ca, and could have a profound influence on the very incompatible element depleted lithosphere that they traverse.

6.4.2 Silicate melt metasomatism

As explored in chapter 4, silicate melt percolating through the sub-continental lithospheric mantle has the potential to overprint pre-existing isotopic signatures and perturb major- and trace-element systematics. In Chapter 4, silicate melt metasomatism is investigated as a suggested metasomatic agent that could re-set the Os isotope system by addition of Re.

The volume of silicate melt is crucial in determining its effect on the depleted peridotite of the lithospheric mantle. Small-fraction melts, if derived as partial melts from the asthenosphere, are expected to show enrichment in the light-REEs and incompatible elements (K, Ca, Ti), and considering the very refractory nature of cratonic peridotite these small-fraction melts would have a significant re-enriching effect (Menzies and Hawkesworth, 1987). They are, however, small-fraction, and suffer thermal 'death' at deep levels within the lithosphere, since their volume is not sufficient to avoid heat loss to the surrounding mantle which is (relatively) cooler than the melt itself (McKenzie, 1989). Therefore it might be predicted that the geochemical signature of percolating small-fraction melts on the host peridotite, i.e., an increase in light-REE content and re-enrichment in incompatible elements and Ti, should be restricted to the deeper mantle. Indeed, in southern Africa these melts are identified as the precursors to MARID (Mica-Amphibole-Rutile-Ilmenite-Diopside) xenoliths (Erlank et al., 1987; Waters. 1987), where highly incompatible compositions crystallise exotic mineralogies. No MARID-type xenoliths have yet been described for the Slave craton, although it is noted that these are an extreme example of silicate melt overprinting.

Larger-volume silicate melt percolation will have a more significant re-fertilizing effect on all the major elements, in particular decreasing the $Mg\#_{ol}$ by addition of Fe. Diffusion times for Fe and Mg in olivine at mantle temperatures and pressures are high enough that complete re-equilibration of the $Mg\#_{ol}$ with a more fertile, larger volume melt is possible on very short timescales (Smith and Boyd, 1992).

It is unlikely that the fertilizing effect of larger-volume silicate melts will dramatically affect the bulk of the lithospheric mantle owing to its highly depleted nature and stability. Unless melt percolates in dunitic-type channels (c.f. Kelemen et al., 1995) it is difficult to

supply enough melt to the lithospheric peridotite such that large amounts of re-equilibration can take place. (c.f. Waff and Holdren, 1981). Therefore the effect of larger-volume silicate melt metasomatism should be limited to the lower lithosphere.

6.4.3 Sulphide melt metasomatism

As outlined in Chapter 4, the effect of a co-existing immiscible sulphide melt and silicate melt (sulphur-saturated melts) will be to dramatically alter the $^{187}Os/^{188}Os$ ratio of the host peridotite, since sulphide melt precipitated as sulphides contains orders of magnitude more highly siderophile elements than the surrounding peridotite and contribute the most to the whole-rock Re-Os budget (Burton et al., 1999). Also, only a tiny fraction of radiogenic sulphide is needed to perturb the original peridotitic $^{187}Os/^{188}Os$ signature owing to its highly unradiogenic nature. This mechanism is thought to have occurred beneath the northern Slave craton, expressed in peridotite xenoliths sampled by the Artemisia kimberlite, overprinting the original ancient lithospheric signature. The pressure-dependence of sulphur saturation in silicate melts (Mavrogenes and O'Neill, 1999) suggests that the maximum sulphur content of a melt *increases* with decreasing depth; therefore it is more likely that deposition of sulphide will occur within the deeper portions of the lithosphere, if all other geochemical parameters remain the same.

It should be noted that metasomatic sulphide is commonly seen in lithospheric lithologies. Sulphide should be exhausted from the residue at ~20 – 25% melting (depending on the initial sulphur content; Lorand et al., 1999; Pearson et al., 2004) and therefore the large abundance and heterogeneous distribution of sulphides seen in highly depleted peridotite (30 – 40% melting), and in particular within eclogite xenoliths, indicates their nature as a secondary phase. However, the mechanism by which this sulphidic material is transported

through the lithosphere and deposited is not clear. The immiscible nature of sulphidic melts and silicate melts of varying volume has been demonstrated petrographically and experimentally (c.f. Mavrogenes and O'Neill, 1999). Therefore the geochemical decoupling of these melts is feasible, and is required in some situations to explain the available geochemical data (e.g. Chapter 4), where siderophile elements indicate sulphide alteration, but silicate major- and trace-elements do not show evidence of large- or small-fraction silicate melt metasomatism. The suggestion that sulphide melts show preferential 'wetting' of grain boundaries compared with silicate melt depending on oxygen fugacity (Clark et al., 1977; Gaetani and Grove, 1999) provides a potential mechanism to separate these two melts, allowing sulphidic melts to percolate through the lithosphere separately to silicate melts.

6.5 LITHOSPHERIC STRATIGRAPHY OF THE SLAVE CRATON

Figure 6.2 shows the available geochemical data from the four kimberlites highlighted in this lithospheric transect. This section will deal with the geochemical observations from the craton, examining to what degree the predictions from the above section can be ascribed to the lithosphere of the Slave craton.

6.5.1 $Mg\#_{ol}$

At all localities where data is available (Jericho, the central Slave and Gahcho Kué), there is a tendency for $Mg\#_{ol}$ to decrease with increasing depth. This relationship is most pronounced in the Jericho xenolith dataset (Figure 6.2). Although the shallowest samples at Gahcho Kué and the central Slave show very high $Mg\#_{ol}$ (up to 92.5), these high values are not exclusively found in the shallow lithosphere as is the case in the Jericho locality - the deep lithosphere also contains xenoliths with high $Mg\#_{ol}$.

A variety of mechanisms can be invoked to explain the apparent difference in $Mg\#_{ol}$ with depth distribution between the southern/central Slave craton and Jericho. Figure 6.3 shows the expected $Mg\#_{ol}$ – depth relationships for melting in an Archean plume-type

environment, a subduction-stacking model (melting at a shallow Archean ridge) and a one-stage hot ridge melting regimen. A gradually decreasing $Mg\#_{ol}$ with depth, crucially with an absence of deep, high $Mg\#_{ol}$ (> 92.5) samples is best represented by a one-stage hot ridge melting regimen; melting in a plume environment would be expected to produce residues with $Mg\#_{ol}$ up to 93.0 – 94.0, and subduction stacking should leave some deep samples with $Mg\#_{ol}$ > 91.5 (melting parameterization from Herzberg and Rudnick, *in press*; trends from Pearson and Wittig, *in press*). However, the $Mg\#_{ol}$ – depth distributions for the central Slave craton and Gahcho Kué can only be explained by the subduction stacking hypothesis, because of the presence of these deep, high $Mg\#_{ol}$ samples and because the abundant, very depleted olivine compositions predicted by the hot plume model are not observed. However, it is prudent to note that the predicted decrease in $Mg\#_{ol}$ towards the base of each 'slab' is not observed, although this could simply be due to the removal of these less depleted, more dense lithologies during the stacking event, or that the P–T errors outlined in previous chapters mean that the data resolution is not high enough to pick out particular 'slabs'.

It is possible that the lithosphere beneath the Jericho kimberlite was formed by a fundamentally different mechanism than the lithosphere beneath the central Slave craton. However, although there are contrasting crustal geologies in these two regions (Kjarsgaard et al., 2002), there is no evidence for a crustal-scale orogenic belt between them, nor are any distinct differences noted on the magnetotelluric survey across the region by Jones et al. (2001). Therefore, either the central and southern Slave localities, or the Jericho locality have been metasomatically altered to change their $Mg\#_{ol}$ – depth systematics. The main metasomatic perpetrator for affecting $Mg\#_{ol}$ is silicate melt, by addition of Fe (and subsequent lowering of the $Mg\#_{ol}$). Jericho is situated in the northern Slave craton, an area that has been suggested to have been dramatically affected by both the Wopmay orogeny,

the major Mackenzie igneous event (Chapter 4). Thus, it seems more likely that the distinct differences in lithosphere compositional characteristics with depth seen in a N-S transect across the Slave craton is related to varying extents of metasomatic alteration than differences in the mode of origin.

The effect of this metasomatic silicate melt overprint is likely to be more pronounced in the deep lithosphere, as explained in 6.4.2, and therefore this fits well with the observation that high $Mg\#_{ol}$ is not observed at depth, but is observed at shallower levels in this lithosphere where these melts have not reached.

In summary, the $Mg\#_{ol}$ – depth distribution seen across the Slave craton broadly matches the predicted observations for the subduction stacking lithosphere formation hypothesis, together with secondary silicate melt overprinting of the northern localities due to the fertilizing influence of the Mackenzie mantle plume and the fluids related to subduction of the Wopmay slab. However, this is probably an oversimplification.

6.5.2 Lithology

Although this thesis focuses primarily on peridotite xenoliths, a number of studies have examined xenoliths of other mantle lithologies such as eclogite and pyroxenite from the Slave craton. In particular, the distribution of eclogite is a key feature that can differentiate between the two lithosphere formation hypotheses; the presence of a distinct layer (or layers) of eclogite in the cratonic keel indicates that it may have formed by subduction of oceanic lithosphere, whereas the random distribution/absence of eclogite would indicate

that the lithospheric mantle is the residua of a deep melting regime, in line with the plume formation hypothesis.

Eclogites have been studied in detail from Diavik (Schmidberger et al., 2007; Aulbach et al., 2007b) and Jericho (e.g.: Heaman et al., 2002; Smart et al., 2009; Smart et al., 2011). The eclogites from Jericho in particular are enigmatic and contain features that indicate multiple modes of formation (c.f. Smart et al., 2009). However; what is necessary for lithospheric stratigraphy are depth estimates from these xenoliths and an estimate of the uncertainty on these values.

Krogh-Ravna (2000) published an updated garnet–clinopyroxene thermometer for use with eclogitic mineralogies. Temperature estimates for published eclogite xenoliths from Schmidberger et al. (2007) and Aulbach et al. (2007b; Diavik) and Smart et al. (2011; Jericho) were projected to the respective xenolith-derived palaeogeotherm calculated using the methods of Mather et al. (2011, Chapter 2). Krogh-Ravna (2000) does not give an estimate of the potential uncertainty in temperature using their geothermometer, and so a conservative estimate of ± 75 °C has been applied, which reflects a depth uncertainty (when projected to the palaeogeotherm) of about ± 20 km, similar to that observed using the single-crystal Ni-in-garnet thermometer (see: 3.3.3).

Figure 6.4 shows a histogram of projected depths (n = 72), together with Gaussian mixture-modelled components, which take into account the large error on the depth estimates. Strikingly, there are two distinct components to the eclogite depth-distribution at ~127 km and ~170 km in the central Slave dataset and (as observed by previous workers) an extremely narrow depth range for the Jericho eclogites, with all samples at or around ~135 km (Heaman et al., 2002)

A layer of eclogite would present a significant seismic reflection because of its density contrast with depleted peridotite (3.3 vs. 3.6 g/cm^3; Anderson, 1989) and interestingly, the two seismic discontinuities identified beneath the central Slave by Snyder (2008) are at exactly these depths (~130, ~170 km) within the lithosphere. Furthermore, the very narrow depth range observed for the Jericho eclogites is within uncertainty of the shallower of the two discontinuities in the central Slave.

The presence of distinct *zones* of eclogite, and indeed the potential correlation of the uppermost region between two localities is strong support for the subduction stacking hypothesis. Schmidberger et al. (2007) note the similarity of the major- and trace-element composition of the central Slave eclogites to ophiolite mafic cumulates and MORB, as well as noting positive Sr and Eu anomalies associated with plagioclase and potential formation at low pressure. No discernable compositional difference is ascribed to the eclogites of either layer. It has also been suggested by Heaman et al. (2002) that eclogites below Jericho are of subducted crustal origin, and therefore there is some evidence that the distinct regions of eclogite seen within the Slave craton are crustally-derived, and fit one of the key predictions in support of the subduction stacking hypothesis.

6.5.3 Age distribution

The only 'section' in the lithospheric transect where a pronounced age – depth relationship is observed is in the central Slave. At Artemisia, there is a suggestion that shallow samples tend to have ages of ~1.8 Ga, in contrast to samples at depth which show a range of ages from the Archean to the Proterozoic. The limitation for the Jericho dataset is that while > 30

samples have been analysed for T_{RD}, only ten of these have corresponding P–T estimates for depth determination. The same is true of the Artemisia kimberlites, except here the limitation is the abundance of fresh silicate minerals for analysis. Therefore there is a significant amount of data for the central Slave regarding age and P–T, but these are limited for other Slave localities at present (Artemisia, Jericho and Gahcho Kué). However, it is interesting to note that both the subduction stacking and the plume melting lithospheric formation hypotheses should produce a lithosphere with two (or more) distinctly aged layers, with the shallow layer older than the deeper layer. Therefore the lack of age – depth information for the Slave craton does not significantly affect our ability to distinguish between which (or both) of the lithospheric formation hypotheses might have been operating.

However, even without the depth constraint, the T_{RD} ages obtained for the Slave craton are very useful as they significantly increase the database size for whole-rock ages for the Slave craton from 6 to ~70 (including unpublished samples from Jericho; Irvine, 2002). They are important because a difficulty presented by previously published data has been the apparent age mismatch between the presence of *thick* lithospheric mantle (3.5 Ga in the diamond stability field; Westerlund et al., 2006) and a granite bloom in the crust (2.6 Ga, Bleeker, 2002); and has even led some workers (e.g. Aulbach, *in press*) to suggest that this dichotomy is a fundamental feature of craton nucleation.

Published age data for the central Slave on peridotite xenoliths, and diamond/olivine sulphide inclusions (Westerlund et al., 2006; Aulbach et al., 2007a; 2009b) have indicated that the lithosphere is > 3.0 Ga, since isochrons for sulphide inclusions in multiple diamonds and olivines yield T_{RD} ages between 3.3 and 3.5 Ga. However, the crustal geology indicates that the lithosphere could not have been thick and stable (required to

form the diamonds that contain the ~3.5 Ga isochron sulphides) since the mid-Archean since large-volume silicic magmatism occurs at ~2.6 Ga (Bleeker, 2002; Davies et al., 2004). Also, significant doubt has been expressed about the accuracy of sulphide Re-Os model ages obtained by LA-ICP-MS (Pearson & Wittig, 2008; Nowell et al., 2008). Since sulphide ages have a large tail where many samples exceed the age of the Earth, it is hard to place much significance on the observation of Meso-Archean ages.

In contrast to the sulphide database (Aulbach et al., 2004) only one > 3.0 Ga sample has been observed from the dataset presented by this thesis. The main 'Archean' peak in ages beneath the central Slave is Neoarchean ~2.5 – 2.7 Ga; beneath Jericho (Irvine, 2002) ~2.7 – 2.9 Ga and beneath Gahcho Kué ~2.6 Ga. Therefore from the data presented here there is no significant mismatch between the age of cratonization (~ 2.7 Ga) and the granite bloom, observed by Davies (2004). In fact, as suggested by Bleeker (2002) and Davies et al. (2004), the granite bloom itself is probably a reflection of the cratonization process.

Close examination of the published whole-rock peridotite ages (Westerlund et al., 2006) indicate that these ages are maxima, since T_{RD} has been calculated using the depleted upper mantle $^{187}Os/^{188}Os$ ratio (e.g. Miesel et al., 2001). Re-calculation of these samples relative to O-Chondrite $^{187}Os/^{188}Os$ — as used in this thesis — yields T_{RD} ages ranging from 2.6 – 3.0 Ga. In addition, the model ages of the sulphides that define the 3.5 Ga isochron correlation of Westerlund et al. (2006) are Neoarchean and hence the "isochron" array could simply be a mixing array (e.g. Heaman and Pearson, 2010). Taking into account the large uncertainty on Re-depletion model ages, there is no significant difference between the ages obtained by Westerlund et al. (2006) and the data presented in this thesis.

Furthermore, the validity of isochron regression for sulphide inclusions in diamonds and olivines is subject to debate. First, there is no evidence that sulphides from multiple olivine/diamond crystals can be combined onto the same isochron; this implies that all crystals formed at the same time, and there is evidence to suggest that for diamonds there may be multiple episodes of formation (Heaman and Pearson, 2010). Second, T_{RD} calculation using the diamond- and olivine-hosted sulphide $^{187}Os/^{188}Os$ ratios and taking into account the effect of in-growth from the significantly higher Re concentration again yields a main peak in T_{RD} ages at ~2.5 Ga, and minor peaks at ~1.7 and ~1.0 Ga, almost identical to the Proterozoic peaks seen in the whole-rock T_{RD} dataset for the central Slave craton (Chapter 5). In conclusion, the evidence for the Slave lithospheric mantle (even in the central Slave) being Mesoarchean is equivocal and most of the evidence is also consistent with a Neoarchean age.

6.5.4 Garnet composition

The lack of fresh silicate phases in the Artemisia peridotite means that trans-lithospheric comparisons (i.e. involving every locality) are limited to the composition of garnet, specifically the major element composition of garnet as trace element data is not available for Jericho or Gahcho Kué. Fortunately, garnet chemistry is sensitive to lithology, formation depth and metasomatism, among other things, and therefore some cross-craton comparisons can be made on the basis of these data.

6.5.4.1 Major elements

It has been noted in Chapter 5 that there is a distinct depth-dependent distribution of garnet type in the mantle lithosphere beneath the central Slave craton, with G11 (high-TiO_2, associated with Ca-Fe-Ti metasomatism; Grütter et al., 2004) and G12 (werhlitic) compositions apparently occupying a region around ~160 km. Interestingly, this depth association is also seen in the garnets from the Jericho kimberlite (Kopylova et al., 1998, 1999; Kopylova and Russell, 2000); beneath Artemisia and Gahcho Kué these G11 and G12 samples are clustered at the base of the lithosphere and are probably the result of silicate melt overprinting (see: 6.4.2).

Explaining the apparent abundance of G11 and G12 garnet-bearing lithologies at ~160 km and their relative absence in deeper lithosphere is complex. The presence of these more fertile major-element compositions initially suggests the effect of silicate melt overprinting, but it is unlikely that percolation of silicate melts with high Fe-Ca-Ti concentrations would have left the deeper lithosphere comparatively untouched. In the central Slave and Jericho, these G11 and G12 lithologies are spatially associated with the deeper layer of eclogite at ~170 km, and this spatial association allows for formation of *speculative* hypotheses of their genesis.

If we assume that the subduction stacking hypothesis is operating, as suggested by the apparent crustal nature of the lower layer of eclogite (suggested by Schmidberger et al; 2007) then it would imply that before this deeper layer was subducted beneath the craton (with associated attached oceanic lithosphere), the base of the *overlying* layer would be subject to the same metasomatic infiltration of small-fraction silicate melts observed in most cratons (c.f. McKenzie, 1989). This could be reflected in an unusual abundance of G11

and G12 garnets immediately above an eclogite layer in a lithospheric column. However, the absence of a G11 – G12 layer co-incident with the shallower eclogite layers in the central Slave and Jericho is not consistent with this hypothesis; although it is feasible that the time between formation of the very shallowest lithosphere (i.e. below 130 km) and subduction of the first eclogite layer was not long enough for extensive infiltration of small-fraction melts into the lithosphere.

Alternatively, the spatial association of eclogite and G11/G12 garnet at ~160 – 170 km could represent melting and reaction of the eclogite with peridotite to form pyroxenite, similar to the mechanism initially suggested by Yaxley and Green (1998) and expanded by Sobolev et al. (2007) for eclogite pods in upwelling asthenosphere. Sobolev et al. (2007) suggest that upwelling crustally-derived (SiO_2-saturated) eclogite will begin to melt at ~ 190 km (at convecting mantle temperatures; in the lithospheric mantle this depth could be considerably shallower), producing a liquid that is extremely reactive with peridotite, replacing the olivine to form a pyroxenitic hybrid lithology. The most fusible elements from the eclogite (Ca, Ti, Fe, K, Si) should be enriched within the pyroxenite, and this is observed. The eclogites, where present, should show depleted compositions, with high Mg (such as those explored by Smart et al., 2009) and relatively low Ti, Ca and K, as well as evidence of melt loss, which is noted in the Diavik eclogites by Aulbach et al. (2007b).

Therefore the spatial association of G11 and G12 garnets with the deeper layer of eclogite in the central Slave craton is consistent with the subduction stacking hypothesis, although it is acknowledged that there is no co-existing ~ 170 km eclogite sampled by the Jericho kimberlite, nor a particularly pronounced seismic discontinuity at that depth in the Jericho region (Snyder, 2008). This, again, could be the result of the influence of the Mackenzie plume event on the lithospheric mantle. Assuming that there was an eclogitic layer at ~170

km to begin with, its absence could potentially be the result of advective *heating* of the lithosphere by the percolating silicate melts that were suggested to have overprinted and re-fertilized the $Mg\#_{ol}$ in the deep lithosphere at Jericho. The extra heat added by these fluids (although small) could potentially have induced greater degrees of melting in the deep eclogite layer at Jericho, since the deeper layer of eclogite will be closer to its solidus, and therefore more likely to 'melt out' of the lithosphere than the shallower layer. Indeed, unusual abundances of pyroxenitic xenoliths have been noted from this region (150 – 180 km) beneath the Jericho kimberlite (Kopylova et al., 1999; Kopylova et al., 2009).

6.5.4.2 Trace elements

Three main REE pattern types are observed in garnets from the central Slave and Artemisia localities analysed in this thesis, and their depth ranges are illustrated on Figure 6.2 as shaded regions that take into account the large errors on the depth estimates. However, the shallow nature of the 'depleted' REE pattern type noted in the central Slave craton (Chapter 5) is also seen in the lithosphere sampled by the Artemisia kimberlite.

These depleted garnet REE pattern types are enigmatic, and are too numerous (in the Artemisia dataset) to be artefacts. They are distinct from the two other main pattern types observed in the garnet dataset. In Chapter 5, these 'depleted' patterns were taken to represent the REE composition of cratonic garnet before addition of diamond-forming fluids, such that in the central Slave they are evidence of regions of the lithosphere not reached by these fluids, and used to postulate that the diamond forming fluids had been 'trapped' beneath the seismic discontinuity, which has been roughly correlated with the

shallowest layer of eclogite at ~130 km resulting in unusually high abundances of precipitated diamond.

7 CONCLUSIONS AND FURTHER WORK

7.1 CONCLUSIONS

This section briefly summarises the main findings of this thesis, and discusses the further work needed to refine the more speculative hypotheses and ideas presented in the above chapters.

7.1.1 The methodology of peridotite xenolith and xenocryst-based studies of the mantle in cratonic regions.

- A new fitting method has been outlined and tested for the construction of lithosphere palaeogeotherms from peridotite xenolith and xenocryst data.
- Palaeogeotherms calculated from numerous well-constrained P–T arrays worldwide indicate that — using this new method — the choice of thermobarometer combination (from those recommended by Nimis and Grütter, 2009 and the popular Brey and Köhler 1990 formulation) does not have a significant effect on the shape of the palaeogeotherm, and subsequent estimation of lithosphere properties. This implies that P–T estimates from both harzburgitic and lherzolite xenoliths from the same locality can be combined to form a more populous P–T array, and better-constrained palaeogeotherm.

- Significant, independent errors affect P–T estimates from xenoliths, arising from electron microprobe analytical procedures (kV, nA, counting times) and thermobarometer calibration. These uncertainties do not affect the fitting of a palaeogeotherm but are shown to be extremely important when constructing lithospheric stratigraphies from xenolith and xenocryst data.

- A new algorithm for estimating optimal P–T from multiple thermobarometer combinations for use in lithospheric stratigraphy has been formulated, which improves on current 'equilibrium' estimates since it can be applied to both lherzolite and harzburgite mineralogies.

7.1.2 A xenolith-based lithospheric transect of the Slave craton, NWT, Canada.

- The lithosphere sampled by the kimberlites across the Slave craton shows geochemical and geophysical evidence of being formed by subduction stacking; namely the presence of crustally-derived eclogite in two distinct layers, $Mg\#_{ol}$ that does not decrease with increasing depth and the presence of clear seismic boundaries at different depths within the lithospheric column.

- The current nucleus of the slave Craton, sampled by the kimberlites studied in this thesis formed at ~2.8 – 2.5 Ga. This is in line with the crustal geology, which indicates that a *thick* cratonic root could not have formed before this time by the presence of a granite bloom at the surface.

- The well-established layer of ultra-depleted lithosphere in the central Slave craton extends much deeper than previous estimates, to approximately 160 – 180 km.

- The northern Slave craton has experienced a large amount of alteration as a result of the influence of the Mackenzie igneous event. The lithosphere beneath the northernmost kimberlite studied (Artemisia) has been metasomatised by sulphidic melt that deposited sulphides, resulting in perturbation of the majority of peridotite whole-rock $^{187}Os/^{188}Os$ ratios. This perturbation is evident, although less so, in the $^{187}Os/^{188}Os$ ratios of the Jericho peridotite xenoliths, consistent with Jericho being further away from the inferred site of the MacKenzie plume head.

- Eclogite in the Slave craton lithosphere is apparently distributed in two distinct layers at ~130 km and ~170 km depth, which correspond with depths of pronounced seismic reflectors. These eclogite layers have variably melted to form pyroxenite, seen at similar depths. The thermal effect of the Mackenzie event could (speculatively) have caused complete melting of the ~170 km eclogite layer at Jericho.

- Much of the lower lithosphere across the Slave craton has been affected by silicate melt overprinting, that has variably decreased $Mg\#_{ol}$ and equilibrated garnet REE profiles to those associated with garnet-facies melting.

- Fluids that have similar trace element characteristics to those that form diamonds, percolating through the lithosphere in the central Slave were trapped beneath the upper eclogite layer at ~130 km, indicated by a lack of sinusoidal garnet REE profiles above this depth. This caused unusually large amounts of diamond to be precipitated, explaining the very high abundance of diamonds noted from the Diavik diamond mine.

7.2 FURTHER WORK

It is the purpose of this section to briefly outline further work that might better elucidate the complex processes operating in the lithospheric mantle beneath the Slave craton.

7.2.1 The nature of the ca. 1.27 Ga signature in the northern Slave

The ca. 1.2 Ga signature in the northern Slave has been ascribed to the metasomatic effect of sulphide addition to the lithospheric mantle. However, the mechanism by which sulphide can percolate and be deposited in the lithospheric mantle is not clear. It is well known that sulphidic and silicate melt are immiscible, yet in many cases only the sulphidic portion of this melt combination is recorded in the geochemistry of the rock through which it percolates, as is seen in the northern Slave.

One way to explore whether the lithosphere beneath the northern Slave is Archean and overprinted, or new lithosphere added by Proterozoic melting, is to analyse individual olivine grains for their osmium isotope composition and T_{RD} age. If these T_{RD} ages are Archean, as is suggested by Burton et al. (1999), then it supports the preferred hypothesis that the lithosphere has been overprinted by metasomatic sulphide (although it does not help in elucidating the mechanism by which this percolation and deposition occurs).

A problem with this idea is that the xenoliths obtained from the Artemisia kimberlite are dramatically weathered such that no fresh olivine is available for these analyses. However, should the kimberlite be mined in the future, fresher xenolith or olivine xenocryst samples may be made available for these analyses.

7.2.2 Garnet REE patterns from Jericho and Gahcho Kué

The similarity of the REE pattern with depth distribution seen at Artemisia and in the central Slave is a tantalizing feature, and it is tempting to correlate the 'depleted' REE pattern type across the craton, indicating a shallow, diamond-forming fluid free layer. Analysis of garnets from the Jericho and Gahcho Kué xenoliths would help to build up a more complete picture of the lithosphere as a whole.

7.2.3 Seismic tomography

A large-scale P- and S-wave seismic tomography project, such as that seen for the Kaapvaal craton (the Kaapvaal Project) would be very enlightening for the *whole* of the Slave craton. Previous studies, although extremely important for our understanding of the lithosphere in this cratonic region (c.f. Snyder, 2008; Jones et al., 2001) often do not stretch as far north as the Artemisia and Jericho kimberlites, and it has been shown in this thesis that these localities show the most alteration and potential modification in comparison to the rest of the craton. High-resolution seismic and magnetotelluric profiles and 3-D analyses in this

region would be of immeasurable benefit in trying to unravel the complex history of this unique craton.

8 REFERENCES

Achenbach, K., **2011**. *Lattice-preferred orientation and microstructure of peridotites from ODP hole 1274A (15 °39 ´N), Mid-Atlantic Ridge: Testing models of mantle upwelling and tectonic exhumation*. Earth and Planetary Science Letters 301, 199-212

Anderson, D.L., **1989.** *Theory of the Earth*. Blackwell ,

Armstrong, J.A., **2012**. *10th International Kimberlite Conference*; Long abstracts ,

Aulbach, S., Griffin, W.L., Pearson, N.J., O'Reilly, S.Y., Kivi, K., Doyle, B.J., **2004**. *Mantle formation and evolution, Slave craton: constraints from HSE abundance and Re-Os isotope systematics of sulfide inclusions in mantle xenocrysts*. Chemical Geology 208, 61-88

Aulbach, S., 2012. Craton nucleation and formation of thick lithospheric roots. Lithos in press 10.1016/j.lithos.2012.02.011

Aulbach, S., Griffin, W.L., Pearson, N.J., O'Reilly, S.Y., Doyle, B.J., **2007a.** *Lithosphere formation in the central Slave craton (Canada): plume subcretion or lithosphere accretion?* Contributions to Mineralogy and Petrology 154, 409-427

Aulbach, S., Pearson, N.J., O'Reilly, S.Y., Doyle, B.J., **2007b**. *Origins of xenolithic eclogites and pyroxenites from the central Slave craton, Canada.* Journal of Petrology 48, 1843-1873

Aulbach, S., Stachel, T., Creaser, R.A., Heaman, L.M., Shirey, S.B., Muehlenbachs, K., Eichenberg, D., Harris, J.W., **2009a**. *Sulphide survival and diamond genesis during formation and evolution of Archean subcontinental lithosphere: A comparison between the Slave and Kaapvaal cratons*. Lithos 112S, 747-757

Aulbach, S., Creaser, R.A., Pearson, N.J., Simonetti, S.S., *Heaman, L.M., Griffin, W.L., Stachel, T., **2009b**. Sulphide and whole-rock Re-Os systematics of eclogite and pyroxenite xenoliths from the Slave Craton, Canada*. Earth and Planetary Science Letters 283, 48-58

Aulbach, S., Stachel, T., Heaman, L.M., Carlson, J.A., **2011a**. *Microxenoliths from the Slave craton: Archives of diamond formation along fluid conduits*. Lithos 126, 419-434

Aulbach, S., Stachel, T., Heaman, L.M., Creaser, R.A., Shirey, S.B., **2011b.** *Formation of cratonic subcontinental lithospheric mantle and complimentary komatiite from hybrid plume sources*. Contributions to Mineralogy and Petrology 161, 947-960

Baier, B., Berckhemer, H., Gajewski, D., Green, R., Grimsel, C., Prodehl, C., Vees, R., **1983**. *Deep seismic sounding in the area of the Damara Orogen, Namibia, South West Africa* in Martin, H., Eder, F. (Eds.), Intracontinental Fold Belts, Springer-Verlag, pp. 885–900,

Bank, C.G., Bostock, M.G., Ellis, R.M., Cassidy, J.F., **2000**. *A reconnaissance teleseismic study of the upper mantle and transition zone beneath the Archean Slave craton in NW Canada*. Tectonophysics 319, 151-166

Baragar, W.R.A., Ernst, R.E., Hulbert, L.J., Peterson, T., **1996**. *Longditudinal petrochemical variation in the Mackenzie dyke swarm, Northwestern Canadian shield*. Journal of Petrology 37, 317-359

Bell, D.R., Schmitz, M.D., Janney, E., **2003**. *Mesozoic thermal evolution of the southern African mantle lithosphere*. Lithos 71, 273-287

Bernstein, S., Kelemen, P.B., Hanghøj, K., **2006**. *Consistent olivine Mg# in cratonic mantle reflects Archean mantle melting to the exhaustion of orthopyroxene*. Geology 35, 459-462

Birch, F., Roy, R.F., Decker, E.R., **1968**. *Heat flow and thermal history in New England and New York* in An-Zen, E., (Ed.), Studies of Appalachian Geology. Wiley-Interscience, New York, p 437–451 .,

Bleeker, W., **2002.** *Archaean tectonics: a review, with illustrations from the Slave craton*. Geological Society of London, Special Publications 199, 151-181

Bostock, M.G., **1997**. *Anisotropic upper-mantle stratigraphy and architecture of the Slave craton*. Nature 390, 392-395

Bowring, S.A. and Grotzinger, J.P., **1992**. *Implications of new chronostratigraphy for tectonic evolution of Wopmay orogen, Northwest Canadian shield*. American Journal of Science 292, 1-20

Bowring, S.A. and Williams, I.S., **1999**. *Priscoan (4.00-4.03 Ga) orthogneisses from northwestern Canada*. Contributions to Mineralogy and Petrology 134, 3-16

Boyd, F.R., **1973**. *A Pyroxene Geotherm*. Geochimica et Cosmochimica Acta 37, 2533-2538

Boyd, F.R. and Nixon, H., **1978**. *Ultramafic nodules from the Kimberley pipes, South Africa*. Geochimica et Cosmochimica Acta 42, 1367-1371

Boyd, F.R., **1989**. *Compositional distinction between oceanic and cratonic lithosphere*. Earth and Planetary Science Letters 96, 15-26

Boyd, F.R., Pearson, D.G., Hoal, K.O., Hoal, B.G., Nixon, H., Kingston, M.J., Mertzman, S.A., **2004**. *Garnet lherzolites from Louwrensia, Namibia. Bulk composition and P/T relations.* Lithos 77, 573–592

Brey, G.P. and Köhler, T., **1990**. *Geothermobarometry in Four-phase Lherzolites II. New Thermobarometers, and Practical Assessment of Existing Thermobarometers*. Journal of Petrology 31, 1353-1378

Burgess, S.R. and Harte, B., **2004**. *Tracing lithosphere evolution through the analysis of heterogenous G9-G10 garnets in peridotite xenoliths II: REE* Chemistry. Journal of Petrology 45, 609-634

Burton, K.W., Schiano, P., Birck, J.L., Allègre, C.J., **1999**. *Osmium isotope disequilibrium between mantle minerals in a spinel-lherzolite.* Earth and Planetary Science Letters 172, 311-322

Canil, D., **1990**. *Experimental study bearing on the absence of carbonate in mantle-derived xenoliths*. Geology 18, 1011-1013

Canil, D. and O'Neill, H.S.C., **1996**. *Distribution of ferric iron in some upper-mantle assemblages.* Journal of Petrology 37, 609-635

Canil, D., **1999**. *The Ni-in-garnet geothermometer: calibration at natural abundances*. Contributions to Mineralogy and Petrology 136, 240-246

Canil, D., Schulze, D.J., Hall, D., Hearn, B.C., Jr., Milliken, S.M., **2003**. *Lithospheric roots beneath western Laurentia: the geochemical signal in mantle garnets*. Canadian Journal of Earth Sciences 40, 1027-1051

Carbno, G.B. and Canil, D., **2002.** *Mantle structure beneath the SW Slave craton, Canada: constraints from garnet geochemistry in the Drybones Bay kimberlite*. Journal of Petrology 43, 129-142

Carswell, D.A. and Gibb, F.G.F., **1987**. *Evaluation of mineral thermometers and barometers applicable to garnet lherzolite assemblages*. Contributions to Mineralogy and Petrology 95, 499-511

Clarke, D.B., Pe, G.G., Mackay, R.M., Gill, K.R., O'Hara, M.J., Gard, J.A., **1977**. *A new potassium-iron-nickel sulphide from a nodule in kimberlite*. Earth and Planetary Science Letters 35, 421-428

Cook, F.A., van der Velden, A.J., Hall, K.W., Roberts, B.J., **1999**. *Frozen subduction in Canada's Northwest Territories. Lithoprobe deep lithospheric reflection profiling of the western Canadian Shield*. Tectonics 18, 1-24.

Cox, K.G., **1980**. *A model for flood basalt volcanism*. Journal of Petrology 21, 629-650

Cox, K.G. and Hawkesworth, C.J., **1985**. *Geochemical stratigraphy of the Deccan traps at Mahabaleshwar, western Ghats, India, with implications for open system magmatic processes*. Journal of Petrology 26, 355-377

Cox, R. and Barnes, S-J., **2005.** *LA-ICP-MS analysis of garnet: Trace-element characterization and single-mineral thermometry applied to diamond exploration*. IVEX Rapport Final Sous-projet SC17,

Creighton, S., Stachel, T., McLean, H., Muehlenbachs, K., Simonetti, A., Eichenberg, D., Luth, R.W., **2008.** *Diamondiferous peridotitic microxenoliths from the Diavik Diamond Mine, NT.* Contributions to Mineralogy and Petrology 155, 541-554

Creighton, S., Stachel, T., Eichenberg, D., Luth, R.W., **2010**. *Oxidation state of the lithospheric mantle beneath Diavik diamond mine, central Slave craton, NWT, Canada*. Contributions to Mineralogy and Petrology 159, 645-657

Dale, C.W., Pearson, D.G., Starkey, N.A., Stuart, F.M., Ellam, R.M., Larsen, L.M., Fitton, J.G., Macpherson, C.G., 2009. *Osmium isotopes in Baffin Island and West Greenland picrites: Implications for the $^{187}Os/^{188}Os$ composition of the convecting mantle and the nature of high $^{3}He/^{4}He$ mantle*. Earth and Planetary Science Letters 278, 267-277

Darbyshire, F.A., **2003**. *Crustal structure across the Canadian High Arctic region from teleseismic receiver function analysis*. Geophysical Journal International. Geophysical Journal International 152, 372-391

Davies, G.F., **1994**. *Thermomechanical erosion of the lithosphere by mantle plumes*. Journal of Geophysical Research – Solid Earth 99, 15709-15722

Davies, R.M., Griffin, W.L., O'Reilly, S.Y., Doyle, B.J., **2004**. *Mineral inclusions and geochemical characteristics of microdiamonds from the DO27, A154, A21, A418, DO18, DD17 and Ranch Lake kimberlites at Lac de Gras, Slave Craton, Canada*. Lithos 77, 39-55

Davies, W.J. and Kjarsgaard, B.A., **1997**. *A Rb-Sr Isochron Age For A Kimberlite From the Recently Discovered Lac De Gras Field, Slave Province, Northwest Canada*. The Journal of Geology 105, 503-510

Davis, W.J., **1997**. *U-Pb zircon and rutile ages from granulite xenoliths in the Slave province: Evidence for mafic magmatism in the lower crust coincident with Proterozoic dike swarms*. Geology 25, 343-346

Dawson, J.B. and Stephens, W.E., **1975**. *Statistical classification of garnets from kimberlite and associated xenoliths.* The Journal of Geology 83, 589-607

Dawson, J.B., **1987**. *The kimberlite clan: relationship with olivine and leucite lamproites, and inferences for upper-mantle metasomatism*. Geological Society of London, Special Publications 30, 95-101

Day, J.M.D., Pearson, D.G., Hulbert, L.J., **2008.** *Rhenium-osmium isotope and platinum-group-element constraints on the origin and evolution of the 1.27 Ga Muskox layered intrusion.* Journal of Petrology 49, 1255-1295

de Hoog, J.C.M., Gall, L., Cornell, D.H., **2010**. *Trace-element geochemistry of mantle olivine and application to mantle petrogenesis and geothermobarometry*. Chemical Geology 270, 196-215

Donnelly, C.L., Stachel, T., Creighton, S., Muehlenbachs, K., Whiteford, S., **2007**. *Diamonds and their mineral inclusions from the A154 South pipe, Diavik Diamond Mine, Northwest territories, Canada*. Lithos 98, 160-176

Dupuy, C., Michard, A., Dostal, J., Dautel, D., Baragar, W.R.A., **1992**. *Proterozoic flood basalts from the Coppermine River area, Northwest Territories: isotope and trace element geochemistry*. Canadian Journal of Earth Sciences 29, 1937-1943

Durrheim, R.J. and Green, R.W.E., **1992**. *A seismic refraction investigation of the Archaean Kaapvaal Craton, South Africa, using mine tremors as the energy source*. Geophysical Journal International 108, 812-832

Erlank, A.J., Waters, F.G., Hawkesworth, C.J., Haggerty, S.E., Allsopp, H.L., Rickard, R.S., Menzies, M.A., **1987**. *Evidence for mantle metasomatism in peridotite nodules from the Kimberly pipes, South Africa* in; Menzies, M.A. and Hawkesworth, C.J. (Eds.) Mantle Metasomatism. London. Academic Press.,

Ernst, R.E. and Baragar, W.R.A., **1992**. Evidence from magnetic fabric for the flow pattern of magma in the Mackenzie giant radiating dyke swarm. Nature 356, 511-513

Fahrig, W.F. and Jones, D.L., **1969**. *Palaeomagnetic evidenc for extent of Mackenzie igneous events*. Canadian Journal of Earth Sciences 6, 679

Finnerty, A.A. and Boyd, F.R., **1984**. *Evaluation of thermobarometers for Garnet Peridotites. Geochimica et Cosmochimica Acta* 48, 15-27

Fouch, M.J., James, D.E., van Decar, J.C., Van der Lee, S., 2004. *Mantle seismic structure beneath the Kaapvaal and Zimbabwe Cratons.* South African Journal of Geology 107, 33–44

Francis, D., **1994**. *Chemical Interaction between Picritic Magmas and Upper Crust along the Margins of the Muskox Intrusion, Northwest Territories*. Geological Survey of Canada Paper 92, 94

Franz, L., Brey, G.P., Okrusch, M., **1996a**. *Reequilibration of Ultramafic Xenoliths from Namibia by Metasomatic Processes at the Mantle Boundary*. The Journal of Geology 104, 599-615

Franz, L., Brey, G.P., Okrusch, M., **1996b**. *Steady state geotherm, thermal disturbances, and tectonic development of the lower lithosphere underneath the Gibeon Kimberlite Province, Namibia*. Contributions to Mineralogy and Petrology 126, 181–198

Gaetani, G.A. and Grove, T.L., **1999**. *Wetting of mantle olivine by sulphide melt: implications for Re/Os ratios in mantle peridotite and late-stage core formation*. Earth and Planetary Science Letters 169, 147-163

Gao, S., Rudnick, R.L., Carlson, R.W., McDonough, W.F., Liu, Y.S., **2002.** *Re-Os evidence for replacement of ancient mantle lithosphere beneath the North China craton*. Earth and Planetary Science Letters 198, 307-322

Gibson, S.A., Malarkey, J., Day, J.A., **2008**. *Melt Depletion and Enrichment beneath the Western Kaapvaal Craton. Evidence from Finsch Peridotite Xenoliths*. Journal of Petrology 49, 1817–1852

Govindaraju, K., **1982.** *Report (1967–1981) on Four ANRT Rock Reference Samples: Diorite DR-N, Serpentine UB-N, Bauxite BX-N and Disthene DT-N*. Geostandards Newsletter 6, 91-159

Govindaraju, K., Potts, P.J., Webb, P.C., Watson, J.S., **1994**. *1994 report on Whin Sill dolerite WS-E from England and Pitscurrie microgabbro PM-S from Scotland: assessment by one hundred and four international laboratories*. Geostandards Newsletter 18, 211-300

Green, R.W.E. and Durrheim, R.J., **1990.** *A Seismic Refraction Investigation of the Namaqualand Metamorphic Complex, South Africa*. Journal of Geophysical Research 95, 19927–19932

Griffin, W.L., Cousens, D.R., Ryan, C.G., Sie, S.H., Suter, G.F., **1989**. *Ni in chrome pyrope garnets: a new geothermometer*. Contributions to Mineralogy and Petrology 103, 199-202

Griffin, W.L., Doyle, B.J., Ryan, C.G., Pearson, N.J., O'Reilly, S.Y., Davies, R., Kivi, K., van Achterbergh, E., Natapov, L.M., **1999a**. *Layered mantle lithosphere in the Lac de Gras area, Slave Craton: Composition, structure and origin*. Journal of Petrology , 705-727

Griffin, W.L., Shee, S.R., Ryan, C.G., Win, T.T., Wyatt, B.A., **1999b**. *Harzburgite to lherzolite and back again: metasomatic processes in ultramafic xenoliths from the Wesselton kimberlite, Kimberley, South Africa*. Contributions to Mineralogy and Petrology 134, 232-250

Griffin, W.L., O'Reilly, S.Y., Abe, N., Aulbach, S., Davies, R.M., Pearson, N.J., Doyle, B.J., Kivi, K., **2003**. *The origin and evolution of Archean lithospheric mantle.* Precambrian Research 127, 19-41

Griffin, W.L., Graham, S., O'Reilly, S.Y., Pearson, N.J., **2004**. *Lithosphere evolution beneath the Kaapvaal craton: Re-Os systematics of sulphides in mantle-derived peridotites*. Chemical Geology 208, 89-118

Griffin, W.L., Powell, W.J., Pearson, N.J., O'Reilly, S.Y., **2008**. *GLITTER: Data reduction software for laser ablation ICP–MS* in Sylvester, P., (Ed) Laser Ablation-ICP-Mass Spectrometry in the Earth Sciences: Current Practices and Outstanding Issues Mineralogical Association of Canada (MAC) Short Course Series, v. 40, 308-311

Grütter, H.S., Latti, D., Menzies, A.H., **2006**. *Cr-saturation arrays in concentrate garnet compositions from kimberlite and their use in mantle barometry*. Journal of Petrology 41, 801-820

Grütter, H.S., **2009.** *Pyroxene xenocryst geotherms; techniques and application*. Lithos 112, 1167-1178

Grütter, H.S., Gurney, J.J., Menzies, A.H., Winter, F., **2004**. *An updated classification scheme for mantle-derived garnet, for use by diamond explorers*. Lithos 77, 841-857

Hansen, S.E., Nyblade, A.A., Julia, J., Dirks, H.G.M., Durrheim, R.J., **2009**. Upper-mantle low-velocity zone structure beneath the Kaapvaal craton from S-wave receiver functions. Geophysical Journal International 178, 1021–1027

Harlow, G.E., **1997.** *K in clinopyroxene at high pressure and temperature. An experimental study*. American Mineralogist 82, 259–269

Harte, B., **1977**. *Rock Nomenclature with Particular Relation to Deformation and Recrystallisation Textures in Olivine-Bearing Xenoliths*. The Journal of Geology 85, 279–288

Heaman, L.M, LeCheminant, A.N., Rainbird, R.H., **1992**. *Nature and timing of Franklin igneous events, Canada - implications for a late Proterozoic mantle plume and the break-up of Laurentia*. Earth and Planetary Science Letters 109, 117-131

Heaman, L.M, Creaser, R.A., Cookenboo, H.O., **2002.** *Extreme enrichment of high field strength elements in Jericho eclogite xenoliths: A cryptic record of Palaeoproterozoic subduction, partial melting and metasomatism beneath the Slave craton, Canada*. Geology 30, 507-510

Heaman, L.M and Pearson, D.G., **2010**. *Nature and evolution of the Slave Province subcontinental lithospheric mantle*. Canadian Journal of Earth Sciences 47, 369-388

Helmstaedt, H. and Schulze, D.J., **1989**. Southern African kimberlites and their mantle sample: implications for the *Archean tectonics and lithosphere evolution.* Geological Society of Australia Special Publication 14, 358-368

Herzberg, C. and Rudnick, R.L., **2012**. *Formation of cratonic lithosphere: An integrated thermal and petrological model*. Lithos in press; 10.1016/j.lithos.2012.01.010,

Hoffman, P.F. and Bowring, S.A., **1984**. *Short-lived 1.9 Ga continental margin and its destruction, Wopmay orogen, Northwest Canada*. Geology 12, 68-72

Hofmeister, A.M., **1999**. *Mantle values of thermal conductivity and the geotherm from phonon lifetimes*. Science 283, 1699–1706

Irvine, G.J., **2002**. *Time constraints on the formation of lithospheric mantle beneath cratons : a Re-Os isotope and platinum group element study of peridotite xenoliths from northern Canada and Lesotho*. PhD Thesis, Durham University.

Irvine, G.J., Pearson, D.G., Kjarsgaard, B.A., Carlson, R.W., Kopylova, M.G., Dreibus, G., **2003.** *A Re-Os isotope and PGE study of kimberlite-derived peridotite xenoliths from Somerset Island and a comparison to the Slave and Kaapvaal cratons*. Lithos 71, 461-488

Ishikawa A., Pearson, D.G., Dale, C.W., **2007**. *Re-Os evidence for ancient mantle beneath the Ontong Java Plateau*. Geochimica et Cosmochimica Acta 71, A430

James, D.E., Fouch, M.J., van Decar, J.C., van der Lee, S., Kaapvaal Seismic, G., **2001**. *Tectospheric structure beneath southern Africa*. Geophysical Research Letters 28, 2485–2488

Janney, P.E., Shirey, S.B., Carlson, R.W., Pearson, D.G., Bell, D.R., LeRoex, A.P., Ishikawa, A., Nixon, P.H., Boyd, F.R., **2010**. *Age, Composition and Thermal Characteristics of South African Off-Craton Mantle Lithosphere*: Evidence for a Multi-Stage History. Journal of Petrology 51, 1849–1890

Jaupart, C., Mareschal, J.C., Guillou-Frottier, L., Davaille, A., **1998**. *Heat flow and thickness of the lithosphere in the Canadian Shield*. Journal of Geophysical Research – Solid Earth 103, 15269–15286

Jaupart, C. and Mareschal, J.C., **2007**. *Heat Flow and Thermal Structure of the Lithosphere* in; Gerald, S. (Ed.), Treatise on Geophysics 6: Crust and Lithosphere Dynamics. Elsevier, Amsterdam, pp. 217–251.,

Jochum, K.P., Wilson, S.A., Abouchami, W., Amini, M., Chmeleff, J., Eisenhauer, A., Hegner, E., Iaccheri, L.M., Kieffer, B., Krause, J., McDonough, W.F., Mertz-Kraus, R., Raczek, I., Rudnick, R.L., Scholz, D., Steinhoefel, G., Stoll, B., Stracke, A., Tonarini, S., Weis, D., Weis, U., Woodhead, J.D., **2011**. *GSD-1G and MPI-DING Reference Glasses for In Situ and Bulk Isotopic Determination*. Geostandards Newsletter 35, 193-226

Jones, A.G., **1999.** *Imaging the continental upper mantle using electromagnetic methods*. Lithos 48, 57-80

Jones, A.G., Ferguson, I.J., Chave, A.D., Evans, R.L., McNeice, G.W., **2001**. *Electric lithosphere of the Slave craton*. Geology 29, 423-426

Jones, A.G., Lezaeta, P., Ferguson, I.J., Chave, A.D., Evans, R.L., Garcia, X., Spratt, J., **2003**. *The electrical structure of the Slave craton*. Lithos 71, 505-527

Jordan, T.H., **1975.** *Continental Tectosphere*. Reviews of Geophysics 13, 1-12

Jordan, T.H., **1988**. *Structure and formation of the continental tectosphere*. Journal of Petrology, Lithosphere Issue , 11-37

Katsura, T., Yoneda, A., Yamazaki, D., Yoshino, T., Ito, E., **2010**. *Adiabatic Temperature Profile in the Mantle*. Physics of the Earth and Planetary Interiors 183, 212-218

Kelemen, P.B., Whitehead, J.A., Aharonov, E., Jordahl, K.A., **1995**. *Experiments on flow focusing in soluble porous-media with applications to melt extraction from the mantle*. Journal of Geophysical Research – Solid Earth 100, 475-496

Kennedy, C.S. and Kennedy, G.C., **1976**. *Equilibrium boundary between graphite and diamond*. Journal of Geophysical Research - Solid Earth 81, 2467-2470

Kent, R.W., Storey, M., Saunders, A.D., **1992**. *Large igneous provinces: Sites of plume impact or plume incubation?* Geology 20, 891-894

Kjarsgaard, B.A. and Levinson, A.A., 2002. *Diamonds in Canada*. Gems and Gemology 38, 208-238

Kjarsgaard, B.A., Wilkinson, L., Armstrong, J., **2002**. *Geology, Lac de Gras kimberlite Field, Central Slave Province, Northwest Territories — Nunavut, (NTS 76C, D, E, F. 1:250,000 scale color map with descriptive notes*. Geological Survey of Canada, Open File 3228

Menzies, M. and Hawkesworth, C.J. (Eds.) *Mantle Metasomatism*. London. Academic Press.,

Klein-BenDavid, O., Izraeli, E.S., Hauri, E., Navon, O., **2004**. *Mantle fluid evolution - a tale of one diamond*. Lithos 77, 243-253

Klein-BenDavid, O., Izraeli, E.S., Hauri, E., Navon, O., **2007**. *Fluid inclusions in diamonds from the Diavik mine, Canada and the evolution of diamond-forming fluids*. Geochimica et Cosmochimica Acta 71, 723-744

Klein-BenDavid, O. and Pearson, D.G., **2009**. *Origins of subcalcic garnets and their relation to diamond-forming fluids — case studies from Ekati (NWT-Canada) and Murowa (Zimbabwe)*. Geochimica et Cosmochimica Acta 73, 837-855

Klein-BenDavid, O., Pearson, D.G., Nowell, G.M., Ottley, C.J., McNeill, J.C.R., Cartigny, P., **2010**. *Mixed fluid sources involved in diamond growth constrained by Sr-Nd-Pb-C-N isotopes and trace elements*. Earth and Planetary Science Letters 289, 123-133

Kopylova, M.G., Russell, J.K., Cookenboo, H.O., **1998**. *Upper-mantle stratigraphy of the Slave craton, Canada: Insights into a new kimberlite province*. Geology 26, 315-318

Kopylova, M.G., Russell, J.K., Cookenboo, H.O., **1999**. *Petrology of peridotite and pyroxenite xenoliths from the Jericho kimberlite: implications for the thermal state of the mantle beneath the Slave craton, Northern Canada*. Journal of Petrology 40, 79-104

Kopylova, M.G. and Russell, J.K., **2000**. *Chemical stratification of cratonic lithosphere: constraints from the Northern Slave craton, Canada*. Earth and Planetary Science Letters 181, 71-87

Kopylova, M.G. and Caro, G., **2002**. *Mantle xenoliths from the South-eastern Slave craton: Evidence for chemical zonation in a thick, cold lithosphere*. Journal of Petrology 45, 1045-1067

Krogh-Ravna, E.J., **2000**. *The garnet–clinopyroxene geothermometer – an updated calibration*. Journal of Metamorphic Geology 18, 211-219

Kusky, T.M., Windley, B.F., Zhai, M.-G., **2007**. *Tectonic evolution of the North China Block: from orogen to craton to orogen*. Geological Society of London, Special Publications 280, 1-34

Lazarov, M., Woodland, A.B., Brey, G.P., **2009**. *Thermal state and redox conditions of the Kaapvaal mantle. A study of xenoliths from the Finsch mine, South Africa*. Lithos 112, 913–923

LeCheminant, A.N. and Heaman, L.M., **1989**. *Mackenzie igneous events, Canada: Middle Proterozoic hotspot magmatism associated with ocean opening*. Earth and Planetary Science Letters 96, 38-48

Lenardic, A. and Moresi, L., **2000**. *A new class of equilibrium geotherms in the deep thermal lithosphere of continents*. Earth and Planetary Science Letters 176, 331–338.

Longerich, H.P., Jackson, S.E., Günther, D., **1996**. *Laser Ablation-Inductively Coupled Plasma-Mass Spectrometric Transient Signal Data Acquisition and Analyte Concentration Calculation*. Journal of Analytical Atomic Spectrometry 11, 899-840

Lorand, J.P., Pattou, L., Gros, M., **1999**. *Fractionation of Platinum-group Elements and Gold in the Upper Mantle: a Detailed Study in Pyrenean Orogenic Lherzolites*. Journal of Petrology 40, 957-981

MacKenzie, J.M. and Canil, D., **1999**. *Composition and thermal evolution of cratonic mantle beneath the central Archean Slave Province, NWT, Canada*. Contributions to Mineralogy and Petrology 134, 313-324

Mather, K.A., Pearson, D.G., McKenzie, D., Kjarsgaard, B.A., Preistley, K., **2011**. *Constraints on the depth and thermal history of cratonic lithosphere from peridotite xenoliths, xenocrysts and seismology*. Lithos 125, 729-742

Mavrogenes, J.A. and O'Neill, H.S.C., **1999**. *The relative effects of pressure, temperature and oxygen fugacity on the solubility of sulfide in mafic magmas*. Geochimica et Cosmochimica Acta 63, 1173-1180

McKenzie, D. and Bickle, M.J., **1988**. *The Volume and Composition of Melt Generated by Extension of the Lithosphere*. Journal of Petrology 29, 625–679.

McKenzie, D., 1989. *Some remarks on the movement of small melt fractions in the mantle*. Earth and Planetary Science Letters 95, 53-72

McKenzie, D. and O'Nions, R.K., **1991**. *Partial melt distributions from inversion of Rare-Earth Element concentrations*. Journal of Petrology 32, 1021-1091

McKenzie, D., Jackson, J., Priestley, K., **2005**. *Thermal structure of oceanic and continental lithosphere*. Earth and Planetary Science Letters 233, 337–349

McKenzie, D. and Priestley, K., **2008**. *The influence of lithospheric thickness variations on continental evolution*. Lithos 102, 1–11

Meisel, T., Walker, R.J., Irving, A.J., Lorand, J-P., **2001**. *Osmium isotopic compositions of mantle xenoliths: A global perspective*. Geochimica et Cosmochimica Acta 65, 1311-1323

Menzies, M.A., Rogers, N., Tindle, A., Hawkesworth, C.J., **1987**. *Metasomatic and enrichment proceses in lithospheric peridotites, an effect of asthenosphere-lithosphere interaction* in; Menzies, M.A. and Hawkesworth, C.J. (Eds.) Mantle Metasomatism. London. Academic Press.,

Menzies, M.A. and Xu, Y.G., **1998**. *Geodynamics of the North China Craton* in; Flower, M.F.J., Chung, S.L., Lo, C.H., and Lee, T.Y. (Eds.), Geodynamics Series, Volume 27: Mantle Dynamics and Plate Interactions in East Asia. Amer Geophysical Union, Washington, pp. 155–165.,

Menzies, M.A., Xu, Y.G., Zhang, H.F., Fan, W.M., **2007**. *Integration of geology, geophysics and geochemistry: A key to understanding the North China Craton*. Lithos 96, 1-21

Menzies,A., Westerlund, K.J., Grütter, H.S., Gurney, J.J., Carlson, J.A., Fung, A., Nowicki, T., **2004**. *Peridotitic mantle xenoliths from kimberlites on the Ekati Diamond Mine property, N.W.T., Canada: major element compositions and implications for the lithosphere beneath the central Slave craton*. Lithos 77, 395-412

Michaut, C. and Jaupart, C., **2007**. *Secular cooling and thermal structure of continental lithosphere*. Earth and Planetary Science Letters 257, 83–96

Michaut, C., Jaupart, C., Bell, D.R., **2007**. *Transient geotherms in Archean continental lithosphere: New constraints on thickness and heat production of the subcontinental lithospheric mantle*. Journal of Geophysical Research – Solid Earth 112, B04408

Michaut, C., Jaupart, C., Mareschal, J.-C., **2009**. *Thermal evolution of cratonic roots.* Lithos 109, 47–60

Mitchell R. H., **1995**. *Kimberlites, Orangeites and Related Rocks*. Plenum, New York. ,

Mitchell, R.H., **1984**. *Garnet lherzolites from the Hanaus-I and Louwrensia kimberlites of Namibia*. Contributions to Mineralogy and Petrology 86, 178–188

Nguuri, T.K., Gore, J., James, D.E., Webb, S.J., Wright, C., Zengeni, T.G., Gwavava, O., Snoke, J.A., Kaapvaal Seismic, G., **2001**. *Crustal structure beneath southern Africa and its implications for the formation and evolution of the Kaapvaal and Zimbabwe cratons*. Geophysical Research Letters 28, 2501–2504

Nickel, K.G. and Green, D.H., **1985**. *Empirical geothermobarometry for garnet peridotites and implications for the nature of the lithosphere, kimberlites and diamonds*. Earth and Planetary Science Letters 73, 158–170

Nimis, P., **1998**. *Evaluation of diamond potential from the composition of peridotitic chromian diopside*. European Journal of Mineralogy 10, 505–519

Nimis, P. and Taylor, W.R., **2000**. *Single Clinopyroxene thermobarometery for garnet peridotites; Part 1: Calibration and testing of a Cr-in-Cpx barometer and an enstatite-in-cpx thermometer*. Contributions to Mineralogy and Petrology 139, 541–554

Nimis, P. and Grütter, H., **2009**. *Internally consistent geothermometers for garnet peridotites and pyroxenites.* Contributions to Mineralogy and Petrology 159, 411–427

Nimis, P. and Grütter, H.S., **2011**. *Discussion of 'The applicability of garnet orthopyroxene geobarometry in mantle xenoliths*. Lithos in press,

Niu, F.L., Levander, A., Cooper, C.M., Lee, C.T.A., Lenardic, A., James, D.E., **2004**. *Seismic constraints on the depth keel beneath the Kaapvaal craton*. Earth and Planetary Science Letters 224, 337-346

Nowell, G.M., Luguet, A., Pearson, D.G., Horstwood, M.S.A., **2008**. *Precise and accurate 186Os/188Os and 187Os/188Os measurements by multi-collector plasma ionisation mass spectrometry (MC-ICP-MS) part I: solution analyses*. Chemical Geology 248, 363-393

Osako, M., Ito, E., Yoneda, A., **2004**. *Simultaneous measurements of thermal conductivity and thermal diffusivity for garnet and olivine under high pressure*. Physics of the Earth and Planetary Interiors 143, 311–320

Pearson, D.G. and Nowell, G.M., **2002**. *The continental lithospheric mantle: characteristics and significance as a mantle reservoir*. Philiosophical Transactions of the Royal Society A - Mathematical, Physical and Engineering Sciences 360, 2383-2410

Pearson, D.G., Canil, D., Shirey, S.B., **2003**. *Mantle samples included in volcanic rocks: xenoliths and diamonds* in: Holland, H.D. and Turekian, K.K. (Eds) Treatise on Geochemistry Vol 2: The Mantle and Core,

Pearson, D.G., Irvine, G.J., Ionov, D.A., Boyd, F.R., Dreibus, G.E., **2004**. *Re-Os isotope systematics and platinum group element fractionation during mantle melt extraction: a study of massif and xenolith peridotite suites*. Chemical Geology 208, 25-59

Pearson, D.G., Parman, S.W., Nowell, G.M., **2007**. *A link between large mantle melting events and continent growth seen in osmium isotopes*. Nature 449, 202-205

Pearson, D.G. and Wittig, N., **2008**. *Formation of Archean continental lithosphere and its diamonds: the root of the problem. Journal of the Geological Society* 165, 985-914

Pearson, D.G. and Wittig, N., **2012**. *The formation and evolution of cratonic subcontinental mantle lithosphere.* in Treatise on Geochemistry, Elsevier, *in press.*

Pearson, N.J., Griffin, W.L., Doyle, B.J., O'Reilly, S.Y., van Achterbergh, E., Kivi, K., **1999**. *Xenoliths from kimberlite pipes of the Lac de gras area, Slave Craton, Canada* in: 7th International Kimberlite Conference Proceedings,

Pollack, H.N. and Chapman, D.S., **1977**. *Regional variation of heat flow, geotherms, and lithospheric thickness*. Tectonophysics 38, 279–296

Preistley, K. and McKenzie, D., **2006**. *The thermal structure of the lithosphere from shear wave velocities* . Earth and Planetary Science Letters 244, 285-301

Read, G., Grütter, H.S., Winter, S., Luckman, N., Gaunt, F., Thomsen, F., **2004**. *Stratigraphic relations, kimberlite emplacement and lithospheric thermal evolution, Quiricó Basin, Minas Gerais State, Brazil*. Lithos 77, 803-818

Renne, P.R. and Basu, A.R., **1991**. *Rapid eruption of the Siberian traps flood basalts at the Permo-Triassic boundary*. Science 253, 176-179

Rudnick, R.L. and Fountain, D.M., **1995**. *Nature and composition of the continental crust. a Lower Crustal Perspective*. Reviews of Geophysics 33, 267-309

Rudnick, R.L., McDonough, W.F., O'Connell, R.J., **1998**. *Thermal structure, thickness and composition of continental lithosphere*. Chemical Geology 145, 395-411

Rudnick, R.L. and Nyblade, A.A., **1999**. *The thickness and heat production of Archean lithosphere, constraints from xenolith thermobarometry and surface heat flow. Mantle Petrology; Field Observations and High-Pressure Experimentation: A Tribute to Francis R. (Joe) Boyd*, The Geochemical Society

Rudnick, R.L. and Walker, R.J., **2009**. *Interpreting ages from Re-Os isotopes in peridotites*. Lithos 112, 1083-1095

Russell, J.K., Dipple, G.M., Kopylova, M.G. ,**2001**. *Heat production and heat flow in the mantle lithosphere, Slave Craton, Canada*. Physics of the Earth and Planetary Interiors 123, 27-44

Ryan, C.G., Griffin, W.L., Pearson, N.J., **1996**. *Garnet geotherms: pressure-temperature data from Cr-pyrope garnet xenocrysts in volcanic rocks*. Journal of Geophysical Research – Solid Earth 101, 5611-5625

Sambridge, M.S. and Compston, W., **1994**. *Mixture modelling of multi-component data sets with application to ion-probe zircon ages*. Earth and Planetary Science Letters 128, 373-390

Sand, K.K., Waight, T.E., Pearson, D.G., Nielsen, T.F.D., Makovicky, E., Hutchison, M.T., **2009**. *The lithospheric mantle below southern West Greenland. A geothermobarometric approach to diamond potential and mantle stratigraphy*. Lithos 112, 1155–1166.

Schmidberger, S.S. and Francis, D., **1999**. *Nature of the mantle roots beneath the North American craton. Mantle xenolith evidence from Somerset Island Kimberlites*. Lithos 48, 195–216.

Schmidberger, S.S., **2001**. *Hf, Sr, Nd and Pb isotope systematics and major and trace element compositions of the Archean subcratonic lithosphere beneath Somerset Island, Arctic Canada.* PhD Thesis, McGill University ,

Schmidberger, S.S., Simonetti, A., Heaman, L.M., Creaser, R.A., Whiteford, S., **2007**. *Lu-Hf, in-situ Sr and Pb isotope and trace element systematics for mantle eclogites from the Diavik diamond mine: Evidence for Paleoproterozoic subduction beneath the Slave craton, Canada*. Earth and Planetary Science Letters 254, 55-68

Shimizu, N., Sobolev, N.V., Yefimova, E.S., **1997**. *Chemical heterogeneity of garnet inclusions and juvenility of peridotite diamonds from Siberia*. Geologiya I Geofizika 38, 337-352

Simon, N.S.C., Carlson, R.W., Pearson, D.G., Davies, G.R., **2007**. *The origin and evolution of the Kaapvaal cratonic lithospheric mantle*. Journal of Petrology 48, 589–625

Skinner, C., **1989**. *The petrology of peridotite xenoliths from the Finsch Kimberlite, South Africa.* South African Journal of Geology 92, 197–206.

Sleep, N.H., **2003**. *Geodynamic implications of xenolith geotherms*. Geochemistry, Geophysics, Geosystems 4, 1079

Smart, K.A., Heaman, L.M., Chacko, T., Simonetti, S.S., Kopylova, M.G., Mah, D., Daniels, D., **2009**. *The origin of high-MgO diamond eclogites from the Jericho Kimberlite, Canada*. Earth and Planetary Science Letters 284, 527-537

Smart, K.A., Chacko, T., Stachel, T., Muehlenbachs, K., Stern, R.A., Heaman, L.M., **2011**. *Diamond growth from oxidised carbon sources beneath the Northern Slave Craton, Canada: A $\delta^{13}C$–N study of eclogite-hosted diamonds from the Jericho kimberlite*. Geochimica et Cosmochimica Acta 75, 6027-6047

Smith, D. and Boyd, F.R., **1992**. *Compositional zonation in garnets in peridotite xenoliths*. Contributions to Mineralogy and Petrology 112, 134-147

Snyder, D.B., Rodenay, S., Bostock, M.G., Lockhart, G.D., **2004**. *Mapping the mantle lithosphere for diamond potential using teleseismic methods*. Lithos 77, 859-872

Snyder, D.B. and Bruneton, M., 2007. *Seismic anisotropy of the Slave caton, NW Canada, from joint interpretation of SKS and Rayleigh waves*. Geophysical Journal International 169, 170-188

Snyder, D.B., **2008**. *Stacked uppermost mantle layers within the Slave craton of NW Canada as defined by anisotropic seismic discontinuities*. Tectonics 27, TC4006.

Sobolev, N.V., Lavrente, Y.G., Pokhilen, N.P., Usova, L.V., **1973**. *Chrome-rich garnets from kimberlites of Yakutia and their paragenesis*. Contributions to Mineralogy and Petrology 40, 39-52

Sobolev, N.V., Hoffman, A.W., Kuzmin, D.V., Yaxley, G.M., Arndt, N.T., Chung, S-L., Danyushevsky, L.V., Elliot, T., et al., **2007**. *The Amount of Recycled Crust in Sources of Mantle-Derived Melts*. Nature 316, 412-417

Spriggs A.J., **1988**. *An isotopic and geochemical study of kimberlites and associated alkaline rocks from Namibia*. PhD

Stachel, T., Aulbach, S., Brey, G.P., Harris, J.W., Leost, I., Tappert, R., Viljoen, K.S., **2004**. *The trace element composition of silicate inclusions in diamonds: a review*. Lithos 77, 1-19

Stachel, T. and Harris, J.W., **2008**. *The origin of cratonic diamonds - constraints from mineral inclusions*. Ore Geology Reviews 34, 5-32

Taylor, S.R. and McLennan, S.M., **1985**. *The Continental Crust; its composition and Evolution.* Blackwell ,

Taylor, W.R., **1998**. *An experimental test of some geothermometer and geobarometer fomulations for upper mantle peridotites with application to the thermobarometery of fertile lherzolite and garnet websterite*. Neues Jarhrbuch fur Mineralogie-Abhandlungen 172, 381–408

Thompson, M., Potts, P.J., Webb, P.C., **1996**. GeoPT1. *International proficiency test for analystical geochemistry laboratories - Report on round 1 (July 1996)*. Geostandards Newsletter 20, 277-287

Thompson, R.N. and Gibson, S.A., **1991**. *Subcontinental mantle plumes, hotspots and pre-existing thinspots*. Journal of the Geological Society 148, 973-977

van der Plas, L. and Tobi, A.C., **1965**. *A chart for judging the reliability of point counting results*. American Journal of Science 263, 87-90

van Hunen, J., **2008**. *Plate tectonics on the early Earth: limitations imposed by strength and buoyancy of subducted lithosphere*. Lithos 103, 217-235

van Rythoven, A.D. and Schulze, D.J., **2009**. *In-situ analysis of diamonds and their inclusions from the Diavik Mine, Northwest Territories, Canada: Mapping diamond growth*. Lithos 112S, 870-879

Waff, H.S. and Holdren, G.R. Jr., **1981**. *The Nature of Grain Boundaries in Dunite and Lherzolite Xenoliths: Implications for Magma Transport in Refractory Upper Mantle Material*. Journal of Geophysical Research – Solid Earth 86, 3677-3683

Walter, **2003**. Melt extraction and compositional variability in mantle lithosphere. Holland, H.D. and Turekian, K.K. (Eds) Treatise on Geochemistry Vol 2: The Mantle and Core,

Waters, F.G., **1987**. *A suggested origin of MARID xenoliths in kimberlites by high pressure crystallization of an ultrapotassic rock such as lamproite*. Contributions to Mineralogy and Petrology 95, 523-533

Westerlund, K.J., Shirey, S.B., Richardson, S.H., Carlson, R.W., Gurney, J.J., Harris, J.W., **2006**. *A subduction wedge origin for Palaeoarchean peridotitic diamond and harzburgites from the Panda kimberlite, Slave craton: evidence from Re-Os isotope systematics*. Contributions to Mineralogy and Petrology 152, 275-294

White, R. and McKenzie, D., **1989**. *Magmatism at rift zones: The generation of volcanic continental margins and flood basalts.* Journal of Geophysical Research – Solid Earth 94, 7685-7729

White, R. and McKenzie, D., **1995**. *Mantle plumes and flood basalts*. Journal of Geophysical Research – Solid Earth 100, 17543-17585

Wittig, N., Pearson, D.G., Webb, M., Ottley, C.J., Irvine, G.J., Kopylova, M., Jensen, S.M., Nowell, G.M., **2008**. *Origin of cratonic lithospheric mantle roots: A geochemical study of peridotites from the North Atlantic Craton, West Greenland*. Earth and Planetary Science Letters 274, 24–33

Wu, C-M. and Zhao, G., **2010**. *The applicability of garnet orthopyroxene geobarometry in mantle xenolith*s. Lithos 125, 1-9

Yaxley, G.M. and Green, D.H., **1998**. *Reactions between eclogite and peridotite: Mantle refertilisation by subduction of oceanic crust*. Schweizeriche Mineralogische und Petrographische Mitteilungen 78, 243-255

Yuan, H.Y. and Romanowicz, B., **2010**. *Lithospheric layering in the North American craton*. Nature 466, 1063–1068

A XENOLITH-BASED LITHOSPHERIC TRANSECT OF THE SLAVE CRATON, N.W.T., CANADA

VOLUME II : FIGURES AND TABLES

Kathy Mather

A thesis submitted in partial fulfilment of the requirements for the degree of Doctor of Philosophy at Durham University

Department of Earth Sciences

Durham University

May 2012

INDEX TO FIGURES

1 INTRODUCTION

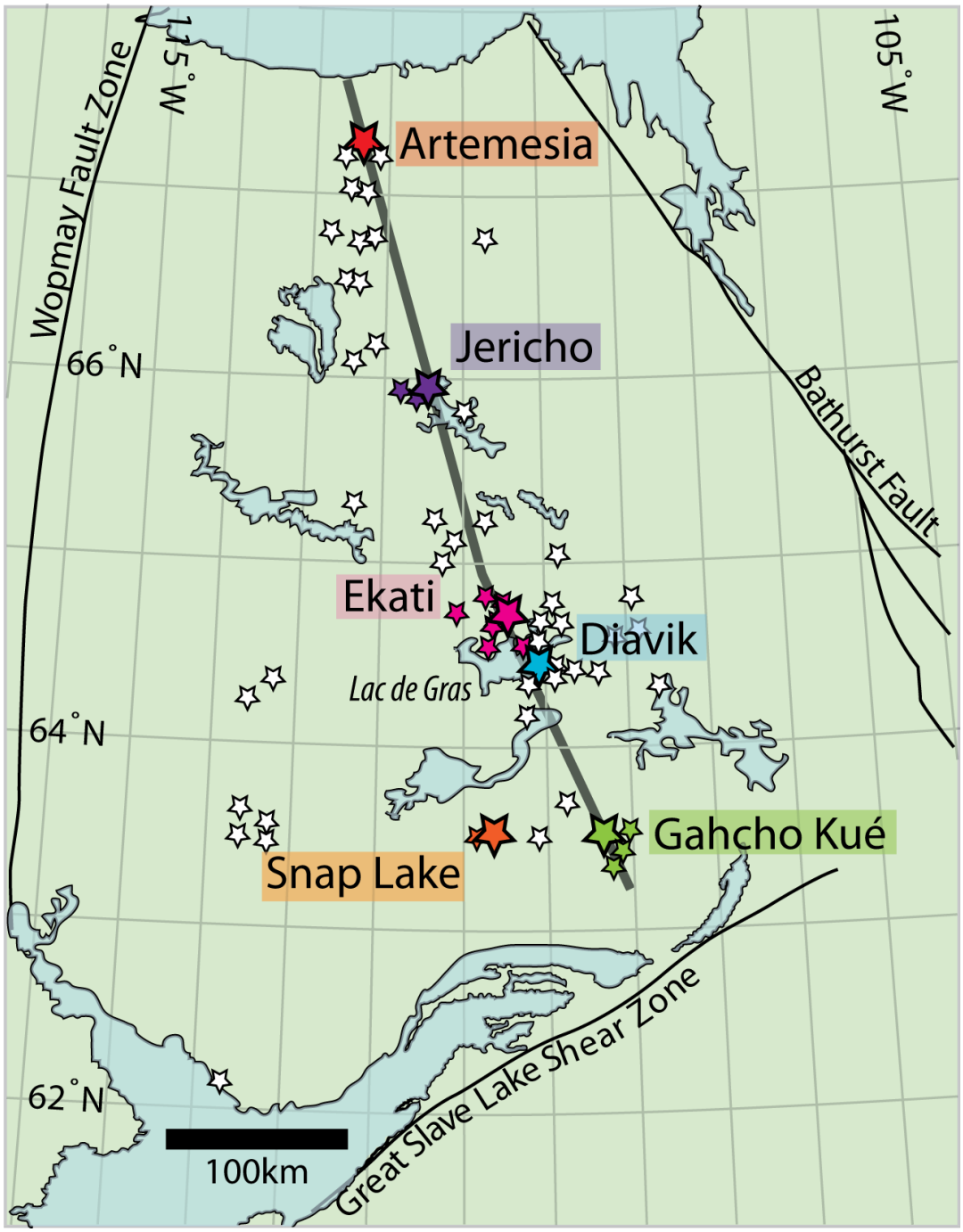

Figure 1.1

Location map of the Slave craton, Canada. Highlighted are the kimberlites (small white stars) and the localities to be studied in this thesis (large coloured stars). Grey line indicates the location of the proposed 'lithospheric transect'. The mainland expression of the Slave craton is bounded by the Great Slave Lake shear zone to the south, the Thelon Magmatic zone to the south and east, and the Wopmay fault zone to the West.

2 CONSTRAINTS ON THE DEPTH AND THERMAL HISTORY OF CRATONIC LITHOSPHERE FROM PERIDOTITE XENOLITHS, XENOCRYSTS AND SEISMOLOGY

This chapter has been published in full in *Lithos*

Figure 2.1

(A) Comparison of the palaeogeotherm fit to the TA98_NG85 P–T mantle xenolith array from Bultfontein (mineral chemistry data from Boyd and Nixon, 1978 and Simon et al., 2007) using the PC77 method (dashed line), and the FITPLOT program (solid line, with dashed shading representing the error envelope). The base of the lithosphere, as defined by the deepest xenolith and the intersection of the PC77 and FITPLOT geotherm with the isentrope are also illustrated.

(B) Comparison of Rudnick and Nyblade (1999) best-fit Kalahari geotherm (black double-dashed line), with the Michaut et al. (2009) 1 Ga and 'today' transient palaeogeotherms (grey dashed lines), and the FITPLOT geotherm (solid line).

Table 2.1:

Output parameters from three palaeogeotherm calculation methods shown in Figure 2.1

Palaeogeotherm Method	*FITPLOT*	PC77	RN99
Lithosphere Thickness	**183 km**	**~227 km**	**~207 km**
Surface Heat Flow	52.6 mWm^{-2}	43 mWm^{-2}	45 mWm^{-2}
Moho Heat Flow	16.8 mWm^{-2}	?	18.0 mWm^{-2}
Crustal Thickness	35 km	n/a	38 km
Mantle Heat Production	0 μWm^{-3}	0.1 - 0.084 μWm^{-3}	0 μWm^{-3}

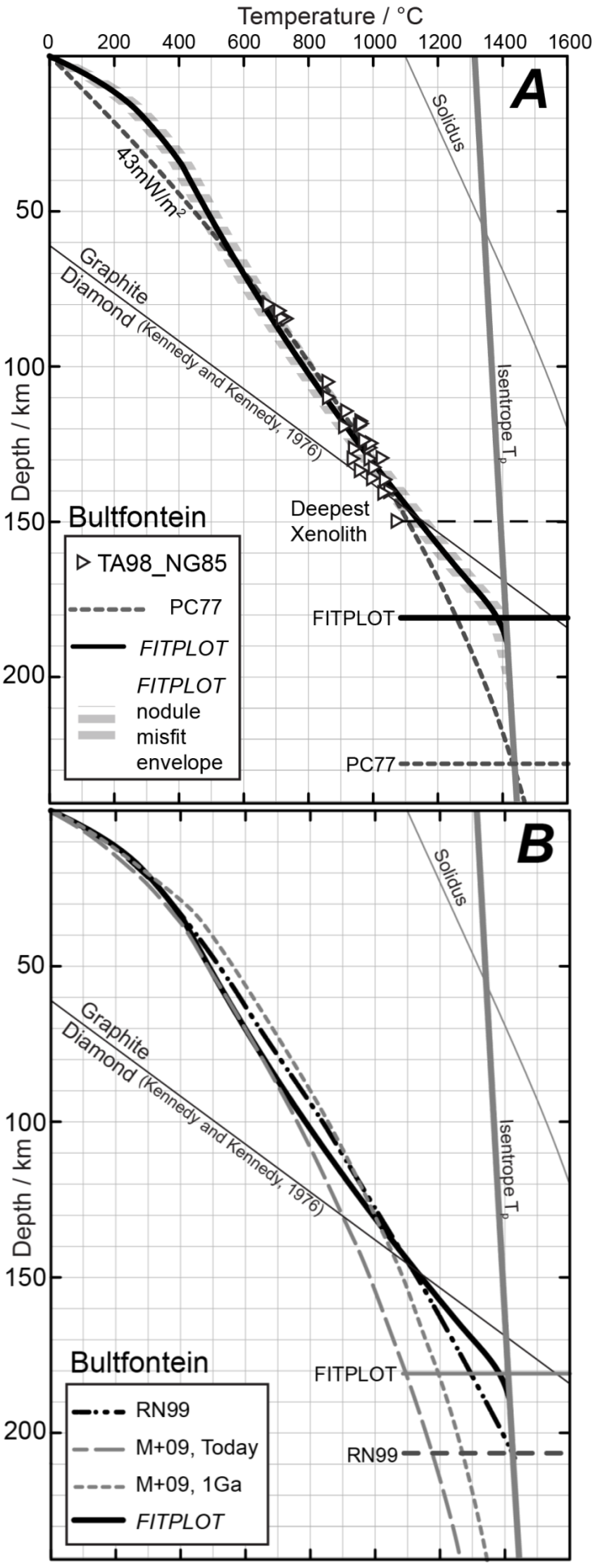
Temperature / °C
0
200
400
600
800
1000
1200
1400
1600
A
Solidus
43mW/m²
Graphite
Diamond (Kennedy and Kennedy, 1976)
Isentrope Tp
Depth / km
50
100
150
200
Bultfontein
TA98_NG85
PC77
FITPLOT
FITPLOT
nodule
misfit
envelope
Deepest
Xenolith
FITPLOT
PC77
B
Solidus
Graphite
Diamond (Kennedy and Kennedy, 1976)
Isentrope Tp
Depth / km
50
100
150
200
Bultfontein
RN99
M+09, Today
M+09, 1Ga
FITPLOT
FITPLOT
RN99

Figure 2.2

Plots of P–T data calculated from the same suite of mantle xenoliths from the Somerset Island kimberlite field (mineral chemistry data from Schmidberger and Francis, 1999 and Schmidberger, 2001), using the three recommended thermobarometer combinations of Nimis and Grütter (2009), and the commonly-used Brey and Köhler (1990) formulation. All palaeogeotherms calculated using FITPLOT. Small dots surrounding data points on all plots indicate the potential P–T 'error cloud', calculated from the standard deviations of average microprobe analyses on each elemental oxide. These are shown enlarged in the grey squares on each plot, (scale shown on NG09_NG85) to emphasise the different 'clouds' for high- and low- temperature samples. Distinct from these error clouds is the error on the thermobarometer combination used, indicated by the heavy black crosses. Brown shaded regions indicate the P–T regions in which the thermobarometers used were calibrated. Note also that the thermometer 'NG09' is calibrated empirically, and therefore the range in temperatures used is illustrated by the grey bar at the top of the NG09_NG85 plot.

Table 2.2:

Output parameters from the palaeogeotherms shown in Figures 2.2 and 2.3

Thermobarometer	NT_NT	TA98_NG85	NG09_NG85	BK90_BK90
Lithosphere Thickness	165 km	163 km	163 km	156 km
Diamond-in	168 +/- 6 km	168 +/- 6 km	168 +/- 5 km	169 +/- 7 km
Xenolith misfit	**102.7 °C**	**61.7 °C**	**49.9 °C**	**79.3 °C**

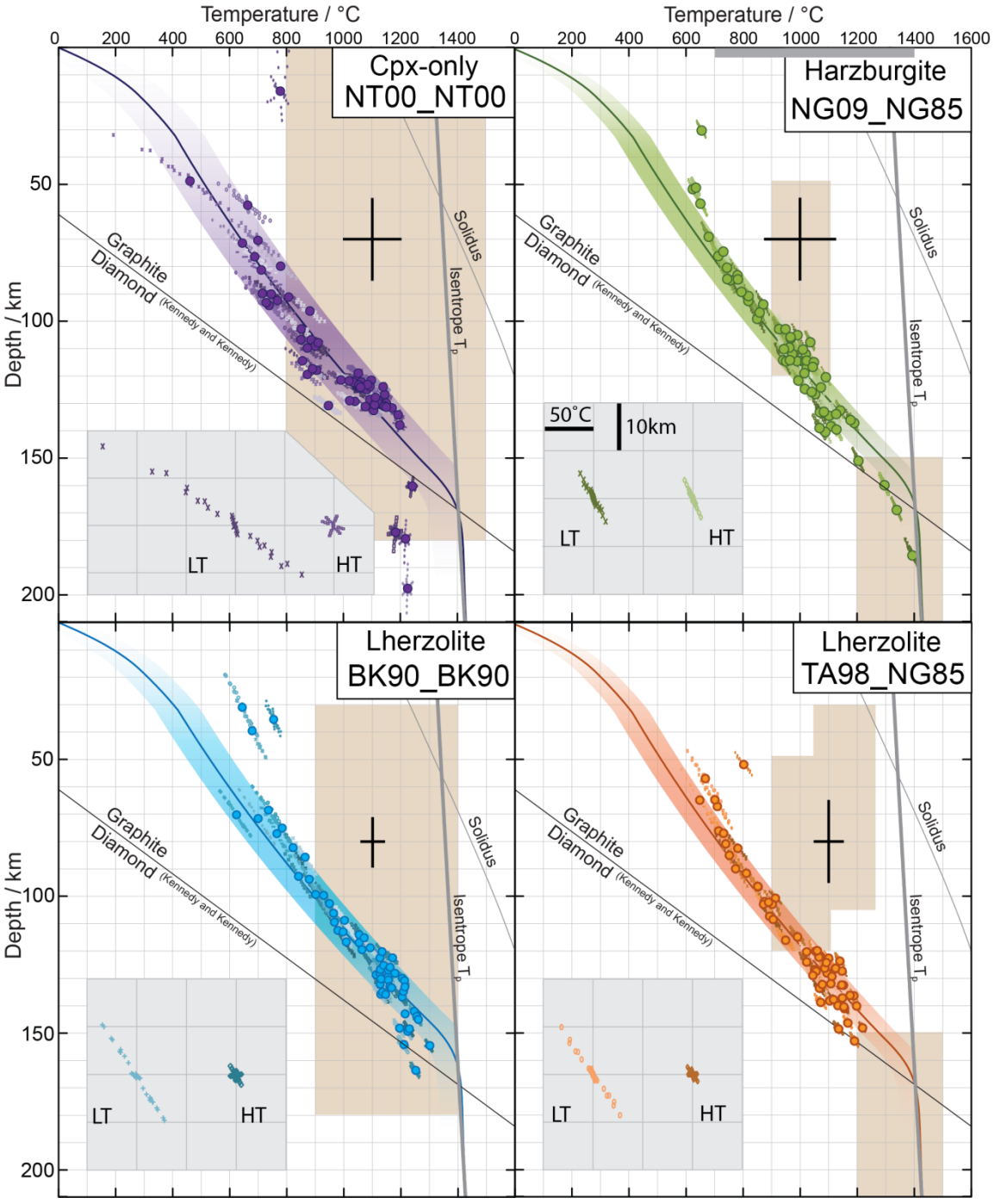
Temperature / °C
Depth / km
Cpx-only
NT00_NT00
Harzburgite
NG09_NG85
Lherzolite
BK90_BK90
Lherzolite
TA98_NG85
Graphite
Diamond (Kennedy and Kennedy)
Solidus
Isentrope T$_p$
LT
HT
50°C
10km

Table 2.3:

Ouput parameters for the TA98_NG85 palaeogeotherms with screens applied to the data, as described in the text.

	All Samples	Equilibrium only	Equilibrated, granular only	Equilibrated, porphyroclastic only
Somerset				
Lithosphere Thickness	163 km	164 km	163 km	
Diamond-in	168 +/- 6km	168 +/- 5km	168 +/- 4km	
Xenolith misfit	61.7°C	46.1°C	39.5°C	
Bultfontein				
Lithosphere Thickness	183 km	182 km	181 km	
Diamond-in	146 +/- 7km	147 +/- 7km	148 +/- 6km	
Xenolith misfit	36.4°C	34.3°C	32.0°C	
Finsch				
Lithosphere Thickness	201 km	192 km	192 km	
Diamond-in	131 +/- 10km	138 +/- 6km	137 +/- 7km	
Xenolith misfit	64.4°C	34.9°C	39.1°C	
Gibeon				
Lithosphere Thickness		167 km	161 km	186 km
Diamond-in		167 +/- 11km	168 +/- 8km	152 +/- 5km
Xenolith misfit		81.8°C	84.2km	34.8°C

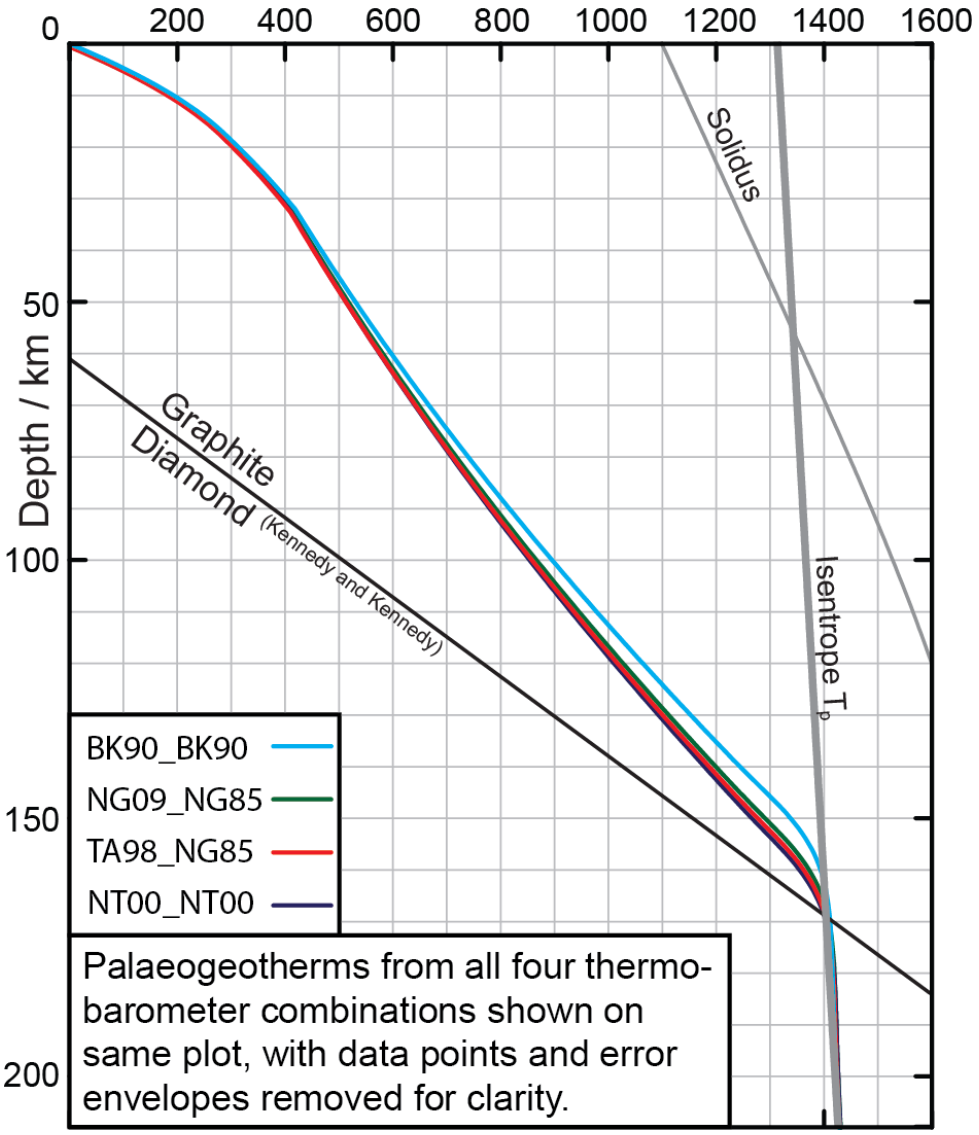

Figure 2.3:

The palaeogeotherms from the four thermobarometer combinations in Figure 2.2 re-plotted without individual data points and error envelopes.

Figure 2.4:

(A) Plots of P–T data calculated for equilibrated (filled triangles) and un-equilibrated (open triangles) mantle xenoliths from Somerset Island (mineral chemistry data from Schmidberger and Francis, 1999 and Schmidberger, 2001).

(B) Plots of P–T data calculated for equilibrated (filled triangles) and un-equilibrated (open triangles) mantle xenoliths from the Bultfontein kimberlite (mineral chemistry data from Boyd and Nixon, 1978 and Simon et al., 2007). Only one geotherm line is visible on both plots because the palaeogeotherms overlap. However, the xenolith misfit (error envelope) is larger for palaeogeotherms calculated using equilibrated plus un-equilibrated samples.

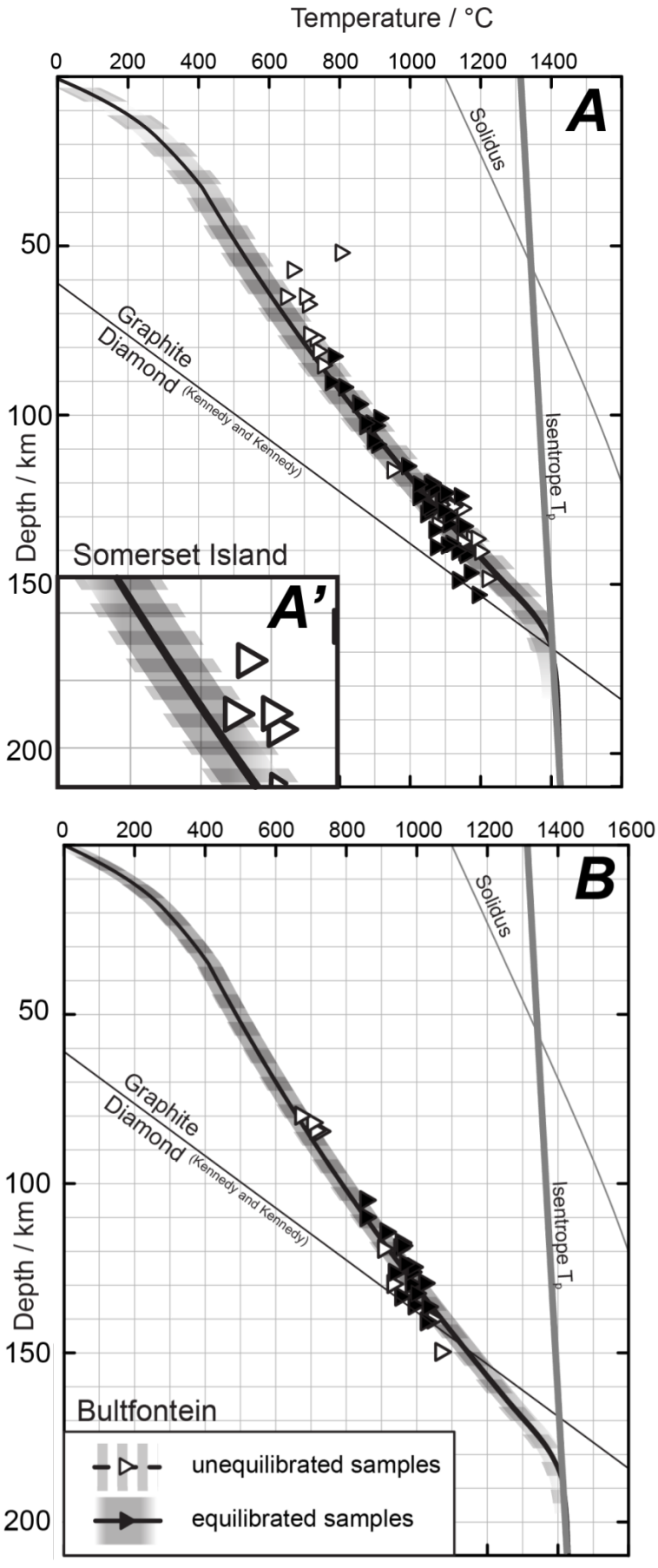
Temperature / °C
0
200
400
600
800
1000
1200
1400
1600
A
B
Solidus
Isentrope T_p
Graphite
Diamond (Kennedy and Kennedy)
Depth / km
50
100
150
200
Somerset Island
A'
Bultfontein
unequilibrated samples
equilibrated samples

Figure 2.5:

A). Plot of P–T data calculated for equilibrated (filled triangles) and unequilibrated (open triangles) mantle xenoliths from the Finsch kimberlite (mineral chemistry from: Gibson et al., 2008 and Lazarov et al., 2009), the palaeogeotherm calculated using all samples (dashed line) is slightly steeper (cooler) than the palaeogeotherm calculated using only equilibrated xenoliths (solid line). The enlarged area A' shows that the palaeogeotherm calculated using only the equilibrium samples lies just within the error envelope of that calculated using the full dataset.

(B) Palaeogeotherms calculated using a modified version of the FITPLOT palaeogeotherm estimation method, to include varying heat production. The equilibrated xenolith array from Finsch is shown. The palaeogeotherm calculated with 0.05 μWm^{-3} (dashed line and shading) yields a much more precise fit to the data than the 0 μWm^{-3} (solid line and shading).

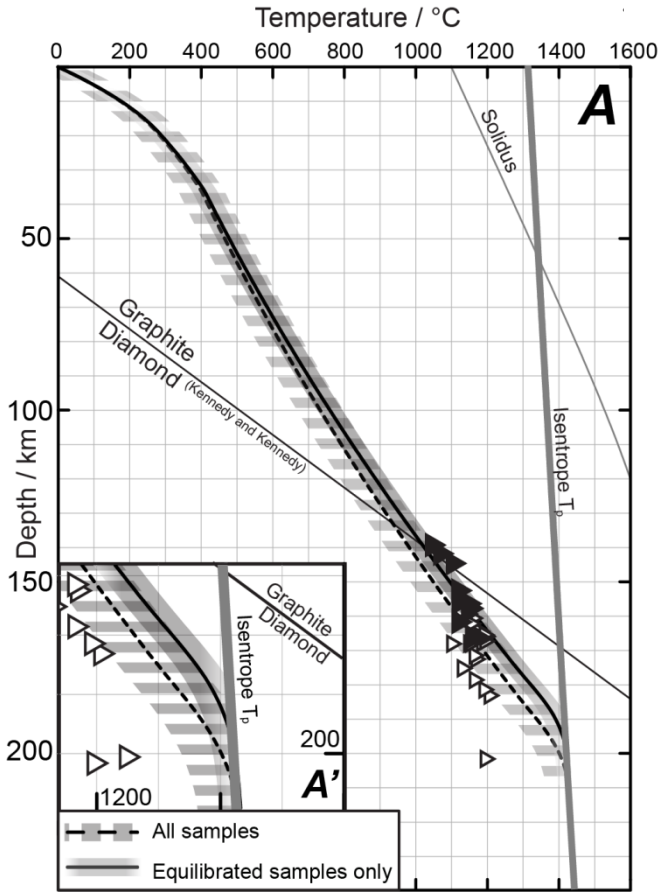
Temperature / °C
0
200
400
600
800
1000
1200
1400
1600
A
Solidus
50
Graphite
Diamond (Kennedy and Kennedy)
100
Depth / km
Isentrope Tp
150
Graphite
Diamond
Isentrope Tp
200
200
A'
1200
All samples
Equilibrated samples only

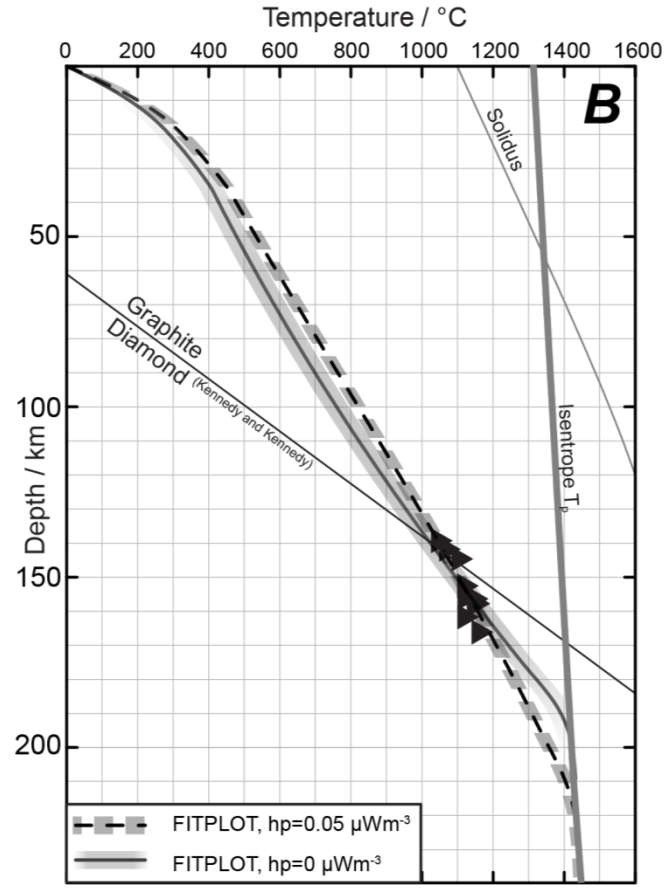
Temperature / °C
0
200
400
600
800
1000
1200
1400
1600
B
Solidus
50
Graphite
Diamond (Kennedy and Kennedy)
100
Depth / km
Isentrope Tp
150
200
FITPLOT, hp=0.05 µWm-3
FITPLOT, hp=0 µWm-3

Figure 2.6:

Plots of P–T data calculated from filtered ('equilibrated') and unfiltered ('all') cpx xenocryst data from the Somerset Island (A) and Bultfontein (B) kimberlites. In each example, palaeogeotherms were calculated for filtered cpx xenocrysts (black solid line and dashed shading) and unfiltered (all) cpx xenocrysts (grey dashed line and solid shading) and compared to the equilibrated granular mantle xenolith palaeogeotherm (red dashed line and shading). The region of single-cpx P-T data from Bultfontein (Nimis and Taylor; 2000) is also shown as blue shaded region

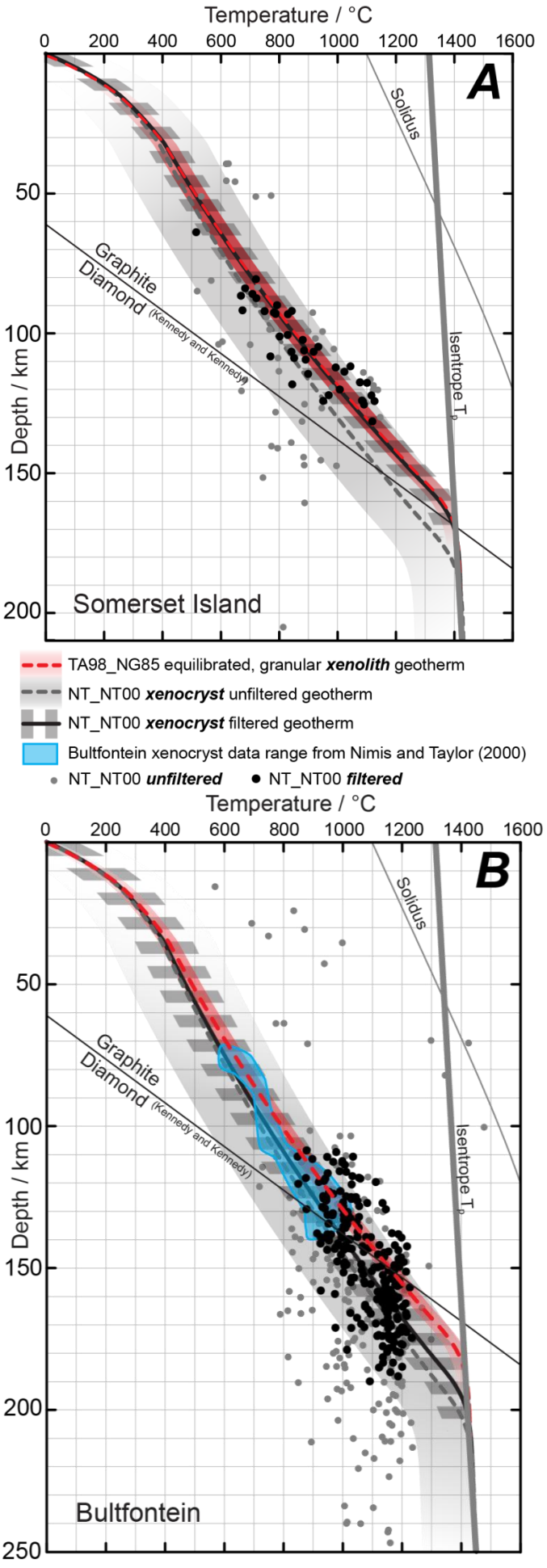
Temperature / °C
0
200
400
600
800
1000
1200
1400
1600
A
Solidus
Isentrope T_p
Graphite
Diamond (Kennedy and Kennedy)
Depth / km
50
100
150
200
Somerset Island
TA98_NG85 equilibrated, granular xenolith geotherm
NT_NT00 xenocryst unfiltered geotherm
NT_NT00 xenocryst filtered geotherm
Bultfontein xenocryst data range from Nimis and Taylor (2000)
NT_NT00 unfiltered
NT_NT00 filtered
Temperature / °C
0
200
400
600
800
1000
1200
1400
1600
B
Solidus
Isentrope T_p
Graphite
Diamond (Kennedy and Kennedy)
Depth / km
50
100
150
200
250
Bultfontein

Figure 2.7:

(A) After Priestley and McKenzie (2006), map of the lithospheric thickness of Southern Africa from shear wave velocities, with the locations of Gibeon (G) and Bultfontien (B) indicated.

(B) Palaeogeotherms calculated from P–T data for equilibrated, granular mantle xenoliths from Gibeon kimberlites (open triangles, dashed line and shading; Franz et al., 1996a,b, and Boyd et al., 2004) and Bultfontein (filled triangles, solid line and shading; Boyd and Nixon, 1978; Simon et al., 2007). The lithospheric thickness calculated from these palaeogeotherms is the same, within error.

(C) Palaeogeotherms calculated from P–T data for equilibrated granular mantle xenoliths (open triangles; dashed line and shading) and equilibrated porphyroclastic xenoliths (filled triangles; solid line and shading) from the Gibeon kimberlite field. The palaeogeotherm calculated from the porphyroclastic samples is shallower than that calculated from the granular samples.

(D) The geotherm obtained from fitting seismic estimates of temperature and depth (solid circles) compared to the equilibrated, granular xenolith palaeogeotherm fit from the Gibeon kimberlite. The seismic geotherm is 50 km shallower than the xenolith palaeogeotherm, suggesting that the heating event indicated by the porphyroclastic xenoliths resulted in lithospheric thinning.

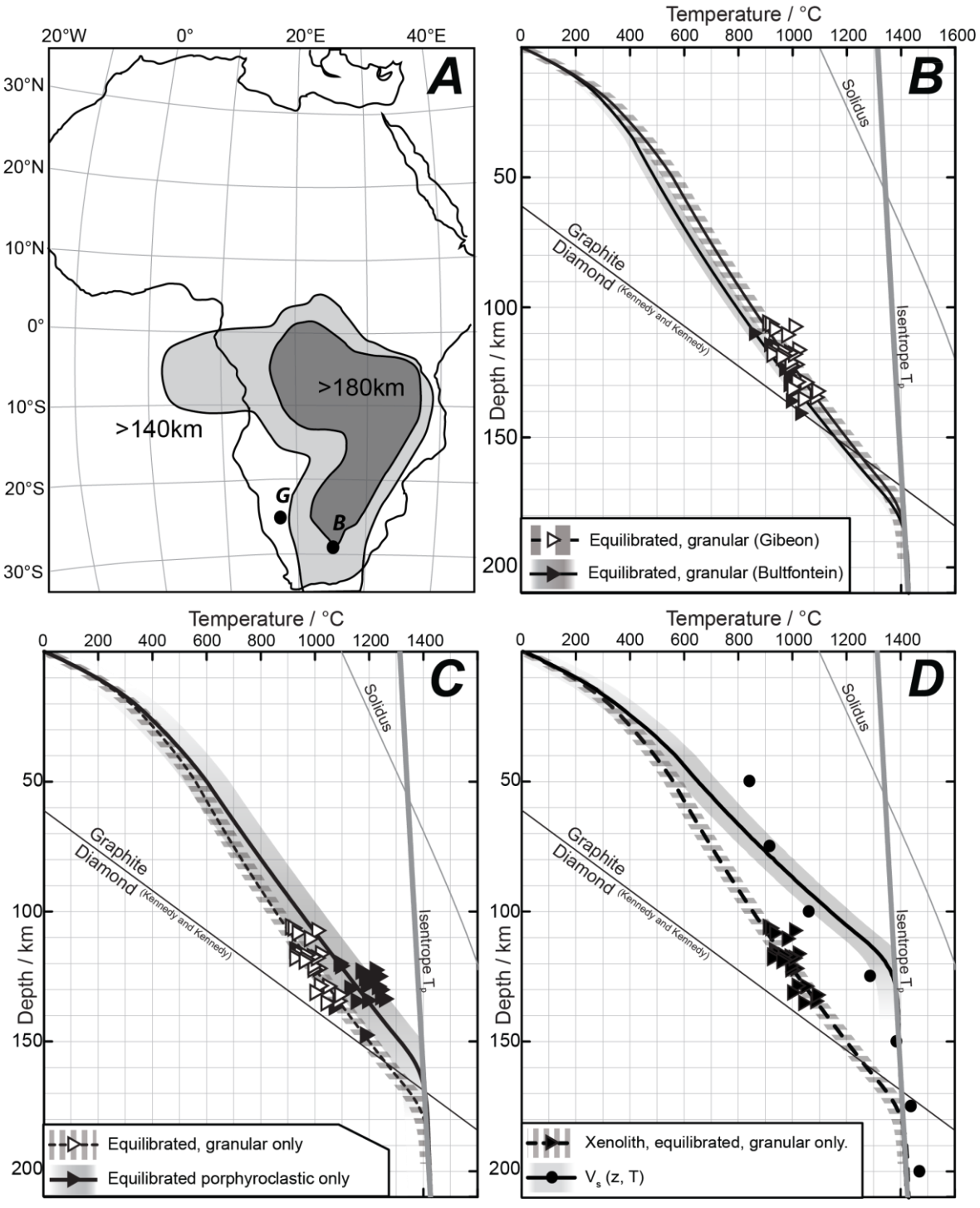
A
20°W
0°
20°E
40°E
30°N
20°N
10°N
0°
10°S
20°S
30°S
>180km
>140km
G
B
B
Temperature / °C
0
200
400
600
800
1000
1200
1400
1600
Solidus
Graphite
Diamond (Kennedy and Kennedy)
Isentrope T_p
Depth / km
50
100
150
200
Equilibrated, granular (Gibeon)
Equilibrated, granular (Bultfontein)
C
Equilibrated, granular only
Equilibrated porphyroclastic only
D
Xenolith, equilibrated, granular only.
V_s (z, T)

3 PRACTICALITIES OF LITHOSPHERIC STRATIGRAPHY

Figure 3.1

Projected depth errors for mid, high and low P-T estimates from example peridotite xenoliths. Brown shaded regions indicate the pressure and temperature range in which the thermobarometer was calibrated. Orthogonal, thick black lines on each plot within brown shaded regions indicate published errors for the respective thermobarometer combinations. This are added to P-T error 'clouds' for the example xenoltihs calculated using average probe standard deviations as described in 2.3.3.2.

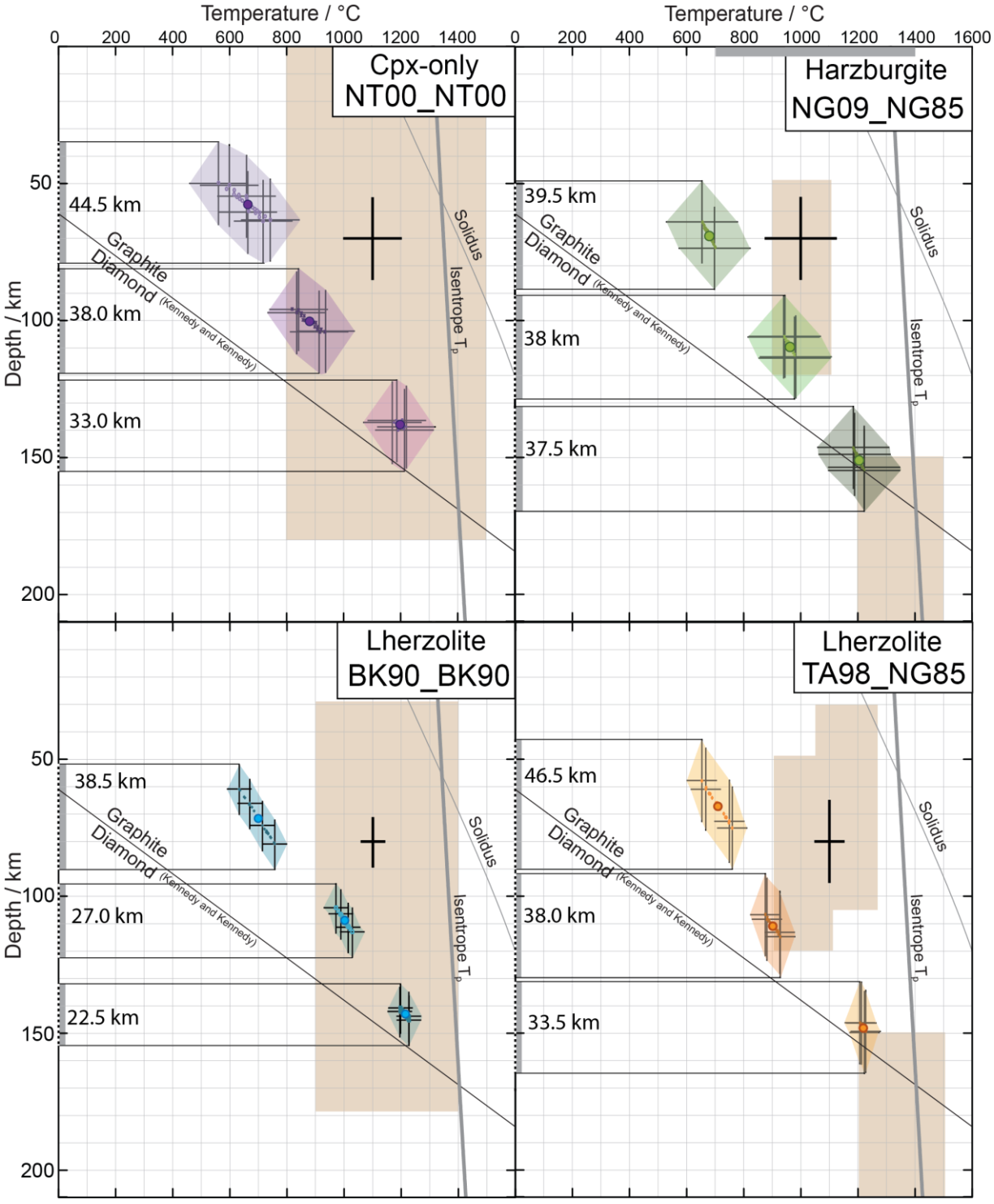
Temperature / °C
0
200
400
600
800
1000
1200
1400
1600
Depth / km
50
100
150
200
Cpx-only
NT00_NT00
44.5 km
38.0 km
33.0 km
Harzburgite
NG09_NG85
39.5 km
38 km
37.5 km
Lherzolite
BK90_BK90
38.5 km
27.0 km
22.5 km
Lherzolite
TA98_NG85
46.5 km
38.0 km
33.5 km
Graphite
Diamond (Kennedy and Kennedy)
Solidus
Isentrope T_p

Figure 3.2

Plot of depth range of P-T estimates calculated using the four thermobarometer combinations outlined in the text. Samples are ordered by the average depth estimate from all available thermobarometer combinations for that sample.

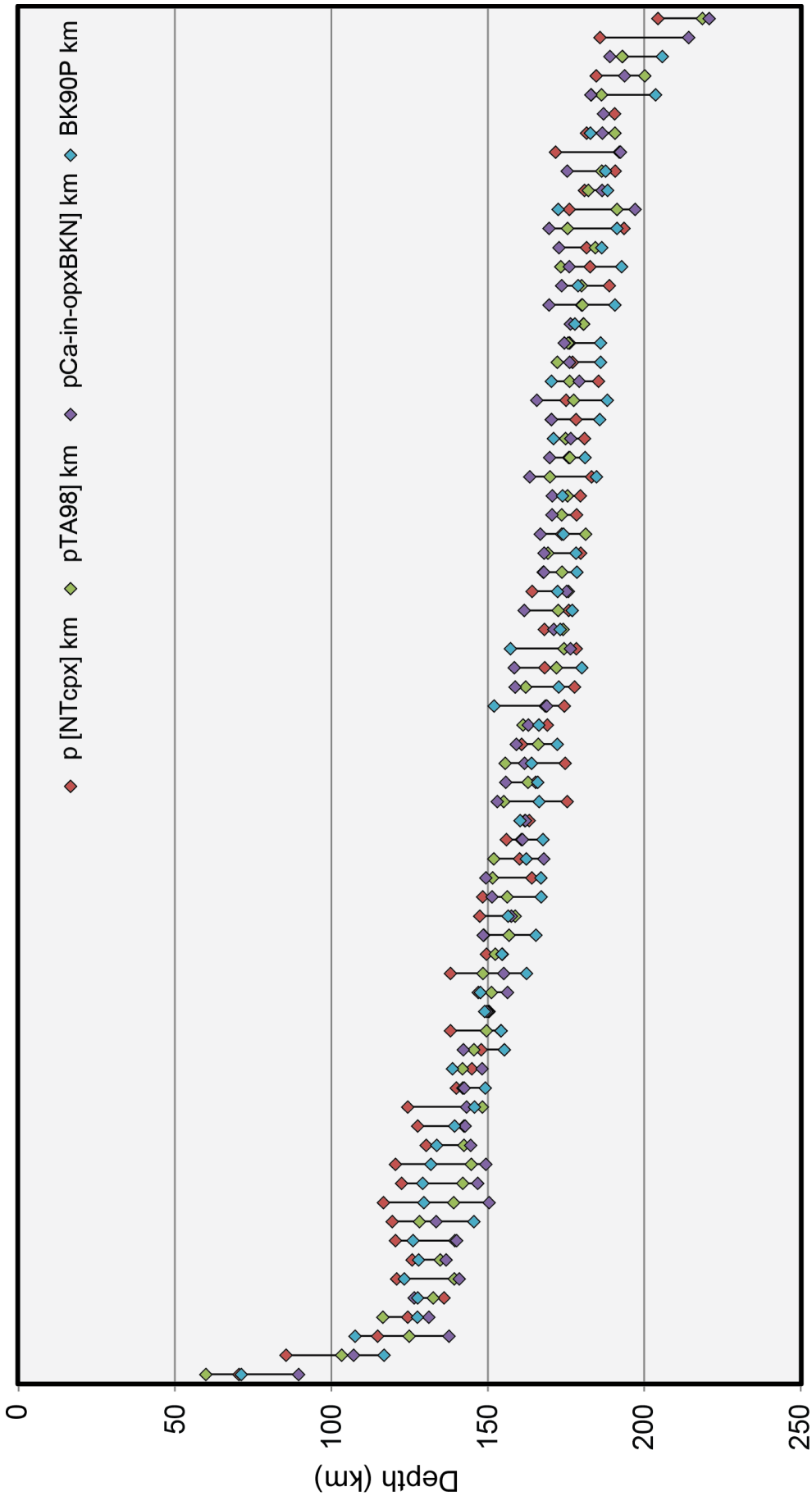
p [NTcpx] km
pTA98] km
pCa-in-opxBKN] km
BK90P km
0
50
100
150
200
250
Depth (km)

Table 3.1

Depths for multiphase xenoliths from central Slave database (Chapter 5), and their relative depth 'order'. Also shown are the range in depth (in km) and the range in depth *order*. Average values are shown in the far right column and samples are ordered by increasing average depth value.

Reference	Sample	NT00_NT00		TA98_NG85		CaOpx_NG85		BK90_BK90		Order Range	Depth Range	Multiphase Average	
		Depth Order	Depth (km)	Depth Order	Depth (km)	Depth Order	Depth (km)	Depth Order	Depth (km)			Depth Order	Depth (km)
Menzies et al., 2004	JJG 5055-1	1	70	1	60	1	89	1	71	0	30	1	73
Menzies et al., 2004	JJG 5051-26	2	85	2	103	2	107	3	117	1	31	2	103
Aulbach et al., 2004	vr19674pg3	3	115	4	125	7	138	2	108	5	30	3	121
Menzies et al., 2004	JJG 5055-6	11	124	3	116	4	131	6	127	8	15	4	125
Creighton et al., 2010	MX5003	15	136	6	132	3	126	7	128	12	10	5	131
Menzies et al., 2004	JJG 5051-7	8	121	9	139	9	141	4	123	5	20	6	131
Menzies et al., 2004	JJG 5051-2	12	126	7	135	6	137	8	128	6	11	7	131
Menzies et al., 2004	JJG 5051-4	7	120	10	139	8	140	5	126	5	20	8	131
Menzies et al., 2004	JJG 5047-30	5	119	5	128	5	133	15	146	10	26	9	132
Aulbach et al., 2004	vr50861	4	117	8	139	21	150	10	129	17	34	10	134
Menzies et al., 2004	JJG 5051-9	9	122	12	142	15	147	9	129	6	24	11	135
Menzies et al., 2004	JJG 5051-6	6	120	16	145	18	149	11	132	12	29	12	137
Menzies et al., 2004	JJG 5051-5	14	130	14	142	14	144	12	134	2	14	13	138
Menzies et al., 2004	JJG 5051-8	13	128	15	142	12	143	14	139	3	15	14	138
Menzies et al., 2004	JJG 5051-3	10	124	18	148	13	143	16	146	8	24	15	140
Aulbach et al., 2004	vr50875	18	140	13	142	11	142	19	149	8	9	16	143
Menzies et al., 2004	JJG 5050-29	19	145	11	142	16	148	13	139	8	9	17	143
Menzies et al., 2004	JJG 5051-23	22	148	17	145	10	142	23	155	13	13	18	148
Menzies et al., 2004	JJG 5049-43	16	138	20	150	24	154	21	154	8	16	19	149
Aulbach et al., 2004	yk2474	26	150	21	150	20	150	18	149	8	1	20	150
Aulbach et al., 2004	vr09370	20	147	22	151	28	156	17	148	11	9	21	150
Aulbach et al., 2004	vr40335	17	138	19	148	26	155	28	162	11	24	22	151
Menzies et al., 2004	JJG 5049-39	25	150	25	152	25	155	22	154	3	5	23	153
Creighton et al., 2010	A154-09CR	24	149	29	157	17	148	30	165	13	17	24	155
Menzies et al., 2004	JJG 5047-38	21	147	30	159	29	157	24	156	9	11	25	155
Menzies et al., 2004	JJG 5047-34	23	148	28	156	22	151	35	167	13	19	26	156
Menzies et al., 2004	JJG 5049-44	31	164	23	151	19	149	34	167	15	18	27	158
Menzies et al., 2004	JJG 5050-63	28	160	24	152	41	168	27	162	17	16	28	160
Aulbach et al., 2004	vr43499	27	156	31	161	33	161	36	168	9	12	29	161
Aulbach et al., 2004	yk2471	30	163	33	162	36	162	26	160	10	3	30	162
Aulbach et al., 2004	yk1919	42	175	26	155	23	153	33	166	19	22	31	162
Creighton et al., 2010	MX5012	33	165	35	163	27	156	31	166	8	10	32	162
Aulbach et al., 2004	vr50886	40	175	27	156	35	162	29	164	13	19	33	164
Menzies et al., 2004	JJG 5047-29	29	161	36	166	32	159	39	172	10	13	34	165
Menzies et al., 2004	JJG 5049-40	37	169	32	161	37	163	32	166	5	8	35	165
Aulbach et al., 2004	vr09361	39	174	37	168	44	169	20	152	24	22	36	166
Menzies et al., 2004	JJG 5047-48	48	178	34	162	31	159	42	173	17	19	37	168
Creighton et al., 2010	MX131	36	168	41	172	30	158	51	180	21	22	38	170
Aulbach et al., 2004	vr67125	50	178	47	174	58	176	25	157	33	21	39	171
Aulbach et al., 2004	vr50914	35	168	46	174	50	171	43	173	15	6	40	172
Menzies et al., 2004	TQY94_17_22B1	43	176	43	172	34	162	46	177	12	15	41	172
Aulbach et al., 2004	vr67112	32	164	52	176	54	175	40	172	22	12	42	172
Creighton et al., 2010	MX162	34	168	45	174	42	168	49	178	15	11	43	172
Menzies et al., 2004	JJG 5047-49	52	180	38	169	43	168	48	178	14	12	44	174
Creighton et al., 2010	MX5011	38	174	59	181	40	167	45	174	21	14	45	174
Creighton et al., 2010	MX5004	51	179	50	175	49	171	44	174	7	9	46	175
Creighton et al., 2010	MX144	61	183	39	170	38	163	54	185	23	21	47	175
Menzies et al., 2004	JJG 5055-11	44	176	54	176	47	170	52	181	10	11	48	176
Aulbach et al., 2004	vr43467	56	181	48	175	60	176	38	171	22	10	49	176
Menzies et al., 2004	JJG 5047-27	49	178	40	170	48	170	55	186	15	15	50	176
Menzies et al., 2004	TANQ93_1_13	41	175	55	177	39	166	60	188	21	23	51	177
Aulbach et al., 2004	yk2472	62	185	53	176	61	179	37	170	25	15	52	178
Menzies et al., 2004	JJG 5047-28	47	177	42	172	57	176	56	186	15	14	53	178
Menzies et al., 2004	JJG 5047-50	46	176	51	176	53	174	57	186	11	12	54	178
Creighton et al., 2010	MX5006	54	180	58	181	59	176	47	178	12	4	55	179
Menzies et al., 2004	JJG 5047-51	53	180	57	180	46	170	62	191	16	21	56	180
Creighton et al., 2010	MX5001	63	189	56	180	52	174	50	179	13	15	57	180
Menzies et al., 2004	JJG 5047-33	59	183	44	173	56	176	64	193	20	19	58	181
Creighton et al., 2010	MX5009	58	182	61	184	51	173	58	186	10	14	59	181
Menzies et al., 2004	JJG 5051-29	66	194	49	175	45	170	63	191	21	24	60	182
Aulbach et al., 2004	vr09359	45	176	65	191	66	197	41	172	25	25	61	184
Aulbach et al., 2004	vr40304	55	181	60	182	63	186	61	188	8	7	62	184
Creighton et al., 2010	MX5000	64	191	63	186	55	175	59	188	9	15	63	185
Creighton et al., 2010	MX165	57	181	64	191	64	187	53	183	11	9	64	185
Creighton et al., 2010	MX5008	60	183	62	186	62	183	65	204	5	21	65	189
Creighton et al., 2010	MX104	65	193	66	193	65	189	66	206	1	17	66	195

Figure 3.3

Depths obtained using Ni-in-garnet thermometers of Ryan et al., (1996; blue diamonds) and Canil (1999; red and green triangles and diamonds), projected to the central Slave geotherm calculated using the methods outlined by Mather et al., (2011; Chapter 2). Shown for comparison are depth estimates from averaged available multiphase P-T estimates with calculated errors (white diamonds, black error bars).

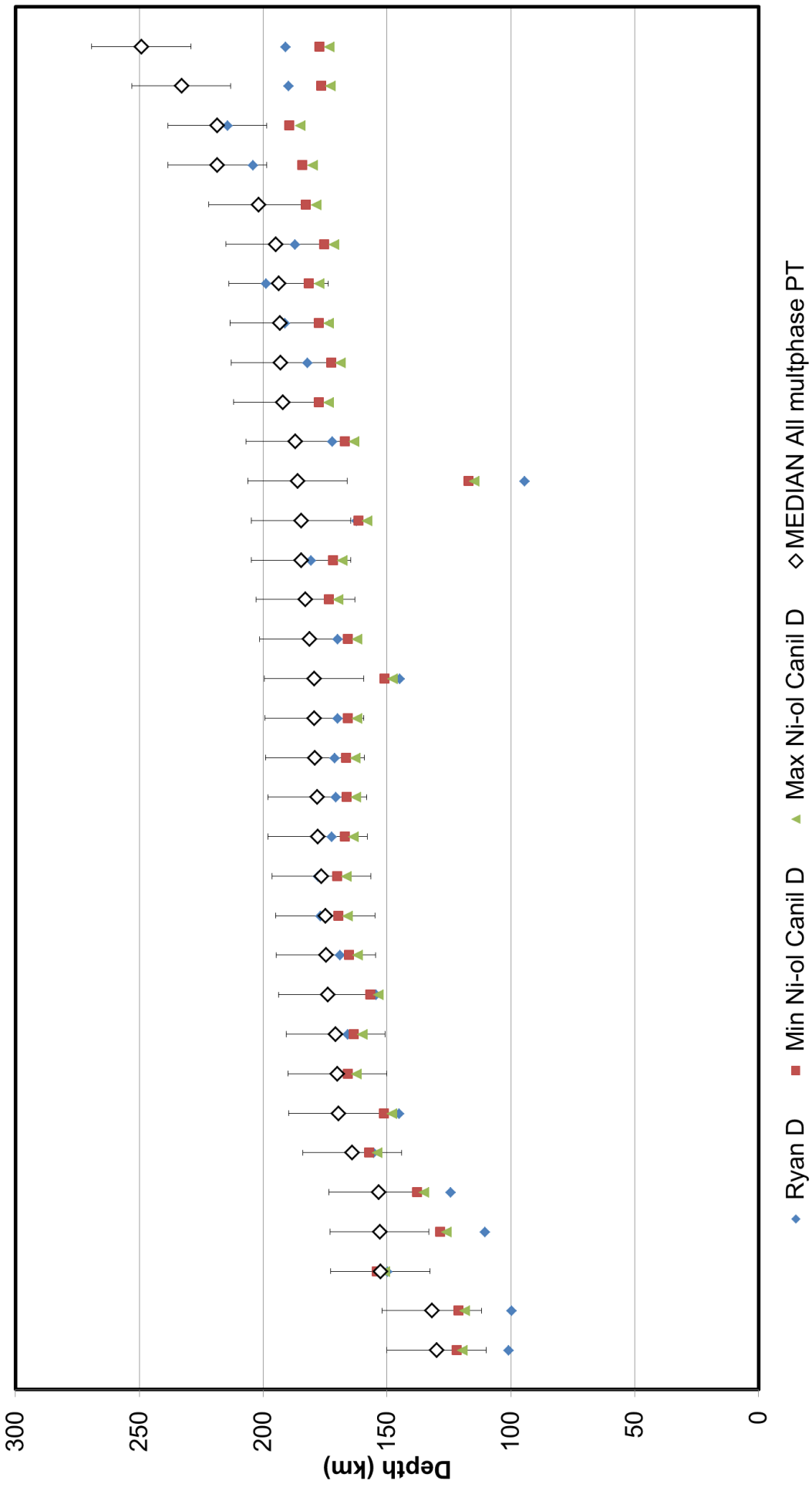
300
250
200
150
100
50
0
Depth (km)
Ryan D
Min Ni-ol Canil D
Max Ni-ol Canil D
MEDIAN All multphase PT

4 THE NORTHERN SLAVE LITHOSPHERE

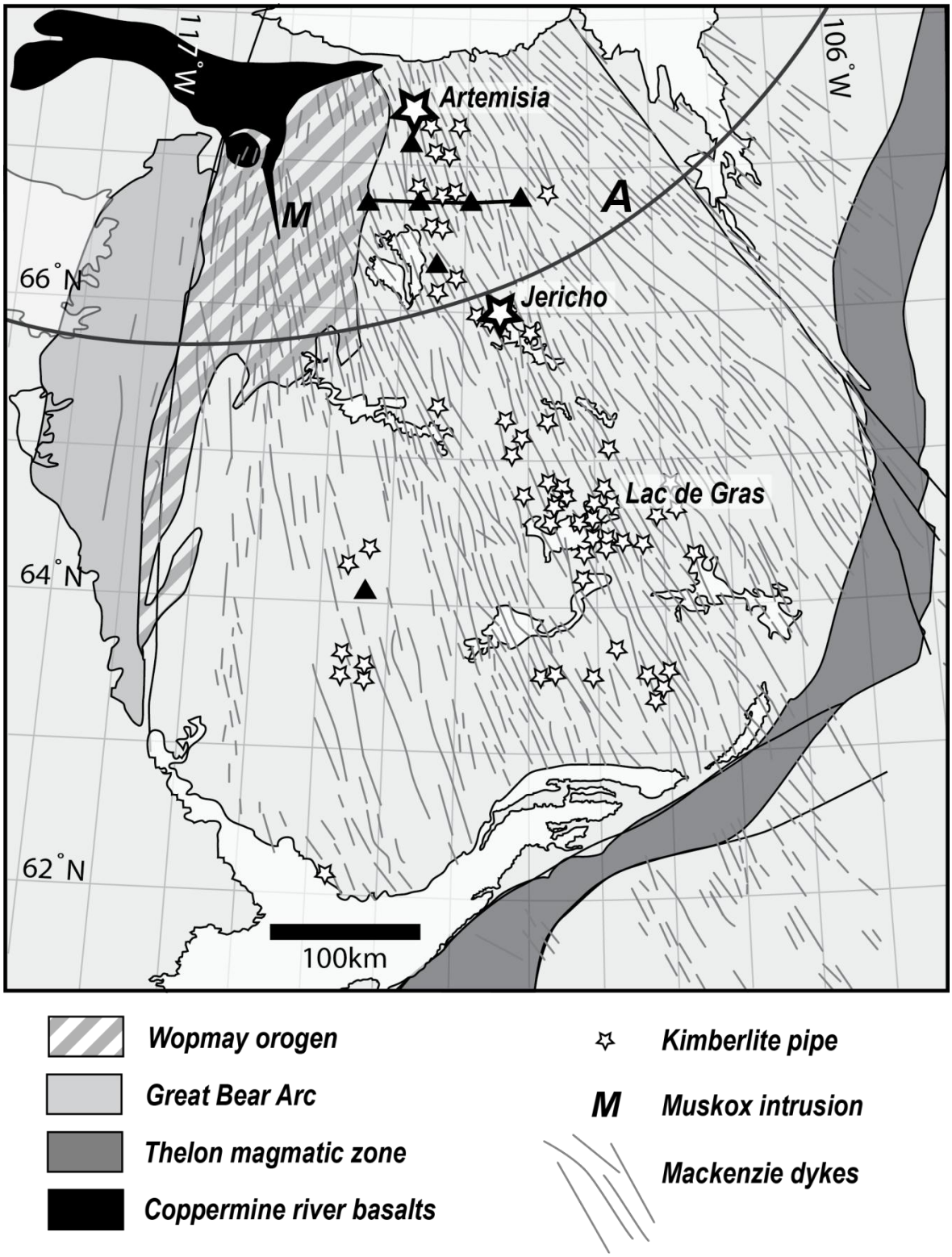

Figure 4.1:

Map of the Slave craton (after Bleeker, 2002), showing locations of the Artemisia, Jericho and Lac de Gras kimberlite regions, the pervasive Mackenzie dyke swarm and Muskox intrusion (after LeCheminant and Heaman, 1989).

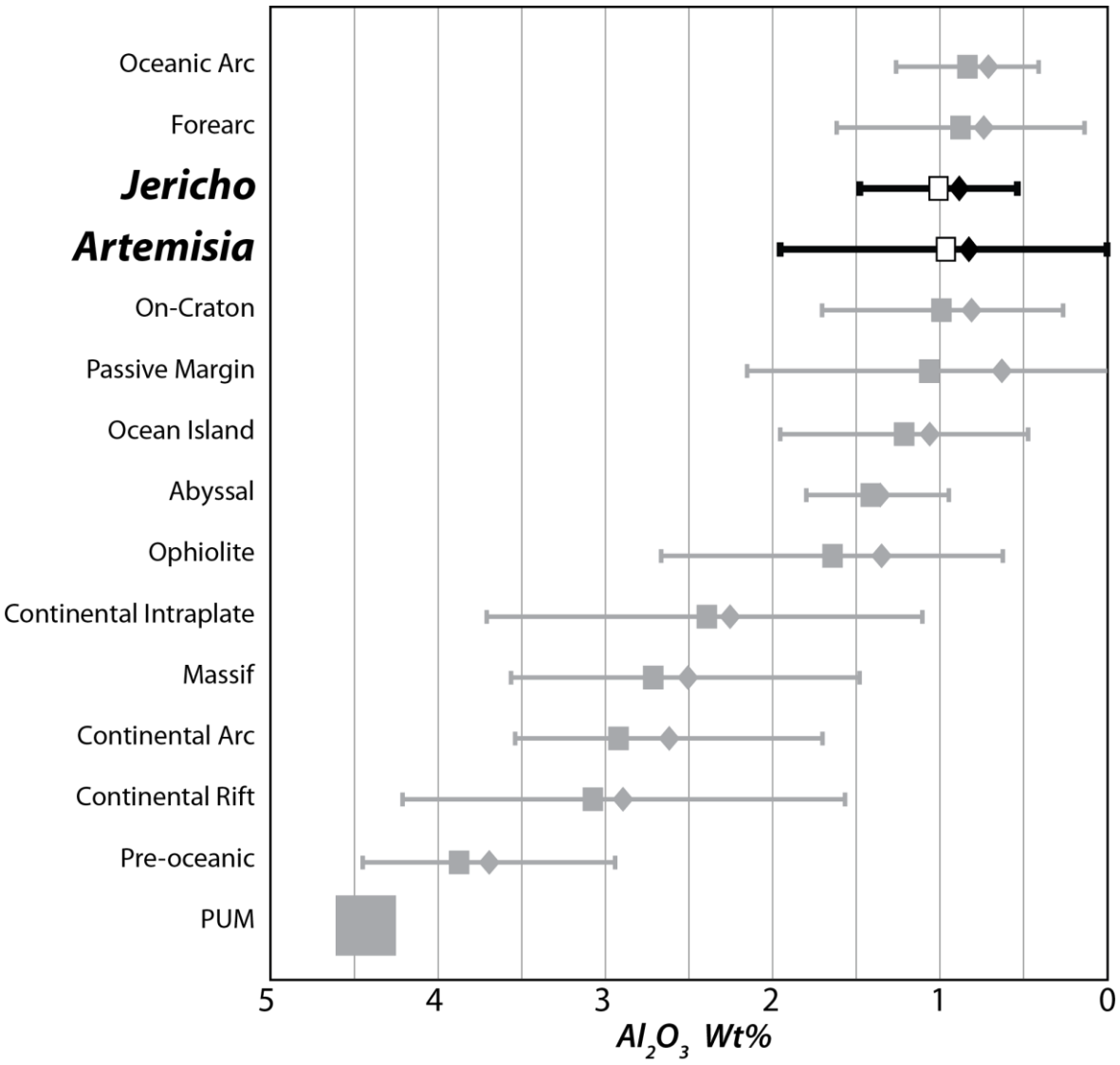

Figure 4.2:

Mean (open square), Median (filled diamond) and 1 standard deviation ranges for bulk Al_2O_3 values for Jericho (Kopylova et al., 2000) and Artemisia peridotite xenoliths, displayed with average values for other tectonic settings (after Pearson and Wittig, 2008). Note the larger standard deviation range for the Artemisia peridotites, possibly reflecting their increased post-eruption alteration.

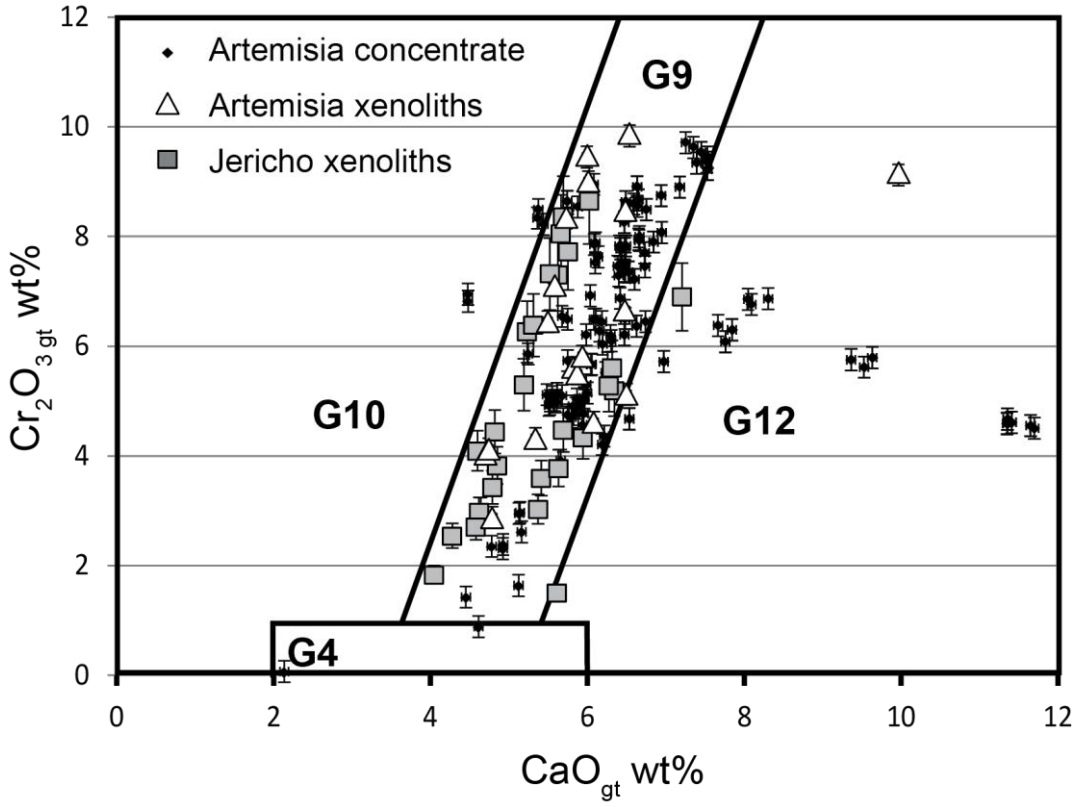

Figure 4.3:

CaO - Cr_2O_3 plot showing compositions of Artemisia xenolith and concentrate garnet, and Jericho xenolith garnet (Kopylova et al., 1999). Note the absence of 'G10' (Dawson & Stephens, 1975; Gurney 1984; Grütter, 2004), low Ca, high-Cr garnet in both the Jericho and Artemisia sample set.

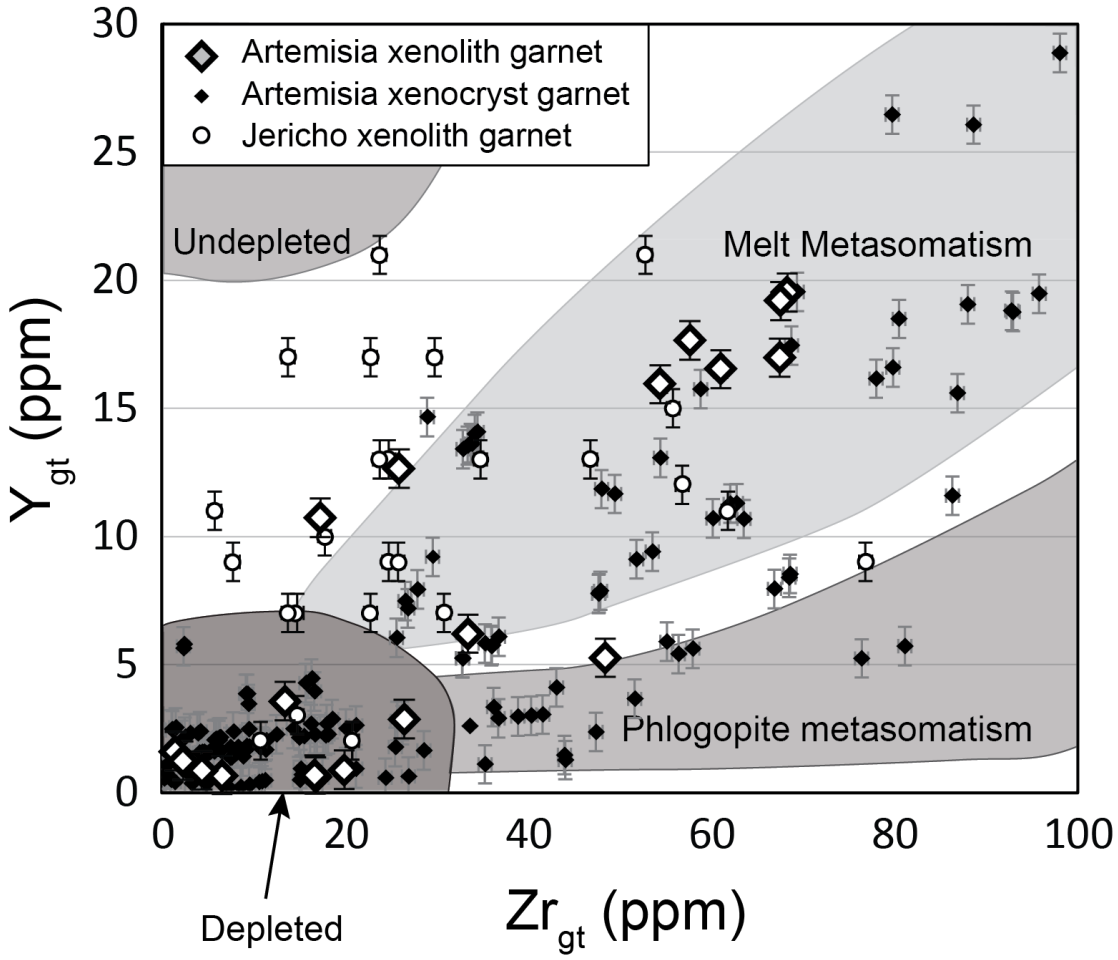

Figure 4.4:

Y-Zr concentrations of garnets from Artemisia xenoliths (large diamonds) and xenocrysts (small black diamonds), and Jericho xenoliths (Kopylova et al., 1999; circles). Errors shown are 2 standard deviations for Artemisia data and published errors for Jericho data. Also shown are the compositional regions of Griffin et al. (1999b).

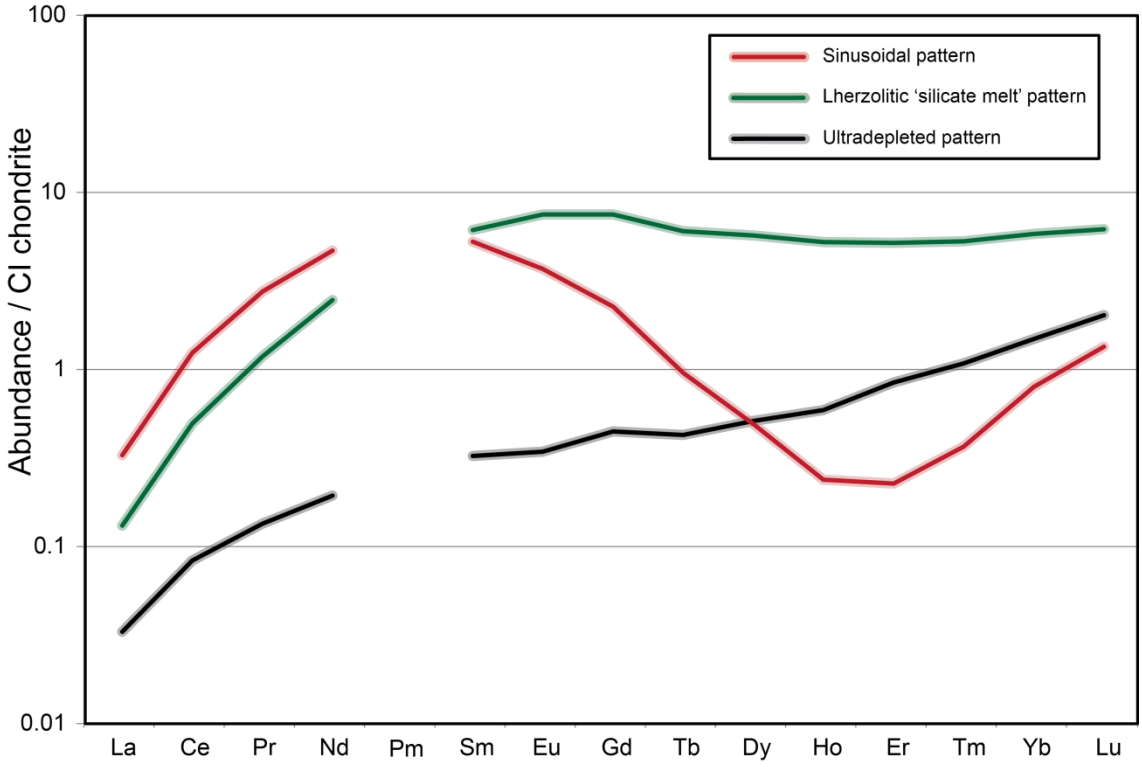

Figure 4.5:

Representative garnet rare-earth element profiles for xenoliths and xenocrysts from the Artemisia kimberlite (n = 161). 'Sinusoidal' patterns (Burgess and Harte, 1994; Stachel et al., 2004) are defined as having $[Gd_n/Dy_n]_{gt} \geq 1.2$, 'Melt-equilibrated' or 'lherzolitic' (Stachel et al., 2004) pattern types are defined by $[Gd_n/Dy_n]_{gt} < 1.2$, $Dy_n > 2$ and ($Dy_n < Tb_n$). 'Depleted' pattern types are defined by $[Gd_n/Dy_n]_{gt} < 1.2$, $Dy_n < 2$ and ($Dy_n > Tb_n$).

Figure 4.6

Distribution of T_{RD} ages for peridotite xenoliths from the Artemisia (top) and Jericho (middle) kimberlites. Also shown is the age of the Mackenzie dyke swarm (1.26 Ga; LeCheminant and Heaman, 1989) and the range in T_{RD} ages that could be ascribed to this event (hatched region) assuming an average error in T_{RD} estimation of 0.2 Ga (Pearson et al., 2004).

Bottom: Gaussian mixture modelling of T_{RD} ages calculated from published whole-rock, single sulphide and diamond inclusion $^{187/188}Os$ data for the Central slave (Diavik and Ekati; Aulbach et al., 2004, Aulbach et al., 2009, Westerlund et al., 2006). Again, approximately 10% of the dataset can be explained by a peak at 1.17 Ga, which is within error of the 1.26 Ga Mackenzie event.

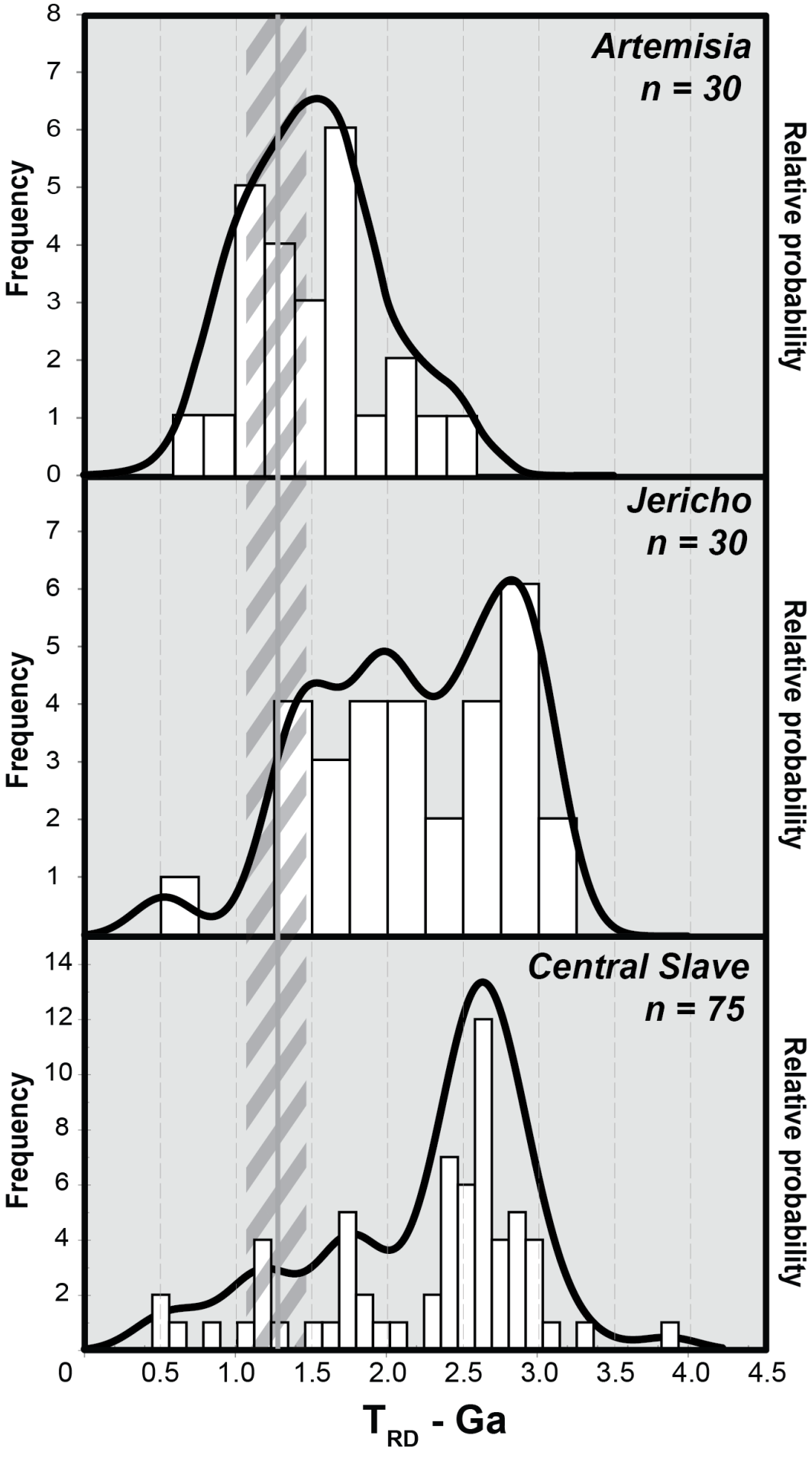
Artemisia
n = 30
Jericho
n = 30
Central Slave
n = 75
Frequency
Relative probability
T_{RD} - Ga

Figure 4.7:

Nickel-in-garnet temperatures for the Artemisia xenoliths projected to the xenolith palaeogeotherm for Jericho, calculated using the methods outlined in Mather et al., (2011) and data from Kopylova et al., (1998) using the Taylor (1998) geothermometer and the Nickel and Green (1985) barometer. Xenoliths are shown as black bars indicating the error in the Nickel-in-garnet T estimate, inset shows how these T errors have been projected onto the palaeogeotherm. Also shown are three estimates of lithosphere thickness in the Artemisia region from seismic methods, for comparison.

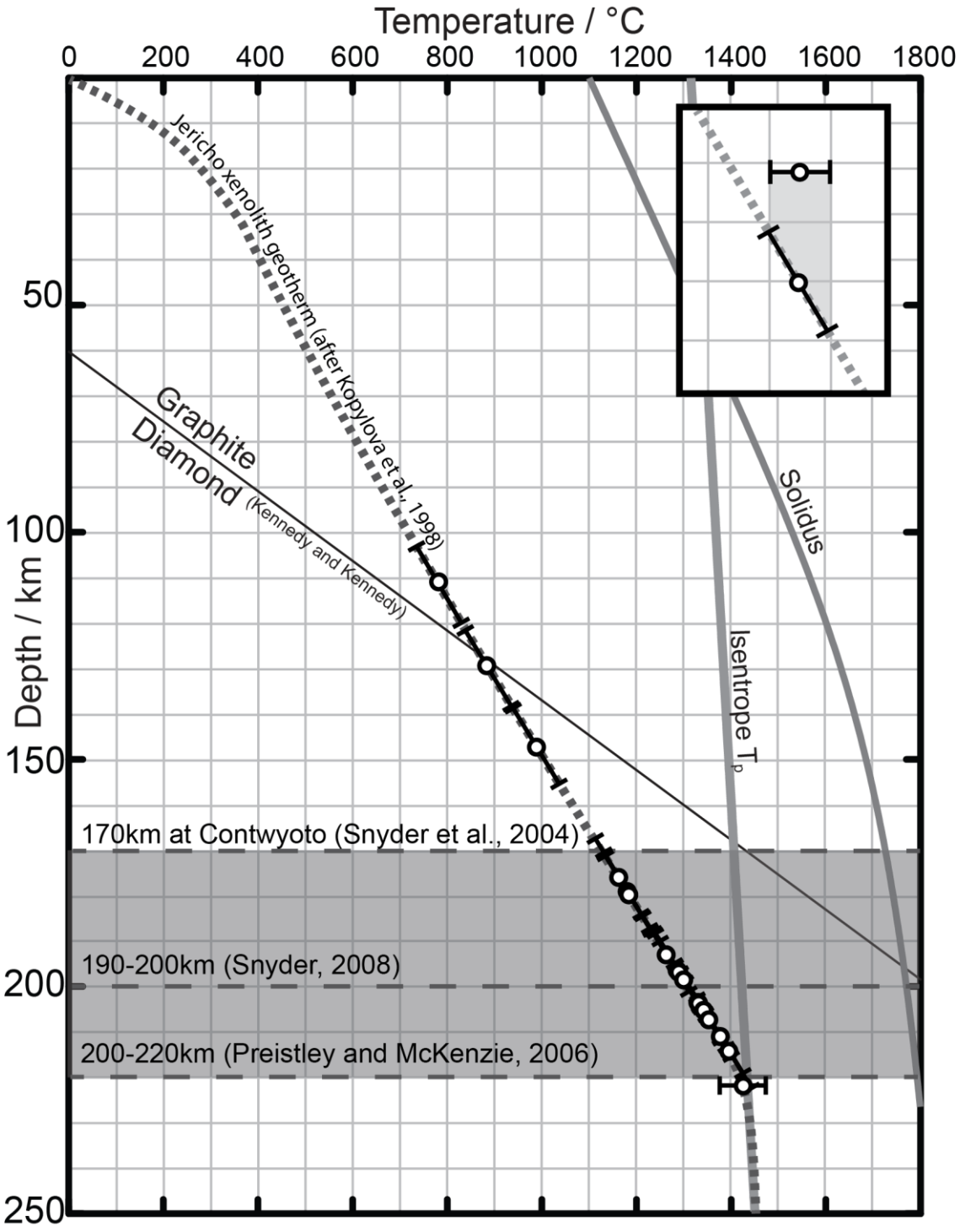
Temperature / °C
0
200
400
600
800
1000
1200
1400
1600
1800
Depth / km
50
100
150
200
250
Jericho xenolith geotherm (after Kopylova et al., 1998)
Graphite
Diamond (Kennedy and Kennedy)
Solidus
Isentrope T_p
170km at Contwyoto (Snyder et al., 2004)
190-200km (Snyder, 2008)
200-220km (Preistley and McKenzie, 2006)

Figure 4.8:

Ni-in-gt (Ryan et al., 1996) temperatures projected to a Jericho geotherm (see Figure 4.7) and resulting depths plotted against:

A

Y-Zr concentration, grouped by degree of alteration (after Griffin et al., 1999b)

B

REE pattern type (see 4.3.3).

C

T_{RD}, calculating using O-Chondrite and assuming Re/Os = 0 at formation and correcting for Re added at time of formation. Error bars are 200 Ma (T_{RD}) and depth error ± 20 km (see: 3.3.3).

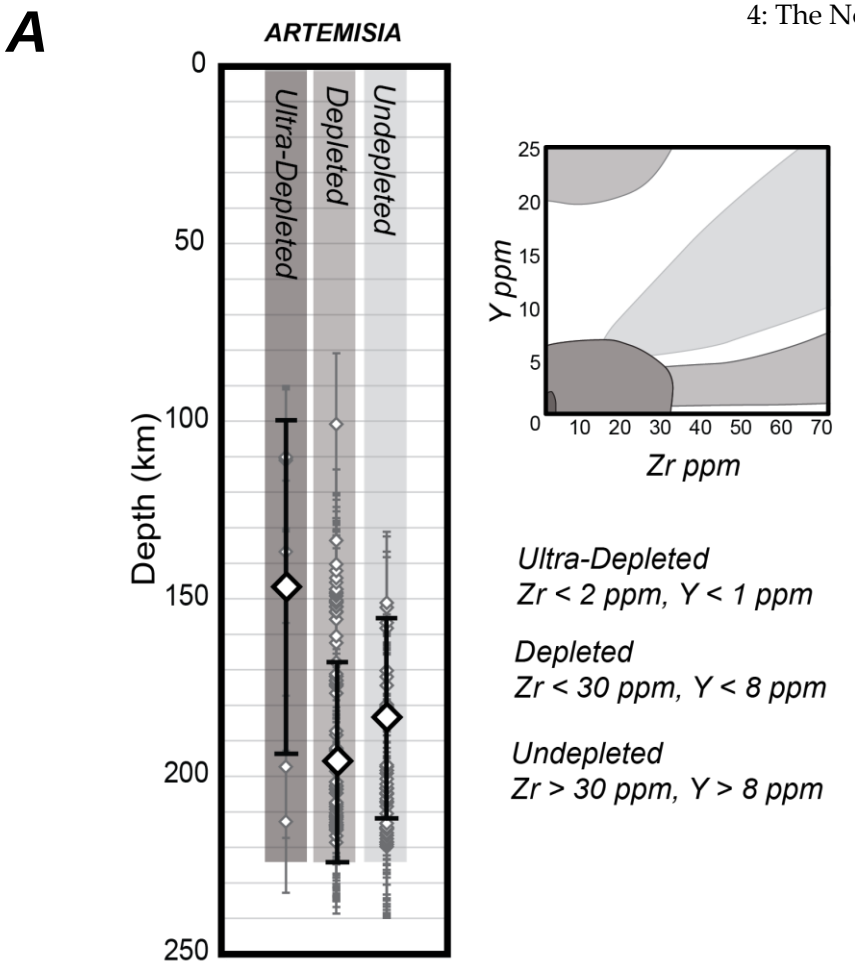
A
ARTEMISIA
Ultra-Depleted
Depleted
Undepleted
Depth (km)
0
50
100
150
200
250
Y ppm
Zr ppm
0
5
10
15
20
25
10
20
30
40
50
60
70
Ultra-Depleted
Zr < 2 ppm, Y < 1 ppm
Depleted
Zr < 30 ppm, Y < 8 ppm
Undepleted
Zr > 30 ppm, Y > 8 ppm

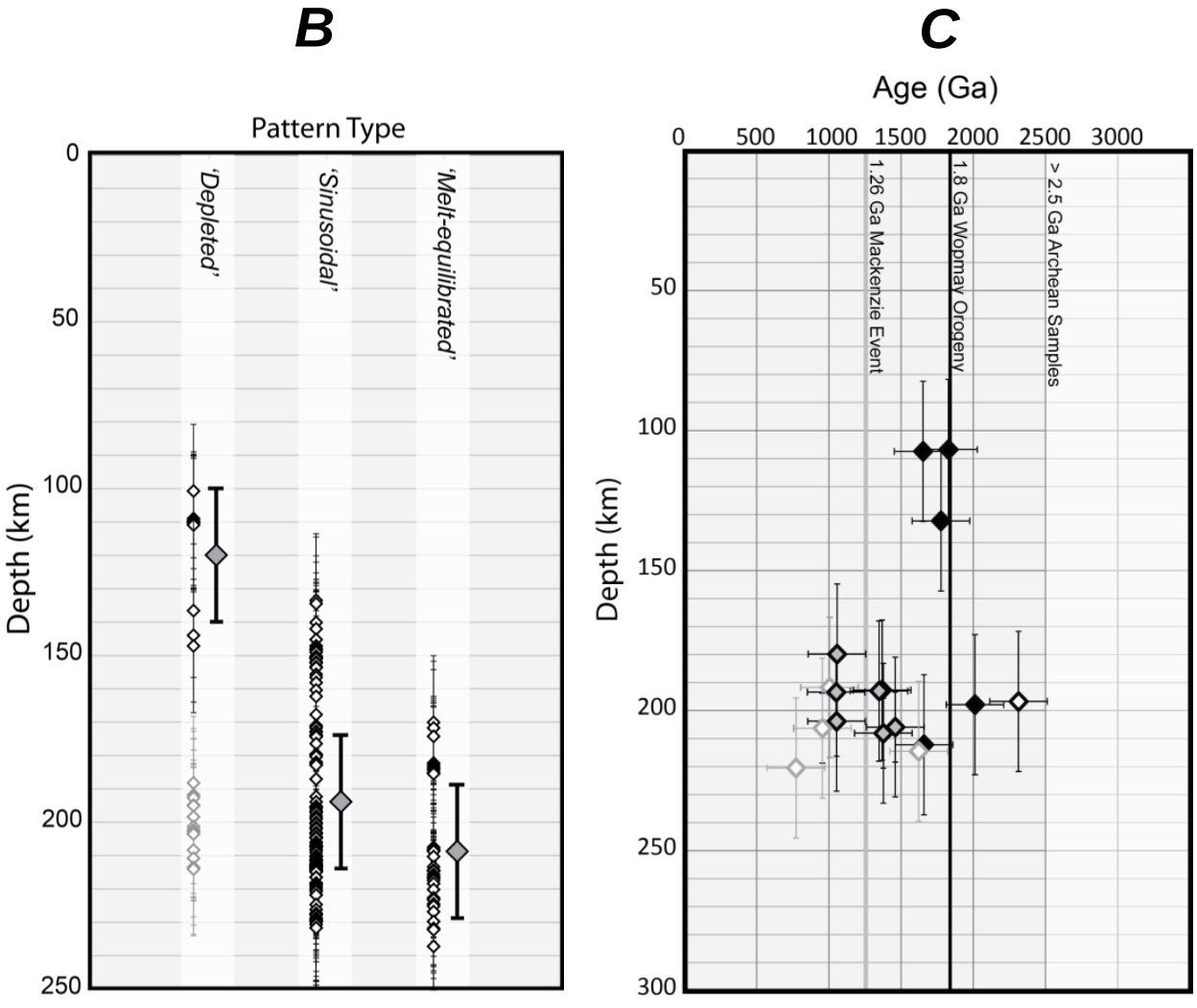
B
Pattern Type
'Depleted'
'Sinusoidal'
'Melt-equilibrated'
Depth (km)
0
50
100
150
200
250
C
Age (Ga)
0
500
1000
1500
2000
2500
3000
1.26 Ga Mackenzie Event
1.8 Ga Wopmay Orogeny
> 2.5 Ga Archean Samples
Depth (km)
50
100
150
200
250
300

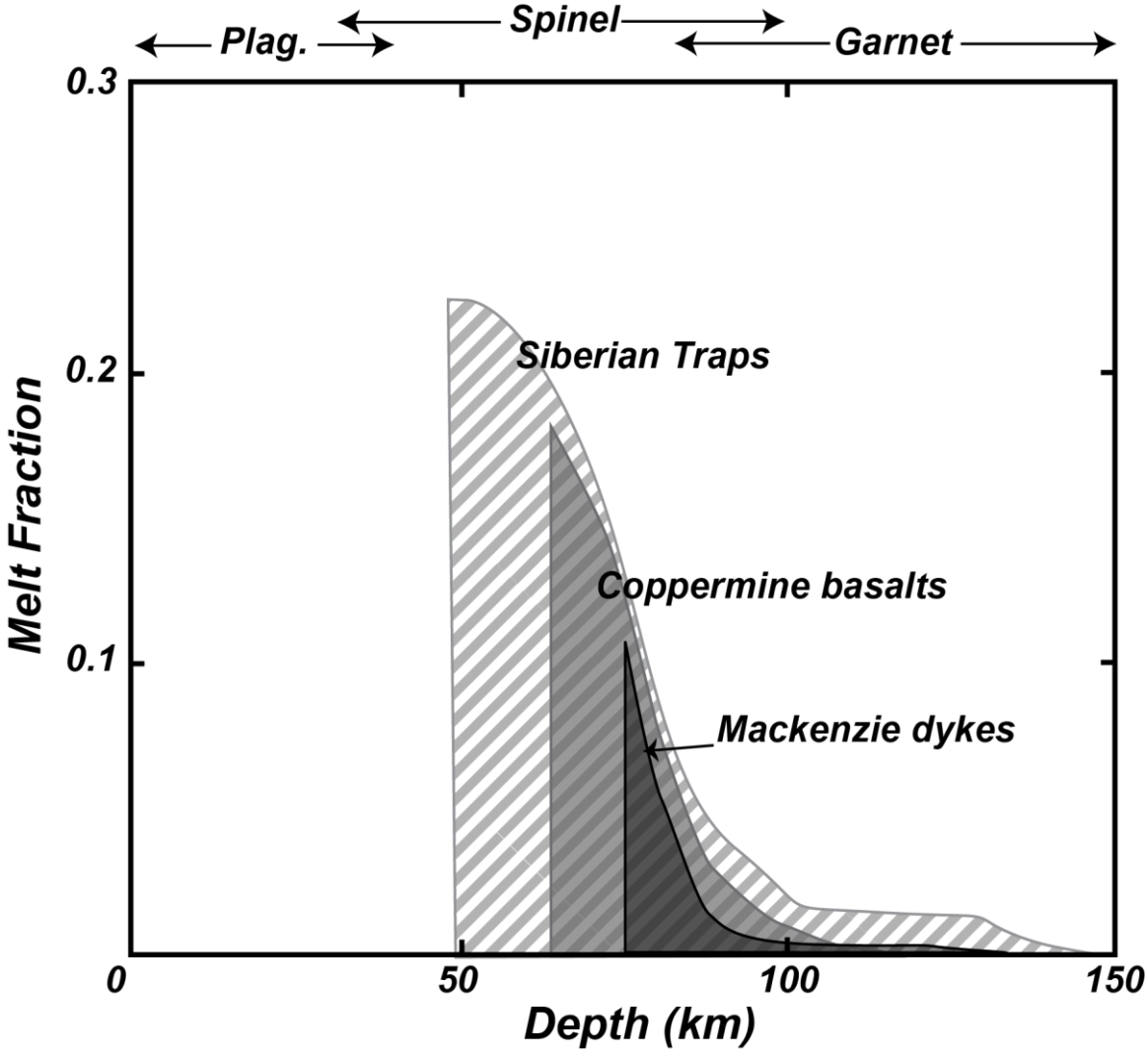

Figure 4.9:

Melt fraction with depth curve from rare-earth element inversion of the Coppermine River flood basalts and the Mackenzie dyke swarm, after White and McKenzie (1995). Also shown for comparison is the same curve calculated for the Siberian Traps. These curves suggest that melting in the Mackenzie event occurred between 100 and 60 km, consistent with the hypothesis that the lithosphere was thinned prior to impingement of the Mackenzie plume.

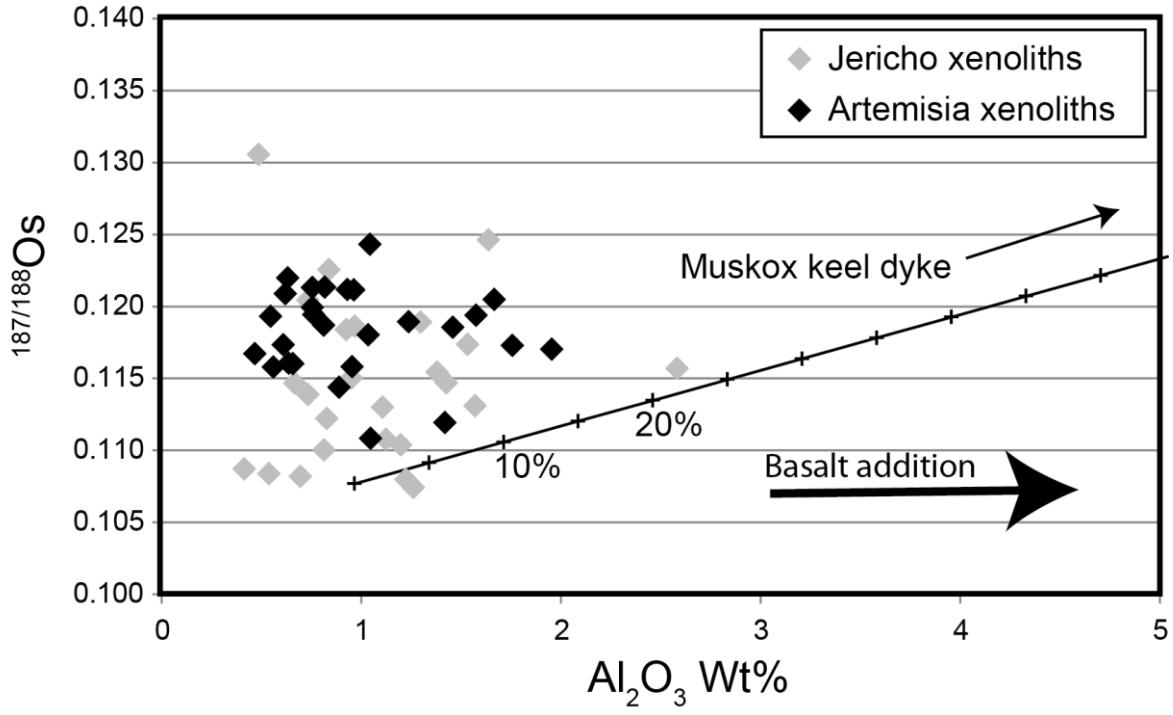

Figure 4.10:

Al_2O_3 vs. $^{187/188}Os$ of the Artemisia (black diamonds) and Jericho (grey diamonds) xenoliths (Jericho Al_2O_3 values from Kopylova and Russell (2000)). Thick black arrow indicates the compositional variation expected from melt-rock reaction as suggested by Rudnick and Walker (2009). Thin black line shows mixing between the most primitive composition of the Mackenzie igneous system (the Keel dyke of the Muskox intrusion, Day et al., (2008)) and average ancient peridotite.

Figure 4.11:

Mixture modelling the addition of a 2.9 Ga depleted peridotite ($^{187/188}$Os = 0.10700, Os ppb 0.5 – 3.5 ppb) with two different sulphide compositions, in order to assess the likelihood of sulphide addition as a mechanism to explain the unusual T_{RD} distribution seen in the Artemisia xenoliths. The osmium and rhenium concentrations of both sulphides were set at the average values seen in peridotitic xenolith sulphides (Os = 10 ppm; Griffin et al., 2004, Re = 0.45 ppm; Westerlund et al., 2006). The high concentrations of rhenium in the sulphides relative to the whole rock required additional forward modelling of ^{187}Os growth from the decay of ^{187}Re between contamination at 1.26 Ga and today. Also shown are the measured compositions of the Artemisia xenoliths (white diamonds) and those that could be construed as showing a 1.26 Ga 'Mackenzie' signature (black diamonds), accounting for the accepted 0.2 Ga error in estimating T_{RD} (Pearson et al,. 2002; also illustrated as horizontal error bars on xenolith data points). Addition of sulphide A (***top***), with a convecting mantle signature at 1.2 Ga can peturb the ancient T_{RD} age without dramatically altering the bulk rock Os content, assuming that the original ancient material had a range in Os concentrations, as evidenced by the >2.5 Ga samples from Jericho. Addition of a suprachondritic sulphide at 1.26 Ga (***bottom***) can explain some of the T_{RD} age distribution, except those with high Os (highlighted in grey).

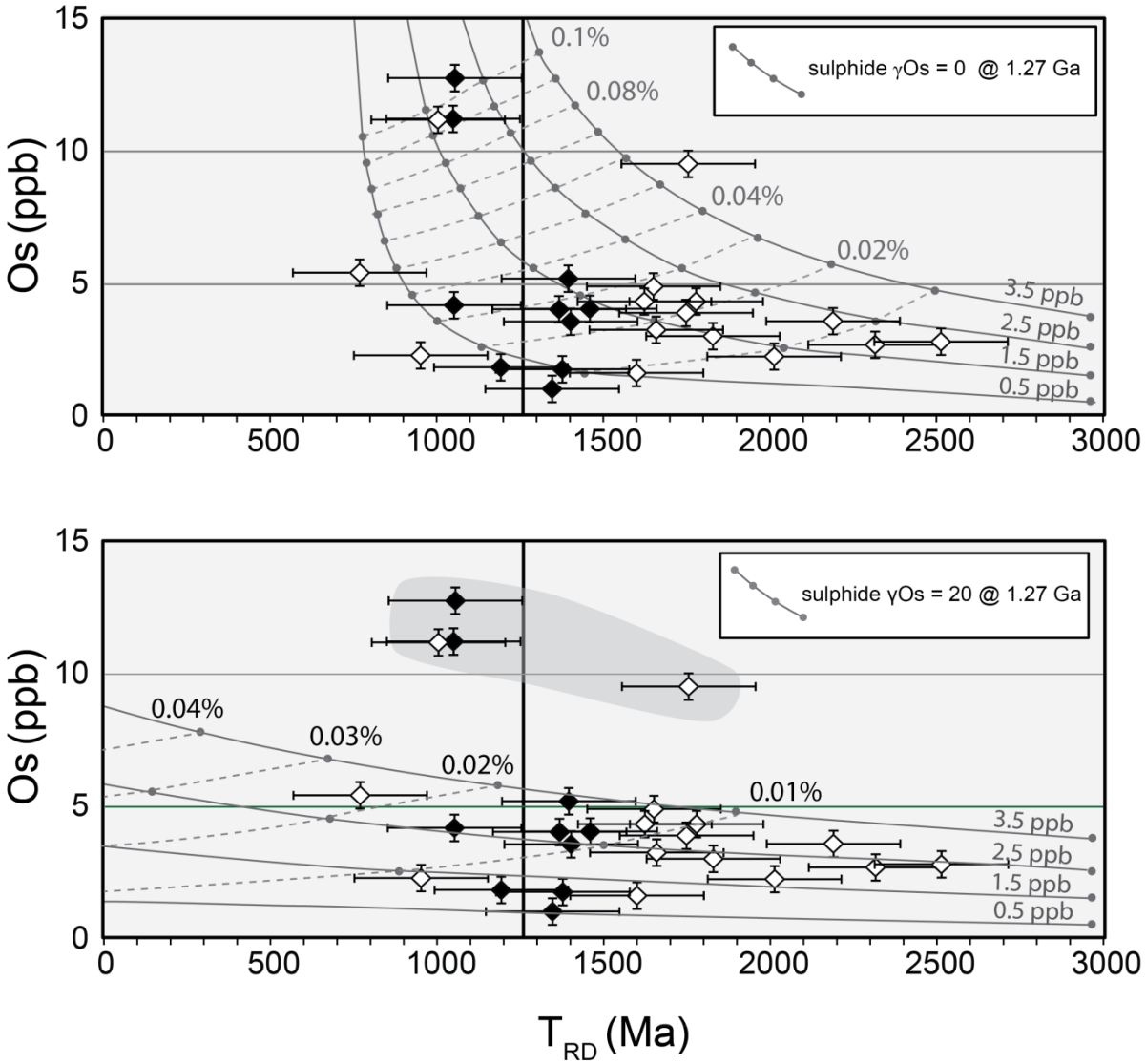
sulphide γOs = 0 @ 1.27 Ga
0.1%
0.08%
0.04%
0.02%
3.5 ppb
2.5 ppb
1.5 ppb
0.5 ppb
Os (ppb)
sulphide γOs = 20 @ 1.27 Ga
0.04%
0.03%
0.02%
0.01%
3.5 ppb
2.5 ppb
1.5 ppb
0.5 ppb
Os (ppb)
T RD (Ma)

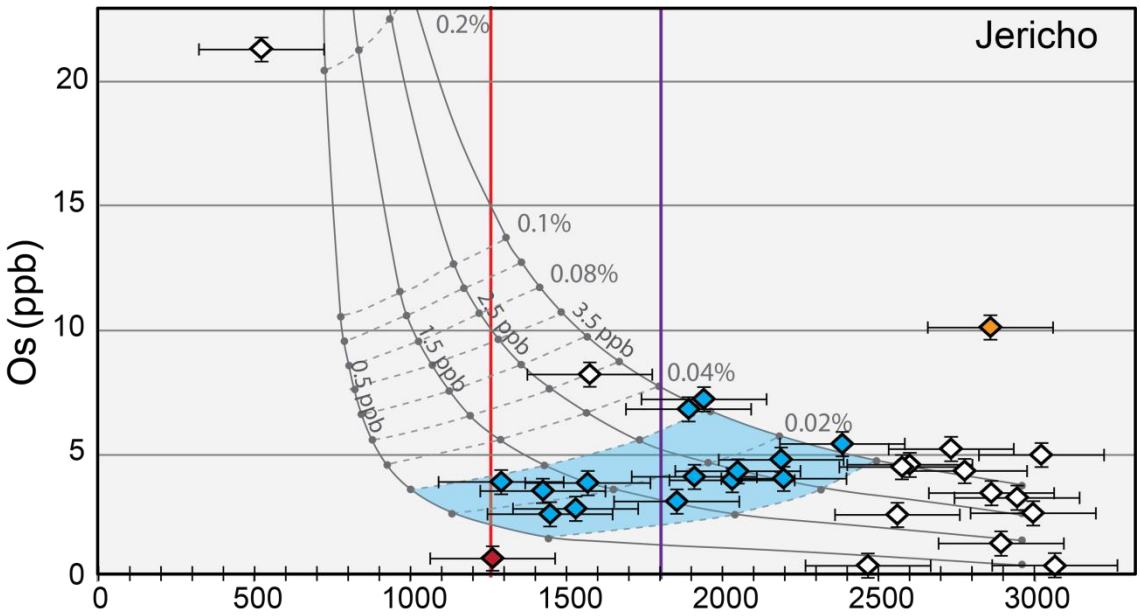

Figure 4.12:

Modelled mixing of a $\gamma Os_{1270} = 0$ sulphide with depleted, Archean cratonic lithosphere, methods as outlined in Figure 4.11. Data shown are Jericho peridotite xenoliths (Irvine, 2002). The blue data points can be adequately modelled by addition of 0.01 – 0.04 wt% sulphide, but the fit is considerably more poor than at Artemisia, since one of the oldest samples (shown in orange) has the highest Os concentration, and one of the youngest (shown in red) has the lowest.

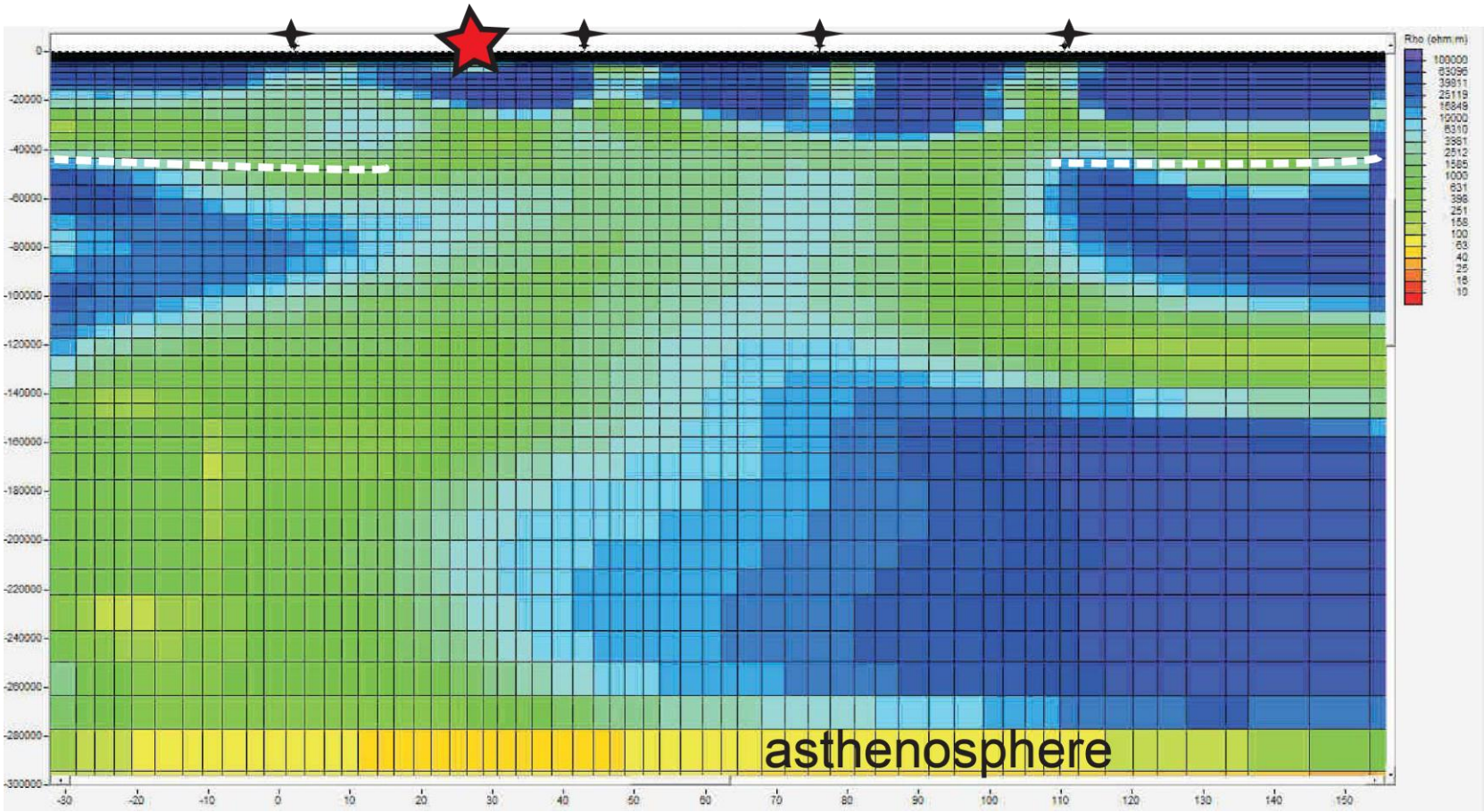

Figure 4.13:

Magnetotelluric profile along the line indicated by the the four joined triangles on Figure 4.1. The projected location of the Artemisia kimberlite isapproximately as indicated by the red star.

Figure 4.14:

Visual explanation of the two alternate mechanisms postulated to be responsible for the unusual Proterozoic peak in the T_{RD} distribution at Artemisia.

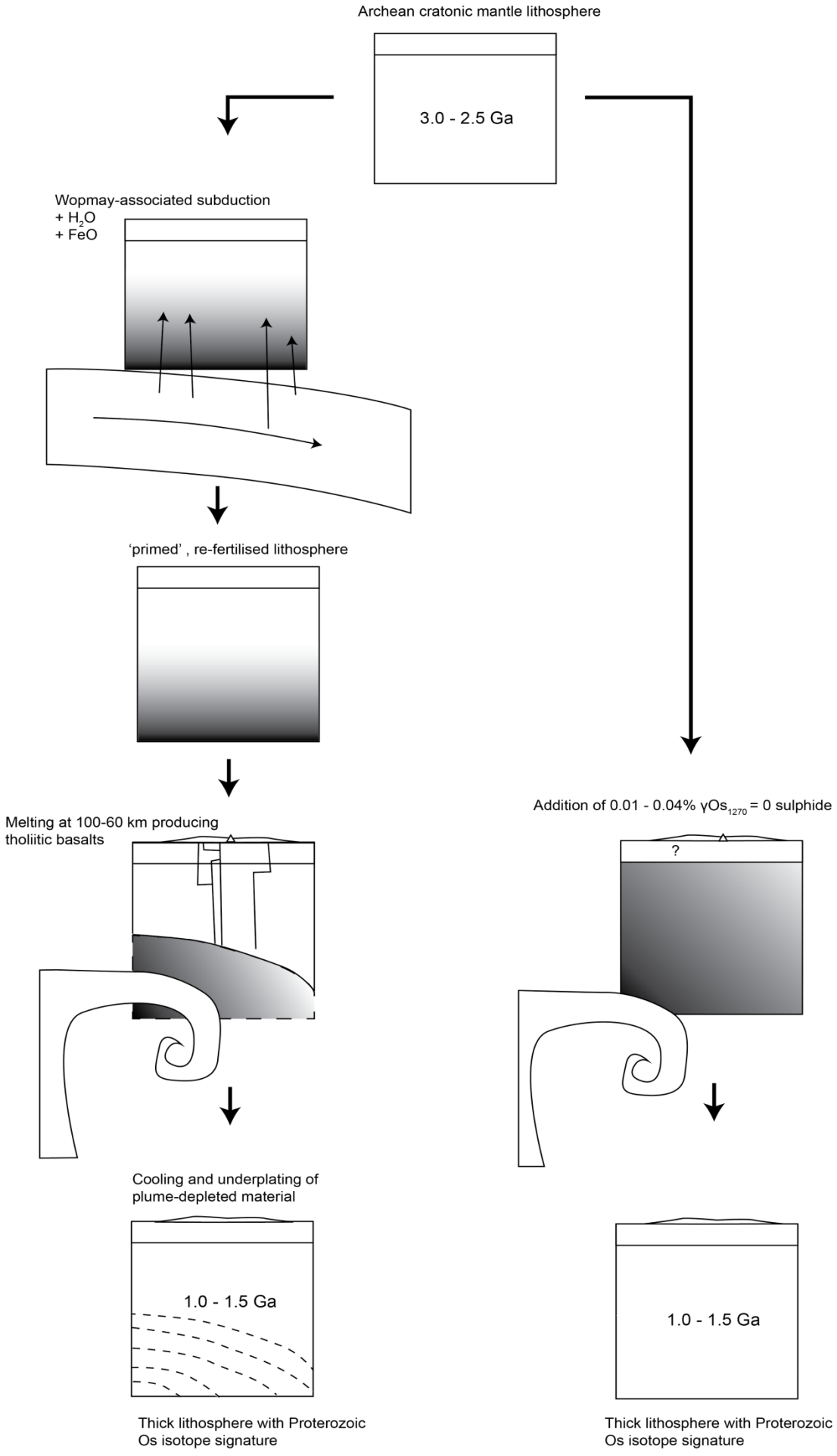
Archean cratonic mantle lithosphere
3.0 - 2.5 Ga
Wopmay-associated subduction
+ H_2O
+ FeO
'primed' , re-fertilised lithosphere
Melting at 100-60 km producing
tholiitic basalts
Addition of 0.01 - 0.04% γOs_{1270} = 0 sulphide
?
Cooling and underplating of
plume-depleted material
1.0 - 1.5 Ga
1.0 - 1.5 Ga
Thick lithosphere with Proterozoic
Os isotope signature
Thick lithosphere with Proterozoic
Os isotope signature

4 THE AGE OF THE ULTRA-DEPLETED LAYER OF THE CENTRAL SLAVE CRATON

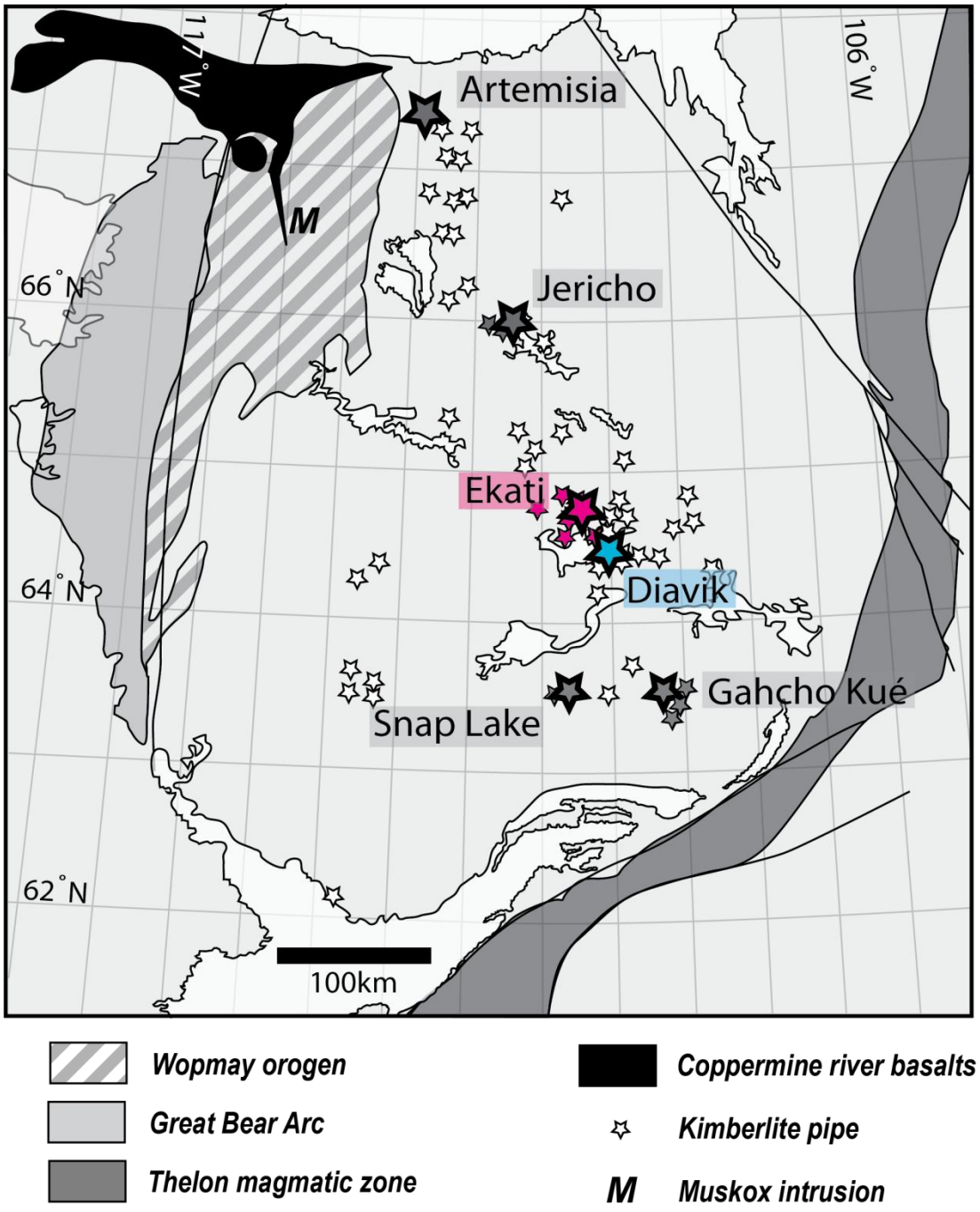

Figure 5.1:

A Map of the Slave Craton kimberlite localities. This study concentrates on samples from the Central Slave kimberlites, Ekati (pink) and Diavik (blue).

Table 5.1:

Estimated mineral modes and garnet morphologies for Diavik xenoliths in this study. Some samples could not be accurately estimated because they were too fragmentary for creation of a thin section.

Sample	Type	Cpx (%)	Gt (%)	Notes (Garnet Morphology)	Other	Texture
MX5056	Harz	<5	10-15	heterogeneous		porphyroclastic rexallised
MX5009	Harz	>5	20	homogenous		porphyroclastic rexallised
MX5022	Lherz	>>5	10-15	homogenous, equant texture same size as other minerals		coarse equant
MX5023	Harz	<<5	10	heterogeneous, large round garnet crystals, larger than other minerals		coarse equant
MX5026	Harz	<<5	10	heterogeneous, large round garnet crystals, larger than other minerals		coarse equant w/ small zones ppcl
MX5044	Harz	<<5	<10	heterogeneous, 'starry' garnets - anhedral	+sp	Coarse equant
MX5054	Harz	<<5	<5	Very little garnet	+sp	Coarse equant
MX5057	Lherz	>5	20	Homogenous.	Oliv rexlls^{n}	Porphyroclastic fluidal
MX5059	Harz	<5	<5		+ sp?	Coarse equant
MX5060	Lherz	>=5	10	Heterogenous, massive circular garnet much larger than other minerals		Porphyroclastic rexallised
MX5062	Lherz	?5	<5		+sp	Coarse equant
DDM_149	Lherz	>>5	25	Transitional – same as other minerals – circular & large		Coarse equant
DDM_327	Lherz	>>5	20	Massive round garnet		Porphyroclastic rexallised
DDM_335	Lherz	>5	20	Homogenous, equant texture same as other minerals		Porphyroclastic rexallised
DDM_359	Lherz	>5	10	Transitional – same as other minerals – circular & large		Coarse Equant
DDM_360	Lherz	?	15-20	Transitional – same as other minerals – circular & large		Coarse equant
DDM_361	Lherz	>5	15	Homogenous, equant texture same as other minerals		Porphyroclastic rexallised
DDM_366	Lherz	>5	10	Cpx & gt concentrated in 'vein'		Porphyroclastic fluidal
DDM_367	Lherz	~5	10	Cpx & gt concentrated in 'vein'		Coarse equant
DDM_368	Lherz	>5	10	homogenous		Coarse equant
DDM_457	Lherz	>5	15	homogenous		Porphyroclastic rexallised
DDM_384	Lherz	~5	15	Homogenous – no primary silicate remaining		Coarse equant
MX160	Harz	<5	n/a	heterogeneous, 'starry' garnets - anhedral	+sp	n/a
MX158	Lherz	n/a	n/a			n/a
DDM_431	Harz	n/a	n/a			
DDM_131	n/a	n/a	n/a			

Figure 5.2:

Examples of garnet morphology in central Slave coarse xenoliths, All images are the same scale, field of view approximately 2cm across.

A – Garnets a similar size and shape to surrounding silicates

B – Garnets similar sized or larger than surrounding silicates and highly rounded

C – Garnets of a similar size to surrounding silicates but with 'starry', resorbed-type edges.

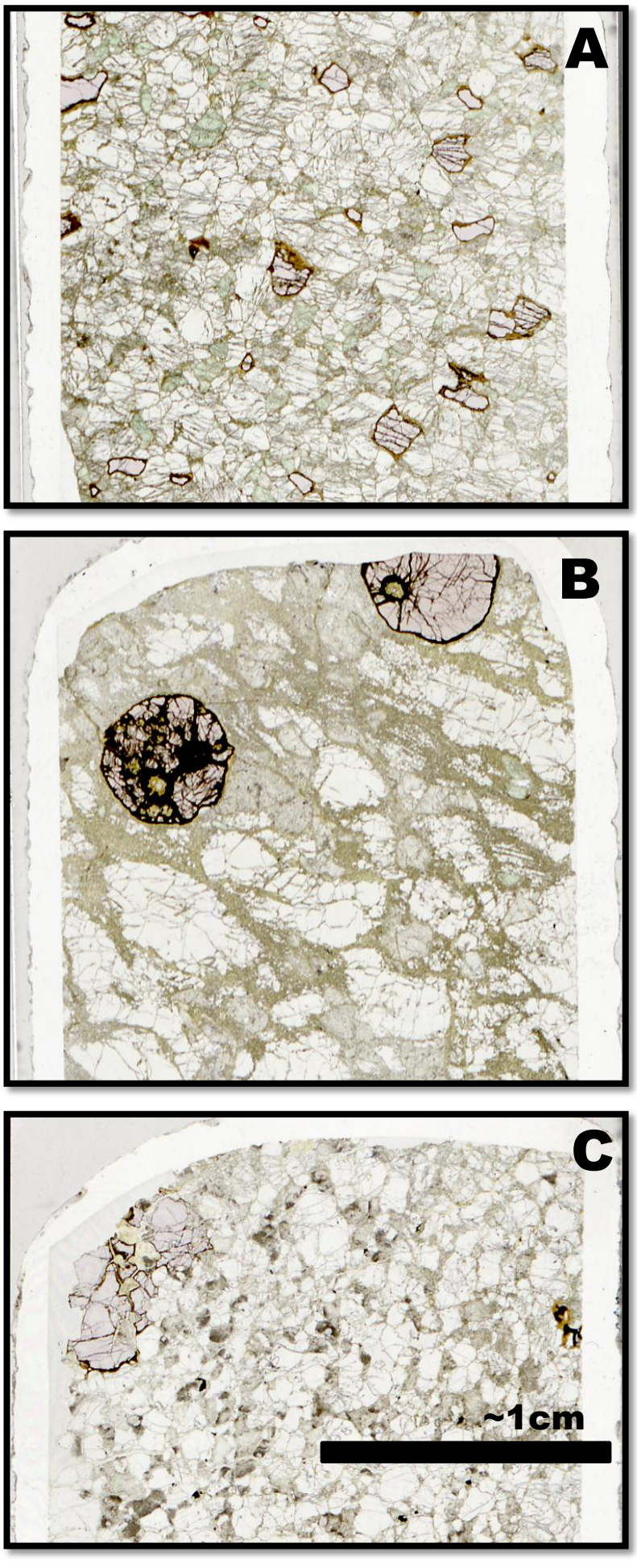
A
B
C
~1cm

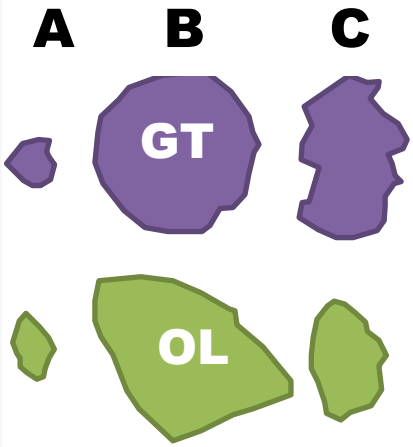
A
B
C
GT
OL

Figure 5.3:

'Vein-like', heterogenous distribution of Garnet and Clinopyroxene.

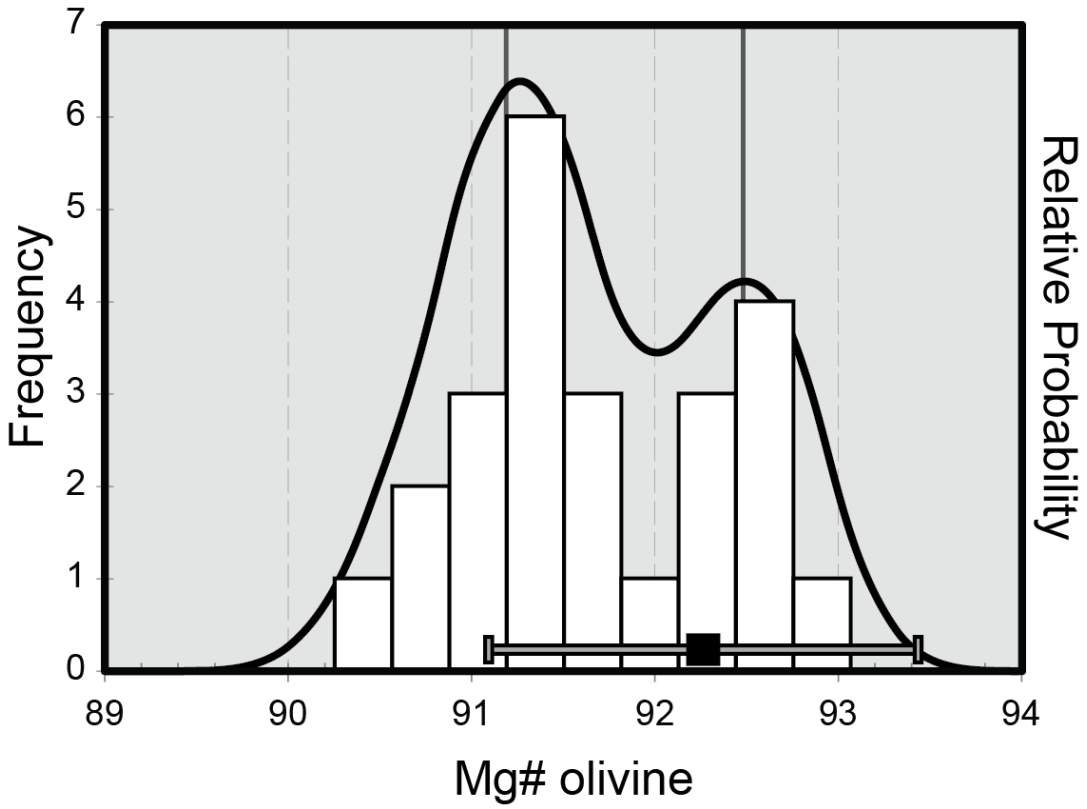

Figure 5.4:

Histogram and relative probability density plot of Mg# (Mg/(Mg+Fe)) in Diavik macroxenoliths. Error in Mg# for Gaussian mixture modelling was fixed for all samples at 0.2. Two peaks are suggested by the data; one at 91.15 and another at 92.48.

Grey range indicates 'average' cratonic mantle olivine Mg# after Pearson and Wittig, (2008).

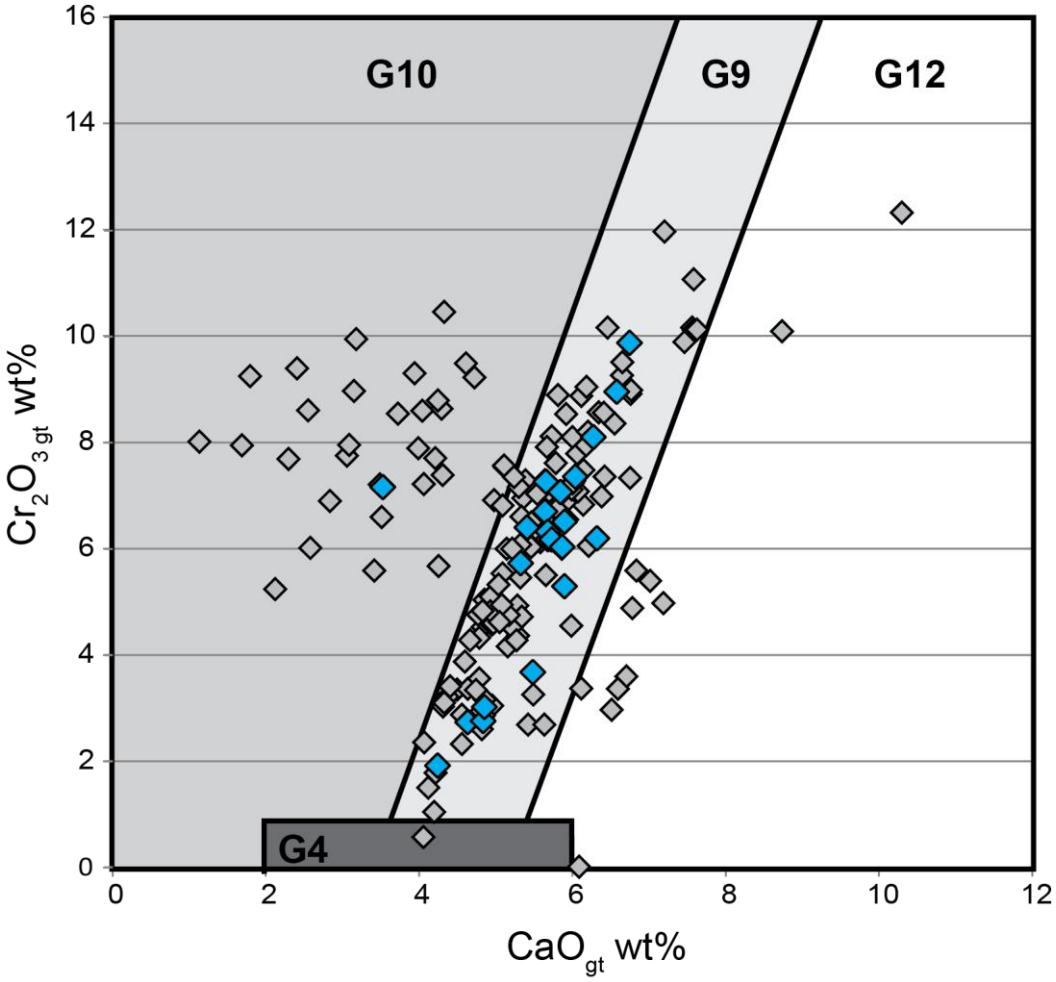

Figure 5.5:

CaO-Cr_2O_3 plot for Diavik macroxenoliths from this study. Fields are as outlined by Grutter (2004) after Sobolev et al., (1973). This study (blue diamonds) shows only one 'G10' composition garnet, in contrast to previously published data from microxenoliths and diamond inclusions (grey diamonds – garnet samples with acceptable mineral stoichiometry (+/-0.02) from Aulbach et al., 2007; Mackenzie and Canil, 1997; Westerlund et al., 2006; Creighton et al., 2010; Davies et al., 2004; Van Rythoven and Schultze, 2009; Donnelly, 2009; Creighton et al., 2008; Klein-BenDavid et al., 2004; Menzies et al., 2004).

Error bars are smaller than data points.

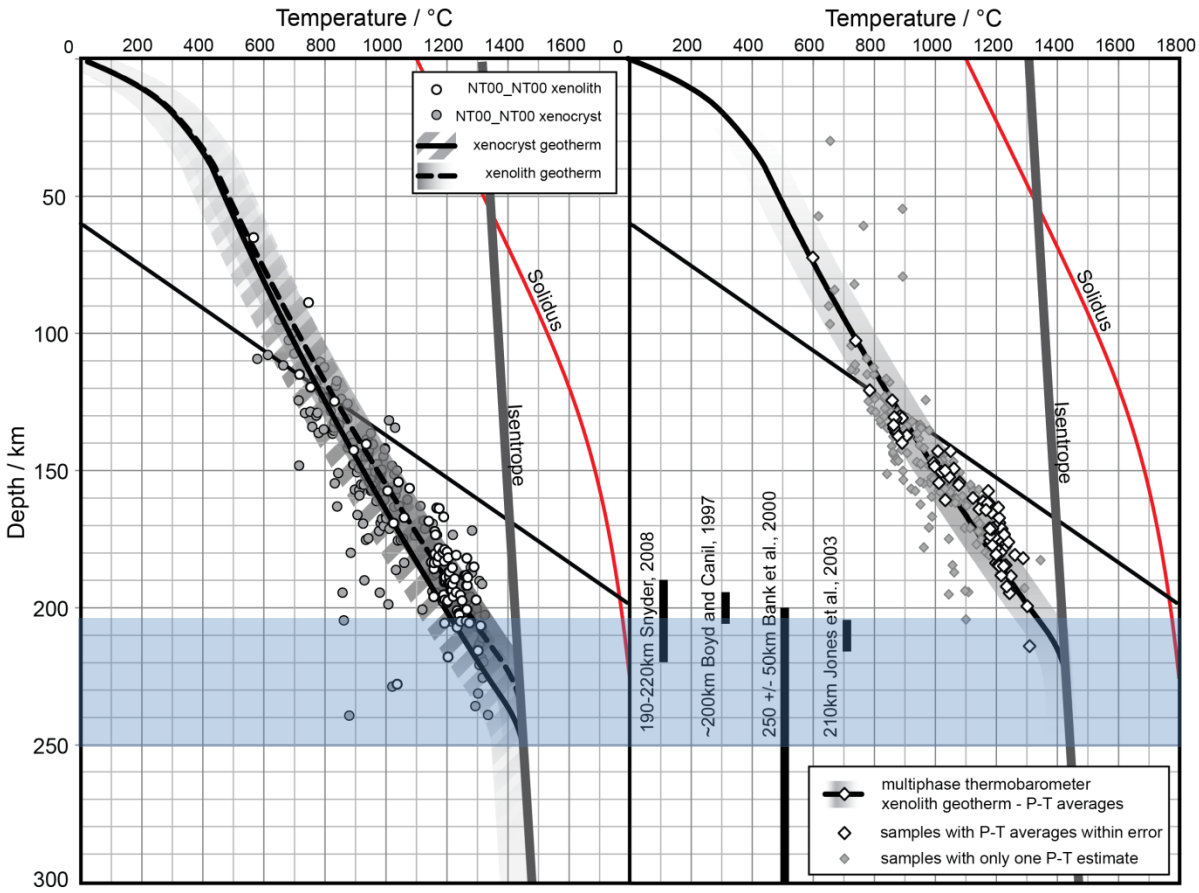

Figure 5.6:

Left:

Single-cpx geothermobarometer palaeogeotherm fits (after Mather et al., 2011) for central Slave xenolith and xenocryst data. Grey circles, solid line and hatcheed shading – clinopyroxene xenocryst geotherm (this study). White circles, dashed line and solid shading – published xenolith data (references as Figure 5.5).

Right:

Multiphase geothermobarometer palaeogeotherm fits (after Mather et al., 2011) for central Slave xenolith data. Diamonds, solid line and shading – published xenolith data (references as Figure 5.5). Also shown as black bars are estimates of lithospheric thickness from independent seismic and magnetotelluric methods with associated references.

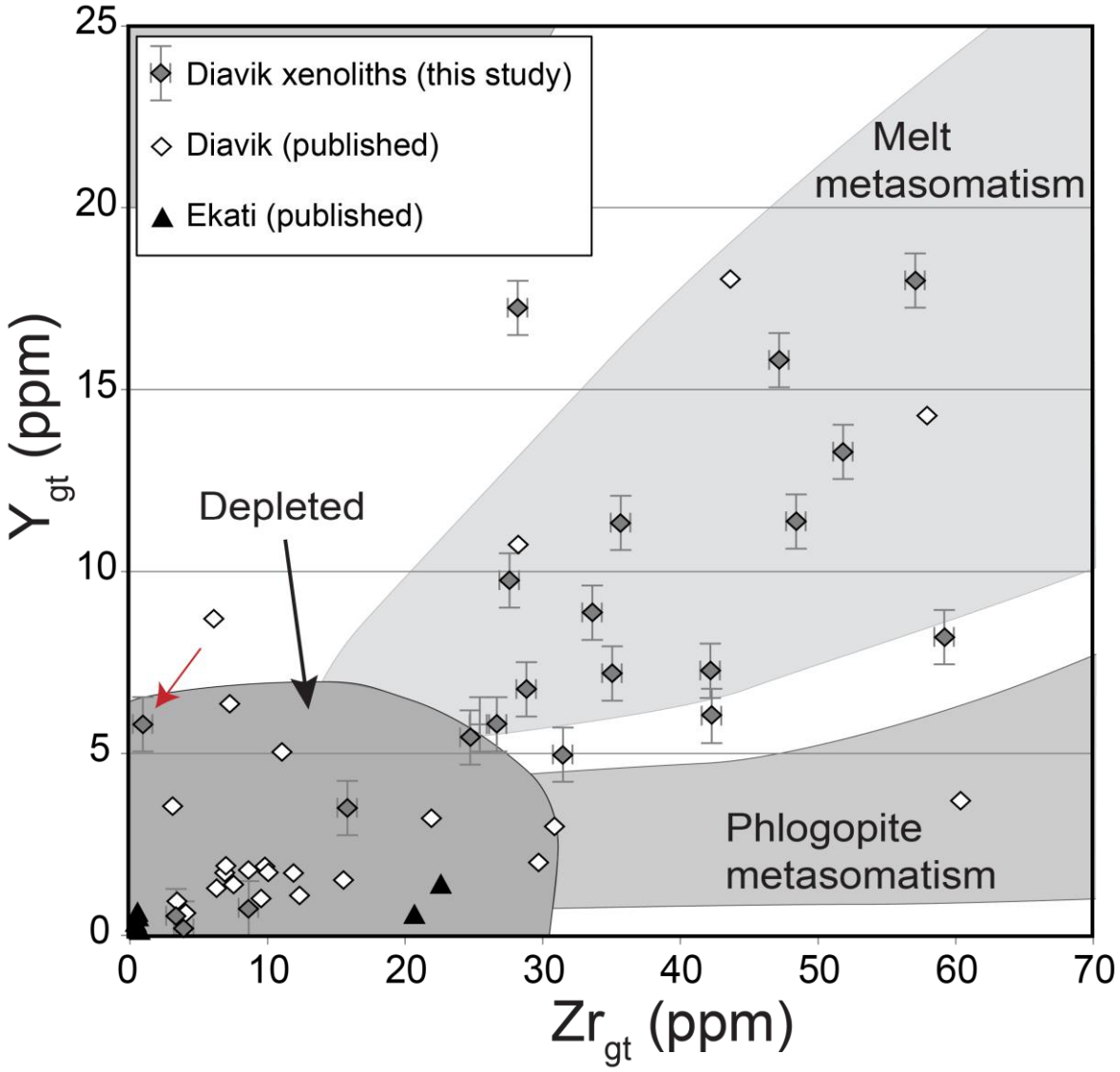

Figure 5.7:

Y-Zr concentrations of garnets from the Diavik macroxenoliths (grey diamonds), published values for the Diavik (white diamonds) and Ekati kimberlites (black triangles). Shaded regions after Griffin et al., (1999). Error bars indicate average degree of variation in measured basaltic glass GSD-1G during analytical run.

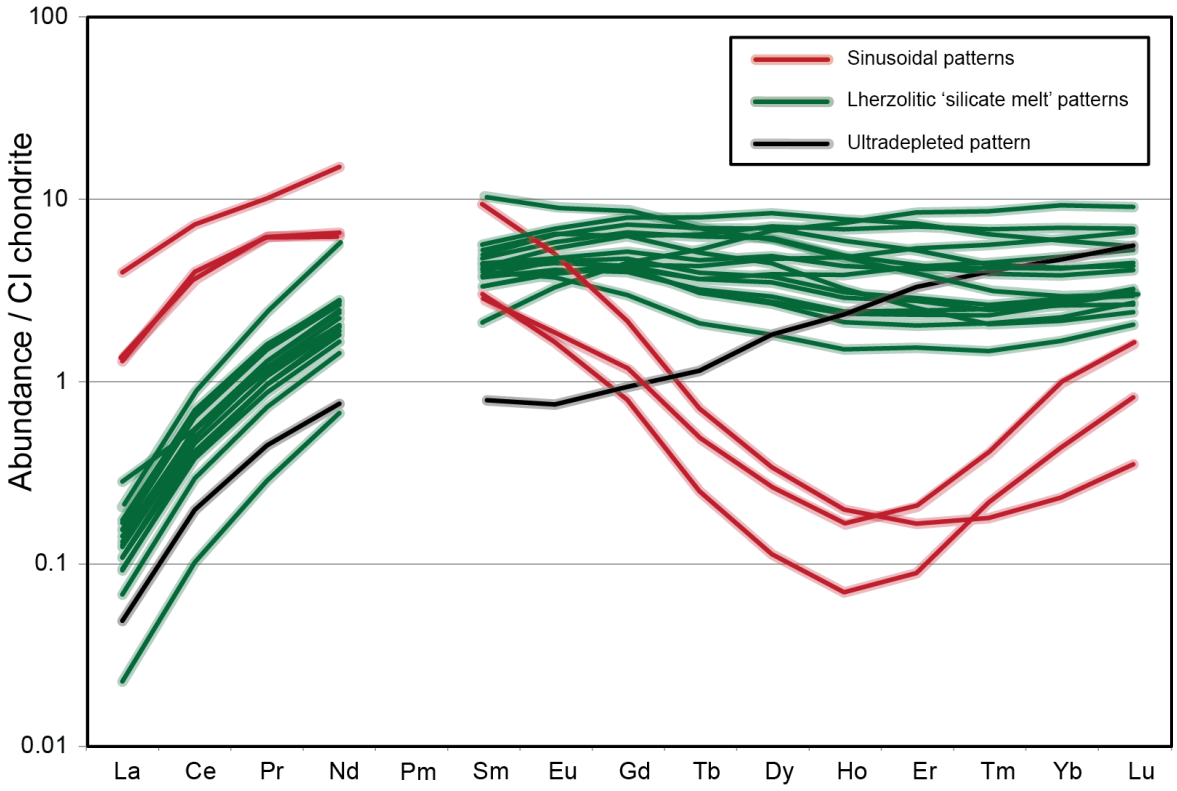

Figure 5.8:

Rare-earth element concentrations for Diavik macroxenolith garnets normalised to CI Chondrite (McDonough and Sun, 1995). Three main pattern types are highlighted, distinguished using the criteria outlined in Figure 4.5. Red lines indicate 'sinusoidal', "G10"-type patterns (Burgess and Harte, 2004; Stachel et al., 2004). Green lines show 'lherzolitic', melt-equilibrated patterns. The black line shows the only 'depleted' pattern (MX 5022). Errors are indicated as shaded regions around individual lines.

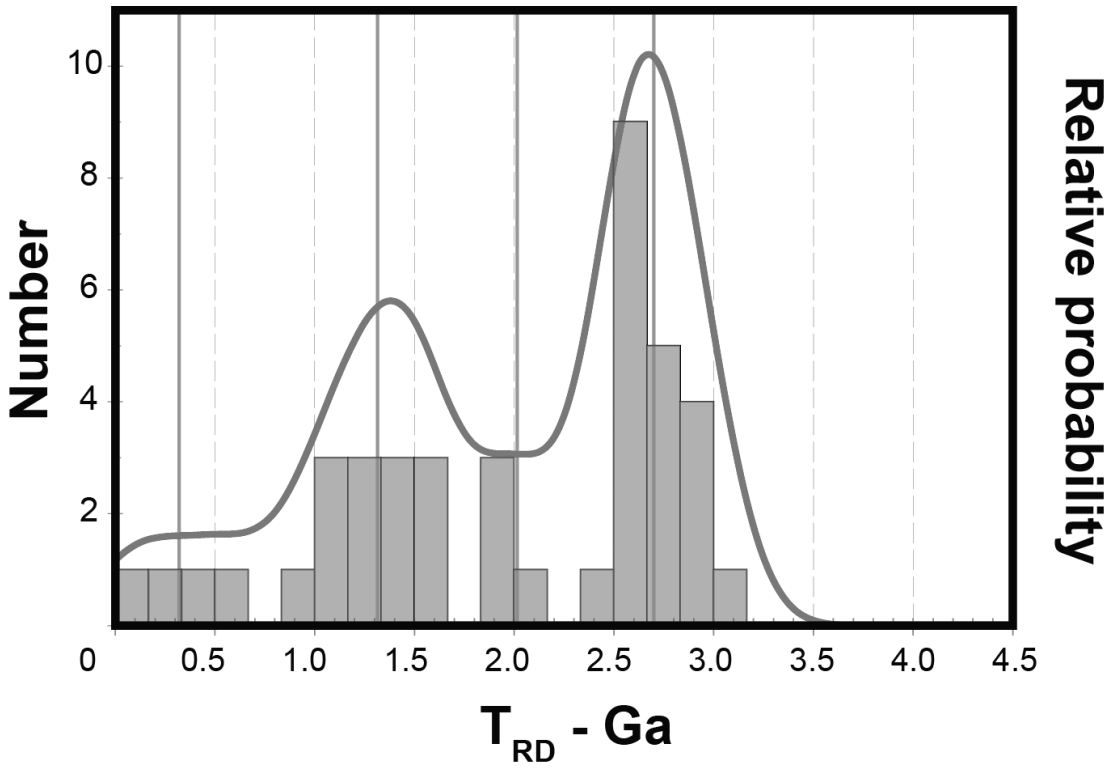

Figure 5.9:

Whole-rock T_{RD} distribution of Diavik macroxenoliths in this study. Mixture-modelling (Sambridge and Compston, 1995) reveals three distinct components to the dataset: one in the Archean at ~2.6 Ga, one in the Mid-Proterozoic at ~1.3 Ga and one in the Palaeoproterozoic at ~2.0 Ga

Figure 5.10:

(a) Top:

Age-depth relationships in Diavik macroxenolith suite. Pressures and temperatures for individual xenolilths are averages of all available thermobarometer combinations (see text). Orange samples are those estimated as older than 2.5 Ga based on whole-rock Re depletion ages. Blue samples are those suggested to be younger than 2.5 Ga. Red rims indicate samples where multiphase/single-cpx P-T estimates were not possible, and are the projection of Ni-in-garnet temperatures to the multiphase xenolith geotherm (Figure 5.6). Large, diamonds indicate the average P and T of samples within each age range. Error bars indicate 1 standard deviation in P–T range for each age group. These averages and standard deviations are also shown in the inset, for clarity. Note that the projected Ni-in-garnet temperatures are for information only and have not been used to calculate the average temperature of the younger samples.

(b) Bottom:

Mg# (Mg/(Mg+Fe) of olivines within samples analysed for whole rock Re depletion ages. Again, blue diamonds indicate samples where whole rock Re depletion ages are younger than 2.5 Ga, orange diamonds are > 2.5 Ga. Note the clear distinction between $Mg\#_{ol}$ between the two datasets.

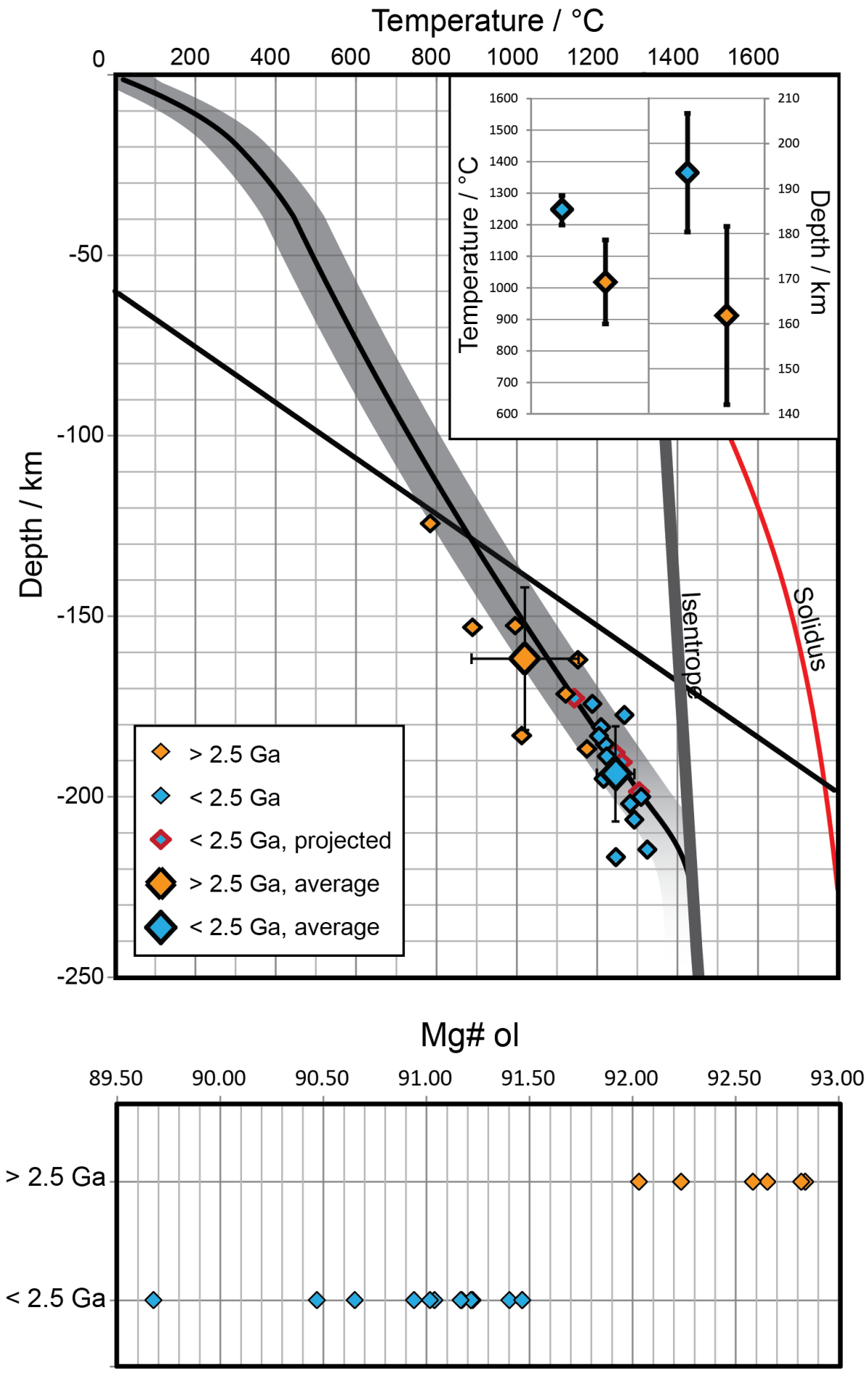
Temperature / °C
0
200
400
600
800
1000
1200
1400
1600
Depth / km
-50
-100
-150
-200
-250
Temperature / °C
1600
1500
1400
1300
1200
1100
1000
900
800
700
600
Depth / km
210
200
190
180
170
160
150
140
Isentrope
Solidus
> 2.5 Ga
< 2.5 Ga
< 2.5 Ga, projected
> 2.5 Ga, average
< 2.5 Ga, average
Mg# ol
89.50
90.00
90.50
91.00
91.50
92.00
92.50
93.00
> 2.5 Ga
< 2.5 Ga

Figure 5.11:

Ti (LA-ICP-MS) content of xenolith garnets from the Diavik kimberlite in this study, and the 7 samples from the Ekati kimberlite of Westerlund et al., (2006). Where available, errors indicated are 1 standard deviation between measurements of different crystals of the same sample.

Highlighted in orange are samples with whole-rock T_{RD} ages that are older than 2.5 Ga, blue are those younger than 2.5 Ga. Large symbols with error bars represent the average and standard deviation of all samples in respective groupings.

A significant difference is noted between the Ti compositions of the Diavik xenolith garnets. Older samples consistently yield lower Ti contents than younger samples, with the exception of MX 5023 (shown with arrow).

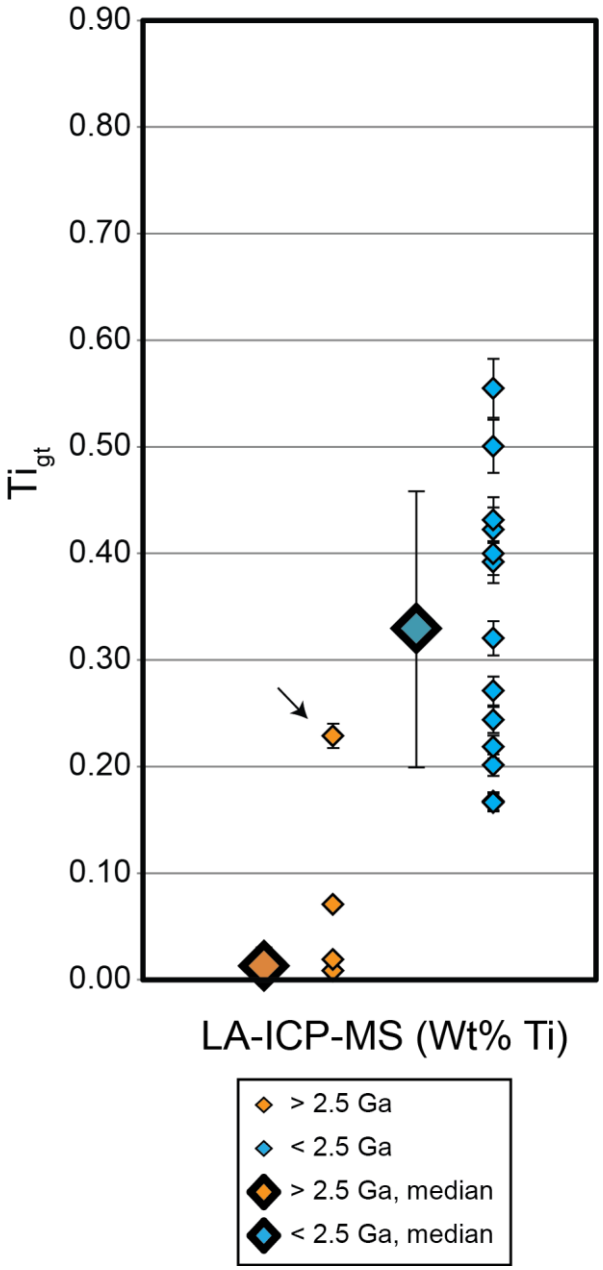
0.90
0.80
0.70
0.60
0.50
0.40
0.30
0.20
0.10
0.00
Ti$_{gt}$
LA-ICP-MS (Wt% Ti)
> 2.5 Ga
< 2.5 Ga
> 2.5 Ga, median
< 2.5 Ga, median

Figure 5.12:

Zr, Y and Ga content of xenolith garnets from Diavik (this study) and Ekati (data from Westerlund et al., 2006). Where available, errors indicate the standard deviation of measurements of different crystals in the same sample. Symbology is as Figure 5.11. In this case, more than one >2.5 Ga sample showed anomalous enrichment and therefore the median value was used rather than the average. Standard deviations shown are for the full range of data illustrated. Grey shaded areas are approximately the range of values within the 'depleted' field of Griffin et al., (1999b).

Again, the older samples (> 2.5 Ga) show a significantly lower concentration of all elements than the younger samples (< 2.5 Ga). These values are similar to those published by Griffin et al., (1999a) for the 'shallow' and 'deeper' layers of the central part of the Central Slave 'geochemical tomography' image.

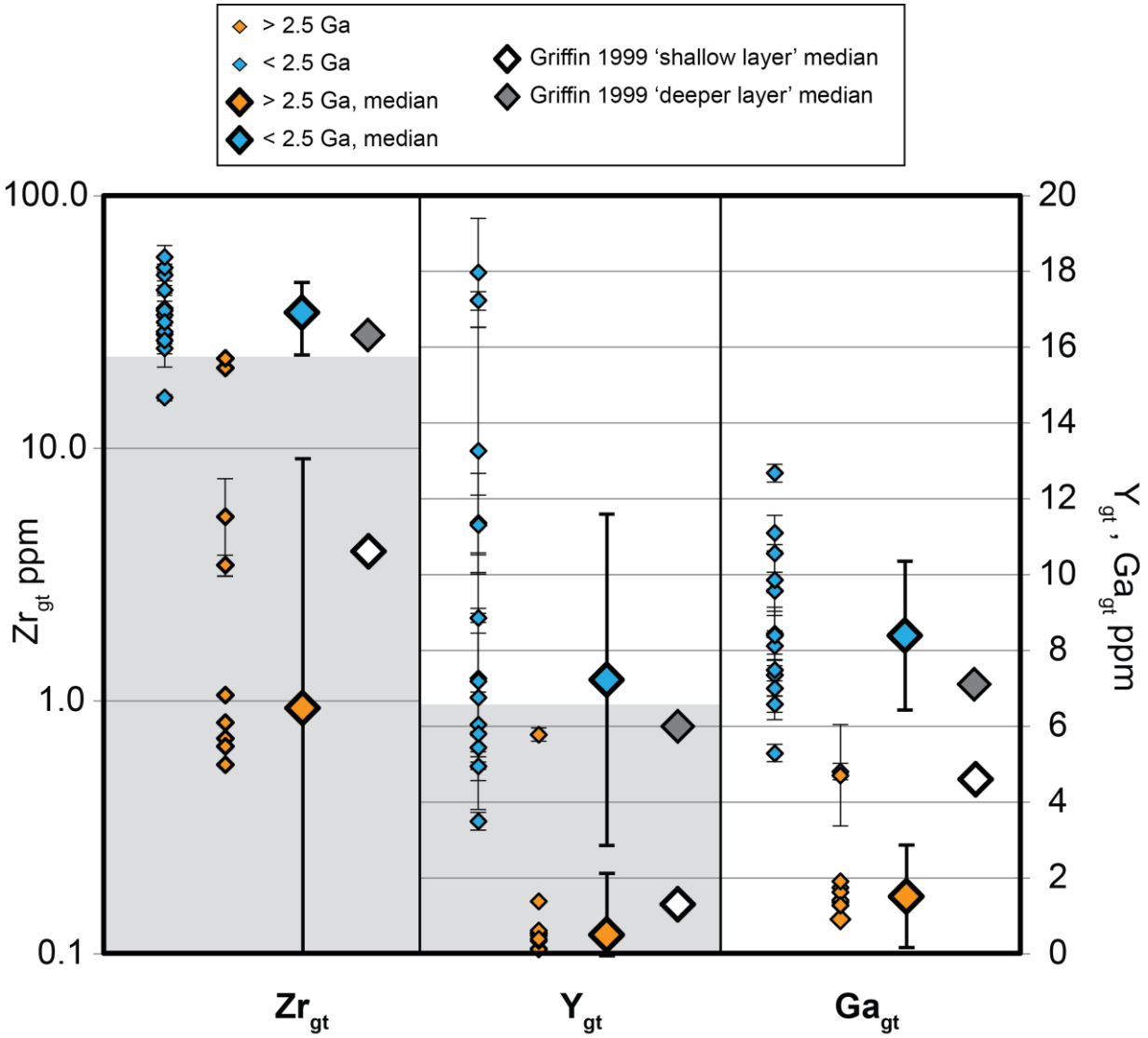
> 2.5 Ga
< 2.5 Ga
> 2.5 Ga, median
< 2.5 Ga, median
Griffin 1999 'shallow layer' median
Griffin 1999 'deeper layer' median
100.0
10.0
1.0
0.1
Zr_gt ppm
20
18
16
14
12
10
8
6
4
2
0
Y_gt , Ga_gt ppm
Zr_gt
Y_gt
Ga_gt

Figure 5.13:

Rare-earth element profiles for Diavik macroxenoliths. Highlighted in orange are samples where whole-rock Re depletion ages are older than 2.5 Ga. Errors are indicated as shaded regions around plotted lines and are the same as in Figure 5.8.

Data from Westerlund et al., (2006; Ekati) are shown as dashed lines.

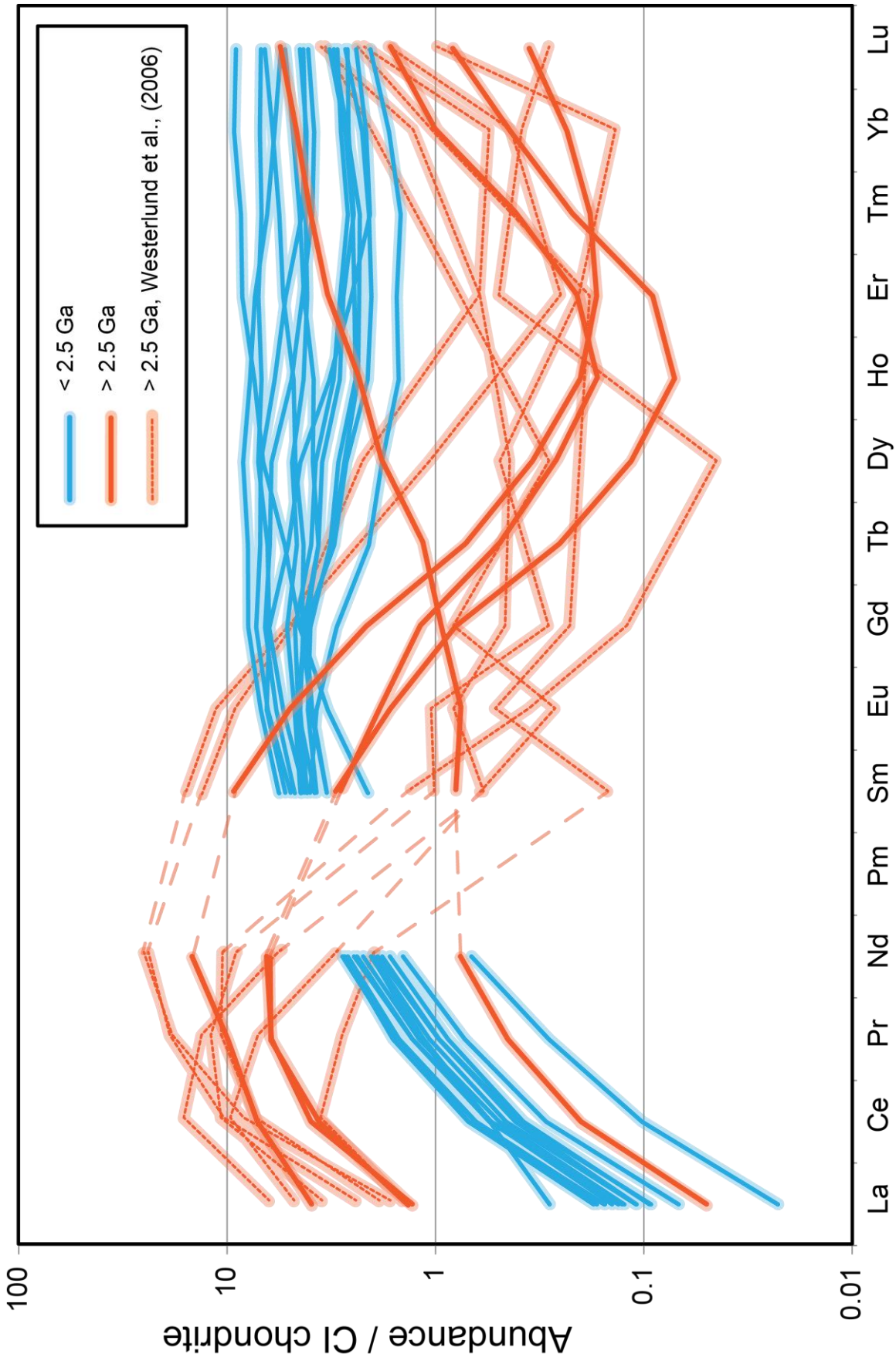
< 2.5 Ga
> 2.5 Ga
> 2.5 Ga, Westerlund et al., (2006)
Abundance / CI chondrite
100
10
1
0.1
0.01
La
Ce
Pr
Nd
Pm
Sm
Eu
Gd
Tb
Dy
Ho
Er
Tm
Yb
Lu

6 SYNTHESIS: A XENOLITH-BASED LITHOSPHERIC TRANSECT

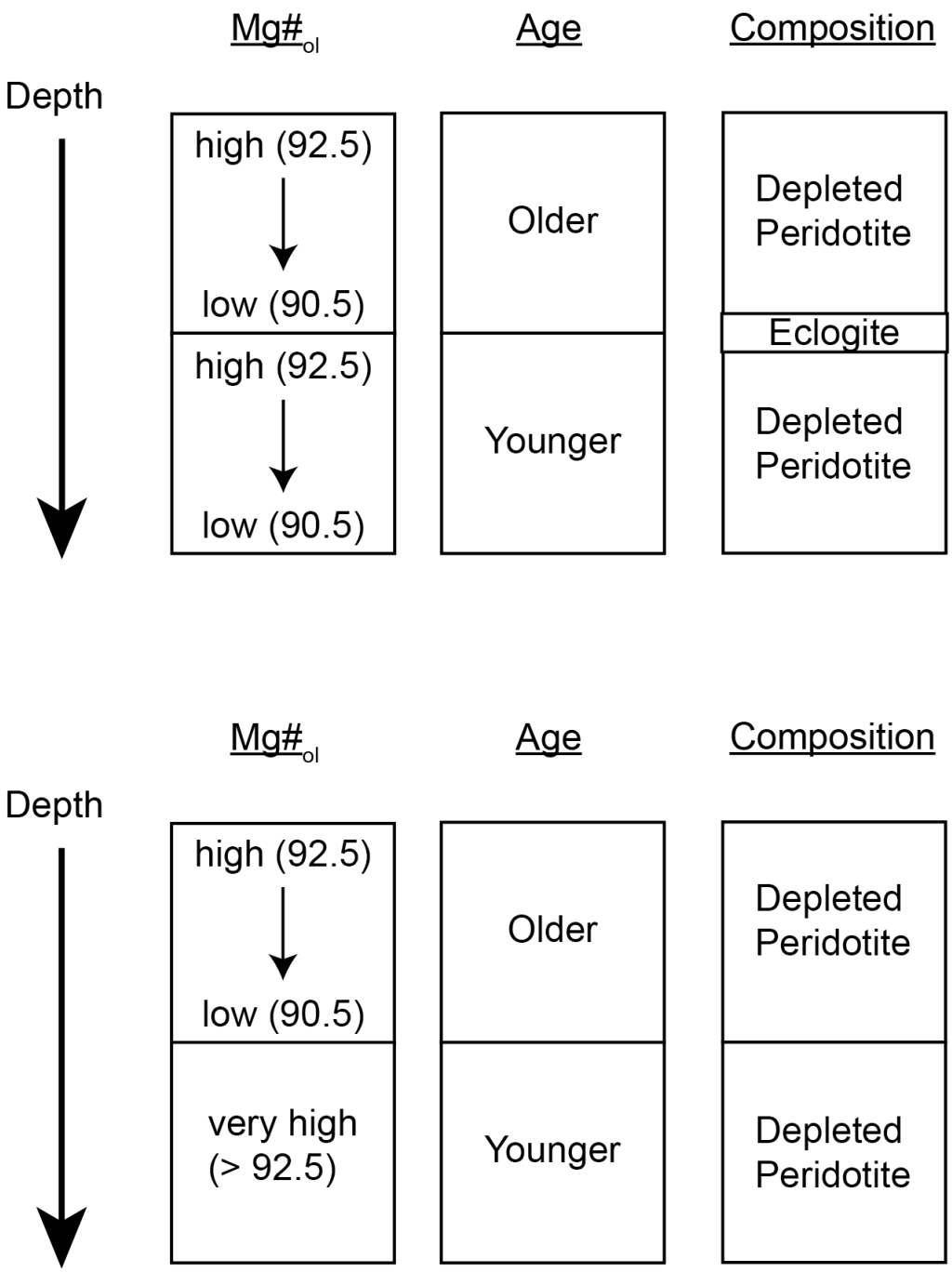

Figure 6.1:

Expected *primary* (i.e. pre-metasomatic) depth distributions of different geochemical parameters resulting from the two endmember lithosphere formation hypotheses (top; subduction stacking; bottom; plume subcretion).

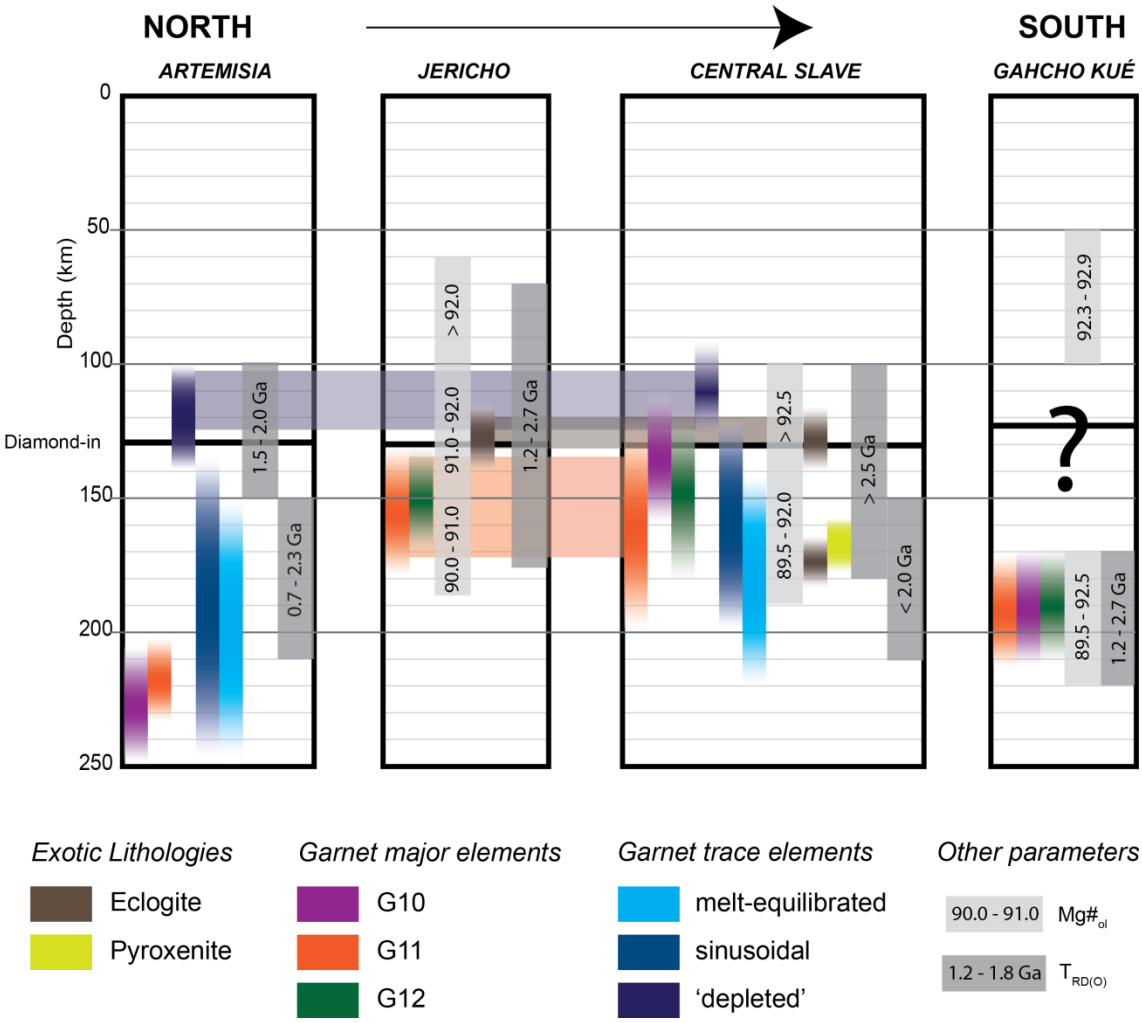

Figure 6.2:

Summary diagram of the lithospheric stratigraphy of the Slave craton from mantle xenolith data presented in this thesis.

Additional data sources:

Kopylova et al., 1998; 1999; 2000; Kopylova and Caro, 2002; Irvine, 2002; Aulbach et al., 2004; 2007; Westerlund et al., 2006; Schmidberger et al., 2007; Smart et al., 2009; Creighton et al., 2010

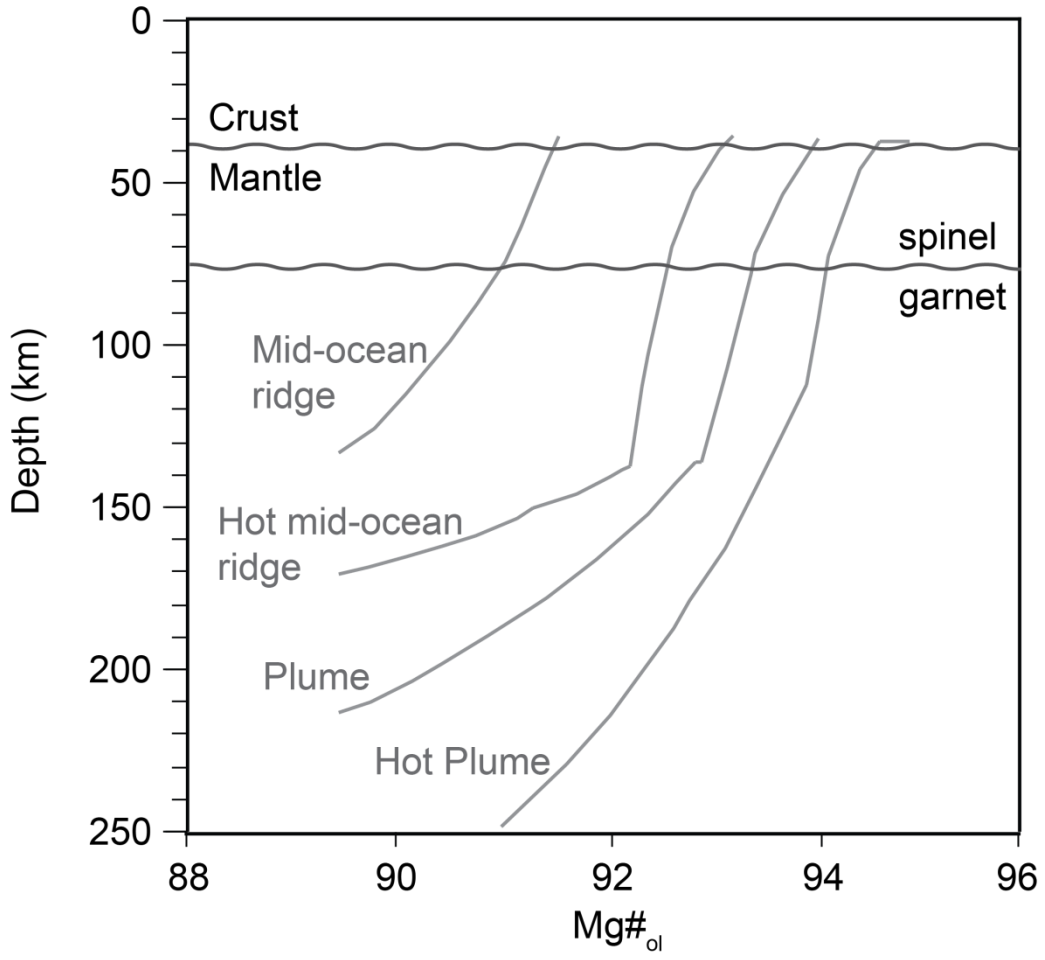

Figure 6.3:

Predicted $Mg\#_{ol}$-depth systematics for different lithosphere production environments, after Pearson and Wittig (*in press)* and using the modelling parameters of Herzberg and Rudnick (*in press).*

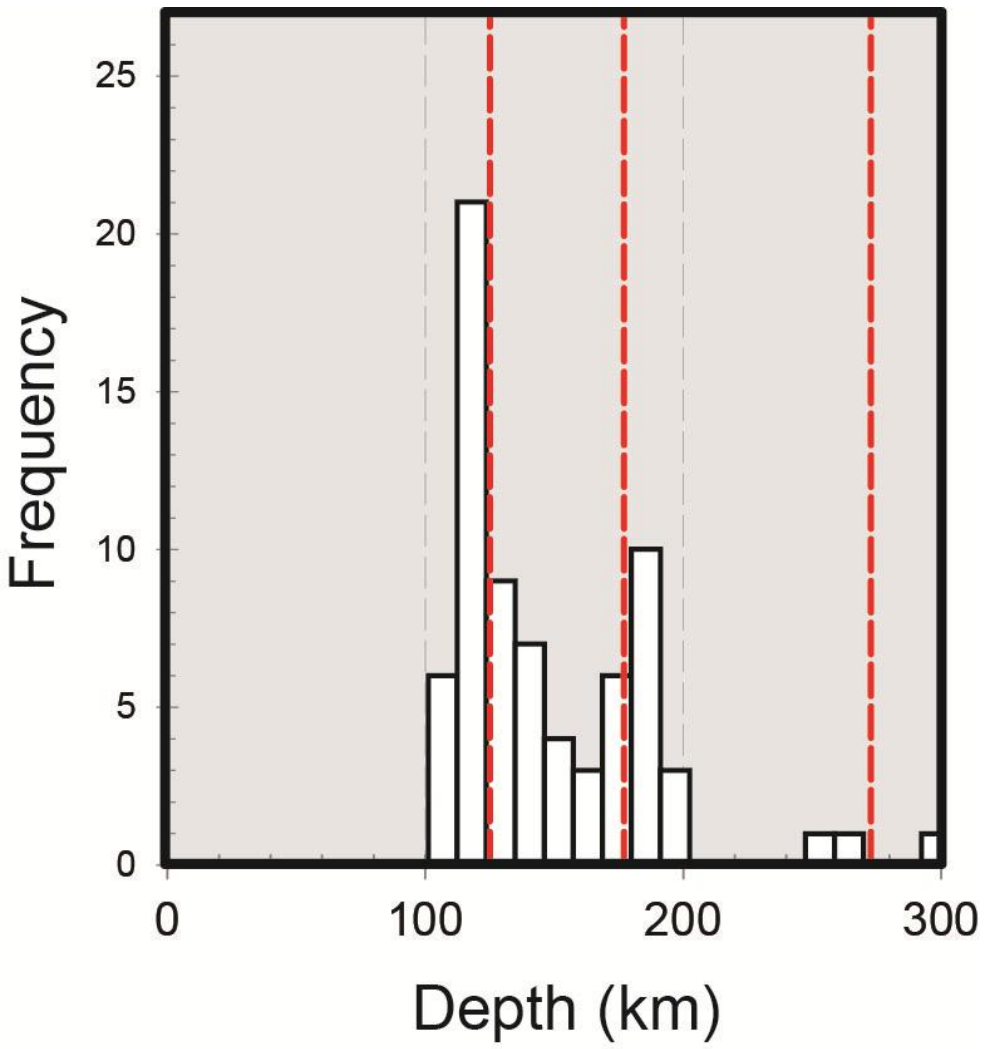

Figure 6.4:

Gaussian mixture modelling of palaeogeotherm-projected Garnet-Cpx temperature estimates (Krogh-Ravna, 2000) from central Slave eclogite xenoliths (Schmidberger et al., 2007, Aulbach et al., 2007). Red dashed lines indicate mixture-modelled components, interpreted to be distinct 'layers' of eclogite within the lithospheric mantle beneath the central Slave.

8 APPENDIX

8.1 ANALYTICAL METHODS

8.1.1 Sample Processing

Thin section billets were cut from all suitable samples on a diamond-blade bench-top saw, and the remaining sample was then crushed using a fly-press.
Approximately 1/8 – 1/16 of this coarse crush was then separated and powdered in an agate ball-mill for 35 – 45 minutes to ensure complete powdering of garnet.

8.1.2 EMP analysis

Three points in the core of each mineral and one point on the rim were analysed to assess heterogeneity. Example analysis locations are shown below:

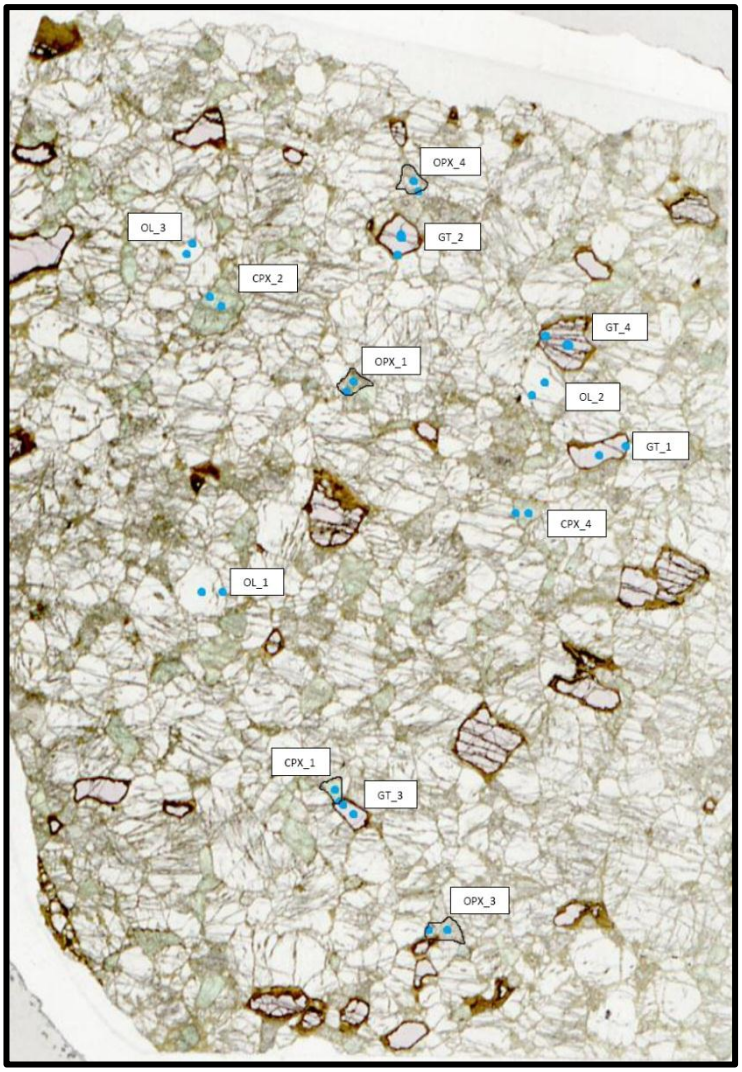

8.1.3 In-situ LA-ICP-MS trace elements

In-Situ LA-ICP-MS analyses were performed on garnet crystals separated from coarse crush of the xenoliths and mounted in epoxy resin pucks. A Photon Machines laser of wavelength 193 nm was coupled to an Agilent 7700x quadrupole ICP-MS and ablated the samples with a beam diameter of 52 μm. Energy density was 7 Jcm^{-2} and the pulse repetition rate was 10 Hz. Dwell time on each sample was 120 seconds, including 45 second gas blank and 75 second ablation time. At least 3 crystals were analysed from each sample to check for variation.
Standard basaltic glass GSD-1G (Jochum et al., 2010) was used for element calibrations and garnet standard PN2 was used (Canil et al., 2003) for high-pressure garnet calibration. Standard values were within 1% of published values for GSD-1G (Jochum et al., 2010) and 5% of published values for PN-2. CaO content was used to normalize the trace element analyses, which were processed using the software GLITTER (Griffin et al., 2008; Longerich et al., 1996; which allowed visual investigation of the analytical signal for accurate selection of good-quality measurements.

8.1.4 Re-Os Isotopes

Re-Os analysis was peformed using the isotope dilution and asher digestion method outlined by Ishikawa et al., 2007; which uses the isotope dilution principles provided by Pearson and Woodland, 2000.

Illustration of the chemical procedure is shown below:

ASHER DIGESTION:

Step 1: Clean asher vessels:

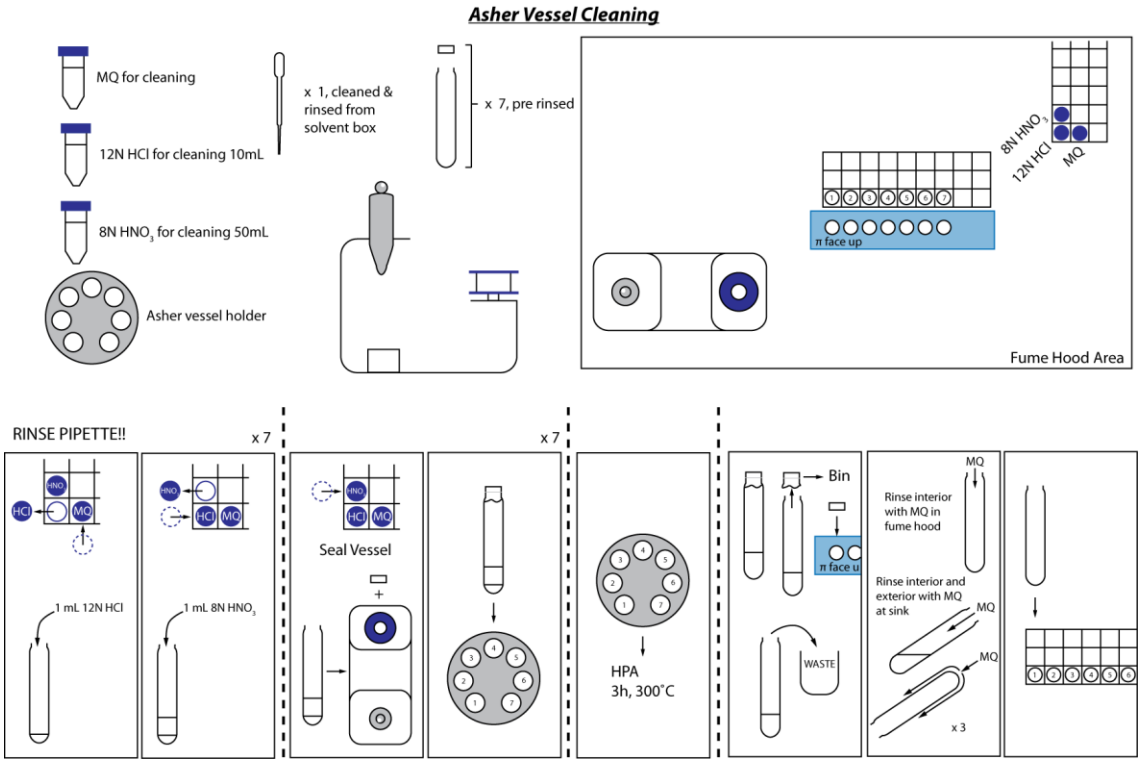

Step 2: Weigh samples into asher vessels

Step 3: Load samples into asher for overnight digestion:

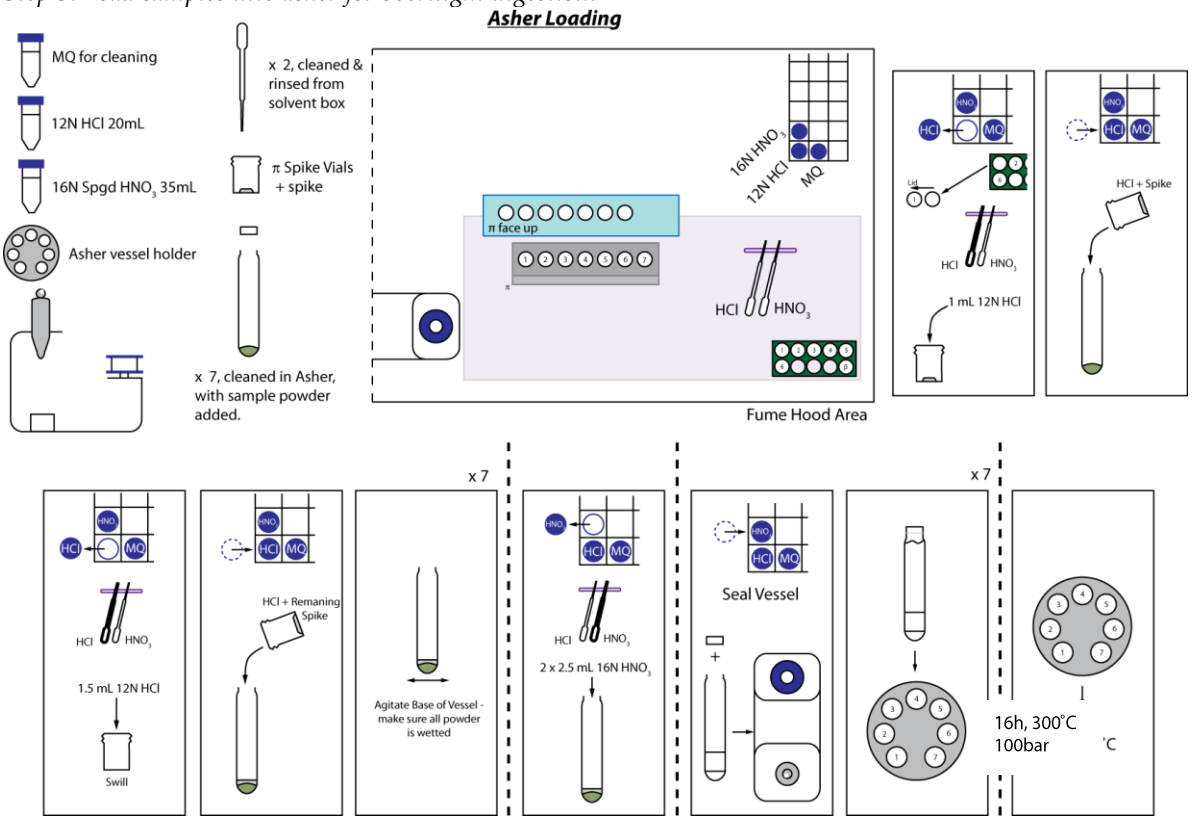

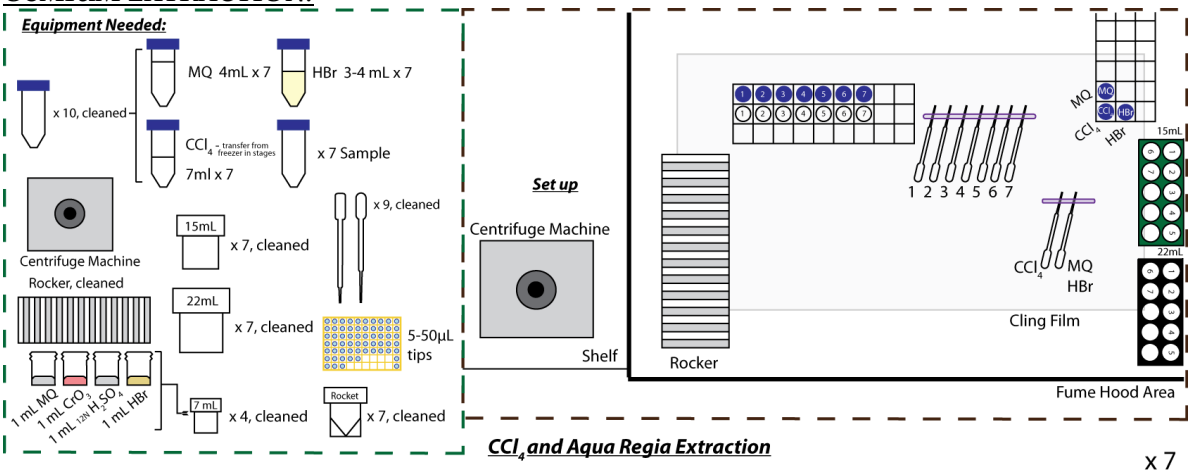

1st CCl_4 & HBr Extraction

x 7

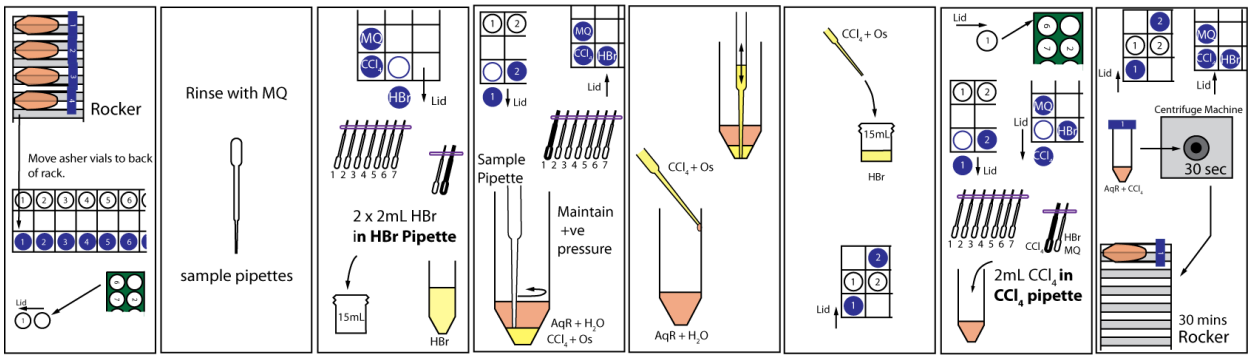

2nd CCl_4 & HBr Extraction

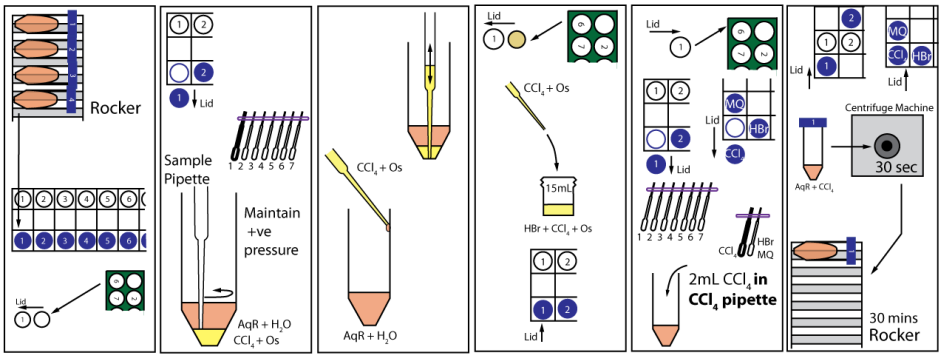

x 7

K. Mather Dec 2008

3rd CCl_4 & HBr Extraction

x 7

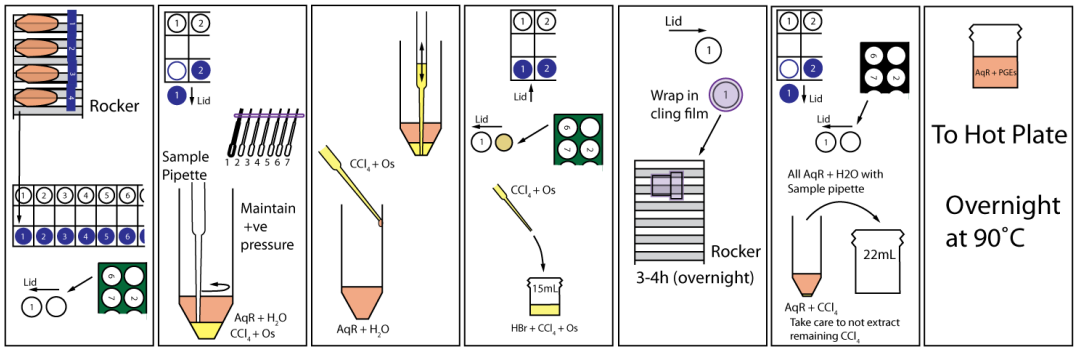

HBr Extraction

x 7

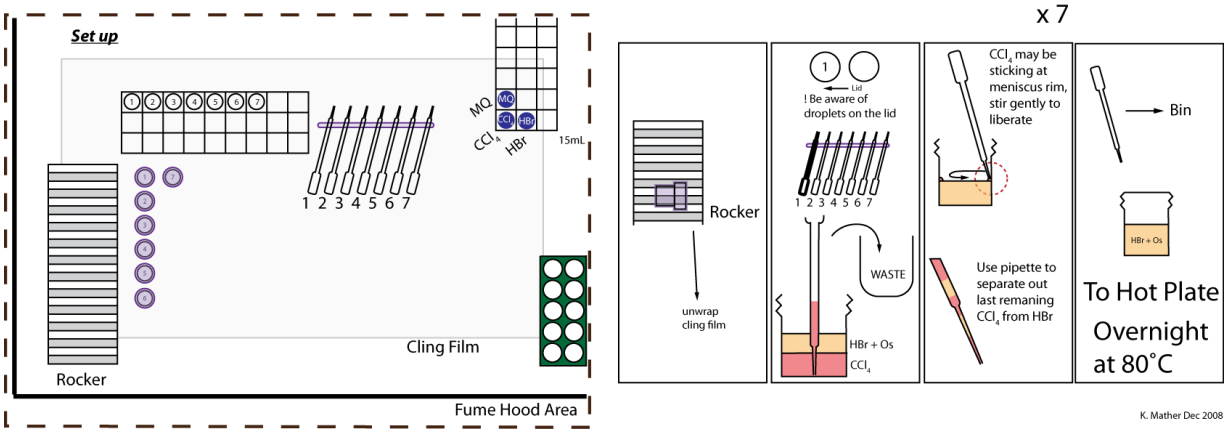

K. Mather Dec 2008

OSMIUM MICRO-DISTILLATION

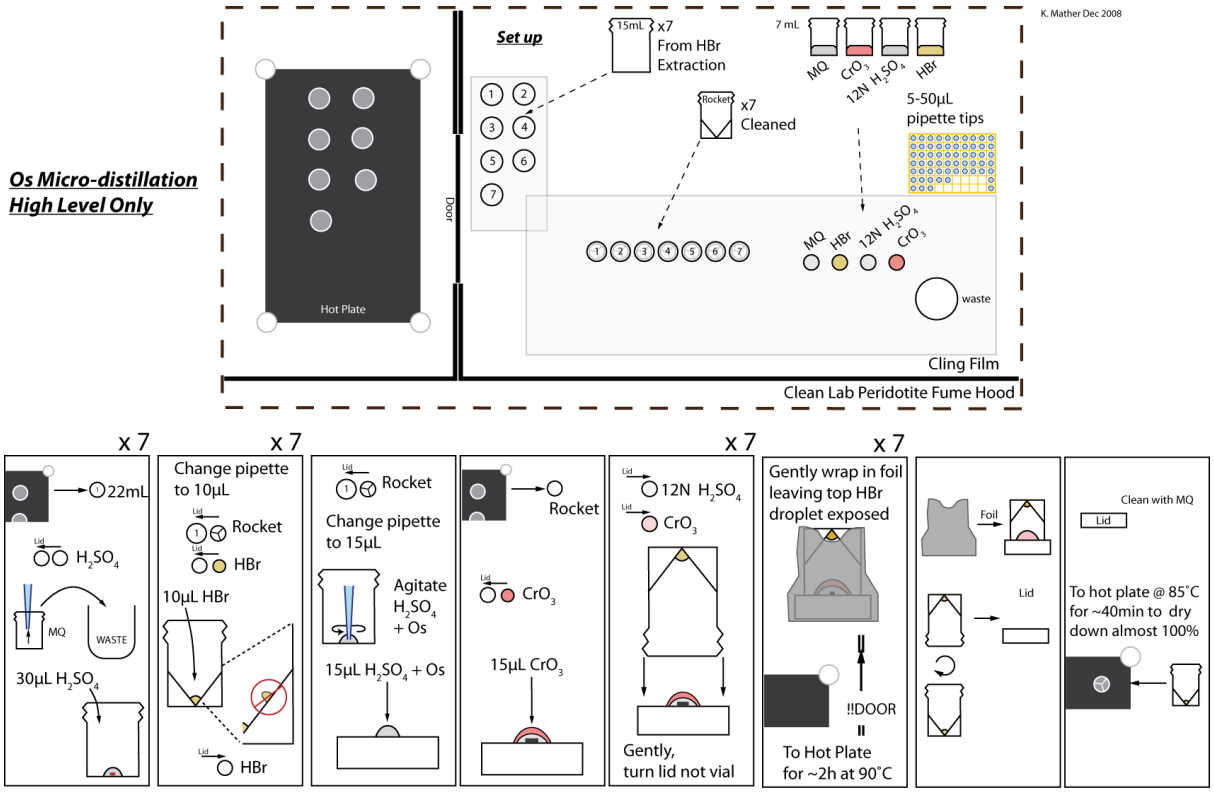

FILAMENT LOADING:

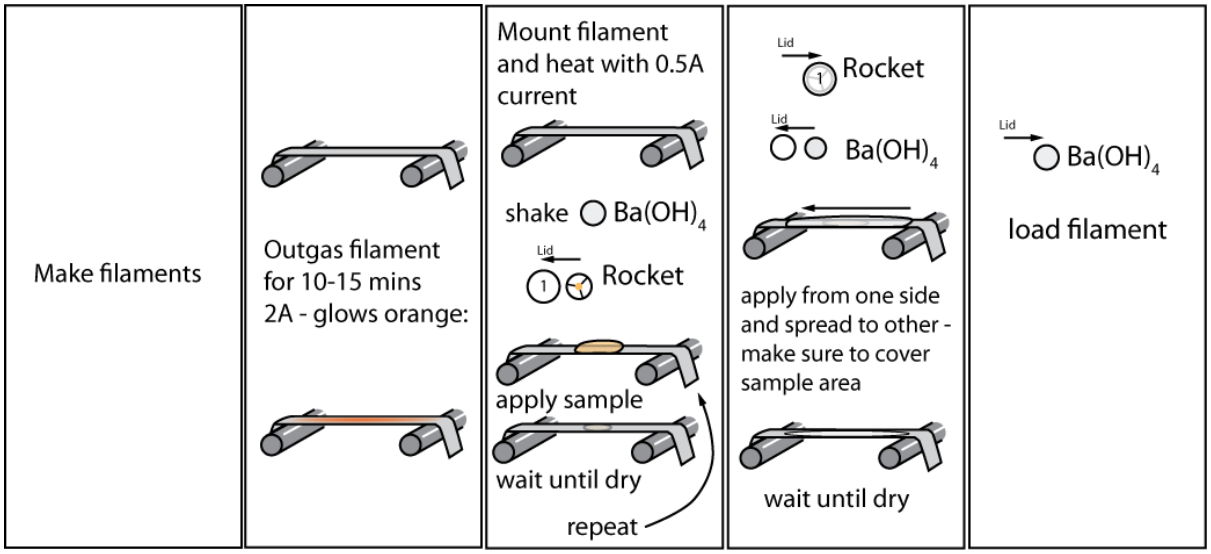

RHENIUM EXTRACTION

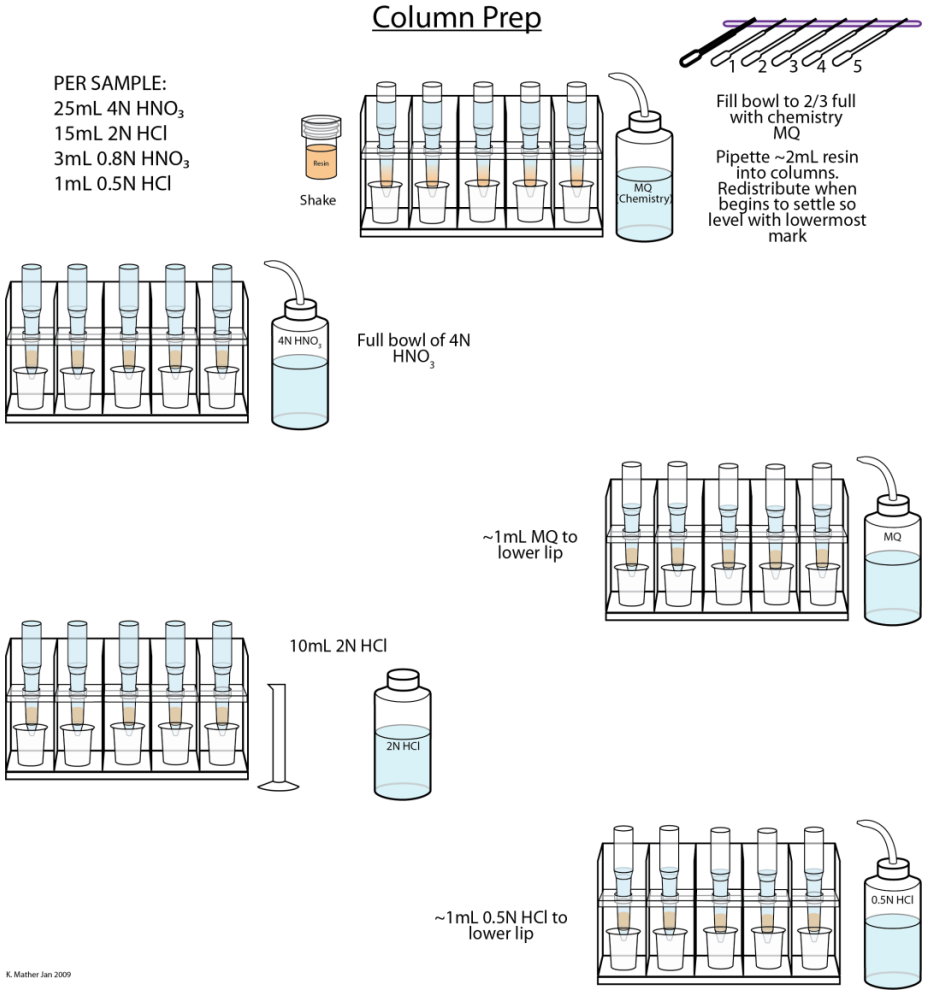

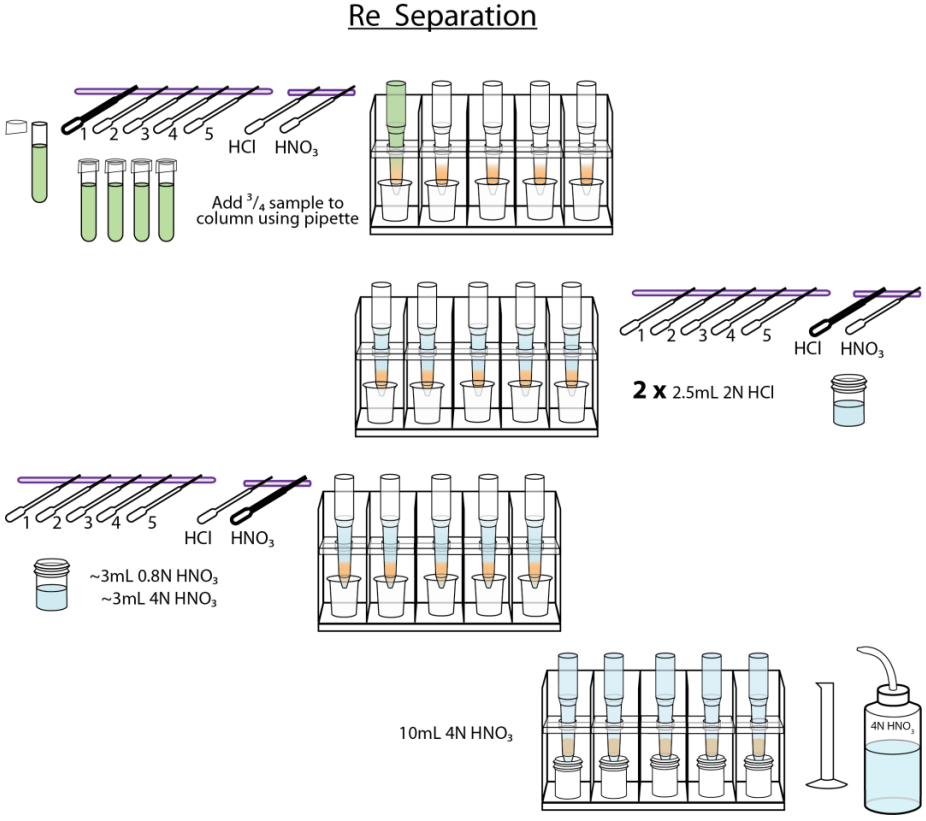

8.2 ELECTRON MICROPROBE DATA

8.2.1 Set-up and operating parameters

Crystal code:
(L)TAP: Thallium acid phalate
(L)PET: Pentaerythritol
(L)LIF: Lithium fluoride

8.2.1.1 University of Cambridge

Element	X Ray Peak	Crystal	Peak time (s)	Background time (ms)	Calibration
Major					
(Al Ka)	15keV 100nA	TAP	21.9	560	Cor
(Si Ka)	15keV 10nA	TAP	21.8	560	Diopside
(Ca Ka)	15keV 10nA	LPET	30.8	560	Diopside
(Fe Ka)	15keV 10nA	LIF	31.0	560	Fayalite
(Mg Ka)	15keV 10nA	TAP	21.9	560	Periclase
Trace					
(K Ka)	15keV 100nA	LPET	30.8	560	KSp
(Ti Ka)	15keV 100nA	LPET	30.8	560	Rutile
(Cr Ka)	15keV 100nA	LIF	31.0	560	Cr
(Mn Ka)	15keV 100nA	LIF	31.0	560	Mn
(Ni Ka)	15keV 100nA	LIF	31.0	560	Ni
(Na Ka)	15keV 10nA	LTAP	21.7	560	Jadeite

8.2.1.2 University of Alberta

Element	X Ray Peak	Crystal	Peak time (s)	Background time (s)	Calibration
Major					
(Na Ka)	20keV 20nA	LTAP	60.0	30.0	Albite
(Si Ka)	20keV 20nA	TAP	60.0	30.0	Diopside
(Ca Ka)	20keV 20nA	LPET	50.0	25.0	Diopside
(Fe Ka)	20keV 20nA	LLIF	30.0	15.0	Hematite
(Mg Ka)	20keV 20nA	LTAP	50.0	30.0	Pyrope
Trace					
(K Ka)	20keV 20nA	LPET	30.0	15.0	Sanidine
(Ti Ka)	20keV 20nA	PET	60.0	30.0	Rutile
(Cr Ka)	20keV 20nA	PET	55.0	30.0	Chromite
(Mn Ka)	20keV 20nA	LLIF	30.0	15.0	Spessartine
(Al Ka)	20keV 20nA	TAP	60.0	30.0	Pyrope

8.2.1.3 Saskatchewan Research Council

Element	X Ray Peak	Crystal	Peak time (s)	Background time (s)	Calibration
Major					
(Na Ka)	15keV 20nA	LTAP	60.0	60.0	Albite
(Si Ka)	15keV 20nA	TAP	30.0	30.0	Pyrope
(Ca Ka)	15keV 20nA	LPET	40.0	40.0	Augite
(Fe Ka)	15keV 20nA	LLIF	30.0	30.0	Almandine
(Mg Ka)	15keV 20nA	TAP	30.0	30.0	Olivine (Fo90)
Trace					
(K Ka)	15keV 20nA	LPET	40.0	40.0	Microcline
(Ti Ka)	15keV 20nA	LPET	40.0	40.0	Ilmenite
(Cr Ka)	15keV 20nA	LPET	40.0	40.0	Cr
(Mn Ka)	15keV 20nA	LLIF	30.0	30.0	Rhodonite

(Al Ka)	15keV 20nA	LTAP	30.0	30.0	Pyrope

8.2.1.4 Birkbeck, University of London

Major element mineral/bulk analyses were obtained using a Jeol 8100 Superprobe (WDS) and an Oxford Instrument Inca system (EDS) at Birkbeck. Analysis was carried out using an accelerating voltage of 15 kV, current of 2.5 nA and a beam diameter of 1 μm. The counting times for all elements were 20 seconds on the peak and 10) seconds each on the high and low backgrounds. The analyses were calibrated against standards of natural silicates, oxides and Specpure® metals with the data corrected using a ZAF program.

8.2.2 Standard compositions

Where standard compositions are not international catalogued samples, their compositions are listed here:

8.2.2.1 University of Cambridge

Diopside :	Mg : 11.2%, Si : 25.9%, Ca : 18.4% O : 44.5%
Jadeite:	Na : 11.3%, Al : 13.2%, Si : 27.8%, Fe : 0.2%, O : 47.5%
Fayalite:	Si : 13.783%, Fe : 54.812%, O : 31.405%
Corundum:	O: 47.1%, Al : 52.9%
Periclase:	O : 39.7%, Mg : 60.3%
Rutile:	Ti : 59.95%, O : 40.05%
Cr:	Cr : 100.%
Mn:	Mn : 100.%
Ni:	Ni : 100.%

8.2.2.2 University of Alberta

Albite (UofA Coll):	Na : 8.49%, Al : 10.47%, Si : 31.82%, O : 48.63%, K : 0.22%
Diopside (UofA Coll):	Ca : 18.39%, Mg : 11.23%, Si : 25.88%, O : 44.29%
Hematite (UofA Coll):	Fe : 69.06%, O : 30.24%, Ti : 1.25%
Sanidine (UofA Coll):	K : 13.27%, Al : 9.48%, Si : 30.11%, O : 45.84%, Na : 0.31%
Rutile (UofA Coll)	Ti : 59.95%, O : 40.05%
Chromite(UofA Coll):	Cr : 68.4195%, O : 31.5805%
Spessartine (UofA Coll):	Mn : 31.29%, Al : 11.37%, Si : 16.79%, O : 39.03%, Fe : 2.24%
Pyrope:	Smithsonian Institution; Jarosewich, 2002

8.2.2.3 Saskatchewan Research Council

Albite:	Harvard; McGuire et al., 1992
Pyrope:	Smithsonian Institution; Jarosewich, 2002
Augite:	Smithsonian Institution; Jarosewich, 2002
Almandine:	Harvard; McGuire et al., 1992
Fo90 Olivine:	Smithsonian Institution; Jarosewich, 2002
Microcline:	Smithsonian Institution; Jarosewich, 2002
Ilmenite:	Smithsonian Institution; Jarosewich, 2002
Cr:	Cameca Cr
Rhodonite:	SPI

8.2.3 Probe data comparison

MX5009

OL	cbg	uoa	src
bbk	0.813	n/a	0.994
	cbg	n/a	0.869
		uoa	n/a
CPX	cbg	uoa	src
bbk	n/a	0.987	0.992
	cbg	n/a	n/a
		uoa	0.999
GT	cbg	uoa	src
bbk	0.930	n/a	0.997
	cbg	n/a	0.927
		uoa	0.999

R^2 correlation coefficients for elemental oxide measured abundances from the four different microprobes used in this study:
bbk = birkbeck, University of London, UK
cbg = Cameca SX100, University of Cambridge, UK
uoa = Cameca SX100, University of Alberta, AB, Canada
src = Cameca SX100, Saskatchewan Research Council, SK, Canada

8.2.4 Measured values

Only core values with cation totals +/- 0.02 of desired value (OL – 3.00, OPX/CPX – 4.00, GT - 8.00) have been used to calculate the averages shown. The number of analyses used to calculate the average values are shown in column 3.

8.2.4.1 Average measured compositions of Diavik minerals in xenoliths analysed in this study

Sample	Min	No.	Na2O	CaO	Al2O3	FeO	SiO2	K2O	MgO	TiO2	Cr2O3	MnO	NiO
DDM_149	OL	5		0.04	0.02	9.48	41.0		50.5	0.01	0.02	0.114	0.361
	OPX	15		0.801	0.695	5.60	57.4		35.3	0.09	0.154	0.122	0.113
	CPX	22	1.90	18.0	2.47	3.24	55.8	0.05	18.1	0.189	0.761	0.136	0.02
	GT	24	0.009	4.21	21.5	7.75	42.3	0.00	21.7	0.493	1.91	0.327	0.00
DDM_327	OL	1		0.05	0.02	9.25	41.5		50.3	0.02	0.04	0.133	0.385
	OPX	2		0.993	0.710	5.72	58.4		35.1	0.131	0.217	0.131	0.144
	CPX	20	1.42	17.8	1.72	3.48	55.9	0.06	19.3	0.218	0.754	0.142	0.04
	GT	19	0.03	4.80	20.2	7.82	42.4	0.003	21.5	0.766	2.75	0.357	0.00
DDM_335	OL	11		0.05	0.01	8.70	40.8		50.6	0.02	0.05	0.116	0.380
	OPX	18		0.914	0.666	5.22	57.5		35.3	0.126	0.339	0.128	0.114
	CPX	15	1.51	17.9	1.61	3.08	55.2	0.04	19.0	0.208	1.41	0.115	0.07
	GT	25		5.80	17.5	7.32	41.4		20.7	0.803	7.07	0.331	
DDM_359	OL	12		0.06	0.02	8.71	40.8		50.4	0.01	0.05	0.115	0.387
	OPX	17		1.02	0.649	5.17	57.9		35.3	0.06	0.318	0.123	0.127
	CPX	14	1.06	18.5	1.24	3.08	55.2	0.05	19.8	0.08	1.06	0.115	0.07
	GT	12	0.04	5.64	18.4	7.19	41.9		20.9	0.452	6.18	0.307	0.01
DDM_360	OL	2		0.04	0.01	8.98	41.2		50.8	0.010	0.02	0.119	0.430
	OPX	4		0.803	0.638	5.44	58.6		35.5	0.06	0.169	0.122	0.127
	CPX	4	1.37	18.9	1.75	3.13	56.3	0.05	19.0	0.112	0.737	0.103	0.06
	GT	18		4.60	21.2	7.72	42.3		21.6	0.367	2.73	0.313	
DDM_361	OL	4		0.04	0.01	8.31	41.6		51.3	0.03	0.05	0.114	0.393
	OPX	9		0.802	0.583	5.04	58.7		35.9	0.152	0.367	0.129	0.119
	CPX	17	1.37	19.1	1.40	2.89	55.7	0.05	19.2	0.241	1.14	0.110	0.06
	GT	14		6.69	15.7	7.20	41.2		19.7	0.829	9.88	0.367	
DDM_366	OL	12		0.05	0.02	8.69	41.3		50.6	0.02	0.05	0.120	0.386
	OPX	16		0.923	0.681	5.25	58.0		35.1	0.124	0.331	0.129	0.125
	CPX	18	1.50	17.8	1.60	3.06	55.1	0.04	19.0	0.202	1.41	0.122	0.06
	GT	26		5.60	17.9	7.25	41.6		20.7	0.711	6.70	0.337	
DDM_367A	OL	20		0.05	0.01	8.70	40.8		50.5	0.02	0.05	0.115	0.381
	OPX	18		0.794	0.586	5.36	57.8		35.6	0.116	0.382	0.125	0.118
	CPX	16	1.47	18.8	1.38	2.97	55.3	0.06	18.7	0.182	1.60	0.113	0.06
	GT	26		6.53	16.2	7.61	41.0		19.6	0.756	8.96	0.362	
DDM_368	OL	4		0.04	0.02	8.49	41.3		51.0	0.01	0.04	0.104	0.403
	OPX	12		0.773	0.599	5.18	58.1		35.9	0.07	0.348	0.122	0.118
	CPX	18	1.44	19.1	1.44	2.79	55.7	0.05	18.6	0.111	1.51	0.117	0.05
	GT	29	0.02	5.82	18.0	7.35	41.7	0.00	20.4	0.417	6.04	0.401	0.00
DDM_384	OPX	15	0.009	0.815	0.581	4.93	58.4		35.7	0.03	0.322	0.124	0.123
	CPX	6	1.11	19.5	1.19	2.71	55.5	0.06	19.2	0.04	1.05	0.109	0.06
DDM_457	OL	7		0.04	0.01	8.58	41.2		51.1	0.01	0.04	0.114	0.390
	OPX	14		0.777	0.577	5.20	58.3		35.8	0.08	0.325	0.128	0.123
	CPX	15	1.33	19.4	1.32	2.88	55.7	0.06	18.8	0.125	1.39	0.105	0.06
	GT	10		5.99	17.9	7.45	41.7		20.4	0.430	7.36	0.351	
MX 160	OPX	9	0.04	0.384	0.453	4.29	57.3	0.001	36.1	0.002	0.210	0.104	0.08
	GT	9	0.003	5.37	19.3	7.43	41.1	0.00	19.8	0.01	6.40	0.409	0.01
MX 5004	OL	5	0.001	0.04	0.01	8.58	40.6	0.001	50.4	0.004	0.05	0.104	0.379
	OPX	6	0.001	0.775	0.567	5.28	58.7	0.001	35.5	0.02	0.311	0.132	0.124
	CPX	6	1.18	19.6	1.21	2.69	56.0	0.07	18.8	0.03	1.33	0.108	0.06
MX 5006	OL	9	0.01	0.04	0.00	8.68	41.0	0.00	48.9	0.01	0.02	0.108	0.384
	OPX	6	0.139	0.770	0.577	5.16	57.5	0.002	35.4	0.08	0.278	0.120	0.115
	CPX	15	1.24	19.4	1.27	2.75	55.5	0.06	18.8	0.09	1.27	0.102	0.06
MX 5007	OL	3	0.006	0.001	0.008	7.12	41.6	0.00	50.4	0.003	0.01	0.10	0.342
	OPX	3	0.07	0.656	0.461	4.25	58.3	0.002	36.0	0.007	0.256	0.108	0.08
	GT	15	0.007	3.50	18.9	7.50	41.5	0.001	21.1	0.005	7.16	0.450	0.003

Sample	Min	No.	Na2O	CaO	Al2O3	FeO	SiO2	K2O	MgO	TiO2	Cr2O3	MnO	NiO
MX 5026	OL	42	0.001	0.06	0.01	7.33	41.0	0.00	50.9	0.003	0.04	0.103	0.371
	OPX	30	0.02	0.689	0.502	4.38	58.1	0.00	36.0	0.007	0.272	0.110	0.114
	CPX	9	0.789	20.7	0.877	2.06	54.7	0.09	18.8	0.01	0.994	0.10	0.06
	GT	18	0.004	5.64	19.2	6.31	41.8	0.00	20.5	0.06	6.32	0.304	0.01
MX 5044	OL	9	0.002	0.002		6.99	41.4	0.002	50.0	0.00	0.008	0.09	0.384
	OPX	10	0.03	0.280	0.626	4.41	58.3	0.007	35.7	0.002	0.189	0.155	0.02
	GT	6	0.01	5.85	18.7	7.06	41.9	0.008	19.5	0.00	5.30	0.519	0.002
MX 5054	OL	9	0.004	0.003	0.006	6.94	41.6	0.001	50.4	0.00	0.008	0.08	0.428
	OPX	8	0.02	0.389	0.567	4.35	58.1	0.003	35.2		0.319	0.109	0.09
	GT	2		6.27	17.7	7.72	42.8	0.02	18.4		6.20	0.504	
MX 5056	OL	1	0.03	0.04		8.46	41.5	0.002	48.7	0.004	0.07	0.10	
	CPX	1	1.25	18.3	1.53	3.01	55.6	0.04	18.1	0.105	1.26	0.106	
	GT	12	0.04	5.69	19.1	7.12	41.7	0.008	19.8	0.398	6.18	0.321	
MX 5057	OL	4	0.04	0.06		8.77	41.4	0.04	48.7	0.01	0.04	0.10	
	OPX	1	0.184	0.997	0.655	5.32	57.7	0.002	33.9	0.07	0.284	0.111	
	CPX	5	1.29	17.8	1.62	3.26	55.8	0.06	18.5	0.108	1.21	0.100	
	GT	14	0.04	5.28	19.8	7.30	41.9	0.002	20.4	0.260	5.73	0.293	
MX 5059	OL	32	0.003	0.04	0.009	7.12	41.3	0.002	51.4	0.005	0.06	0.10	0.374
	OPX	36	0.03	0.675	0.510	4.30	58.5	0.00	36.0	0.03	0.422	0.109	0.109
	CPX	22	1.47	19.4	1.25	2.13	55.3	0.06	18.3	0.05	2.15	0.09	0.06
MX 5060	OL	8	0.01	0.03	0.001	7.52	41.7	0.004	50.3	0.006	0.03	0.10	0.369
	OPX	8	0.127	0.742	0.587	4.51	58.6	0.002	35.0	0.03	0.313	0.105	0.113
	CPX	9	1.33	19.5	1.61	2.42	55.4	0.06	17.9	0.05	1.52	0.09	0.05
	GT	12	0.03	5.85	17.1	6.65	42.5	0.002	20.0	0.235	6.51	0.318	0.005
MX 5062	OL	9	0.003	0.003		7.44	41.8	0.002	50.4	0.003	0.008	0.08	0.409
	OPX	9	0.03	0.438	0.547	4.64	58.5	0.007	35.3	0.003	0.301	0.110	0.08
	CPX	9	0.740	22.4	1.00	1.49	55.2	0.134	17.6		1.18	0.07	0.04
MX 5009	OL	20	0.02	0.05	0.01	8.33	40.9	0.002	49.2	0.01	0.03	0.109	0.314
	OPX	6	0.192	0.923	0.670	5.05	57.9	0.01	34.3	0.123	0.280	0.196	0.001
	CPX	21	1.40	18.1	1.49	3.01	55.1	0.05	18.5	0.176	1.20	0.134	0.03
	GT	23	0.04	5.61	16.6	7.24	41.6	0.001	19.9	0.533	7.27	0.346	0.004
MX 5016	OL	6	0.03	0.03	0.01	8.19	41.0	0.01	49.4	0.003	0.03	0.109	0.389
	OPX	7	0.09	0.753	0.564	4.93	57.6	0.007	35.2	0.004	0.186	0.116	0.126
	CPX	4	0.826	20.2	1.07	2.47	54.8	0.06	18.6	0.01	0.721	0.10	0.07
	GT	8	0.03	4.81	21.4	6.85	42.3	0.006	20.6	0.06	3.02	0.303	0.01
MX 5022	OL	10	0.006	0.006	0.00	7.76	41.5	0.001	49.5	0.00	0.001	0.08	0.355
	OPX	9	0.04	0.312	0.398	4.77	58.4	0.003	35.0	0.004	0.165	0.106	0.05
	CPX	11	1.41	22.3	1.58	1.48	55.5	0.02	16.2	0.002	1.17	0.05	0.02
	GT	27	0.009	5.44	21.6	8.46	41.8	0.00	19.0	0.02	3.68	0.445	0.00
MX 5023	OL	1	0.01	0.02		7.21	42.0	0.010	50.1		0.03	0.08	0.344
	OPX	10	0.107	0.606	0.507	4.37	58.5	0.008	35.5	0.06	0.306	0.172	0.001
	GT	14	0.03	6.23	17.6	6.42	41.6	0.005	19.9	0.406	8.10	0.364	0.01

8.2.4.2 Average measured compositions of Artemisia xenoliths analysed in this study

Sample	Min	No.	Na2O	CaO	Al2O3	FeO	SiO2	K2O	MgO	TiO2	Cr2O3	MnO	NiO
ART-01	GT	5	0.01	6.08	20.1	8.67	42.0		18.3	0.03	4.61	0.508	0.007
ART-02	GT	5	0.02	6.50	15.8	7.04	41.6		19.1	0.010	8.48	0.329	0.010
ART-08	GT	5	0.01	6.51	19.5	8.90	41.4		17.8	0.005	5.12	0.546	0.00
ART-12	GT	5	0.05	5.36	19.3	7.26	42.6		20.5	0.460	4.31	0.319	0.010
ART-14	GT	15	0.007	6.55	15.2	6.91	41.5		19.2	0.02	9.89	0.333	0.004
ART-16	GT	17	0.007	6.53	18.4	8.63	41.6		17.9	0.03	6.64	0.591	0.002
ART-17	GT	14	0.007	6.50	15.1	6.93	41.6		19.1	0.02	9.83	0.326	0.005
ART-19	GT	5	0.007	6.02	15.5	6.90	41.4		19.6	0.05	8.96	0.322	0.02
ART-22	GT	22	0.01	5.52	17.9	7.01	42.4		20.4	0.312	6.45	0.309	0.002
ART-23	GT	28	0.02	5.62	16.7	7.37	41.8		20.6	1.06	7.03	0.275	0.004
ART-24	GT	27	0.01	4.73	20.2	6.57	42.5		21.7	0.287	4.04	0.281	0.004
ART-25	GT	5	0.05	5.90	17.4	7.83	41.5		19.9	0.829	5.50	0.320	0.010
ART-26	GT	5	0.06	5.95	17.2	7.81	41.6		19.8	0.843	5.81	0.313	0.01
ART-29	GT	5	0.06	5.84	17.4	7.81	41.9		19.6	0.833	5.61	0.307	0.02
ART-32	GT	11	0.02	6.02	15.4	6.90	41.4		19.7	0.428	9.48	0.325	0.009
ART-33	GT	29	0.01	4.81	19.8	6.76	42.8		21.6	0.351	4.17	0.283	0.003
ART-44	GT	2	0.04	5.75	15.8	6.85	41.6		20.1	0.298	8.35	0.310	0.05
ART-45	GT	6	0.09	4.81	20.2	7.33	42.7		21.4	0.876	2.86	0.285	0.009

8.2.4.3 Average measured compositions of Artemisia xenocrysts analysed in this study

Sample	Min	Na2O	CaO	Al2O3	FeO	SiO2	K2O	MgO	TiO2	Cr2O3	MnO
ART-1-1	GT	0.08	5.71	16.4	7.41	43.6		19.9	1.19	6.23	0.255
ART-1-10	GT	0.00	5.74	15.1	6.70	42.9		19.7	0.07	8.68	0.254
ART-1-11	GT	0.005	6.68	15.9	6.77	43.1		19.0	0.210	8.01	0.274
ART-1-12	GT	0.04	6.21	15.0	6.78	42.9		19.5	0.900	8.09	0.269
ART-1-13	GT	0.02	5.75	19.4	8.14	43.5		19.0	0.04	4.83	0.422
ART-1-14	GT	0.003	6.24	17.4	6.63	43.0		19.7	0.124	6.11	0.259
ART-1-15	GT	0.00	5.74	15.2	6.70	42.5		19.7	0.07	8.61	0.263
ART-1-16	GT	0.005	5.76	15.2	6.69	42.6		19.8	0.07	8.65	0.251
ART-1-18	GT	0.02	6.25	18.4	7.66	41.3		18.6	0.06	5.51	0.425
ART-1-19	GT	0.01	6.67	15.8	6.79	42.6		18.9	0.214	7.96	0.287
ART-1-20	GT	0.02	11.4	18.6	6.74	42.6		16.0	0.119	4.60	0.304
ART-1-21	GT	0.02	6.68	15.9	6.80	42.6		19.0	0.198	7.93	0.281
ART-1-22	GT	0.01	11.3	18.8	6.82	42.7		16.0	0.123	4.58	0.309
ART-1-23	GT	0.02	6.28	16.4	6.96	43.2		19.5	0.507	7.09	0.283
ART-1-24	GT	0.02	11.4	18.6	6.75	42.8		15.9	0.116	4.66	0.302
ART-1-27	GT	0.07	4.80	19.8	10.6	41.2		18.9	1.01	2.33	0.341
ART-1-31	GT	0.01	6.22	16.5	6.59	42.8		19.6	0.174	7.35	0.264
ART-1-34	GT	0.00	7.19	15.2	6.81	41.5		18.4	0.07	8.91	0.297
ART-1-35	GT	0.05	4.68	19.9	10.6	43.1		19.0	0.989	2.44	0.335
ART-1-38	GT	0.02	11.6	18.6	6.73	41.0		15.8	0.117	4.54	0.305
ART-1-39	GT	0.06	5.50	17.4	7.26	41.8		20.2	0.830	5.11	0.271
ART-1-4	GT	0.05	5.85	17.0	7.13	42.7		19.8	0.845	5.72	0.291
ART-1-43	GT	0.04	6.96	14.5	7.44	41.7		18.7	1.14	8.08	0.307
ART-1-44	GT	0.07	4.95	19.6	10.7	41.3		18.7	1.13	2.36	0.338
ART-1-45	GT	0.00	6.49	15.5	6.58	41.9		19.1	0.153	8.27	0.298
ART-1-49	GT	0.009	6.46	16.1	6.61	42.6		19.4	0.243	7.52	0.282
ART-1-5	GT	0.03	5.67	18.1	7.04	42.8		19.8	0.495	5.20	0.261
ART-1-50	GT	0.008	6.23	16.5	6.56	42.9		19.6	0.157	7.17	0.266
ART-1-51	GT	0.06	5.04	19.9	7.48	43.5		20.6	0.807	2.95	0.299
ART-1-52	GT	0.04	5.05	19.9	7.10	43.7		20.9	0.588	3.11	0.267
ART-1-53	GT	0.001	5.73	20.7	8.66	43.0		18.4	0.010	3.61	0.474
ART-1-54	GT	0.05	5.18	20.0	7.60	42.1		20.4	0.806	2.59	0.291
ART-1-55	GT	0.05	5.16	19.7	7.56	42.6		20.5	0.813	2.95	0.298
ART-1-56	GT	0.004	5.68	19.6	9.17	41.1		18.2	0.004	3.90	0.434
ART-1-58	GT	0.07	4.94	19.6	10.7	41.2		18.6	1.15	2.28	0.340
ART-1-59	GT	0.007	6.23	19.7	8.76	41.5		17.9	0.007	4.35	0.510
ART-1-6	GT	0.008	5.76	15.2	6.75	42.4		19.8	0.07	8.65	0.284
ART-1-60	GT	0.02	5.92	18.9	7.98	41.7		18.7	0.04	4.91	0.423
ART-1-61	GT	0.007	5.81	15.1	6.70	42.9		19.8	0.07	8.69	0.257
ART-1-62	GT	0.01	5.97	19.4	7.91	41.8		18.8	0.04	4.76	0.432
ART-1-63	GT	0.009	5.14	22.3	9.28	41.7		18.9	0.03	1.61	0.434
ART-1-7	GT	0.00	6.95	15.4	6.75	41.7		18.5	0.07	8.76	0.314
ART-1-8	GT	0.02	11.4	18.7	6.71	42.5		15.9	0.110	4.58	0.315
ART-1-9	GT	0.02	5.82	19.3	8.08	42.0		18.8	0.04	4.69	0.414
ART-2-10	GT	0.009	6.15	15.8	6.58	42.0		19.7	0.401	7.63	0.287
ART-2-11	GT	0.009	9.53	17.1	7.06	41.5		17.3	0.427	5.61	0.267
ART-2-12	GT	0.00	4.50	16.9	6.39	42.9		21.1	0.09	6.95	0.277
ART-2-14	GT	0.07	4.63	21.8	7.41	43.4		21.6	0.716	0.854	0.236
ART-2-15	GT	0.07	6.61	13.8	7.31	42.5		19.0	1.25	8.60	0.283
ART-2-16	GT	0.00	5.46	15.3	6.49	42.8		20.3	0.05	8.23	0.241
ART-2-17	GT	0.04	6.00	16.8	7.02	41.7		19.7	0.643	6.21	0.296
ART-2-18	GT	0.02	9.37	17.1	7.00	42.5		17.2	0.428	5.75	0.283
ART-2-2	GT	0.06	4.47	20.8	9.33	43.6		20.5	0.914	1.40	0.275
ART-2-20	GT	0.05	4.66	20.4	6.38	43.5		21.5	0.398	3.02	0.249
ART-2-21	GT	0.02	5.69	18.7	6.49	41.9		20.0	0.136	5.09	0.293
ART-2-22	GT	0.02	6.50	15.0	6.85	42.4		19.1	0.291	8.65	0.290
ART-2-23	GT	0.01	5.57	19.0	6.53	43.0		20.3	0.05	5.07	0.317
ART-2-24	GT	0.00	4.50	16.9	6.45	43.0		21.1	0.09	6.82	0.272
ART-2-25	GT	0.01	6.12	15.9	6.65	42.5		19.7	0.413	7.53	0.273
ART-2-26	GT	0.01	5.49	19.0	6.53	43.5		20.3	0.05	4.95	0.299
ART-2-27	GT	0.01	5.54	19.0	6.49	42.7		20.2	0.04	5.00	0.306
ART-2-28	GT	0.01	5.63	18.8	6.54	42.6		20.0	0.05	5.13	0.318
ART-2-29	GT	0.02	5.54	19.0	6.53	43.3		20.2	0.05	5.08	0.318
ART-2-3	GT	0.06	6.12	15.7	7.10	41.5		19.7	1.14	6.49	0.274
ART-2-30	GT	0.02	6.00	18.7	7.32	41.6		19.1	0.02	5.29	0.405
ART-2-31	GT	0.02	5.63	18.8	6.55	42.0		20.1	0.04	4.97	0.318

Sample	Min	Na2O	CaO	Al2O3	FeO	SiO2	K2O	MgO	TiO2	Cr2O3	MnO
ART-2-33	GT	0.02	5.49	19.0	6.53	43.6	0.002	20.3	0.04	5.09	0.310
ART-2-34	GT	0.01	6.75	17.6	8.04	42.4	0.00	17.9	0.125	6.45	0.452
ART-2-35	GT	0.02	5.54	19.1	6.47	42.8	0.00	20.2	0.05	4.93	0.317
ART-2-36	GT	0.003	6.20	17.1	6.45	42.6	0.001	19.8	0.143	6.45	0.269
ART-2-37	GT	0.02	5.60	18.9	6.59	42.5	0.00	20.1	0.05	5.00	0.320
ART-2-38	GT	0.02	5.47	19.1	6.51	43.4	0.00	20.3	0.04	5.01	0.324
ART-2-39	GT	0.006	5.69	15.9	6.61	43.2	0.00	19.8	0.221	7.72	0.285
ART-2-4	GT	0.00	6.75	16.1	6.80	42.5	0.00	18.9	0.213	7.45	0.301
ART-2-40	GT	0.01	6.42	15.5	6.84	42.0	0.00	19.2	0.211	7.83	0.283
ART-2-41	GT	0.02	5.53	19.1	6.46	43.0	0.00	20.3	0.05	4.91	0.298
ART-2-5	GT	0.02	6.49	15.4	6.84	42.2	0.00	19.2	0.589	7.79	0.310
ART-2-6	GT	0.01	6.65	15.3	7.10	42.8	0.00	18.7	0.09	8.56	0.306
ART-2-7	GT	0.02	9.64	17.1	7.03	42.0	0.00	17.2	0.425	5.79	0.294
ART-2-8	GT	0.07	6.05	15.4	7.13	42.3	0.00	19.6	1.20	6.92	0.272
ART-2-9	GT	0.02	6.44	15.5	6.90	42.0	0.00	19.3	0.573	7.79	0.292
ART-3-1	GT	0.02	5.39	15.1	6.54	43.1	0.00	20.4	0.00	8.50	0.267
ART-3-10	GT	0.03	8.31	16.9	6.98	42.9	0.00	17.6	0.363	6.87	0.338
ART-3-12	GT	0.06	5.77	16.6	7.36	42.8	0.00	20.0	0.964	5.73	0.254
ART-3-13	GT	0.03	8.10	16.9	7.11	42.6	0.00	17.9	0.396	6.76	0.324
ART-3-14	GT	0.02	5.38	15.1	6.54	42.4	0.00	20.4	0.383	8.35	0.264
ART-3-15	GT	0.07	6.99	16.4	7.52	42.0	0.002	19.0	1.17	5.71	0.281
ART-3-16	GT	0.03	7.68	17.3	7.19	43.3	0.00	18.2	0.418	6.38	0.311
ART-3-17	GT	0.04	6.51	15.5	6.95	42.4	0.00	19.2	0.677	7.83	0.303
ART-3-18	GT	0.07	6.10	16.0	7.46	42.6	0.00	19.7	1.10	6.49	0.290
ART-3-19	GT	0.00	6.40	16.7	6.54	43.4	0.00	19.6	0.08	7.32	0.294
ART-3-2	GT	0.002	7.36	14.5	6.81	42.7	0.002	18.4	0.08	9.64	0.287
ART-3-20	GT	0.02	5.89	19.1	7.80	42.4	0.00	19.1	0.07	5.03	0.423
ART-3-21	GT	0.02	5.85	19.1	7.70	43.2	0.00	19.1	0.07	5.12	0.411
ART-3-22	GT	0.01	5.76	17.4	6.52	41.8	0.001	20.0	0.215	6.49	0.313
ART-3-23	GT	0.01	5.69	17.5	6.55	42.7	0.00	20.1	0.224	6.54	0.298
ART-3-24	GT	0.00	6.12	16.0	6.76	41.9	0.00	19.5	0.07	7.89	0.317
ART-3-25	GT	0.009	6.12	18.8	7.73	42.8	0.00	18.9	0.02	5.51	0.408
ART-3-27	GT	0.002	7.54	14.3	6.75	41.6	0.00	18.3	0.09	9.46	0.304
ART-3-28	GT	0.01	5.73	17.2	6.54	43.0	0.00	20.0	0.224	6.69	0.310
ART-3-29	GT	0.008	5.87	18.5	6.52	42.7	0.00	20.4	0.10	4.86	0.256
ART-3-31	GT	0.05	6.65	13.8	7.62	41.6	0.00	18.7	0.991	8.92	0.273
ART-3-32	GT	0.02	7.86	17.2	7.08	42.0	0.00	18.1	0.404	6.30	0.331
ART-3-33	GT	0.02	5.72	19.3	7.76	42.9	0.00	19.2	0.08	4.84	0.401
ART-3-34	GT	0.01	6.64	17.8	7.62	41.7	0.00	18.3	0.02	6.36	0.415
ART-3-35	GT	0.006	6.01	19.0	7.78	42.2	0.00	18.9	0.02	5.14	0.434
ART-3-36	GT	0.003	5.76	19.5	7.68	42.5	0.00	19.2	0.02	4.74	0.405
ART-3-37	GT	0.03	5.07	18.3	6.72	42.9	0.003	20.3	0.09	6.05	0.327
ART-3-38	GT	0.009	5.98	19.0	7.65	41.3	0.00	18.9	0.02	5.01	0.401
ART-3-39	GT	0.07	6.06	16.4	7.76	42.4	0.001	19.5	1.18	5.66	0.262
ART-3-40	GT	0.01	6.49	17.8	7.55	41.4	0.00	18.6	0.03	6.21	0.388
ART-3-41	GT	0.007	6.27	18.5	7.60	42.0	0.00	18.8	0.03	5.69	0.414
ART-3-42	GT	0.00	7.40	14.4	6.72	41.9	0.00	18.4	0.08	9.36	0.288
ART-3-44	GT	0.006	6.37	15.8	6.81	43.2	0.00	19.5	0.291	7.49	0.277
ART-3-45	GT	0.02	6.49	17.5	6.76	42.4	0.00	19.1	0.180	6.51	0.332
ART-3-46	GT	0.03	7.77	17.5	7.12	42.4	0.00	18.1	0.404	6.08	0.330
ART-3-47	GT	0.005	6.07	17.7	6.54	42.8	0.00	20.1	0.201	5.67	0.267
ART-3-49	GT	0.004	5.84	18.5	6.52	42.4	0.00	20.3	0.10	4.74	0.265
ART-3-5	GT	0.005	7.46	14.4	6.74	42.1	0.00	18.4	0.08	9.55	0.288
ART-3-50	GT	0.009	6.50	15.8	6.93	42.4	0.00	19.5	0.291	7.51	0.277
ART-3-51	GT	0.03	6.17	16.8	6.75	42.0	0.00	19.8	0.569	6.28	0.281
ART-3-52	GT	0.010	5.83	18.4	6.58	43.2	0.00	20.4	0.09	4.90	0.262
ART-3-53	GT	0.00	6.21	17.4	6.62	42.9	0.003	19.9	0.04	6.04	0.263
ART-3-54	GT	0.03	5.26	18.2	6.81	41.9	0.001	20.1	0.110	5.86	0.335
ART-3-55	GT	0.005	6.50	15.8	6.86	42.2	0.00	19.4	0.288	7.36	0.279
ART-3-56	GT	0.002	6.49	15.8	6.71	42.0	0.00	19.5	0.299	7.37	0.269
ART-3-57	GT	0.03	6.33	16.2	6.94	42.4	0.00	19.2	0.369	7.44	0.288
ART-3-58	GT	0.007	6.38	18.0	7.61	43.0	0.00	18.6	0.03	6.25	0.371
ART-3-59	GT	0.003	5.98	19.0	7.72	41.8	0.00	19.0	0.02	5.05	0.434
ART-3-6	GT	0.03	6.40	16.2	7.18	43.1	0.00	19.2	0.618	7.10	0.302
ART-3-7	GT	0.004	5.86	14.9	6.36	43.2	0.00	19.9	0.152	9.32	0.273

Appendix

8.3 RE-OS ISOTOPE DATA

8.3.1 Standard data – DROsS

(Durham Re-Os Standard)

Table 8.3.1: Measured values of DROsS during analytical runs on the Thermo-Finnigan TRITON TIMS at the Northern Centre for Isotopic and Elemental Tracing, Durham University.

	Run Information and Conditions						Average Signal			Oxide and Fractionation corrected ratios (except Re)						
Magazine	Sample Name	Filament type	Date	Detector	Size of Load (ng)	mA	No Ratios	192	240Os (CPS)	185 233Os (CPS)	240/233	190Os/188Os	2SE abs	189Os/188Os	2SE abs	187Os/188Os	2SE abs	186Os/188Os	2SE abs
572	DROsS 4a	Williams May2007	21-Jan-09	SEM	0.10	761	100		370830	2.7	139621	1.99394	0.00026	1.22035	0.00020	0.16077	0.00006	0.11998	0.0001
572	DROsS 4a	Williams May2007	22-Jan-09	SEM	0.10	758	80		327972	1.9	173021	1.99461	0.00032	1.22084	0.00036	0.16076	0.00009	0.12001	0.0001
635	DROsS4a	Williams May 2007	22-Jul-09	SEM	0.10	1095	80		286677	1.5	196921	1.98712	0.00035	1.21974	0.00026	0.16079	0.00009	0.11975	0.0001
659	DROsS 4a	Williams 1	23-Oct-09	SEM	0.10	1100	90		257106	2.3	111737	1.98504	0.00047	1.22102	0.00032	0.16084	0.00010	0.11989	0.0001
660	DROsS 4a	Williams 1	25-Oct-09	SEM	0.10	1085	90		156114	9.7	16162	1.98593	0.00055	1.22029	0.00048	0.16092	0.00013	0.12103	0.0001
720	DROsS 4a	Williams 1	12-Apr-10	SEM	0.10	1075	100		55088	0.9	64551	1.98474	0.00170	1.22081	0.00105	0.16108	0.00016	0.12053	0.0004
728	DROsS 4a	Williams 1	24-Apr-10	SEM	0.10	1120	90		193149	1.2	165397	1.98522	0.00096	1.22081	0.00063	0.16085	0.00009	0.12000	0.0002
780	DROsS 5a	Williams 1	23-Sep-10	SEM	0.01	1170	60		23664	5.9	4037	1.98980	0.00285	1.21981	0.00280	0.16167	0.00037	0.12473	0.0006
780	DROsS 5a	Williams 1	23-Sep-10	SEM	0.01	1083	84		39086	4.3	9107	1.98697	0.00182	1.21748	0.00192	0.16100	0.00024	0.12158	0.0005
788	DROsS3a	Williams 1	13-Oct-10	SEM	1.00	1121	100		387794	1.8	216272	1.98697	0.00053	1.22166	0.00045	0.16046	0.00006	0.11902	0.0001
788	DROsS3a	Williams 1	16-Oct-10	SEM	1.00	1045 - 1035	92		66714	0.2	271759	1.98427	0.00149	1.21942	0.00077	0.16087	0.00015	0.11994	0.0003
788	DROsS3a	Williams 1	16-Oct-10	SEM	1.00	1027	100		53802	0.3	202463	1.98409	0.00256	1.21952	0.00157	0.16094	0.00024	0.11990	0.0004
788	DROsS3a	Williams 1	16-Oct-10	SEM	1.00	1035	100		156522	0.5	298055	1.98386	0.00096	1.21965	0.00050	0.16068	0.00012	0.11981	0.0002
788	DROsS3a	Williams 1	16-Oct-10	SEM	1.00	1050	80		440226	1.2	371332	1.98329	0.00067	1.21947	0.00043	0.16091	0.00010	0.11986	0.0001
788	DROsS3a	Williams 1	16-Oct-10	SEM	1.00	-	40		472245	1.4	348170	1.98401	0.00077	1.21971	0.00045	0.16083	0.00008	0.12005	0.0001
789	DROsS3a	Williams 1	17-Oct-10	SEM	1.00	975	80		60882	0.3	242076	1.98439	0.00143	1.21997	0.00099	0.16097	0.00016	0.11991	0.0003
789	DROsS3a	Williams 1	17-Oct-10	SEM	1.00	994	60		183743	0.4	473491	1.98466	0.00100	1.21973	0.00065	0.16074	0.00014	0.12009	0.0002
803	DROsS 4a	Williams 1	13-Dec-10	SEM	0.10	977	80		93700	38.2	2454	1.98212	0.00115	1.21910	0.00122	0.16105	0.00014	0.12586	0.0005
803	DROsS 4a	Williams 1	14-Dec-10	SEM	0.10	1068	100		239041	9.5	25176	1.98400	0.00062	1.21980	0.00054	0.16081	0.00007	0.12067	0.0002
803	DROsS 4a	Williams 1	14-Dec-10	SEM	0.10	1215	100		256069	21.2	12103	1.98678	0.00072	1.22011	0.00056	0.16106	0.00006	0.12148	0.0002
804	DROsS 4a	Williams 1	15-Dec-10	SEM	0.10	1131	100		257808	13.5	19034	1.98424	0.00078	1.21974	0.00060	0.16090	0.00008	0.12087	0.0002
805	DROsS 4a	Williams 1	16-Dec-10	SEM	0.10	1108	100		202842	35.6	5692	1.98437	0.00070	1.22047	0.00062	0.16087	0.00008	0.12123	0.0002
806	DROsS 4a	Williams 1	17-Dec-10	SEM	0.10	1127	100		312226	10.5	29670	1.98286	0.00076	1.21906	0.00070	0.16076	0.00008	0.12043	0.0002
807	DROsS 4a	Williams 1	18-Dec-10	SEM	0.10	1112	84		315315	7.2	43660	1.98316	0.00064	1.21929	0.00059	0.16077	0.00008	0.12026	0.0002
										Average		1.98568	0.00100	1.21991	0.00078	0.16089	0.00012	0.12070	0.00023
										DROsS Nowell et al., (2004)		1.98379	0.00001	1.21971	0.00002	0.16092	0.00002	0.11993	0.00001

Figure 8.3.1: DROsS $^{187}Os/^{188}Os$ variation during the course of the analytical runs. Highlighted are measurements made on magazines included in this study. Shown in grey are measurements made on the same instrument but for other sample types and studies.

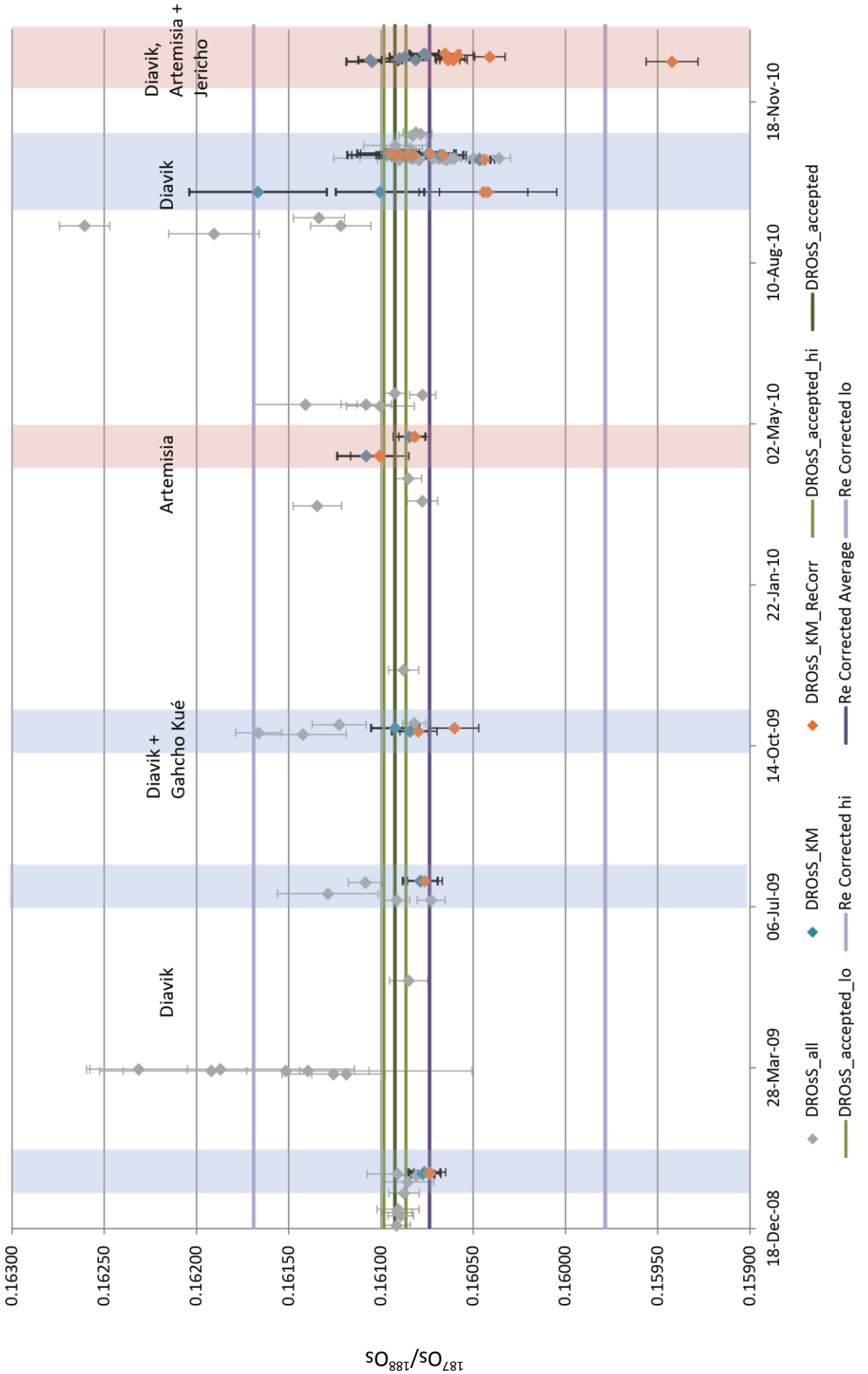

8.3.2 Standard data: GP13 (Global peridotite standard)

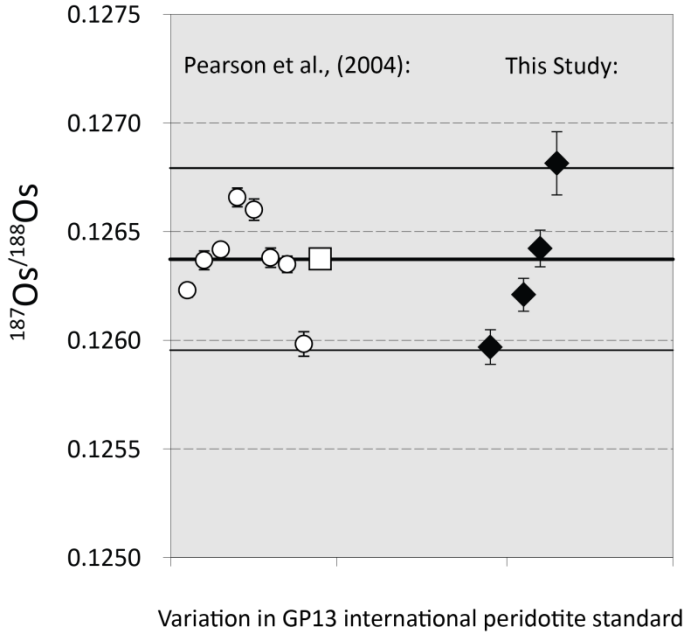

Date	Mag#	187/188Os	1SE
Nov-08	572	0.12597	0.00008
Sep-10	804	0.12621	0.00008
Nov-10	806	0.12642	0.00008
Nov-10	804	0.12681	0.00015
Average		0.12635	0.00010
Pearson et al. (2004)		0.12637	0.00042

Figure 8.3.2: Measured variation in GP13 international peridotite standard (Pearson et al., 2004) analysed on a Thermo-Finnigan TRITON TIMS. Hollow symbols: values (circles) from Pearson et al., (2004) and mean (square). Solid diamonds; values from this study. Errors are 2 Standard Error on $^{187/188}$Os measured by TIMS.

8.3.3 Standard data: pge 1 ppb ICP-MS standard solution

	Re185/Re187	Ir191/Ir193	Pt194/Pt195	Pt194/Pt196
13/08/2009	**0.5960**	**0.5894**	**0.9717**	**1.2977**
	0.0070	*0.0079*	*0.0144*	*0.0251*
09/11/2010	**0.6017**	**0.5979**	**0.9735**	**1.3088**
	0.0084	*0.0089*	*0.0191*	*0.0277*
26/10/2010	**0.6029**	**0.5972**	**0.9749**	**1.3069**
	0.0070	*0.0149*	*0.0226*	*0.0226*
NATURAL	**0.5974**	**0.5949**	**0.9734**	**1.3004**

Summary of 1ppb pge standard solution run on the ThermoFinnigan *ELEMENT2*. A standard is run at intervals during the analytical session in order to correct for mass bias drift. The relative difference between the measured ratios and the accepted (natural) ratios is used to correct the measured sample data. Shown is the ratio measured after the first set of samples for each analytical run.

8.3.4 Measured values

8.3.4.1 Osmium – ordered by run date

Date	Mag#	Locality	batch	No	Name	189/188Os	2 SE	187/188 Os	2 SE	187/188 Os*	186/188 Os	2 SE	OS PPB
Nov-08	557	Diavik	144	5	MX0160	1.21227	0.00100	**0.10941**	0.00011	0.10943	0.12001	0.00000	1.9
Nov-08	557	Diavik	144	6	MX0158	1.21587	0.00065	**0.13374**	0.00008	0.13376	0.11986	0.00000	3.3
Nov-08	572	Std	148	2	GP13	1.21711	0.00086	**0.12597**	0.00008	0.12599	0.11989	0.00000	3.8
Nov-08	572	Diavik	148	3	MX5026	1.22114	0.00069	**0.10849**	0.00007	0.10851	0.11934	0.00000	3.5
Nov-08	572	Diavik	148	4	MX5007	1.20724	0.00120	**0.10647**	0.00012	0.10649	0.11992	0.00000	1.0
Nov-08	572	Diavik	148	5	MX5006	did not run							
Jun-09	572	Diavik	148	6	MX5004	1.21736	0.00063	**0.11894**	0.00007	0.11896	0.11948	0.00000	3.7
Jun-09	635	Diavik	162	1	MX5009	1.21627	0.00083	**0.11432**	0.00009	0.11426	0.11944	0.00000	3.7
Jun-09	635	Diavik	162	2	MX5016	1.21774	0.00062	**0.12031**	0.00008	0.12025	0.11948	0.00000	3.9
Jun-09	635	Diavik	162	3	MX044	1.21053	0.00096	**0.12115**	0.00011	0.12097	0.11974	0.00000	1.1
Jun-09	635	Diavik	162	4	MX5059	1.21676	0.00065	**0.10864**	0.00008	0.10857	0.11978	0.00000	3.7
Jun-09	635	Diavik	162	5	MX5056	1.21773	0.00073	**0.12764**	0.00008	0.12760	0.11975	0.00000	5.3
Jun-09	635	Diavik	162	6	MX5022	1.21316	0.00094	**0.10899**	0.00009	0.10882	0.12054	0.00000	1.4
Aug-09	661	Gahcho Kué	168	2	GAH-02	1.21673	0.00096	**0.11726**	0.00010	0.11726	0.11987	0.00000	3.5
Aug-09	661	Gahcho Kué	168	3	GAH-04	1.21527	0.00080	**0.13038**	0.00013	0.13034	0.12012	0.00000	2.7
Aug-09	660	Gahcho Kué	168	4	GAH-05	1.21813	0.00088	**0.11173**	0.00010	0.11171	0.11991	0.00000	5.4
Aug-09	660	Gahcho Kué	168	5	GAH-10	did not run							
Aug-09	660	Gahcho Kué	168	6	GAH-07	1.21586	0.00102	**0.12130**	0.00012	0.12130	0.11975	0.00000	3.6
Aug-09	789	Gahcho Kué	168	7	GAH-08	1.21624	0.00367	**0.15139**	0.00168	0.14482	0.13366	0.00021	3.4
Aug-09		Diavik	170	1	MX5060	did not run							
Aug-09	660	Gahcho Kué	170	4	GAH-01	1.21840	0.00102	**0.11157**	0.00013	0.11154	0.12011	0.00000	4.5
Aug-09	660	Gahcho Kué	170	5	GAH-09	1.21797	0.00065	**0.11521**	0.00011	0.11520	0.11969	0.00000	5.0
Aug-09	659	Gahcho Kué	170	6	GAH-11	1.21715	0.00095	**0.11059**	0.00009	0.11057	0.11997	0.00000	2.4
Aug-09	661	Gahcho Kué	170	7	GAH-13	1.21322	0.00136	**0.11047**	0.00014	0.11042	0.12021	0.00001	1.7
Sep-09	659	Diavik	171	1	MX5057	1.21589	0.00524	**0.14920**	0.00109	0.14391	0.13417	0.00027	2.7
Sep-09	659	Diavik	171	2	MX5022	1.21694	0.00080	**0.10888**	0.00008	0.10888	0.12020	0.00000	2.7
Sep-09	659	Diavik	171	3	MX5023	1.21876	0.00055	**0.10959**	0.00006	0.10959	0.11962	0.00000	4.2
Sep-09	659	Diavik	171	4	MX5006	1.21901	0.00072	**0.11782**	0.00007	0.11778	0.11995	0.00000	6.5
Sep-09	659	Diavik	171	5	MX5054	1.20640	0.00140	**0.11009**	0.00014	0.11013	0.12021	0.00001	0.74
Sep-09	659	Diavik	171	6	MX5060	1.20743	0.00194	**0.11001**	0.00015	0.11002	0.11986	0.00001	0.74
Mar-10	728	Artemisia	183	1	ART-04	1.21732	0.00069	**0.11438**	0.00010	0.11427	0.11986	0.00000	3.6
Mar-10	720	Artemisia	183	2	ART-09	1.21792	0.00085	**0.11603**	0.00010	0.11603	0.11975	0.00000	3.9
Mar-10	720	Artemisia	183	3	ART-21	1.21156	0.00168	**0.12110**	0.00016	0.12062	0.12170	0.00002	1.4
Mar-10	720	Artemisia	183	4	ART-25	1.21336	0.00115	**0.12107**	0.00014	0.12091	0.12013	0.00001	1.9
Mar-10	728	Artemisia	183	5	ART-32	1.20736	0.00154	**0.11992**	0.00018	0.11949	0.12184	0.00002	1.0
Mar-10	720	Artemisia	183	6	ART-34	1.21799	0.00073	**0.11579**	0.00009	0.11570	0.12019	0.00000	4.8
Mar-10	728	Artemisia	184	2	ART-12	1.21418	0.00172	**0.11193**	0.00019	0.11033	0.12427	0.00010	2.7
Mar-10	728	Artemisia	184	3	ART-13	1.21702	0.00257	**0.11870**	0.00023	0.11620	0.12442	0.00006	5.2
Mar-10	728	Diavik	184	4	MX5022	1.21269	0.00252	**0.10969**	0.00027	0.10857	0.12115	0.00005	1.9
Mar-10	728	Artemisia	184	5	ART-16	1.21679	0.00104	**0.11671**	0.00011	0.11661	0.12004	0.00000	3.0
Mar-10	728	Artemisia	184	6	ART-17	1.21898	0.00069	**0.12133**	0.00006	0.12131	0.11961	0.00000	11.2
Mar-10	728	Artemisia	184	7	ART-14	1.21981	0.00059	**0.12089**	0.00007	0.12084	0.11954	0.00000	12.7
Mar-10	720	Artemisia	185	1	ART-22	1.21427	0.00092	**0.11802**	0.00012	0.11725	0.12174	0.00002	2.2
Mar-10	720	Artemisia	185	2	ART-23	1.21772	0.00132	**0.12431**	0.00014	0.12360	0.12169	0.00002	5.4
Mar-10	720	Artemisia	185	3	ART-24	1.21873	0.00074	**0.11855**	0.00008	0.11831	0.12017	0.00001	4.0
Mar-10	728	Artemisia	185	4	ART-26	1.21542	0.00161	**0.12197**	0.00015	0.12034	0.12484	0.00003	1.8
Mar-10	728	Artemisia	185	6	ART-33	1.21601	0.00129	**0.11937**	0.00015	0.11908	0.12097	0.00001	3.5
Mar-10	728	Artemisia	185	7	ART-35	1.21357	0.00126	**0.11931**	0.00011	0.11875	0.12100	0.00001	1.6
Aug-10	780	Diavik	190	1	DDM_149	1.21867	0.00049	**0.12802**	0.00006	0.12801	0.11965	0.00000	3.7
Aug-10	780	Diavik	190	2	DDM_366	1.21883	0.00055	**0.12009**	0.00006	0.12005	0.11965	0.00000	6.0
Aug-10	780	Diavik	190	3	DDM_327	1.22424	0.00110	**0.11919**	0.00011	0.11919	0.11818	0.00000	2.1
Aug-10	780	Diavik	190	4	DDM_360	1.22137	0.00118	**0.11957**	0.00013	0.11957	0.11818	0.00000	2.1
Aug-10	780	Diavik	190	5	DDM_361	0.97185	0.00678	**0.13170**	0.00056	0.13160	0.12408	0.00007	0.03
Aug-10	780	Diavik	190	6	DDM_335	1.22489	0.00098	**0.11434**	0.00010	0.11432	0.11799	0.00000	3.1
Aug-10	780	Diavik	191	1	DDM_339	1.22381	0.00088	**0.11779**	0.00011	0.11778	0.11788	0.00000	2.3
Aug-10	780	Diavik	191	2	DDM_368	1.22615	0.00082	**0.11678**	0.00008	0.11678	0.11818	0.00000	3.6
Aug-10	780	Diavik	191	3	DDM_367	1.22128	0.00120	**0.11802**	0.00012	0.11801	0.11763	0.00000	1.0
Aug-10	780	Diavik	191	4	DDM_359	1.22700	0.00082	**0.11410**	0.00007	0.11411	0.11798	0.00000	1.9
Aug-10	780	Diavik	191	5	DDM_164	1.22669	0.00054	**0.10979**	0.00006	0.10979	0.11722	0.00000	4.5
Aug-10	780	Diavik	191	6	DDM_384	1.22570	0.00113	**0.12194**	0.00011	0.12193	0.11788	0.00000	1.2
Aug-10		Std	191	7	GP13	did not run							
Aug-10	780	Diavik	192	2	DDM_332	1.21347	0.00148	**0.12405**	0.00018	0.12399	0.11847	0.00001	0.43
Aug-10	788	Diavik	192	3	DDM_372	1.21785	0.00066	**0.11753**	0.00008	0.11753	0.11931	0.00000	3.2
Aug-10	780	Std	192	4	GP13	1.22801	0.00071	**0.12469**	0.00007	0.12466	0.11784	0.00000	3.9
Aug-10	788	Diavik	192	5	DDM_380	0.79708	0.00316	**0.24031**	0.00040	0.23741	0.12653	0.00003	0.02
Aug-10	788	Diavik	192	6	DDM_444	1.21732	0.00044	**0.11716**	0.00008	0.11716	0.11953	0.00000	3.9
Aug-10	788	Diavik	192	7	MX0160	1.21578	0.00036	**0.10969**	0.00006	0.10969	0.11979	0.00000	2.1

Appendix

Date	Mag#	Locality	batch	No	Name	189/188	2 SE	187/188	2 SE	187/188*	186/188	2 SE	OS PPB
Sep-10	804	Diavik	193	1	MX5026	1.21188	0.00130	**0.10662**	0.00014	0.10652	0.12012	0.00001	1.2
Sep-10	804	Diavik	193	2	MX5007	1.21765	0.00097	**0.10892**	0.00012	0.10890	0.12010	0.00000	3.2
Sep-10	789	Diavik	193	3	MX0158	1.21670	0.00068	**0.13513**	0.00012	0.13513	0.11969	0.00000	3.2
Sep-10	789	Diavik	193	4	MX5056	1.21816	0.00038	**0.12636**	0.00007	0.12637	0.11994	0.00000	6.0
Sep-10	789	Diavik	193	5	MX5059	1.21702	0.00053	**0.11044**	0.00007	0.11043	0.11976	0.00000	3.1
Sep-10	789	Diavik	193	6	MX5022	1.21652	0.00055	**0.10884**	0.00010	0.10885	0.11969	0.00000	2.8
Sep-10	789	Artemisia	194	1	ART-01	1.21724	0.00034	**0.11729**	0.00005	0.11729	0.11980	0.00000	4.9
Sep-10	789	Artemisia	194	2	ART-02	1.21880	0.00028	**0.12114**	0.00006	0.12114	0.11981	0.00000	11.2
Sep-10	803	Artemisia	194	3	ART-08	1.21728	0.00078	**0.11582**	0.00007	0.11576	0.12015	0.00000	4.3
Sep-10	803	Artemisia	194	4	ART-19	1.21726	0.00067	**0.11942**	0.00007	0.11932	0.12003	0.00000	4.0
Sep-10	805	Artemisia	194	5	ART-27	1.19724	0.01463	**0.15493**	0.00143	0.10922	0.27885	0.00222	0.81
Sep-10	804	Std	194	7	GP13	1.21718	0.00080	**0.12621**	0.00008	0.12619	0.12022	0.00000	3.8
Nov-10	805	Jericho	198	1	JCO-01	1.18806	0.00179	**0.13017**	0.00026	0.12861	0.12575	0.00003	0.27
Nov-10	805	Jericho	198	2	JCO-02	1.21384	0.00091	**0.10848**	0.00009	0.10819	0.12120	0.00001	2.3
Nov-10	805	Jericho	198	3	JCO-03	1.21754	0.00088	**0.10829**	0.00008	0.10775	0.12200	0.00002	3.5
Nov-10	805	Jericho	198	4	JCO-04	1.21840	0.00062	**0.10673**	0.00006	0.10654	0.12042	0.00000	4.9
Nov-10	807	Jericho	198	5	JCO-05	1.21636	0.00080	**0.10756**	0.00009	0.10654	0.12246	0.00001	2.1
Nov-10	806	Jericho	198	6	JCO-06	1.21677	0.00085	**0.11907**	0.00009	0.11866	0.12124	0.00001	4.7
Nov-10	806	Std	198	7	GP13	1.21786	0.00069	**0.12642**	0.00008	0.12593	0.12144	0.00001	3.8
Nov-10	804	Artemisia	199	1	ART-03	1.18541	0.00256	**0.15423**	0.00048	0.13618	0.17496	0.00035	0.36
Nov-10	805	Artemisia	199	2	ART-21	1.21357	0.00095	**0.11983**	0.00010	0.11935	0.12180	0.00001	1.8
Nov-10	805	Artemisia	199	3	ART-25	1.21435	0.00132	**0.12155**	0.00014	0.12023	0.12449	0.00002	2.3
Nov-10	805	Artemisia	199	4	ART-37	1.21960	0.00067	**0.11604**	0.00008	0.11591	0.12012	0.00000	9.5
Nov-10	805	Artemisia	199	5	ART-46	1.21900	0.00133	**0.11733**	0.00014	0.11674	0.12216	0.00001	4.3
Nov-10	804	Std	199	6	GP13	1.21750	0.00136	**0.12681**	0.00015	0.12661	0.12003	0.00001	3.7
Nov-10	804	n/a	199	7	MetallicA	0.14956	0.00018	**1.21817**	0.00000	0.10654	0.00121	0.00000	1.9
Dec-10	806	Gahcho Kué	200	1	GAH-08	1.21401	0.00114	**0.11367**	0.00015	0.11082	0.12973	0.00005	2.2
Dec-10	806	Gahcho Kué	200	2	GAH-10	1.10795	0.01869	**0.13237**	0.00162	0.06417	0.39692	0.00156	0.05
Dec-10	806	Artemisia	200	3	ART-36	1.21462	0.00124	**0.11892**	0.00015	0.11589	0.12937	0.00003	1.6
Dec-10	807	Artemisia	200	4	ART-43	1.21560	0.00096	**0.11083**	0.00012	0.11024	0.12208	0.00001	2.8
Dec-10	807	Artemisia	200	5	ART-44	1.21681	0.00083	**0.12118**	0.00009	0.12156	0.12323	0.00002	4.2
Dec-10	807	Artemisia	200	6	ART-45	1.21680	0.00086	**0.11701**	0.00009	0.11742	0.12307	0.00001	3.2

187/188* Re correction applied

8.3.4.2 Rhenium – ordered by run date

Locality	Name	Re ppt	-	+	187/185Re	Uncertainty	Batch	#
Diavik	MX0160	1.30	0.984	1.67	0.0384	0.0015	144	5
Diavik	MX0158	203	181	231	0.8944	0.0247	144	6
Std	GP13	272	253	294	1.0012	0.0150	148	2
Diavik	MX5026	62.4	58.3	67.1	0.5327	0.0124	148	3
Diavik	MX5006	162	154	172	0.8191	0.0117	148	5
Diavik	MX5004	99.9	94.7	106	0.7165	0.0110	148	6
Diavik	MX5009	104	97.9	110	0.6639	0.0116	162	1
Diavik	MX5016	134	129	140	0.7685	0.0081	162	2
Diavik	MX044	296	277	319	1.0872	0.0134	162	3
Diavik	MX5059	67.0	62.0	72.8	0.5016	0.0135	162	4
Diavik	MX5056	317	285	358	1.1142	0.0209	162	5
Diavik	MX5022	44.2	38.5	51.6	0.3750	0.0199	162	6
Gahcho Kué	GAH02	123	107	144	0.7330	0.0301	168	2
Gahcho Kué	GAH04	612	524	736	1.3234	0.0234	168	3
Gahcho Kué	GAH05	149	131	173	0.8091	0.0286	168	4
Gahcho Kué	GAH10	42.3	37.5	48.3	0.3644	0.0171	168	5
Gahcho Kué	GAH07	640	538	789	1.3388	0.0254	168	6
Gahcho Kué	GAH08	92.8	81.7	107	0.6195	0.0259	168	7
Gahcho Kué	GAH02	123	107	144	0.7330	0.0301	168	2
Gahcho Kué	GAH04	612	524	736	1.3234	0.0234	168	3
Gahcho Kué	GAH05	149	131	173	0.8091	0.0286	168	4
Gahcho Kué	GAH10	42.3	37.5	48.3	0.3644	0.0171	168	5
Gahcho Kué	GAH07	640	538	789	1.3388	0.0254	168	6
Gahcho Kué	GAH08	92.8	81.7	107	0.6195	0.0259	168	7
Diavik	MX5060	137	118	162	0.8867	0.0327	170	1
Gahcho Kué	GAH01	218	187	261	1.0741	0.0316	170	4
Gahcho Kué	GAH09	107	91.5	128	0.7865	0.0343	170	5
Gahcho Kué	GAH11	106	95.0	119	0.7804	0.0231	170	6
Gahcho Kué	GAH-13	47.3	40.0	57.6	0.4778	0.0298	170	7

Locality	Name	Re ppt	-	+	187/185Re	Uncertainty	Batch	#
Diavik	MX5057	66.2	54.8	83.4	0.5969	0.0387	171	1
Diavik	MX5022	45.4	39.4	53.4	0.4668	0.0244	171	2
Diavik	MX5023	68.8	58.4	83.5	0.6118	0.0336	171	3
Diavik	MX5006	154	125	200	0.9357	0.0474	171	4
Diavik	MX5054	115	97.2	140	0.8173	0.0376	171	5
Diavik	MX5060	142	121	170	0.9032	0.0341	171	6
Artemisia	ART-04	126	111	147	0.7403	0.0282	183	1
Artemisia	ART-09	15.6	12.9	19.5	0.1707	0.0135	183	2
Artemisia	ART-21	35.4	30.4	42.1	0.3201	0.0196	183	3
Artemisia	ART-25	83.9	73.5	97.5	0.5828	0.0261	183	4
Artemisia	ART-32	24.5	20.7	29.8	0.2402	0.0168	183	5
Artemisia	ART-12	12.2	10.4	14.7	0.1406	0.0093	184	2
Artemisia	ART-13	33.2	28.4	39.9	0.3055	0.0197	184	3
Diavik	MX5022	40.4	34.9	47.8	0.3513	0.0204	184	4
Artemisia	ART-16	89.1	79.8	101	0.6024	0.0218	184	5
Artemisia	ART-17	32.6	27.7	39.3	0.2980	0.0199	184	6
Artemisia	ART-14	19.3	15.9	24.2	0.1997	0.0161	184	7
Artemisia	ART-22	186	163	217	0.8968	0.0295	185	1
Artemisia	ART-23	159	140	184	0.8265	0.0281	185	2
Artemisia	ART-24	52.0	45.7	60.2	0.4201	0.0206	185	3
Artemisia	ART-26	122	109	139	0.7273	0.0242	185	4
Artemisia	ART-35	70.3	61.3	82.3	0.5176	0.0255	185	6
Diavik	DDM_149	260	209	345	1.1395	0.0447	190	1
Diavik	DDM_327	199	171	237	1.0370	0.0317	190	3
Diavik	DDM_360	105	91.7	122	0.7796	0.0296	190	4
Diavik	DDM_339	97.5	81.0	122	0.7481	0.0416	191	1
Diavik	DDM_368	157	137	184	0.9483	0.0300	191	2
Diavik	DDM_367	152	128	187	0.9291	0.0385	191	3
Diavik	DDM_359	345	279	453	1.2361	0.0386	191	4
Diavik	DDM_164	198	169	240	1.0371	0.0343	191	5
Diavik	DDM_384	222	185	277	1.0806	0.0381	191	6
Std	GP13	296	247	368	1.1858	0.0342	191	7
Diavik	DDM_332	291	242	365	1.1944	0.0349	192	2
Diavik	DDM_372	140	119	172	0.8991	0.0381	192	3
Std	GP13	310	261	382	1.1996	0.0322	192	4
Diavik	DDM_380	409	336	523	1.2874	0.0325	192	5
Diavik	DDM_444	168	143	204	0.9709	0.0358	192	6
Diavik	MX0160	79.0	69.9	90.7	0.6628	0.0255	192	7
Diavik	MX5026	71.1	61.4	84.3	0.6232	0.0302	193	1
Diavik	MX5007	290	287	293	1.1830	0.0020	193	2
Artemisia	ART-01	75.7	73.2	78.4	0.5844	0.0063	194	1
Artemisia	ART-02	62.7	61.0	64.6	0.5179	0.0049	194	2
Artemisia	ART-08	17.1	16.9	17.2	0.1976	0.0007	194	3
Artemisia	ART-19	68.9	68.6	69.3	0.5517	0.0009	194	4
Artemisia	ART-27	17.3	17.3	17.4	0.2008	0.0002	194	5
Std	GP13	259	256	263	1.1369	0.0026	194	7
Jericho	JCO-01	276	270	283	1.1618	0.0042	198	1
Jericho	JCO-02	39.7	39.6	39.9	0.4257	0.0006	198	2
Jericho	JCO-03	32.8	32.6	32.9	0.3701	0.0005	198	3
Jericho	JCO-04	18.8	18.7	18.8	0.2428	0.0002	198	4
Jericho	JCO-05	7.23	7.22	7.24	0.1177	0.0000	198	5
Jericho	JCO-06	110	109	111	0.7980	0.0022	198	6
Std	GP13	271	267	275	1.1543	0.0027	198	7
Artemisia	ART-03	19.7	19.6	19.7	0.2164	0.0002	199	1
Artemisia	ART-21	36.2	36.1	36.3	0.3449	0.0003	199	2
Artemisia	ART-25	80.5	80.3	80.7	0.6083	0.0005	199	3
Artemisia	ART-37	51.4	51.3	51.5	0.4548	0.0004	199	4
Artemisia	ART-46	51.6	51.5	51.8	0.4541	0.0005	199	5
Std	GP13	264	264	264	1.1454	0.0000	199	6
Artemisia	ART-36	65.6	65.4	65.9	0.5349	0.0007	200	3
Artemisia	ART-43	31.9	31.9	32.0	0.3228	0.0003	200	4
Artemisia	ART-44	28.2	28.1	28.3	0.2926	0.0003	200	5
Artemisia	ART-45	35.1	35.0	35.2	0.3456	0.0004	200	6

8.3.5 Blanks

8.3.5.1 Osmium (all blanks, with average)

ID	**Os Blk pg**	189/188 Os	187/188 Os	186/188 Os	184/188 Os
144-7	**0.95**	1.21937	0.14051	0.12163	0.00150
148-1	**0.69**	1.20823	0.14658	0.00089	0.00150
162-7	**1.1**	1.25101	0.41511	0.23449	0.00150
168-1	**2.0**	1.21346	0.15094	0.14399	0.00150
171-7	**0.36**	1.09793	0.25462	0.43763	0.00150
183-7	**1.3**	1.22252	0.12447	0.17703	0.00150
184-1	**1.9**	1.16651	0.33608	0.33371	0.00150
190-7	**0.61**	1.30422	0.23609	0.19293	0.00150
193-7	**0.45**	1.19546	0.21391	0.12518	0.00150
200-7	**2.2**	1.22583	0.11837	0.15921	0.00150
AVERAGE BLANK	**1.1**	1.21045	0.21367	0.19267	0.00150

8.3.5.2 Rhenium (all blanks, with average)

ID	Asher vial #	Re **ppt**
162	7	**b.d.l.**
168	1	**0.59**
171	7	**0.54**
183	7	**b.d.l.**
184	1	**0.47**
190	7	**15.2**
192	1	**144**
AVERAGE BLANK		**32**

8.4 BULK-ROCK X-RAY FLOURESCENCE

8.4.1 Standard Data

BATCH 1				
wt. %	WS-E 3	WS-E 26	WS-E Recommended	**% variation**
SiO2	51.3	51.2	51.1	**0.30%**
TiO2	2.42	2.42	2.43	**0.16%**
Al2O3	13.8	13.9	13.8	**0.50%**
Fe2O3 (T)	13.2	13.2	13.2	**0.22%**
MnO	0.170	0.167	0.171	**1.6%**
MgO	5.63	5.61	5.55	**1.3%**
CaO	9.03	9.02	8.95	**0.82%**
Na2O	2.41	2.42	2.47	**2.2%**
K2O	0.993	0.992	1.000	**0.77%**
P2O5	0.300	0.300	0.302	**0.67%**
LOI	0.850	0.850	0.850	
BATCH 1				
wt. %	G94 2	G94 25	G94 Recommended	**% variation**
SiO2	69.8	69.7	69.9	**0.30%**
TiO2	0.311	0.313	0.314	**0.63%**
Al2O3	14.6	14.6	14.7	**0.35%**
Fe2O3 (T)	3.07	3.06	3.05	**0.32%**
MnO	0.08	0.07	0.08	**1.0%**
MgO	1.06	1.06	1.04	**2.0%**
CaO	1.35	1.35	1.34	**0.89%**
Na2O	4.63	4.66	4.60	**0.98%**
K2O	2.97	2.96	2.96	**0.18%**
P2O5	0.166	0.169	0.165	**1.5%**
LOI	1.97	1.97	1.97	
BATCH 1				
wt. %	UB-N 1	UB-N 24	UB-N Recommended	**% variation**
SiO2	40.1	40.2	39.9	**0.58%**
TiO2	0.10	0.102	0.110	**8.5%**
Al2O3	2.84	2.86	2.94	**3.2%**
Fe2O3 (T)	8.48	8.47	8.45	**0.25%**
MnO	0.120	0.121	0.120	**0.45%**
MgO	35.6	35.6	35.7	**0.22%**
CaO	1.23	1.23	1.22	**0.83%**
Na2O	0.119	0.143	0.100	**31%**
K2O	0.02	0.02	0.02	**16%**
P2O5	0.02	0.02	0.04	**55%**
LOI	11.1	11.1	11.1	

BATCH 2				
wt. %	WS-E 5	WS-E 24	WS-E commend	**% variation**
SiO2	51.3	51.2	51.1	**0.29%**
TiO2	2.42	2.42	2.43	**0.10%**
Al2O3	13.9	13.9	13.8	**0.76%**
Fe2O3 (T)	13.2	13.2	13.2	**0.30%**
MnO	0.172	0.170	0.171	**0.67%**
MgO	5.64	5.61	5.55	**1.3%**
CaO	9.00	9.02	8.95	**0.65%**
Na2O	2.42	2.42	2.47	**2.1%**
K2O	0.992	0.991	1.000	**0.83%**
P2O5	0.301	0.297	0.302	**0.97%**
LOI	0.850	0.850	0.850	
BATCH 2				
wt. %	G94 4	G94 23	G94 commend	**% variation**
SiO2	69.7	69.8	69.9	**0.25%**
TiO2	0.312	0.309	0.314	**1.0%**
Al2O3	14.6	14.6	14.7	**0.34%**
Fe2O3 (T)	3.06	3.05	3.05	**0.18%**
MnO	0.08	0.08	0.08	**0.40%**
MgO	1.05	1.06	1.04	**1.5%**
CaO	1.35	1.35	1.34	**0.93%**
Na2O	4.63	4.64	4.60	**0.77%**
K2O	2.98	2.96	2.96	**0.32%**
P2O5	0.168	0.166	0.165	**1.3%**
LOI	1.97	1.97	1.97	
BATCH 2				
wt. %	UB-N 3	UB-N 22	UB-N commend	**% variation**
SiO2	40.1	40.2	39.9	**0.50%**
TiO2	0.101	0.102	0.110	**7.9%**
Al2O3	2.84	2.85	2.94	**3.18%**
Fe2O3 (T)	8.46	8.47	8.45	**0.17%**
MnO	0.120	0.121	0.120	**0.46%**
MgO	35.7	35.6	35.7	**0.03%**
CaO	1.24	1.22	1.22	**0.82%**
Na2O	0.128	0.139	0.100	**34%**
K2O	0.02	0.01	0.02	**18%**
P2O5	0.02	0.02	0.04	**55%**
LOI	11.1	11.1	11.1	

Table 8.4.1: Bulk-rock XRF standard repeatability for Whin-Sill dolerite (WS-E), Threkeld microgranite (G94) and Serptentinite (UB-N) from both analytical runs. % variation from accepted values, shown in bold.

8.4.2 Measured values

Whole-rock XRF major elements from Artemisia and Diavik xenoliths. Owing to the high LOI (Artemisia – red italic) and CaO (Diavik – red italic), only the Al_2O_3 values have been used in this thesis, since these are relatively immune to the effects of post-eruption weathering and alteration.

8.4.2.1 Artemisia xenoliths

	Weight % (ah)									
Sample	**SiO2**	**TiO2**	**Al2O3**	**FeO***	**MnO**	**MgO**	**CaO**	**Na2O**	**K2O**	***Volat***
ART-01	48.8	0.05	1.76	7.09	0.07	33.7	0.596	0.02	0.04	***11.0***
ART-02	49.9	0.09	0.964	6.78	0.05	34.0	0.596	0.01	0.05	***9.69***
ART-03	51.4	0.10	0.717	6.55	0.03	33.5	0.384	0.02	0.04	***10.9***
ART-04	49.0	0.03	0.891	6.56	0.05	36.0	0.137	0.00	0.02	***11.4***
ART-08	50.1	0.01	0.956	6.88	0.05	33.9	0.395	0.00	0.02	***10.4***
ART-09	49.0	0.09	0.659	6.93	0.05	34.9	0.557	0.02	0.02	***10.3***
ART-12	48.6	0.148	1.42	6.57	0.06	35.4	0.483	0.01	0.03	***10.3***
ART-13	51.0	0.03	0.812	6.18	0.04	34.8	0.176	0.02	0.02	***9.53***
ART-14	48.9	0.02	0.621	6.79	0.05	35.7	0.379	0.03	0.02	***11.8***
ART-16	49.9	0.04	0.469	6.53	0.04	35.6	0.165	0.02	0.03	***11.4***
ART-17	49.2	0.03	0.818	6.77	0.05	34.8	0.766	0.02	0.02	***10.1***
ART-19	51.3	0.05	0.763	6.71	0.04	33.5	0.183	0.00	0.03	***11.3***
ART-21	49.2	0.05	1.67	6.24	0.06	35.0	0.826	0.03	0.04	***11.4***
ART-22	47.4	0.08	1.04	6.62	0.06	37.1	0.275	0.00	0.02	***11.5***
ART-23	48.6	0.10	1.04	6.27	0.04	36.6	0.390	0.004	0.01	***11.3***
ART-24	49.7	0.08	1.46	6.45	0.06	34.3	0.666	0.03	0.04	***10.4***
ART-25	47.6	0.08	0.824	7.01	0.05	36.5	0.153	0.010	0.02	***11.3***
ART-26	47.1	0.07	0.688	7.31	0.05	36.4	0.161	0.01	0.02	***11.6***
ART-27	47.6	0.10	0.632	6.59	0.06	37.5	0.225	0.00	0.02	***11.5***
ART-29	46.9	0.08	0.736	7.36	0.05	36.5	0.190	0.00	0.02	***10.7***
ART-32	49.1	0.09	0.756	6.55	0.06	34.9	1.28	0.02	0.02	***9.58***
ART-33	49.1	0.07	1.58	6.64	0.07	34.3	0.840	0.02	0.03	***11.6***
ART-34	52.8	0.02	0.561	5.98	0.04	33.8	0.109	0.04	0.03	***10.2***
ART-35	48.8	0.06	0.546	5.97	0.05	37.8	0.172	0.003	0.02	***11.1***
ART-36	49.1	0.144	1.24	7.06	0.05	34.2	0.319	0.02	0.03	***11.1***
ART-37	48.8	0.07	0.638	6.25	0.05	37.0	0.187	0.00	0.02	***11.0***
ART-43	49.6	0.006	1.05	5.96	0.04	36.5	0.239	0.00	0.02	***10.3***
ART-44	51.5	0.08	0.931	6.31	0.05	33.4	0.613	0.02	0.04	***11.1***
ART-45	47.9	0.149	1.95	7.11	0.06	34.1	0.737	0.006	0.04	***10.6***
ART-46	48.9	0.07	0.611	6.02	0.05	37.5	0.157	0.00	0.02	***10.9***

8.4.2.2 *Diavik xenoliths*

	Weight % (ah)									
Sample	**SiO2**	**TiO2**	**Al2O3**	**FeO***	**MnO**	**MgO**	***CaO***	**Na2O**	**K2O**	**Volat**
Diavik										
DDM-149	40.4	0.150	4.19	6.67	0.167	32.1	***8.37***	0.269	0.159	5.13
DDM-164	44.6	0.010	1.69	6.55	0.07	39.4	***0.36***	0.00	0.02	3.46
DDM-327	39.0	0.159	2.86	6.72	0.340	31.5	***11.7***	0.142	0.07	5.41
DDM-332	42.1	0.05	0.768	7.02	0.108	41.4	***0.74***	0.006	0.04	3.15
DDM-335	37.5	0.108	1.42	6.67	0.376	36.6	***9.72***	0.04	0.08	7.77
DDM-336	43.9	0.156	2.27	7.30	0.143	35.4	***2.56***	0.09	0.05	7.40
DDM-339	39.2	0.121	1.88	7.37	0.241	35.8	***6.91***	0.153	0.07	5.21
DDM-359	38.3	0.07	0.780	7.06	0.265	40.1	***5.33***	0.02	0.09	1.80
DDM-360	38.6	0.09	2.07	7.06	0.189	38.0	***5.65***	0.06	0.316	6.49
DDM-361	39.9	0.102	0.877	7.13	0.190	39.7	***4.00***	0.03	0.10	5.66
DDM-367	38.0	0.104	0.668	7.20	0.194	39.8	***5.76***	0.005	0.159	10.2
DDM-368	40.8	0.07	0.824	6.71	0.148	40.0	***3.80***	0.04	0.143	1.42
DDM-372	41.2	0.177	3.19	6.11	0.270	32.4	***9.68***	0.124	0.05	8.83
DDM-380	35.2	0.04	0.185	7.67	0.208	40.0	***8.05***	0.00	0.02	4.88
DDM-384	41.9	0.07	0.915	6.04	0.210	37.3	***6.29***	0.06	0.354	4.77
DDM-444	42.8	0.06	1.18	7.04	0.111	39.4	***1.31***	0.05	0.163	4.46
MX0158	43.0	0.155	2.66	6.25	0.141	33.2	***7.05***	0.300	0.218	5.32
MX0160	42.3	0.04	0.576	6.10	0.153	36.2	***7.62***	0.04	0.123	2.36
MX044	38.0	0.147	2.44	10.2	0.151	28.7	***8.66***	0.219	0.08	2.96
MX5004	39.0	0.04	1.21	6.89	0.227	38.6	***6.27***	0.03	0.06	2.14
MX5006	39.7	0.08	0.845	6.98	0.174	40.7	***3.53***	0.03	0.198	3.92
MX5007	39.1	0.09	0.531	6.62	0.103	45.2	***0.84***	-0.01	0.103	5.91
MX5009	35.8	0.09	0.980	6.73	0.319	37.8	***10.7***	0.04	0.02	3.78
MX5016	40.4	0.03	2.02	6.41	0.174	36.7	***6.94***	0.07	0.07	10.1
MX5022	39.7	0.05	1.50	6.30	0.244	38.3	***6.49***	0.07	0.268	2.47
MX5023	41.1	0.05	0.715	6.08	0.128	42.4	***2.70***	0.009	0.03	7.44
MX5026	41.8	0.03	1.18	5.93	0.156	40.6	***3.52***	0.03	0.133	6.13
MX5054	44.1	0.09	0.579	6.37	0.10	40.9	***0.59***	0.02	0.133	5.49
MX5056	44.5	0.140	1.85	7.50	0.117	36.3	***1.09***	0.07	0.05	3.23
MX5057	39.5	0.10	1.23	6.93	0.146	37.3	***6.90***	0.07	0.123	0.860
MX5059	40.2	0.03	0.240	6.00	0.175	42.6	***4.07***	0.01	0.02	9.01
MX5060	38.2	0.06	1.49	6.14	0.311	36.5	***10.3***	0.06	0.05	4.98

8.5 LA-ICP-MS TRACE ELEMENTS

8.5.1 Standard Data

8.5.1.1 GSD-1G

	Accepted	Measured	1 st dev (%)
Ba	67	67	1.3%
Ca	51463	51463	0.0%
Ce	41.4	41.5	1.2%
Co	40	40	2.1%
Dy	51.2	51.4	2.3%
Er	40.1	40.3	2.4%
Eu	41	41	1.7%
Fe	103390	103643	1.6%
Ga	54	54	1.8%
Gd	50.7	50.9	2.3%
Hf	39	39	2.5%
Ho	49	49	2.4%
La	39.1	39.2	1.7%
Lu	51.5	51.7	2.5%
Mg	21715	21741	1.4%
Mn	220	220	1.2%
Nb	**53.2**	**42.1**	**1.2%**
Nd	44.7	44.8	1.6%
Ni	58	58	2.8%
P	860	862	2.7%
Pr	45	45	1.4%
Rb	37.3	37.4	1.6%
Sc	52	52	1.6%
Si	248722	249490	2.9%
Sm	47.8	48.0	2.0%
Sr	69.4	69.5	0.9%
Ta	40	40	2.5%
Tb	47	47	2.2%
Ti	7435	7436	0.6%
Tm	49	49	2.5%
V	44	44	1.0%
Y	42	42	1.8%
Yb	50.9	51.1	2.5%
Zn	54	54	2.7%
Zr	42	42	1.7%

8.5.1.2 PN-2 mantle garnet

	AVERAGE MEASURED	Cox and barnes	Schmidberger et al., 2007	2 sigma	Canil et al., min.	Canil et al., max.
Ni	43.6	47.5				
Ga	6.05					
Rb	0.01		5.40		7.45	
Sr	0.220		0.340		0.240	0.300
Y	58.0		54.0	*6.90*	50.7	54.3
Zr	42.1		44.4	*5.20*	36.5	49.0
Ba	0.004				0.010	0.02
La	0.02	0.03	0.02		0.010	0.03
Ce	0.193	0.200	0.190	*0.03*	0.140	0.210
Pr	0.08	0.09	0.07	*0.010*	0.08	0.09
Nd	0.949	1.23	0.700	*0.06*	0.910	1.50
Sm	1.14	1.32	1.08	*0.08*	1.10	1.40
Eu	0.705	0.820	0.740	*0.05*	0.670	0.890
Gd	3.67	3.83	2.74	*0.270*	3.23	4.06
Tb	0.901	1.06	0.820	*0.05*	0.870	1.08
Dy	8.19	9.53	8.44	*0.600*	7.94	9.98
Ho	2.15	2.29	2.03	*0.140*	2.04	2.44
Er	7.46	7.31	6.49	*0.520*	6.13	8.32
Tm	1.10	0.905	0.910	*0.09*	0.820	0.990
Yb	7.99	6.64	6.14	*0.580*	4.73	8.55
Lu	1.21	1.04	0.870	*0.09*	0.620	1.45
Hf	0.838		0.720	*0.08*	0.770	0.940

8.5.2 Measured values

8.5.2.1 Diavik garnet

Other trace elements

Sample	Ni ppm	Y ppm	Zr ppm	Ga ppm	Ti ppm
DDM-131	96.0	15.8	47.2	11.7	3969
DDM-149	84.2	17.2	28.2	12.7	2709
DDM-164	576719	4.04	441	14763	83297
DDM-327	110	11.3	35.7	10.6	3996
DDM-332	56.6	3.49	15.9	5.28	1675
DDM-335	95.0	13.3	51.8	8.39	4312
DDM-339	91.8	5.79	26.7	6.99	2183
DDM-360	92.4	8.85	33.6	9.57	2014
DDM-361	83.6	7.26	42.2	8.44	4786
DDM-366	98.4	11.4	48.4	8.11	3919
DDM-367	82.3	6.75	28.9	9.86	4221
DDM-368	79.6	5.43	24.8	7.48	2435
DDM-372	87.5	7.18	35.1	7.34	3204
DDM-384	810	6.04	42.3	90.2	5549
DDM-431	29.1	0.173	3.98	2.45	42
DDM-444	68.4	4.94	31.5	6.57	1662
MX160	19.6	0.519	3.44	1.74	83
MX5007	11094	0.719	8.70	6.08	705
MX5009	104	18.0	57.1	11.1	5004
MX5022	15.6	5.78	1.05	4.80	188
MX5023	64.8	8.17	59.2	4.97	2287
MX5069	58.1	9.74	27.6	5.93	1533

Rare-earth elements:

CI Chondrite (McDonough and Sun, 1995) Normalised														
Sample	La	Ce	Pr	Nd	Sm	Eu	Gd	Tb	Dy	Ho	Er	Tm	Yb	Lu
DDM-131	0.109	0.459	1.07	1.98	4.25	5.38	6.29	6.41	7.10	6.84	7.09	6.84	6.97	6.89
DDM-149	0.02	0.102	0.286	0.673	2.12	3.29	4.49	5.29	6.71	7.41	8.47	8.60	9.27	9.08
DDM-327	0.09	0.379	0.871	1.66	3.32	3.97	4.37	4.30	4.71	4.80	5.38	5.63	6.05	6.60
DDM-332	0.155	0.639	1.50	2.63	3.99	3.73	2.99	2.09	1.81	1.50	1.54	1.47	1.67	2.05
DDM-335	0.133	0.551	1.29	2.46	4.96	6.38	7.25	6.94	6.90	5.92	5.24	4.38	4.22	4.31
DDM-339	0.142	0.542	1.18	2.03	3.73	4.10	3.99	3.20	2.92	2.42	2.45	2.50	2.71	3.22
DDM-360	0.07	0.294	0.723	1.43	3.33	3.91	4.19	3.64	3.88	3.84	4.28	4.49	4.84	5.28
DDM-361	0.174	0.692	1.57	2.80	5.27	6.47	6.28	5.09	4.46	3.23	2.54	2.07	2.16	2.41
DDM-366	0.124	0.494	1.20	2.22	4.75	5.81	6.59	6.24	6.13	4.91	4.35	3.90	3.83	4.09
DDM-367	0.168	0.696	1.60	2.73	4.14	4.46	4.32	3.65	3.50	2.88	2.77	2.47	2.62	2.65
DDM-368	0.127	0.540	1.29	2.38	4.36	4.60	4.16	3.13	2.75	2.36	2.33	2.31	2.66	3.08
DDM-372	0.09	0.395	0.960	1.80	3.81	4.56	4.73	3.95	3.76	3.09	2.87	2.63	2.85	2.96
DDM-384	0.150	0.614	1.54	2.96	4.77	4.82	4.43	3.24	2.97	2.26	2.08	1.96	2.16	2.48
DDM-431	1.30	4.00	6.21	6.57	3.02	1.64	0.795	0.251	0.113	0.07	0.09	0.218	0.434	0.820
DDM-444	0.283	0.548	1.14	2.04	4.14	4.61	4.25	3.06	2.68	2.12	2.03	2.09	2.25	2.71
MX160	3.97	7.27	10.1	15.0	9.36	5.01	2.15	0.712	0.339	0.199	0.166	0.179	0.231	0.352
MX5007	1.36	3.62	6.23	6.28	2.86	1.85	1.18	0.489	0.262	0.166	0.209	0.413	0.999	1.64
MX5009	0.154	0.646	1.52	2.76	5.66	6.90	7.93	7.96	8.40	7.77	7.37	6.43	5.93	5.52
MX5022	0.05	0.198	0.447	0.757	0.793	0.750	0.937	1.15	1.81	2.33	3.30	4.00	4.67	5.57
MX5069	0.108	0.414	0.965	1.90	4.45	4.75	5.16	4.63	4.88	4.30	4.13	4.21	4.16	4.48

8.5.2.2 Artemisia xenolith garnet

Other trace elements:

Sample	Ni ppm	Y89 ppm	Zr90 ppm	Ga69 ppm	Ti49 ppm
ART-01	19.8	1.58	1.35	3.62	167
ART-02	95.4	0.608	23.6	5.54	91
ART-08	39.7	0.608	2.63	3.62	50
ART-12	99.3	2.83	26.3	7.00	2795
ART-14	93.9	0.570	17.4	5.60	91
ART-16	19.8	1.46	1.30	4.08	275
ART-17	93.3	0.437	19.7	5.49	92
ART-19	95.8	0.992	1.03	5.19	283
ART-22	100.7	5.22	48.3	6.31	2652
ART-23	136.3	20.1	79.7	12.0	5917
ART-24	105.2	10.9	15.7	9.66	1558
ART-25	112.8	19.4	67.8	11.1	4891
ART-26	113.5	19.5	68.2	10.9	4904
ART-29	111.5	19.2	67.6	10.8	4839
ART-32	95.3	2.75	21.9	5.49	2311
ART-33	113.7	12.1	18.3	10.1	1726
ART-44	108.0	3.54	13.3	4.65	1854
ART-45	118.8	15.9	54.3	10.8	4594
ART-46	121.8	16.5	60.9	11.0	5224

Rare-earth elements:

CI Chondrite (McDonough and Sun, 1995) Normalised														
Sample	La	Ce	Pr	Nd	Sm	Eu	Gd	Tb	Dy	Ho	Er	Tm	Yb	Lu
ART-01	0.108	0.265	0.417	0.540	0.696	0.626	0.621	0.512	0.587	0.650	0.915	1.14	1.60	2.14
ART-02	0.356	1.38	3.13	5.49	7.48	5.84	3.45	1.38	0.605	0.254	0.206	0.378	0.792	1.37
ART-08	0.170	0.459	0.835	1.10	1.22	1.04	0.746	0.389	0.273	0.187	0.185	0.249	0.384	0.485
ART-12	0.160	0.643	1.70	4.12	8.57	7.29	4.30	1.86	1.23	1.13	1.48	2.02	2.74	3.57
ART-14	0.375	1.42	3.16	5.37	6.05	4.26	2.58	1.08	0.550	0.259	0.241	0.393	0.871	1.49
ART-16	0.03	0.08	0.139	0.207	0.334	0.356	0.438	0.405	0.492	0.565	0.816	1.09	1.47	1.96
ART-17	0.365	1.43	3.20	5.52	6.94	5.15	2.89	1.07	0.443	0.195	0.188	0.379	0.844	1.49
ART-19	0.692	1.26	1.30	0.695	0.209	0.293	0.273	0.251	0.315	0.406	0.595	1.01	1.62	2.30
ART-22	0.215	0.706	1.52	2.81	6.43	7.21	6.51	4.29	3.28	2.37	2.09	1.98	2.27	2.76
ART-23	0.296	0.990	2.15	3.79	7.90	9.78	11.2	10.6	10.9	9.50	8.85	7.64	6.96	6.21
ART-24	0.192	0.605	1.18	1.92	2.93	3.38	3.75	3.81	4.45	4.67	5.26	5.49	5.99	6.21
ART-25	0.252	0.883	1.83	3.06	5.92	7.15	8.14	8.11	9.21	8.84	9.03	8.33	8.24	7.91
ART-26	0.312	0.938	1.91	3.15	6.00	7.30	8.31	8.35	9.38	9.01	9.18	8.60	8.28	7.72
ART-29	0.250	0.888	1.85	3.05	5.94	7.07	8.07	8.09	9.07	8.75	8.84	8.19	8.09	7.70
ART-32	0.482	1.07	2.29	3.89	3.22	1.86	1.12	0.458	0.590	0.840	1.12	1.75	2.36	2.50
ART-33	0.171	0.575	1.12	1.80	2.91	3.44	3.93	4.05	4.73	4.88	5.44	5.60	5.93	6.12
ART-44	0.318	1.10	2.32	3.92	4.15	2.97	1.97	1.40	1.47	1.58	1.94	2.26	2.77	3.69
ART-45	0.173	0.656	1.47	2.67	5.67	6.65	7.30	6.70	7.26	6.93	7.25	7.01	7.30	7.17
ART-46	0.176	0.670	1.54	2.79	6.12	7.33	7.65	7.20	7.61	7.10	7.29	7.16	7.10	6.94

8.5.2.3 Artemisia xenocryst garnet

Other trace elements:

Sample	Ni ppm	Y ppm	Zr ppm	Ga ppm	Ti ppm
ART1-1	135	22.6	109	15.6	7159
ART1-10	139	1.85	9.50	6.48	448
ART1-11	113	2.67	21.2	7.25	1271
ART1-12	139	16.2	78.0	6.89	5182
ART1-13	42.9	2.24	2.50	3.79	253
ART1-14	118	2.54	14.3	6.64	769
ART1-15	136	1.83	8.26	6.08	446
ART1-16	136	1.84	7.44	6.00	440
ART1-17	109	0.283	8.56	5.02	455
ART1-18	51.3	0.998	21.2	7.24	416
ART1-19	106	2.74	16.3	6.79	1252
ART1-2	114	4.32	15.7	6.03	882
ART1-20	80.7	13.6	33.8	4.94	699
ART1-21	106	2.84	26.2	6.86	1199
ART1-22	80.0	13.6	33.7	4.88	693
ART1-23	117	9.13	51.8	7.64	2951
ART1-24	83.6	13.6	33.4	5.12	691
ART1-25	142	2.28	17.9	6.70	676
ART1-26	106	11.7	49.4	8.91	4808
ART1-27	68.7	19.5	95.7	11.9	6132
ART1-28	118	11.3	62.0	7.58	3664
ART1-29	138	1.87	9.21	6.20	462
ART1-3	132	1.79	8.19	5.99	433
ART1-30	39.8	0.607	4.56	4.35	245
ART1-31	127	3.10	41.6	6.47	1009
ART1-32	126	11.3	62.7	8.00	3766
ART1-33	121	9.43	53.5	7.93	3028
ART1-34	94.6	2.45	4.15	5.68	394
ART1-35	67.0	18.7	92.9	11.3	5809
ART1-36	38.5	0.965	0.438	4.70	62.8
ART1-37	142	2.25	15.5	6.72	683
ART1-38	81.5	14.0	34.1	4.93	699
ART1-39	142	18.5	80.4	10.8	4901
ART1-4	133	17.4	68.7	10.5	4830
ART1-40	20.2	0.696	0.400	3.38	72.6
ART1-41	117	1.71	28.6	6.35	1875
ART1-42	82.1	14.1	34.4	5.04	704
ART1-43	119	28.8	98.0	12.5	6611
ART1-45	117	4.50	16.3	6.08	890
ART1-46	125	2.95	36.7	6.20	955
ART1-47	116	2.85	25.7	7.26	1240
ART1-48	85.3	0.367	9.51	5.41	246
ART1-49	124	2.69	26.2	6.94	1425
ART1-5	124	5.45	56.4	7.50	3000
ART1-50	126	3.06	40.3	6.38	1003
ART1-51	106	11.9	48.0	8.92	4706
ART1-52	126	15.7	58.8	9.80	3501
ART1-53	20.0	0.637	0.239	3.53	59.7
ART1-54	119	19.5	69.3	12.8	4869
ART1-55	109	13.1	54.4	9.32	4884
ART1-56	68.9	1.85	16.9	4.48	481
ART1-57	20.5	0.706	0.189	3.64	102
ART1-58	71.3	22.4	107	13.6	6673
ART1-59	57.4	2.11	2.13	4.84	75.4
ART1-6	134	1.81	9.15	6.04	441
ART1-60	49.9	2.44	7.78	5.00	263
ART1-61	139	1.85	10.9	6.32	454
ART1-62	41.3	0.762	15.2	4.46	282
ART1-63	15.4	5.75	2.35	2.71	222
ART1-7	91.9	2.36	3.87	5.79	406
ART1-8	82.2	13.4	32.9	5.02	691
ART1-9	45.6	2.36	3.04	3.93	250
ART-2-1	90.9	3.91	9.14	11.5	537
ART-2-10	129	2.33	18.1	5.91	2251
ART-2-11	107	8.56	68.6	7.96	2406
ART-2-12	119	1.42	7.44	5.35	558
ART-2-14	150	10.7	60.1	11.0	4080
ART-2-15	130	21.9	102	12.2	7062
ART-2-16	138	1.48	8.83	5.22	299
ART-2-17	108	5.66	57.9	7.57	3777
ART-2-18	104	7.98	66.8	7.84	2425
ART-2-19	116	0.475	1.38	5.52	205
ART-2-2	132	34.1	94.5	10.7	5385
ART-2-20	83.1	14.7	29.0	9.87	2285
ART-2-21	73.6	1.79	10.7	5.37	640
ART-2-22	105	4.00	16.6	6.31	1610
ART-2-23	71.0	1.70	6.37	5.53	301
ART-2-24	115	1.45	7.59	5.17	552
ART-2-25	122	2.56	20.1	5.58	2401
ART-2-26	71.5	1.63	4.52	5.39	295
ART-2-27	64.6	1.63	5.18	4.66	282
ART-2-29	68.0	1.64	5.07	5.11	292
ART-2-3	139	18.8	92.7	11.7	6759
ART-2-30	51.0	0.643	24.4	4.44	149
ART-2-31	68.6	1.65	5.12	5.26	286
ART-2-32	97.1	0.552	0.949	5.56	262
ART-2-33	68.6	1.65	4.58	5.18	278
ART-2-34	34.8	2.53	9.46	6.14	701
ART-2-35	70.0	1.59	4.79	5.17	288
ART-2-36	111	3.51	9.41	6.23	803
ART-2-37	71.0	1.66	5.65	5.28	308
ART-2-38	70.9	1.62	4.04	5.33	278
ART-2-39	110	2.73	18.0	5.19	1241
ART-2-4	99.4	3.39	36.2	6.44	1259
ART-2-40	113	2.92	18.6	6.86	1223
ART-2-41	69.7	1.65	4.32	5.29	282
ART-2-5	113	4.15	43.1	5.92	3427
ART-2-6	86.6	3.91	9.30	11.1	514
ART-2-7	105	8.42	68.4	8.01	2459
ART-2-8	124	16.6	79.8	10.6	6742
ART-2-9	111	3.02	38.8	5.58	3264
ART-3-1	141	5.28	76.4	5.36	2112
ART-3-10	77.0	5.28	32.8	8.58	2148
ART-3-12	143	26.4	79.7	12.1	5588
ART-3-13	79.8	5.76	36.0	9.15	2334
ART-3-14	137	5.76	81.1	5.50	2220
ART-3-15	120	27.1	133	12.7	6815
ART-3-16	77.3	5.86	35.3	9.06	2266
ART-3-17	105	5.93	55.1	6.03	3901
ART-3-18	123	19.0	88.0	13.4	6315
ART-3-19	102	0.267	7.22	4.73	430
ART-3-2	105	2.15	5.96	7.79	501
ART-3-20	45.6	2.33	16.7	6.58	458
ART-3-21	45.6	2.10	11.4	6.63	393
ART-3-22	101	7.91	47.9	6.44	1274
ART-3-23	98.4	7.79	47.7	6.33	1257
ART-3-24	91.4	0.724	4.86	5.35	408
ART-3-25	48.7	0.501	10.9	6.52	155
ART-3-26	105	2.11	5.68	7.68	500
ART-3-27	104	2.20	6.22	7.76	503
ART-3-28	97.1	7.82	47.7	6.29	1264
ART-3-29	111	2.48	1.15	7.46	554
ART-3-3	102	2.11	6.21	7.48	483
ART-3-30	95.5	0.989	15.1	5.43	452
ART-3-31	130	26.0	88.6	12.9	5788
ART-3-32	80.5	6.12	36.7	9.08	2311
ART-3-33	44.0	2.21	14.9	6.30	408
ART-3-34	48.9	0.644	17.5	7.31	177
ART-3-35	46.6	0.423	3.22	5.92	150
ART-3-36	47.2	0.401	4.79	5.75	134
ART-3-37	53.9	2.42	47.4	3.45	579
ART-3-38	48.2	0.555	15.0	6.35	143
ART-3-39	121	30.0	107	15.6	6918
ART-3-4	110	11.6	86.3	6.63	5061
ART-3-40	50.0	1.17	35.3	6.75	210
ART-3-41	48.5	0.541	11.2	6.53	152
ART-3-42	104	2.13	5.88	7.75	491
ART-3-43	117	7.23	26.8	6.43	1724
ART-3-44	114	7.51	26.5	6.39	1684
ART-3-45	49.7	1.83	25.5	4.78	991
ART-3-46	80.7	5.80	36.0	9.13	2317
ART-3-47	119	1.73	11.3	7.11	1180
ART-3-48	98.6	2.22	6.34	7.30	513
ART-3-49	118	2.60	1.49	7.82	561
ART-3-5	105	2.15	5.82	7.86	500
ART-3-50	119	6.08	25.6	6.24	1717
ART-3-51	119	15.6	86.8	8.81	3145
ART-3-52	118	2.53	1.05	7.76	556
ART-3-53	114	0.687	3.14	6.06	267
ART-3-54	55.3	3.71	51.6	3.58	622
ART-3-55	129	9.23	29.6	7.28	1740
ART-3-56	118	7.96	27.9	6.53	1690
ART-3-57	96.5	1.53	43.9	6.06	1980
ART-3-58	48.9	1.33	44.0	6.39	197
ART-3-59	53.0	0.696	26.9	6.56	149
ART-3-6	103	10.7	63.5	8.28	3522
ART-3-7	112	2.33	12.5	6.13	924
ART-3-8	77.8	5.29	32.8	8.79	2127
ART-3-9	46.3	0.476	10.6	6.11	156

Appendix

Rare-earth elements:

CI Chondrite (McDonough and Sun, 1995) Normalised														
Sample	La	Ce	Pr	Nd	Sm	Eu	Gd	Tb	Dy	Ho	Er	Tm	Yb	Lu
ART1-1	0.264	0.935	2.02	3.65	8.98	11.7	12.8	12.2	12.2	10.1	9.21	7.52	5.87	4.78
ART1-10	0.572	1.79	3.61	5.71	5.37	3.79	2.19	0.912	0.765	0.906	1.02	1.46	1.97	2.87
ART1-11	0.410	1.41	2.98	5.34	6.57	4.71	2.93	1.63	1.21	1.06	1.27	1.41	1.90	2.36
ART1-12	0.425	1.36	2.96	5.22	10.0	10.8	11.6	9.76	8.83	6.85	6.03	5.32	4.86	5.10
ART1-13	0.08	0.214	0.426	0.662	0.668	0.748	0.634	0.520	0.644	0.986	1.48	2.05	2.88	3.88
ART1-14	0.270	0.871	1.71	2.36	2.02	1.83	1.59	1.14	1.12	1.04	1.21	1.42	1.74	2.50
ART1-15	0.566	1.80	3.52	5.14	4.31	2.90	1.64	0.842	0.758	0.760	1.01	1.35	2.00	2.77
ART1-16	0.589	1.81	3.61	5.12	4.09	2.67	1.45	0.835	0.787	0.855	1.01	1.39	1.95	2.75
ART1-17	0.378	1.33	2.76	3.86	2.93	1.75	0.913	0.261	0.112	0.127	0.224	0.489	0.933	1.67
ART1-18	0.351	1.04	1.94	2.61	2.57	2.14	1.56	0.993	0.742	0.457	0.348	0.299	0.508	0.521
ART1-19	0.410	1.39	3.09	5.31	5.62	3.99	2.49	1.42	1.24	1.10	1.27	1.24	2.03	2.50
ART1-2	0.508	1.40	2.04	2.10	2.03	2.49	2.33	1.85	1.96	1.90	2.02	2.30	2.73	3.55
ART1-20	0.906	2.44	3.75	4.64	5.00	4.04	5.17	4.64	5.26	5.80	7.27	8.81	10.5	12.7
ART1-21	0.403	1.37	2.91	5.06	6.90	5.39	3.72	1.90	1.42	1.21	1.21	1.48	1.94	2.50
ART1-22	0.894	2.39	3.67	4.72	5.24	4.29	5.12	4.56	5.13	5.72	7.00	8.42	10.4	12.2
ART1-23	0.348	1.17	2.45	4.31	6.93	6.91	7.04	5.72	5.21	4.30	3.80	3.54	3.49	3.84
ART1-24	0.867	2.40	3.82	5.20	6.16	4.97	5.55	4.96	5.20	5.76	7.10	8.48	10.3	12.2
ART1-25	0.426	1.33	2.50	3.60	5.07	4.55	3.60	1.90	1.22	1.03	1.19	1.52	2.12	2.63
ART1-26	0.131	0.506	1.18	2.30	6.17	7.36	7.38	6.02	5.77	5.02	5.16	5.33	5.67	6.28
ART1-27	0.09	0.348	0.818	1.52	5.11	7.29	8.93	8.57	8.97	8.73	9.06	9.22	9.97	10.3
ART1-28	0.349	1.15	2.44	4.24	7.70	8.29	8.48	6.75	6.33	5.24	4.81	4.36	4.66	5.15
ART1-29	0.567	1.81	3.64	5.60	4.85	3.32	1.93	0.909	0.760	0.826	1.00	1.43	2.00	2.70
ART1-3	0.552	1.77	3.60	5.16	4.43	3.04	1.69	0.777	0.755	0.759	0.969	1.31	1.81	2.68
ART1-30	0.316	0.638	0.813	0.858	0.773	0.587	0.505	0.310	0.283	0.304	0.348	0.473	0.641	0.808
ART1-31	0.356	1.40	3.30	5.89	6.86	5.56	3.46	1.82	1.49	1.31	1.54	1.93	2.69	3.58
ART1-32	0.361	1.18	2.52	4.35	7.63	8.38	8.38	7.15	6.35	5.14	4.64	4.36	4.46	5.13
ART1-33	0.370	1.21	2.51	4.30	7.39	7.38	7.46	5.90	5.33	4.48	4.19	3.72	3.70	4.09
ART1-34	0.392	1.42	2.98	3.71	1.44	1.91	1.23	1.02	1.15	1.03	1.31	1.70	2.18	3.11
ART1-35	0.09	0.340	0.779	1.46	4.88	7.27	8.73	7.92	8.52	8.11	9.06	8.95	9.61	10.1
ART1-36	0.128	0.221	0.277	0.283	0.260	0.397	0.292	0.281	0.320	0.398	0.506	0.642	0.741	0.815
ART1-37	0.430	1.34	2.53	3.82	5.26	4.66	3.30	1.78	1.26	1.01	1.03	1.38	2.11	3.01
ART1-38	0.926	2.43	3.70	4.83	5.65	4.29	5.26	4.89	5.31	5.92	7.37	8.83	10.1	12.5
ART1-39	0.258	0.837	1.83	3.40	7.34	8.75	9.83	8.89	9.13	8.33	8.38	7.67	6.95	6.41
ART1-4	0.353	1.10	2.23	3.62	6.85	8.15	9.68	9.07	9.03	7.95	7.46	6.73	7.14	7.29
ART1-40	0.09	0.190	0.253	0.240	0.211	0.219	0.158	0.172	0.235	0.280	0.371	0.437	0.586	0.631
ART1-41	0.353	1.16	2.21	3.28	3.57	2.99	2.42	1.37	1.04	0.767	0.796	1.17	1.69	2.44
ART1-42	0.905	2.43	3.67	4.70	5.35	4.36	5.20	4.71	5.27	5.94	7.27	8.53	10.4	12.4
ART1-43	0.418	1.40	2.97	5.08	9.66	10.9	12.5	12.6	13.8	13.4	13.4	12.0	11.1	10.6
ART1-45	0.500	1.41	1.95	2.09	2.28	2.54	2.42	2.02	2.07	1.87	2.17	2.28	2.77	3.59
ART1-46	0.424	1.64	4.00	6.61	6.16	4.61	3.02	1.64	1.30	1.23	1.46	1.82	2.82	3.94
ART1-47	0.426	1.42	3.10	5.35	6.97	5.31	3.54	1.74	1.45	1.12	1.21	1.46	1.86	2.54
ART1-48	0.288	1.13	3.06	6.25	6.13	3.81	1.94	0.732	0.313	0.160	0.123	0.175	0.217	0.408
ART1-49	0.480	1.93	3.74	4.72	3.80	3.52	2.78	1.72	1.45	1.20	1.29	1.62	2.14	3.14
ART1-5	0.242	0.808	1.64	3.04	7.76	7.63	5.86	3.22	2.47	2.34	2.68	3.30	3.79	4.76
ART1-50	0.382	1.43	3.41	5.95	6.81	5.17	3.43	1.89	1.50	1.32	1.57	2.01	2.68	3.75
ART1-51	0.130	0.490	1.18	2.45	6.13	7.50	7.49	6.03	5.71	5.22	5.19	5.27	5.82	6.18
ART1-52	0.190	0.627	1.31	2.21	4.33	5.12	6.48	5.99	6.97	7.20	7.77	7.86	7.52	7.85
ART1-53	0.03	0.07	0.09	0.102	0.107	0.09	0.109	0.140	0.204	0.263	0.399	0.430	0.579	0.759
ART1-54	0.135	0.461	1.08	1.91	4.54	5.64	7.04	7.40	8.58	8.77	9.34	9.10	8.93	8.81
ART1-55	0.289	0.625	1.28	2.44	5.95	7.48	7.90	6.64	6.49	5.71	5.91	5.89	6.23	6.70
ART1-56	0.188	0.707	1.68	2.84	2.91	2.21	1.44	0.799	0.709	0.790	1.02	1.36	1.83	2.41
ART1-57	0.03	0.06	0.08	0.09	0.107	0.116	0.126	0.145	0.225	0.292	0.403	0.507	0.614	0.741
ART1-58	0.102	0.376	0.913	1.59	4.80	6.97	9.83	9.68	10.5	10.0	10.5	10.5	10.5	10.8
ART1-59	0.512	0.997	1.40	1.54	1.51	1.63	1.09	0.937	0.897	0.883	1.23	1.45	1.51	1.66
ART1-6	0.571	1.78	3.57	5.40	4.91	3.36	1.72	0.920	0.735	0.792	1.01	1.34	1.77	2.84
ART1-60	0.156	0.422	0.784	1.17	1.21	1.04	0.920	0.700	0.766	1.08	1.50	2.12	3.19	4.26
ART1-61	0.563	1.77	3.57	5.86	5.86	4.11	2.43	1.06	0.793	0.779	0.976	1.25	1.84	2.67
ART1-62	0.822	2.00	2.71	2.88	2.28	1.82	1.26	0.679	0.478	0.353	0.417	0.449	0.638	1.01
ART1-63	0.001	0.003	0.01	0.04	0.280	0.460	0.832	1.19	1.90	2.27	2.83	3.23	3.75	4.05
ART1-7	0.390	1.40	2.69	2.64	1.18	1.88	1.14	1.05	1.09	0.968	1.33	1.57	2.18	3.25
ART1-8	0.905	2.49	3.73	4.50	5.12	3.98	5.01	4.54	5.19	5.55	7.10	8.68	10.3	12.8
ART1-9	0.115	0.338	0.623	0.860	0.823	0.751	0.636	0.578	0.745	1.02	1.64	2.08	3.12	4.35

Cl Chondrite (McDonough and Sun, 1995) Normalised														
Sample	La	Ce	Pr	Nd	Sm	Eu	Gd	Tb	Dy	Ho	Er	Tm	Yb	Lu
ART-2-15	0.405	1.35	2.93	5.28	10.7	13.0	14.1	12.3	11.9	9.44	7.88	6.32	5.62	5.26
ART-2-16	0.522	1.71	3.32	4.52	2.59	1.64	1.09	0.739	0.686	0.662	0.781	0.962	1.75	2.61
ART-2-17	0.211	0.780	1.88	3.81	7.76	7.53	6.43	3.76	2.98	2.46	2.39	2.64	3.09	3.67
ART-2-18	0.673	2.20	4.56	7.47	11.6	11.7	10.4	6.52	5.12	3.57	3.13	3.06	2.98	3.40
ART-2-19	0.399	1.01	1.28	1.31	0.643	0.506	0.314	0.208	0.148	0.179	0.290	0.479	0.933	1.73
ART-2-2	0.126	0.508	1.20	2.44	6.66	8.91	11.8	12.6	14.4	14.9	16.1	16.0	16.0	15.4
ART-2-20	0.137	0.691	1.74	2.84	4.11	4.40	4.79	4.86	5.98	6.30	6.88	7.20	7.18	7.65
ART-2-21	0.152	0.654	1.74	2.84	2.44	1.80	1.36	0.798	0.675	0.782	1.03	1.34	1.64	2.70
ART-2-22	0.423	1.42	3.23	5.63	5.49	4.15	2.77	1.84	1.74	1.69	2.00	2.44	2.98	3.73
ART-2-23	0.130	0.604	1.66	2.41	1.76	1.17	0.968	0.607	0.600	0.686	0.986	1.32	1.80	2.49
ART-2-24	0.471	1.30	2.08	2.27	1.69	1.28	0.999	0.780	0.596	0.546	0.982	1.33	1.94	2.70
ART-2-25	0.469	1.45	2.89	4.75	5.72	4.55	2.87	1.44	1.12	0.943	1.16	1.66	2.30	3.10
ART-2-26	0.137	0.688	1.71	2.33	1.30	0.922	0.765	0.536	0.602	0.682	0.937	1.27	1.76	2.36
ART-2-27	0.136	0.682	1.78	2.43	1.50	1.10	0.837	0.550	0.611	0.729	0.963	1.21	1.87	2.52
ART-2-29	0.122	0.610	1.64	2.35	1.46	1.02	0.729	0.530	0.576	0.696	0.965	1.25	1.76	2.47
ART-2-3	0.304	1.02	2.26	4.06	8.98	10.7	12.1	10.7	10.1	8.14	7.32	6.37	5.52	5.24
ART-2-30	0.669	2.32	3.41	3.60	3.11	2.59	1.82	0.804	0.491	0.294	0.391	0.532	0.945	1.54
ART-2-31	0.120	0.606	1.61	2.33	1.46	0.970	0.723	0.545	0.601	0.625	0.979	1.17	1.80	2.41
ART-2-32	0.390	0.998	0.859	0.441	0.131	0.144	0.151	0.132	0.123	0.184	0.338	0.739	1.43	2.38
ART-2-33	0.126	0.591	1.63	2.24	1.37	0.852	0.775	0.546	0.563	0.668	0.882	1.27	1.83	2.30
ART-2-34	0.227	0.631	1.19	1.96	2.64	2.01	2.22	1.52	1.19	1.02	1.07	1.09	1.45	1.87
ART-2-35	0.139	0.709	1.77	2.47	1.63	1.05	0.799	0.536	0.563	0.653	0.919	1.17	1.86	2.29
ART-2-36	0.225	0.936	2.34	3.49	2.94	2.65	2.12	1.53	1.57	1.51	1.65	1.78	2.24	2.72
ART-2-37	0.126	0.613	1.66	2.44	1.55	1.20	0.853	0.569	0.592	0.670	0.919	1.22	1.81	2.54
ART-2-38	0.134	0.709	1.73	2.11	1.18	0.842	0.747	0.466	0.596	0.612	0.886	1.11	1.70	2.47
ART-2-39	0.280	1.14	2.69	4.17	3.52	2.78	2.05	1.33	1.35	1.17	1.15	1.33	1.73	2.10
ART-2-4	0.246	0.956	2.28	4.26	7.09	6.44	4.81	2.58	1.89	1.41	1.42	1.72	2.26	3.01
ART-2-40	0.413	1.26	2.40	3.35	3.27	2.87	2.40	1.64	1.50	1.22	1.32	1.47	2.03	2.69
ART-2-41	0.122	0.653	1.64	2.23	1.20	0.850	0.690	0.533	0.529	0.602	0.949	1.24	1.82	2.57
ART-2-5	0.338	1.16	2.44	4.23	6.87	6.15	5.42	3.44	2.58	1.76	1.60	1.61	2.01	2.72
ART-2-6	1.39	4.03	5.57	4.96	2.53	1.57	1.80	1.51	1.56	1.75	2.05	2.13	2.76	3.13
ART-2-7	0.708	2.28	4.75	8.13	12.1	11.9	10.4	6.57	5.10	3.82	3.25	3.34	3.01	3.80
ART-2-8	0.291	0.978	2.11	3.91	8.78	10.3	10.8	9.59	9.22	7.10	6.01	5.19	4.94	4.89
ART-2-9	0.351	1.11	2.40	4.11	6.56	5.86	4.51	2.66	1.87	1.27	1.23	1.24	1.86	2.56
ART-3-1	0.468	1.45	2.99	5.10	9.24	9.56	8.66	5.61	3.72	2.28	1.89	1.67	2.16	2.77
ART-3-10	0.480	1.77	4.26	7.58	9.68	8.45	5.97	3.38	2.87	2.35	2.48	2.77	3.36	4.10
ART-3-12	0.395	1.24	2.54	4.31	8.57	10.8	12.8	11.9	12.5	11.4	11.4	10.4	10.2	9.42
ART-3-13	0.460	1.70	4.17	7.13	10.0	9.33	7.12	4.29	3.29	2.51	2.60	2.75	3.40	4.21
ART-3-14	0.455	1.46	3.03	5.09	9.38	10.0	9.03	6.14	4.30	2.65	1.92	1.68	2.14	2.87
ART-3-15	0.383	1.25	2.69	4.85	11.3	14.1	16.5	14.7	14.6	12.4	11.7	10.1	9.47	8.67
ART-3-16	0.424	1.59	3.82	6.61	9.57	8.86	7.07	4.53	3.48	2.62	2.59	2.76	3.31	4.22
ART-3-17	0.355	1.15	2.41	3.99	7.17	7.49	7.09	4.79	3.52	2.44	2.02	2.00	2.26	2.62
ART-3-18	0.341	1.10	2.34	4.08	8.52	11.0	11.9	10.2	10.0	8.64	7.70	6.60	6.13	5.55
ART-3-19	0.350	1.24	2.62	3.59	2.70	1.67	0.779	0.189	0.09	0.09	0.195	0.456	0.865	1.35
ART-3-2	0.805	1.64	1.97	1.78	1.03	0.894	0.689	0.613	0.766	0.906	1.27	1.66	2.31	3.31
ART-3-20	0.229	0.445	0.676	0.998	1.51	1.54	1.46	1.22	1.08	0.923	1.20	1.36	1.97	2.66
ART-3-21	0.202	0.335	0.519	0.704	1.09	1.14	1.08	0.880	0.893	0.856	1.04	1.49	1.97	2.50
ART-3-22	0.278	1.05	2.44	4.25	7.64	8.04	7.73	5.35	4.53	3.49	3.59	4.50	5.99	8.31
ART-3-23	0.272	1.03	2.39	4.24	7.79	7.73	7.51	5.24	4.30	3.39	3.65	4.45	5.82	8.06
ART-3-24	0.351	1.07	2.24	3.10	2.61	1.55	0.811	0.338	0.241	0.307	0.512	0.943	1.54	2.44
ART-3-25	0.508	1.64	2.81	3.09	1.95	1.13	0.742	0.293	0.199	0.194	0.341	0.465	0.732	1.05
ART-3-26	0.715	1.59	1.99	1.84	0.966	0.877	0.698	0.701	0.753	0.861	1.23	1.53	2.21	3.05
ART-3-27	1.14	1.79	2.04	1.82	1.03	0.856	0.806	0.714	0.754	0.945	1.31	1.65	2.33	3.13
ART-3-28	0.290	1.06	2.33	4.22	7.74	7.79	7.58	5.35	4.36	3.42	3.55	4.34	5.71	7.87
ART-3-29	0.329	0.995	1.35	1.15	1.03	0.806	0.767	0.567	0.760	0.947	1.50	2.30	2.96	4.13
ART-3-3	0.945	1.71	1.95	1.68	0.917	0.856	0.755	0.636	0.812	0.938	1.20	1.67	2.43	3.22
ART-3-30	0.300	1.12	2.56	4.25	4.95	3.91	2.63	1.07	0.598	0.395	0.552	0.906	1.52	2.26
ART-3-31	0.688	2.00	3.87	6.31	12.1	14.2	16.6	14.8	14.8	12.1	10.5	8.37	7.11	6.21
ART-3-32	0.432	1.58	3.77	6.87	9.52	9.06	7.29	4.74	3.56	2.72	2.64	2.73	3.17	3.85
ART-3-33	0.203	0.372	0.578	0.835	1.32	1.29	1.29	1.13	1.00	1.04	1.18	1.37	1.91	2.39
ART-3-34	0.658	2.17	3.82	4.64	3.02	2.03	1.24	0.552	0.335	0.272	0.359	0.594	0.842	1.18
ART-3-35	0.526	1.24	1.66	1.47	0.656	0.391	0.265	0.150	0.150	0.163	0.271	0.430	0.669	1.02
ART-3-36	0.428	1.20	1.81	1.82	0.911	0.555	0.325	0.171	0.146	0.162	0.226	0.355	0.674	0.910
ART-3-37	0.166	0.776	2.06	3.60	6.14	5.83	4.58	2.68	1.89	1.10	0.776	0.715	0.994	1.68
ART-3-38	0.459	1.50	2.71	3.30	2.57	1.70	1.07	0.513	0.309	0.236	0.302	0.419	0.683	1.01
ART-3-39	0.305	1.01	2.22	3.96	8.76	11.3	13.7	13.8	14.8	13.7	13.2	11.8	10.4	9.09
ART-3-4	0.286	0.978	2.17	4.22	9.19	10.4	10.6	7.94	6.73	4.98	3.98	3.47	3.43	3.63
ART-3-40	0.568	1.97	3.79	5.53	5.78	4.65	2.88	1.46	0.801	0.526	0.462	0.557	0.754	1.13

Appendix

CI Chondrite (McDonough and Sun, 1995) Normalised														
Sample	La	Ce	Pr	Nd	Sm	Eu	Gd	Tb	Dy	Ho	Er	Tm	Yb	Lu
ART-3-41	0.577	1.71	2.80	3.17	1.93	1.24	0.784	0.347	0.233	0.181	0.288	0.448	0.700	1.04
ART-3-42	0.828	1.64	1.95	1.80	0.888	0.961	0.762	0.601	0.758	0.867	1.27	1.68	2.31	3.20
ART-3-43	0.379	1.30	2.73	4.63	8.86	8.85	7.36	4.19	3.29	2.77	2.80	2.80	3.21	3.67
ART-3-44	0.376	1.27	2.67	4.60	9.27	8.64	6.97	3.95	3.38	2.97	2.97	3.02	3.39	3.78
ART-3-45	0.430	1.48	2.82	3.58	3.46	2.78	2.31	1.53	1.14	0.830	0.673	0.630	0.786	0.944
ART-3-46	0.411	1.55	3.77	6.55	9.34	8.60	6.98	4.30	3.35	2.57	2.56	2.67	3.29	3.88
ART-3-47	0.808	1.96	2.62	2.43	1.48	1.23	0.995	0.613	0.605	0.698	1.05	1.53	2.47	3.52
ART-3-48	1.19	1.80	1.94	1.79	1.00	0.884	0.776	0.682	0.793	0.891	1.25	1.71	2.16	3.11
ART-3-49	0.304	1.04	1.43	1.25	1.01	0.925	0.891	0.653	0.760	0.952	1.55	2.20	3.01	4.04
ART-3-5	0.781	1.58	1.88	1.83	0.955	0.914	0.758	0.704	0.814	0.869	1.25	1.74	2.29	3.01
ART-3-50	0.386	1.32	2.71	4.61	9.21	8.71	6.79	3.65	2.83	2.56	2.58	2.48	2.84	3.33
ART-3-51	0.283	0.991	2.21	4.13	7.81	8.35	9.40	7.96	7.96	7.20	7.00	6.41	6.46	6.63
ART-3-52	0.330	1.01	1.24	1.14	1.08	0.902	0.768	0.615	0.732	0.956	1.54	2.25	3.07	4.11
ART-3-53	0.279	0.985	2.16	3.76	3.69	2.20	1.06	0.391	0.336	0.288	0.470	0.653	1.17	1.87
ART-3-54	0.171	0.791	2.10	3.90	6.82	6.40	5.33	3.60	2.72	1.45	1.06	0.935	1.13	1.65
ART-3-55	0.401	1.34	2.78	4.71	8.79	9.49	7.57	4.54	4.12	3.76	3.90	3.95	4.37	4.65
ART-3-56	0.380	1.29	2.75	4.64	9.17	8.95	7.61	4.29	3.67	3.18	3.34	3.17	3.65	4.09
ART-3-57	0.266	0.945	2.15	4.13	7.05	6.50	4.67	2.29	1.18	0.668	0.479	0.716	1.23	2.02
ART-3-58	0.438	1.77	3.84	5.78	6.69	4.96	3.64	1.66	1.04	0.603	0.518	0.543	0.917	1.22
ART-3-59	0.346	1.38	2.93	4.22	3.75	2.96	1.97	0.835	0.464	0.316	0.319	0.459	0.737	1.06
ART-3-6	0.305	1.11	2.50	4.10	7.67	8.29	8.63	7.00	6.26	4.87	4.11	3.64	3.55	3.99
ART-3-7	0.632	1.86	3.10	3.43	2.44	1.99	1.59	0.946	0.824	0.909	1.45	2.24	3.32	4.44
ART-3-8	0.454	1.73	4.18	7.16	9.69	8.41	6.24	3.64	2.89	2.30	2.40	2.64	3.43	3.96
ART-3-9	0.516	1.61	2.77	3.17	1.84	1.10	0.645	0.278	0.213	0.186	0.301	0.397	0.647	0.999
ART-2-1	0.645	2.30	4.49	5.24	2.96	1.83	1.86	1.61	1.61	1.63	1.91	2.32	2.66	3.30
ART-2-10	0.494	1.50	3.04	4.95	6.30	4.60	2.68	1.30	0.964	0.963	1.29	1.57	2.36	3.25
ART-2-11	0.675	2.19	4.54	7.67	12.0	11.6	10.4	6.87	5.27	3.84	3.41	3.00	3.05	3.77
ART-2-12	0.471	1.34	2.09	2.22	1.66	1.36	1.09	0.666	0.559	0.619	0.840	1.20	1.77	2.73
ART-2-13	0.009	0.03	0.435	2.79	39.3	6.31	71.2	83.1	100.0	92.2	85.0	73.5	67.1	61.7
ART-2-14	0.118	0.431	0.974	1.82	4.33	5.65	6.61	6.11	5.76	4.59	3.86	3.01	2.60	2.29

Lithos 125 (2011) 729–742

Contents lists available at ScienceDirect

Lithos

journal homepage: www.elsevier.com/locate/lithos

Constraints on the depth and thermal history of cratonic lithosphere from peridotite xenoliths, xenocrysts and seismology

Kathy A. Mather [a,*], D. Graham Pearson [b], Dan McKenzie [c], Bruce A. Kjarsgaard [d], Keith Priestley [c]

[a] Department of Earth Sciences, Durham University, Science Laboratories, South Road, Durham, DH1 3LE, UK
[b] Department of Earth and Atmospheric Sciences, University of Alberta, Edmonton, AB, T6G 2E3, Canada
[c] Bullard Laboratories, University of Cambridge, Madingley Road, Cambridge, CB3 0EZ, UK
[d] Geological Survey of Canada, 601 Booth Street, Ottawa, ON, K1A 0E8, Canada

ARTICLE INFO

Article history:
Received 7 December 2010
Accepted 5 April 2011
Available online 12 April 2011

Keywords:
Geotherm
Peridotite
Xenolith
Xenocryst
Lithosphere
Seismic

ABSTRACT

Despite the relatively long-standing availability of numerical approaches for estimating palaeogeotherms using peridotite xenolith Pressure–Temperature (P–T) data, the practise of fitting xenolith P–T arrays to simple models of lithospheric heat generation, in a non-quantitative manner, remains widespread. The lack of quantification in both the magnitude and uncertainty of heat flow and lithosphere thickness estimates leads to difficulty in evaluating proposed models for lithosphere evolution on a local and regional scale.

Here, we explore the advantages of using a numerical approach to palaeogeotherm fitting, in terms of the ability to make objective comparisons of the effect that differing thermobarometer combinations and varying states of mineral and textural equilibrium have on the shape of the palaeogeotherm, and the resulting estimates of lithospheric thickness and heat flow. We also make quantitative comparisons between lithospheric mantle properties estimated using peridotite xenoliths versus single mineral xenocrysts. Using two reference peridotite xenolith databases from Bultfontein (S. Africa) and Somerset Island (Canada) we show that the same lithospheric mantle properties are predicted using harzburgite versus lherzolite thermobarometry methods. Filtering mineral data for the effects of inter-mineral disequilibrium does not produce significantly different palaeogeotherms but does increase the quality of fit of the palaeogeotherm to the P–T data, allowing more confidence to be placed in comparisons between locations. Palaeogeotherms calculated using xenocryst data, screened for peridotitic affinities, show misfits that are 2–3 times greater than those obtained using xenoliths. Lithospheric properties calculated from the Somerset Island xenocryst-based geotherm yield results that are within error of the xenolith estimate.

A mutually consistent and quantitative palaeogeotherm fitting approach is used to evaluate existing hypotheses for the evolution of the southern African lithosphere. We find very similar estimates for the heat flow and thickness of the lithosphere between SW Namibia (off-craton) and Bultfontein (on-craton). This supports suggestions of a cratonic thermal regime and equivalent lithospheric thickness across that region of southern Africa at the time of kimberlite sampling, with concurrent local thermal disturbance evident in Namibia. Complimentary, novel, seismically-obtained geotherm estimates show that the lithosphere in Namibia is now significantly thinner than the estimate at 70 Ma obtained from xenolith thermobarometry.

1. Introduction

The estimation of palaeogeotherms from mantle xenolith Pressure–Temperature (P–T) data has been an integral part of studying the ancient roots of continents for over 30 years (Boyd, 1973). While thermobarometry methods have steadily evolved and have been subject to intense scrutiny (e.g., Brey and Köhler, 1990; Finnerty and Boyd, 1984; Nimis and Grütter, 2009), the most commonly-used method for estimating mantle palaeogeotherms from these P–T data has remained the same (Pollack and Chapman, 1977). This is surprising in the light of improved understanding of the thermal properties of the lithospheric mantle (e.g., Hofmeister, 1999; Jaupart et al., 1998), and advancing computational techniques. There have been multiple efforts to formulate more accurate palaeogeotherms (e.g. McKenzie and Bickle, 1988; McKenzie et al., 2005; Michaut et al., 2007; Rudnick and Nyblade, 1999; Russell et al., 2001) but these are often specific to particular localities and datasets, and have not been widely adopted. In this contribution, we compare the extensively-used Pollack and Chapman (1977; PC77) formulation that is usually fitted to data in a qualitative manner, with a modern, numerical palaeogeotherm fitting program, *FITPLOT* (McKenzie and Bickle, 1988; McKenzie et al., 2005) that can be applied to P–T data from a variety of localities. In this way, we aim to

* Corresponding author. Tel.: +44 19 13 34 23 00.
E-mail address: kathy@mather.com (K.A. Mather).

0024-4937/$ – see front matter © 2011 Elsevier B.V. All rights reserved.
doi:10.1016/j.lithos.2011.04.003

show the limitations of the PC77 approach, as commonly used by petrologists, and highlight the advantages of using more quantitative fitting methods to estimate palaeogeotherms from peridotite xenolith data. We show how these more quantitative fits allow objective evaluation of different models for regional lithosphere evolution, using a specific case study. In addition, the quantitative nature of the fitting method we adopt allows an evaluation of the relative accuracy and precision of palaeogeotherms derived from single-cpx xenocryst chemical data versus those derived from multi-phase peridotite xenoliths.

We also compare seismically-obtained geotherm parameterizations (c.f. Preistley and McKenzie, 2006) to those made using peridotite xenolith thermobarometry, to evaluate alternate methods of obtaining lithosphere thickness and thermal properties.

2. Mantle palaeogeotherms

Mantle palaeogeotherms derived from peridotite xenolith thermobarometry can be used to directly estimate information about the properties of the lithosphere at the time of eruption of the kimberlite, such as lithospheric thickness and thermal state. A geotherm is a description of the changing temperature of the Earth between the surface and the convecting mantle interior. Temperature increases fairly rapidly with depth within the crust; then reduces to a more linear gradient increase in the lithospheric mantle. The mantle lithosphere — where the Rayleigh number is much less than critical and therefore heat is transported by conduction — moves rigidly with respect to the crust above and is known as the Mechanical Boundary Layer (MBL; McKenzie and Bickle, 1988). As the geotherm curve approaches the ambient temperature of the asthenosphere, the gradient increases until it is parallel with the asthenospheric isentrope. The region in which this occurs has a Rayleigh number close to critical and is known as the Thermal Boundary Layer (TBL). Within this layer, heat is transported by both conduction and convection. The base of both these different regions of heat-flow (MBL, TBL) can be used to define different types of lithosphere. In this study we use the general term "lithospheric thickness", to be consistent with common terminology used in mantle geotherm studies. This "lithospheric thickness" is the depth where the projection of the MBL (i.e. conductive) geotherm intersects the isentrope; this value falling within the TBL (see: Michaut et al., 2009, their Fig. 1). As pointed out by Rudnick and Nyblade (1999), any geotherm which does not meet the isentrope cannot be an accurate description of the way in which heat is conducted between the asthenosphere (represented by the isentrope) and the surface of the Earth.

Many of the PC77 palaeogeotherms that appear to fit peridotite xenolith P–T datasets (30–40 mW m^{-2}) do not cross the isentrope at any point and therefore it is not possible to estimate lithospheric thickness from the intersection of the geotherm with the isentrope. In these cases, other methods must be used to assess lithosphere thickness, such as the deepest xenolith erupted (Finnerty and Boyd, 1984). It is unlikely that kimberlites sample the lithosphere in a consistent and representative manner; this is clear from the variable spread in P–T data points produced by different kimberlite localities. Therefore, it is difficult to assess the accuracy of lithosphere thicknesses estimated using this method. A further problem is that PC77 palaeogeotherms are not unique for a given P–T array because they are calculated without reference to the P–T data, and the best-fit is estimated qualitatively by eye. As a result, two PC77 palaeogeotherms, with different surface heat flow, will often appear to fit the P–T data array equally well. Together, these problems create significant uncertainty when using PC77 palaeogeotherms as a tool for investigating craton evolution and diamond potential. Despite the lack of quantitative application of the PC77 formulation by many petrologists, far-reaching conclusions are often made on the basis of evidence provided by such palaeogeotherms, regardless of the fact that they were not initially intended for this purpose.

A palaeogeotherm formulation that is calculated using P–T data, that intersects the convecting mantle isentrope, and which provides some estimate of its accuracy would improve our assessment of the properties of the lithospheric mantle obtained using xenolith data. We aim to compare the results of such a quantitative fitting method: *FITPLOT* (McKenzie and Bickle, 1988; McKenzie et al., 2005) with those obtained using the commonly applied PC77 approach and other techniques, in order to assess its potential as a tool for evaluating the thermal evolution of cratonic regions. We evaluate the effects on resultant estimates of the lithosphere thickness and other palaeogeotherm parameters (e.g. shape, "diamond window" thickness and heat flow). We also use the ability of the *FITPLOT* technique to produce unique palaeogeotherm fits from individual P–T arrays to quantitatively investigate the effects that using a) different thermobarometer combinations, b) non-equilibrated xenoliths, and c) xenolith-and xenocryst-derived P–T estimates have on the shape of the palaeogeotherm.

3. Methods

3.1. Xenolith and xenocryst suites

Data from four suites of garnet peridotite xenoliths and two suites of single-cpx xenocryst data were used. These suites were chosen based on the abundance of samples from a wide range in depth, and, for two localities, the availability of complimentary xenocryst data for comparison. Published xenolith suites used are from Finsch (Gibson et al., 2008; Lazarov et al., 2009; Skinner, 1989), Bultfontein (Boyd and Nixon, 1978; Simon et al., 2007), Somerset Island (Schmidberger, 2001; Schmidberger and Francis, 1999), and Gibeon (Boyd et al., 2004; Franz et al., 1996a,b). In addition to these, new mineral chemical data are included in this study from Somerset Island (see Supplementary data).

We use clinopyroxene xenocrysts from Somerset Island and Bultfontein, which have been screened for peridotitic association (3.3.3). The Somerset Island dataset is from this study, and the Bultfontein xenocryst dataset was obtained courtesy of DeBeers.

3.2. Computation of the palaeogeotherm, and previous computation-based palaeogeotherm fits

We re-calculated P–T estimates from xenolith major-element data, rather than using published P–T values. Fe^{3+} content of constituent minerals was assumed to be zero. The spreadsheet 'ptexl3' was used to calculate pressures and temperatures which were then used as input data for palaeogeotherm fitting using the *FITPLOT* program.

FITPLOT, was written by McKenzie in 1988 (McKenzie and Bickle, 1988), and expanded by McKenzie et al. (2005); a more comprehensive description of the way that the geotherm is calculated can be found there, and in the supplementary data. In brief, *FITPLOT* uses equations describing the thermal properties of the lithospheric mantle, together with a range of input parameters for the crust and mantle (Section 3.3; and supplementary data) to iterate a series of discrete palaeogeotherms with varying Mechanical Boundary Layer (MBL) thicknesses. In this MBL, thermal conductivity varies with temperature. In the TBL, the temperature variation with depth depends on the viscosity.

Importantly, the quantitative fit to the P–T data is obtained by calculating the misfit for each of these calculated palaeogeotherms to the input P–T array, using a root mean square distribution of ΔT from the calculated palaeogeotherm line. The palaeogeotherm output by the program is that which shows the lowest misfit (ΔT) with the input Pressure–Temperature data. Additionally, the lithospheric thickness

and other key parameters such as crustal heat flow and heat flow through the Moho are also generated as outputs by *FITPLOT*.

In contrast to *FITPLOT*, the principle independent variable within PC77 palaeogeotherm formulations is the heat flow at the Earth's surface. They are curved within the crust and upper part of the lithosphere, and their gradients increase dramatically at depth, especially at low crustal heat flow values.

There are several advantages of a scheme that attempts a best-fit of P–T data to calculated geotherm parameters, such as *FITPLOT* and the approaches of Rudnick and Nyblade (1999), Russell et al. (2001) and Michaut et al. (2007), over the use of PC77 formulations. Firstly, they use more recent approximations for the thermal structure of the lithosphere, and numerical calculation methods that were not used in PC77. Particular to *FITPLOT* is the ability to produce a 'xenolith misfit' value as an output parameter; a quantitative estimate of how well the output palaeogeotherm fits the P–T array. Quantitative estimates of the fit of PC77 palaeogeotherms to available data are possible, but not normally attempted. The calculated misfit ($\pm\Delta T$) can be used to provide an estimate of the precision of the palaeogeotherm fit, to infer uncertainty on other output values such as the lithospheric thickness, and also allow quantitative assessment of the similarity of palaeogeotherms from different localities.

3.3. Inputs

3.3.1. Pressure–temperature estimates

Nimis and Grütter (2009) have extensively discussed the accuracy of geothermometer and geobarometer combinations applicable to mantle peridotites, and suggested a best practise that should be implemented when calculating pressures and temperatures from xenolith mineral chemical data. We test the effect of their guidelines on the resulting palaeogeotherm by comparing the shape and outputs from the *FITPLOT* palaeogeotherm fits.

We have calculated P–T estimates using the lherzolite thermobarometer combinations of Taylor (1998) and Nickel and Green (1985; hereafter TA98_NG85), and Brey and Köhler (1990; BK90_BK90). We also use the newly modified orthopyroxene-garnet harzburgite thermometer of Nimis and Grütter (2009; NG09_NG85), and the single-clinopyroxene (cpx) thermometer and barometer of Nimis and Taylor (2000; NT00_NT00) for our xenolith data. As well as providing an independent test of garnet-orthopyroxene barometry, as proposed by Bell et al. (2003), it also allows us to directly compare the precision of xenolith- and xenocryst-derived palaeogeotherms.

3.3.2. Errors in pressure–temperature estimation

Taylor (1998) lists the errors associated with some of the commonly-used thermometers and barometers. These errors relate to the precision of the geothermometer or barometer calibration and are not necessarily correlated.

Additional, but rarely investigated uncertainties arise from counting statistics, instrumental drift and noise during electron microprobe analyses of mineral oxides. These are an external error, unrelated to internal stoichiometry of the minerals. We have taken the average standard deviation (1σ) for each oxide in each mineral measured on a modern microprobe (Cameca SX100; total peak time: cpx: 290 s; opx: 300 s; gt: 260 s). It is important to note that in some cases — especially where very short counting times are used — that the standard deviations may be significantly higher than those used here. Hence, larger errors may be evident in some xenocryst-derived geotherms that largely reflect analytical protocols rather than deficiencies in the thermobarometer.

These average instrumental uncertainties are used to calculate a range of mineral compositions around the average value, yielding slightly modified mineral compositions. From these new mineral compositions, the associated P–T was calculated using the methods outlined above. Varying each oxide composition up or down by 1, 1.5 and 2 standard deviations away from the mean yields a range of different possible mineral compositions, resulting in a 'cloud' of data points in P–T space. It should be noted that these errors are correlated. Error correlations have not been taken into account in the 'xenolith misfit' values on the palaeogeotherms.

Although the above method is a simplification, it maps out the way in which uncertainties correlate in P–T space, and therefore gives a greater appreciation of the likely uncertainties relating to particular data points than simply stating the geothermobarometer calibration errors. Nonetheless, we have shown the published calibration errors (Brey and Köhler, 1990; Nickel and Green, 1985; Nimis and Grütter, 2009; Nimis and Taylor, 2000; Taylor, 1998) as lines on the palaeogeotherm plots, along with the P–T range in which the thermometers and barometers were calibrated. This allows ready identification of data points lying outside this calibration range.

From consideration of these analytical errors, we find that for the TA98_NG85, NT00_NT00 and BK90_BK90 thermobarometer combinations, the slope of the error correlation varies from low P–T samples to high P–T samples (Fig. 2). In addition, for these thermobarometers, the magnitude of the uncertainty increases with decreasing P and T. The exception is the NG09_NG85 combination, where analytical uncertainties result in rather uniform correlated errors of relatively constant slope (Fig. 2).

3.3.3. Evaluating equilibrium

Of particular interest with respect to defining palaeogeotherm shape is the definition by Nimis and Grütter (2009) of 'equilibrated' and 'non-equilibrated' samples (with respect to inter-mineral equilibrium) within the xenolith dataset. It is important to be certain that the P–T estimates used to estimate palaeogeotherms represent the lithosphere at the time of kimberlite eruption, and have been minimally disturbed by recent events. The degree of inter-mineral equilibrium is defined in two ways: pyroxene equilibrium is estimated from the magnitude of the variation between temperature estimates calculated using two thermometer combinations; the NT00 single-cpx thermometer and the TCa-in-opx thermometer. Garnet-pyroxene equilibrium is estimated by the magnitude of the variation between the new NG09 thermometer and the NT00 thermometer. A more extensive discussion on xenolith disequilibrium is presented by Nimis and Grütter (2009).

We use the above criteria to select and exclude xenolith samples from the dataset that are not in equilibrium, and comment on the effect that this has on the calculated palaeogeotherm shape and the degree of fit to the P–T data.

In the same way, xenocryst data were screened according to the guidelines of Nimis (1998) and Grütter (2009, their Appendix B) to select grains that are in equilibrium and of peridotite paragenesis; this resulted in the culling of 45% (Somerset) to 48% (Bultfontein) of the data.

Any samples with mosaic porphyroclastic or porphyroclastic textures (Harte, 1977), or containing metasomatic minerals such as mica or amphibole were defined as 'porphyroclastic' samples and were excluded from the 'granular' sample dataset.

The definitions of Nimis and Grütter (2009) regarding inter-mineral equilibrium were strictly obeyed. If a sample showed either pyroxene disequilibrium or garnet-pyroxene disequilibrium – or both – it was discarded from the subsequent 'equilibrium' dataset. It should be noted that the majority of samples excluded in this way showed only one type of disequilibrium (e.g. showed pyroxene, but not garnet-pyroxene, equilibrium).

3.3.4. Mantle input parameters

3.3.4.1. Heat Production. There has been significant discussion on the problem of accurately estimating the heat produced within the lithospheric mantle (Jaupart and Mareschal, 2007; Michaut et al.,

2007; Rudnick et al., 1998; Rudnick and Nyblade, 1999). We note that Michaut et al. (2007) show that the highest probability density of geotherms modelled with realistic lithosphere thicknesses require mantle heat production to be $\leq 0.02\ \mu W\ m^{-3}$, and that Rudnick and Nyblade's best-fitting Kalahari geotherm has a lithospheric heat production of $0\ \mu W\ m^{-3}$. Rudnick et al. (1998) outline various reasons why determining lithospheric heat production from measurements of heat producing elements (HPEs) in xenoliths is essentially arbitrary. This is due to the difficulty in quantifying the effect of secondary addition of these elements (K, U, Th) to the xenolith during metasomatism and the emplacement of the host kimberlite. While heat production in the lithosphere can be varied within *FITPLOT*, we have chosen to use Rudnick and Nyblade's best-fitting value of $0\ \mu W\ m^{-3}$. Therefore, when calculating the palaeogeotherm to fit to the data, *FITPLOT* assumes that the heat flux through the base of the lithosphere is the same as the heat flux through the Moho. Assuming a heat production in the lithosphere of $0\ \mu W\ m^{-3}$ – consistent with the above studies – reduces the problem outlined by Michaut et al. (2007) of long-wavelength thermal transients in thick, cooling lithosphere. They suggest that these transients will artificially shallow xenolith-based estimates of lithospheric thickness. With no heat production in the lithospheric mantle, such transient thermal effects are minimised unless the lithosphere initial thickness is very large (>400 km, see Michaut and Jaupart, 2007; their Fig. 6).

3.3.4.2. Potential temperature. The mantle parameters outlined are considered to be broadly uniform on a global scale, and have been kept constant between different localities for consistency.

We have used Tp = 1315 °C for the asthenospheric isentrope, which accounts well for the globally constant 7 km thickness of oceanic crust generated at mid-ocean ridges (McKenzie and Bickle, 1988). The error in this value can be estimated from the variation in oceanic crustal thickness worldwide, which has a standard deviation of about 1 km. This translates to a variation in potential temperature of about 13 °C (McKenzie and Priestley, 2008). On our figures, 13 °C is approximately the thickness of the isentrope line. In addition, Katsura et al. (2010) used the olivine — wadsleyite transition to estimate the mantle potential temperature and yielded almost the same value, within error (1337 °C ± 37).

It is possible that the mantle potential temperature might be higher than the steady-state value beneath the oceans at the time of kimberlite emplacement (Mitchell, 1984; Sleep, 2003). However, the increase in temperature would have to be small; large changes would alter the nature of melting regime at the base of the lithosphere and small-volume, volatile-rich kimberlitic melts would not be produced, being swamped by larger melt fractions e.g. McKenzie and Bickle (1988).

3.3.5. Crustal input parameters

The ability to vary crustal thickness, the proportion of upper and lower crust and their heat flow properties is important for any accurate palaeogeotherm estimation. In some previous studies, the thermal properties of the crust have been identified as a significant source of uncertainty when calculating cratonic palaeogeotherms (Russell et al., 2001) and often this complexity has not been included in an effort to increase accuracy. Rudnick and Nyblade (1999) used generalised global heat production values for Archean crust in their model. We attempt to use the best available local estimates for the structure of the crust and its heat production to obtain the most appropriate mantle palaeogeotherm.

3.3.5.1. Crustal thickness. FITPLOT assumes a two-layer crust with independent heat generation parameters, rather than a model where the estimated bulk crustal heat production is distributed between layers of equal thickness (c.f; Rudnick and Nyblade, 1999). This enables us to independently modify the upper and lower crustal thicknesses to satisfy available seismic refraction studies, while keeping the total crustal thickness the same to match crustal thicknesses derived from local receiver function analyses.

The seismic structure of the crust beneath Southern Africa and the Kaapvaal craton (Finsch, Bultfontein) and the Proterozoic crust of the Rehoboth Terrane (Gibeon) are well constrained via the Kaapvaal project (James et al., 2001; Nguuri et al., 2001) as well as other large- and small-scale seismic refraction studies (Baier et al., 1983; Durrheim and Green, 1992; Green and Durrheim, 1990). For Somerset Island fewer direct studies are available (Bank et al., 2000; Darbyshire, 2003), but there are many seismic investigations of the crust in other parts of the Superior and Slave cratons that can be used to estimate crustal thickness and structure (Cook et al., 1999; Snyder, 2008).

Our crustal thickness estimates are within the range of values used in previous studies of the thermal structure of the lithosphere in these regions. Rudnick and Nyblade (1999) used a 41 km thick crust for all their geotherms, regardless of locality. Michaut and Jaupart (2007) and Michaut et al. (2007) used 35 km for crustal thickness in their modelling of the thermal structure of the cratonic lithosphere, which is similar to our values. While this is an appreciable difference in total crustal thickness (~6 km), our upper crustal thicknesses are similar to those used by Rudnick and Nyblade (1999). Since the upper crust produces significantly more heat than the lower crust, we suggest that this difference may not significantly affect comparisons between the palaeogeotherms.

3.3.5.2. Heat production. The crustal heat production values (Supplementary data, Table 2) have been determined by using best estimates from both thermal modelling of the lithosphere (e.g. Michaut et al., 2007) and from combining seismic refraction studies (Baier et al., 1983; Durrheim and Green, 1992; Green and Durrheim, 1990) with laboratory estimates for seismic velocities and heat production of different crustal materials (Rudnick and Fountain, 1995; Taylor and McLennan, 1985) to estimate compositional structure (Supplementary data, Fig. 1). Our chosen values are within the range of similar studies (Michaut et al., 2007; Rudnick and Nyblade, 1999).

4. Results and discussion

4.1. Comparison of palaeogeotherm shapes and resulting lithospheric thicknesses obtained using the FITPLOT, Rudnick and Nyblade (1999) and PC77 methods

The shape of the palaeogeotherm fitted using the *FITPLOT* methodology is quite distinct from other constructions. For comparison, the TA98_NG85 xenolith P–T array from Bultfontein, with the closest-fitting PC77 palaeogeotherm ($43\ mW\ m^{-2}$), the calculated *FITPLOT* output, and the best-fitting 'Kalahari' geotherm calculated by Rudnick and Nyblade (1999) (RN99) are shown in Fig. 1. In addition, although they are not directly comparable, the computed time-integrated geotherms of Michaut et al. (2009) (M + 09) are also plotted.

The most obvious difference between the resulting palaeogeotherm estimates is that the PC77, M + 09 and RN99 formulations all indicate thicker lithosphere than the *FITPLOT* method (Table 1), with the PC77 estimate being 44 km thicker than the *FITPLOT* estimate. The distinct shape of the *FITPLOT* palaeogeotherms is the result of 1) the ability of *FITPLOT* to model the change in temperature with depth within the TBL, which is absent in the other models, 2) the assumed absence of heat production within the lithosphere, and 3) the inclusion in the *FITPLOT* method of the term for the temperature dependence of thermal conductivity (k = k(T)). A further refinement to *FITPLOT* is the possibility to include a pressure dependence for thermal conductivity. Recent experimental results have shown that thermal conductivity in mantle minerals may also vary with pressure (Osako et al., 2004). To assess the potential importance of this result

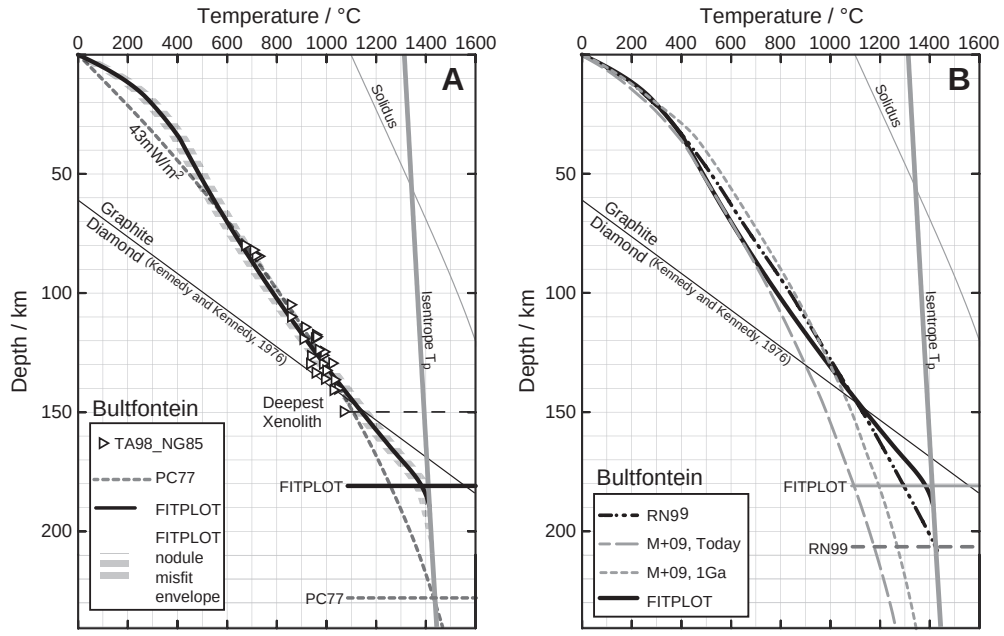

Fig. 1. (A) Comparison of the palaeogeotherm fit to the TA98_NG85 P–T mantle xenolith array from Bultfontein (mineral chemistry data from Boyd and Nixon, 1978 and Simon et al., 2007) using the PC77 method (dashed line), and the FITPLOT program (solid line, with dashed shading representing the error envelope). The base of the lithosphere, as defined by the deepest xenolith, and the intersection of the PC77 and FITPLOT geotherm with the isentrope are also illustrated. (B) Comparison of Rudnick and Nyblade (1999) best-fit Kalahari geotherm (black double-dashed line), with the Michaut et al. (2009) 1 Ga and 'today' transient palaeogeotherms (grey dashed line), and the FITPLOT geotherm (solid line).

we made several geotherm fits including this term and found that the resulting fits were within error of the fits made using only temperature-dependence.

In the RN99 and PC77 models, heat flow at the surface is a primary contributor to the modelled heat flow through the lithosphere, in a 'top-down' approach. In these models, surface heat flow is reduced to the amount of heat flowing through the Moho by the linear relationship proposed by Birch et al. (1968) between heat flow and the vertical distribution of heat production in the crust. Jaupart and Mareschal (2007) suggested that this relationship could not account for the highly variable nature of Archean crust, and that surface heat flow reflects only shallow differences in heat production. The Birch et al. (1968) relationship is not used by *FITPLOT* to estimate heat flux at the Moho, and contributes to the distinct difference in estimated palaeogeotherm shape. This also goes some way to explain the higher surface heat flow estimated by the *FITPLOT* method, as surface heat flow is an output of the palaeogeotherm calculation and is not fixed to measured values. Surface heat flow in both the Kaapvaal and at Somerset Island estimated using *FITPLOT* is in the range 51–58 mW m^{-2}, which is significantly higher than that measured for Archean cratons worldwide (41 ± 11 mW m^{-2}; Rudnick et al., 1998). We attribute this difference in part to the crustal parameters that we have input, since the Moho heat flux estimated using *FITPLOT* is within the ranges used in the other approaches (Table 1).

Surface heat flow and mantle xenolith P–T estimates are independent primary controls for estimating the palaeogeotherm. Since the measured values of surface heat flow reflect the thermal structure of the lithosphere today, and mainly reflect the thermal state of the crust and shallow lithosphere (Jaupart and Mareschal, 2007), we consider xenolith P–T estimates as a more robust primary control with which to fit a geotherm model.

Table 1
Output parameters from three palaeogeotherm calculation methods shown in Fig. 1.

Palaeogeotherm method	*FITPLOT*	PC77	RN99
Lithosphere thickness	**183 km**	**~227 km**	**~207 km**
Surface heat flow	52.6 mW m^{-2}	43 mW m^{-2}	45 mW m^{-2}
Moho heat flow	16.8 mW m^{-2}	?	18.0 mW m^{-2}
Crustal thickness	35 km	n/a	38 km
Mantle heat production	0 μW m^{-3}	0.1–0.084 μW m^{-3}	0 μW m^{-3}

4.2. Constraining the geotherm using different thermobarometer combinations

The quantitative fitting of *FITPLOT* palaeogeotherms to xenolith data allows an objective assessment of the effect of different thermobarometer combinations on the palaeogeotherm shape and output parameters. Using the three different recommended thermobarometer combinations of Nimis and Grütter (2009) (see: 3.2.2) as well as the extensively used Brey and Köhler (1990) formulation, we produce a series of P–T arrays for the Somerset Island dataset (Figs. 2 and 3) in order to investigate whether the palaeogeotherms calculated from these P–T arrays are significantly different. We use the Somerset Island dataset because it contains the highest number of xenolith samples and shows the widest range in depth estimates of the datasets in this study.

It has been shown previously that the absolute P–T values generated by the different thermobarometer formulations vary for any given sample (Bell et al., 2003; Brey and Köhler, 1990; Finnerty and Boyd, 1984; Nimis and Grütter, 2009). Here, our focus is to examine how these resulting differences affect the shape of the calculated geotherm and the resulting derived parameters such as lithospheric thickness and surface heat flow. We recognise that the inter-dependence of P–T calculations naturally result in correlated data arrays in P–T space, but this effect is seen in all iteratively-calculated P–T estimates. Accepting that the data are correlated, we examine how well these arrays approximate a geotherm, using the xenolith misfit value unique to *FITPLOT*.

Similar palaeogeotherms might be expected for the NG09_NG85 and TA98_NG85 combinations since they use the same barometer, but not for the NT_NT combination which is based only on cpx composition. We observe no significant difference between palaeogeotherms calculated using the three recommended thermobarometer formulations (Fig. 3). The Brey and Köhler (1990) formulation yields shallower lithosphere thickness estimates than the other

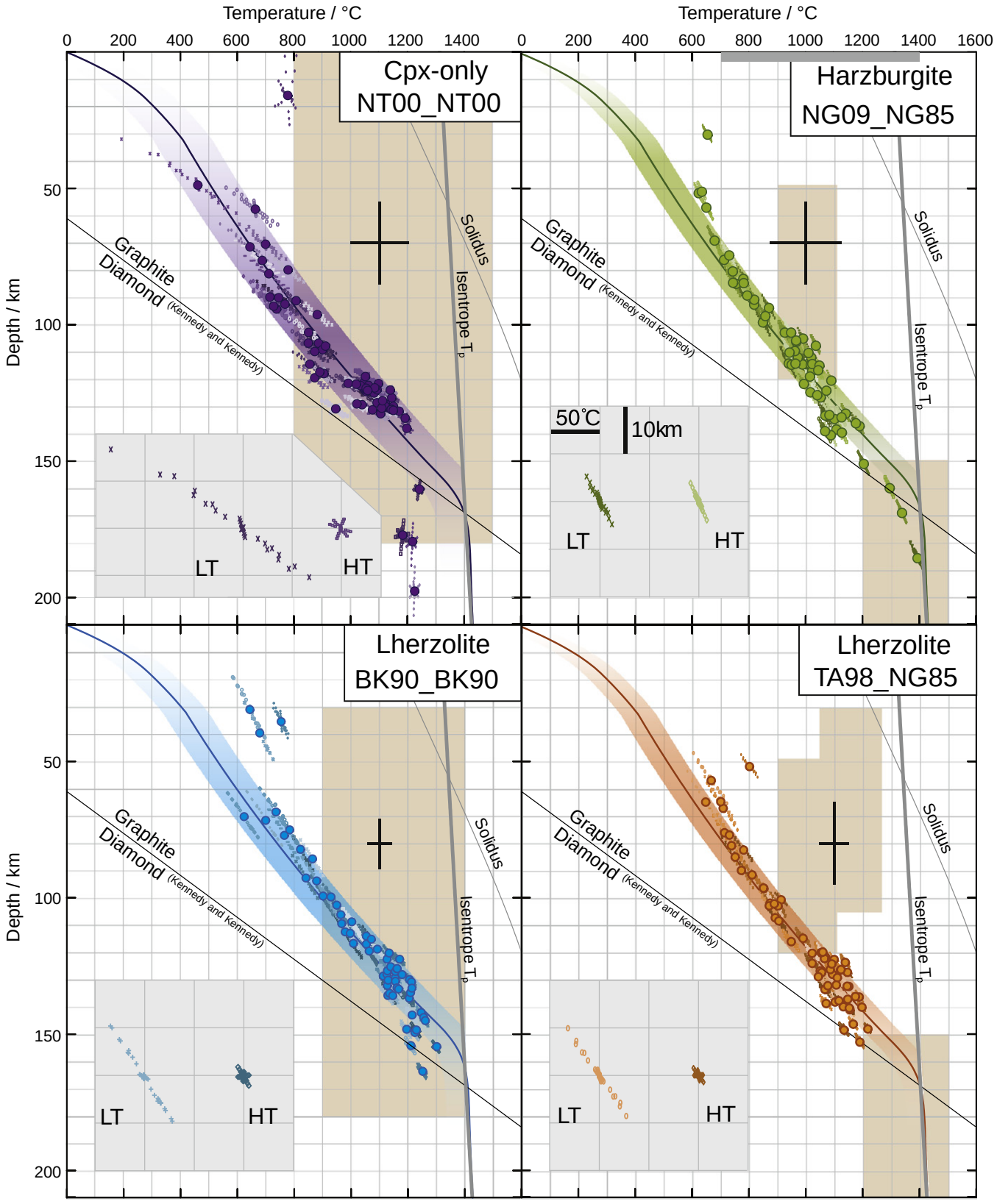

Fig. 2. Plots of P–T data calculated from the same suite of mantle xenoliths from the Somerset Island kimberlite field (mineral chemistry data from Schmidberger and Francis, 1999 and Schmidberger, 2001), using the three recommended thermobarometer combinations of Nimis and Grütter (2009), and the commonly-used Brey and Köhler (1990) formulation. All palaeogeotherms calculated using FITPLOT. Small dots surrounding data points on all plots indicate the potential P–T 'error cloud', calculated from the standard deviations of average microprobe analyses on each elemental oxide. These are shown enlarged in the grey squares on each plot, (scale shown on NG09_NG85) to emphasise the different 'clouds' for high- and low- temperature samples. Distinct from these error clouds is the error on the Thermobarometer combination used, indicated by the heavy black crosses. Brown shaded regions indicate the P–T regions in which the thermobarometers used were calibrated. Note also that the thermometer 'NG09' is calibrated empirically, and therefore the range in temperatures used is illustrated by the grey bar at the top of the NG09_NG85 plot.

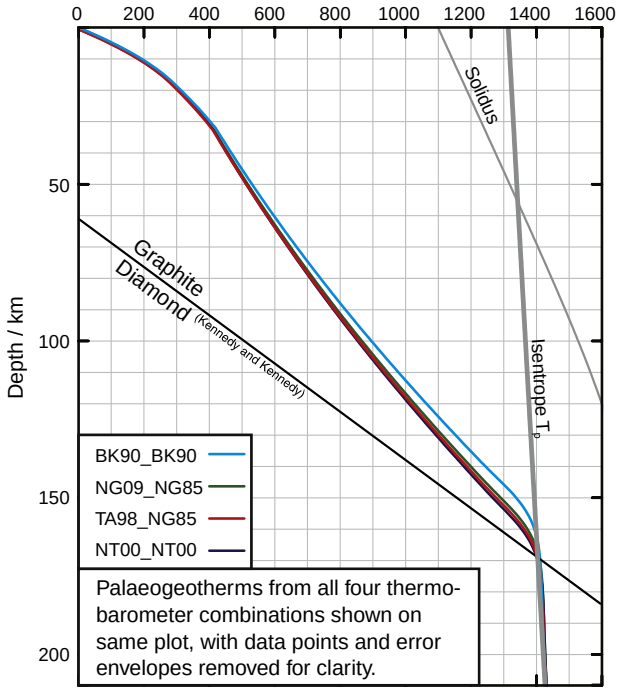

Fig. 3. The palaeogeotherms from the four thermobarometer combinations in Fig. 2 replotted without individual data points and error envelopes.

formulations (156 km vs. 163–165 km); but it is still within their xenolith misfit envelopes.

Notably, the TA98_NG85 and NG09_NG85 estimates show smaller xenolith misfits, and therefore yield more precise estimates of both the thickness of the lithosphere and the diamond window compared to the single grain cpx thermobarometer (Table 2) and the formulation of Brey and Köhler (1990). This result quantitatively confirms the findings of Nimis and Grütter (2009), i.e. all three recommended thermobarometer combinations tested yield the same palaeogeotherm, within error; thus indicating that they produce a similar P–T array even though the individual P–T values vary.

Subsequent comparative tests will only use palaeogeotherms calculated using the TA98_NG85 thermobarometer combination, which Nimis and Grütter (2009) suggest is the most accurate.

4.3. Lherzolite vs. harzburgite thermometry and palaeogeotherm shape

Some mantle xenolith suites are dominated by harzburgites (Wittig et al., 2008). In these cases, the only way to obtain temperature estimates, for palaeogeotherm estimation, is to use opx-gt Fe–Mg exchange thermometry ("harzburgite thermometry"). The accuracy of these formulations has been questioned, due to the inability to account for the effects of the oxidation state of Fe^{3+} on Fe–Mg equilibrium (Canil and O'Neill, 1996; Nimis and Grütter, 2009). Differences in absolute P–T estimates using harzburgite versus lherzolite thermometry are clear, but the effect of these differences on resulting palaeogeotherms has not been quantitatively evaluated.

Here, we have calculated pressures and temperatures for a suite of lherzolite xenoliths using both harzburgite thermometry (ignoring the cpx) and lherzolite (using both cpx and opx) thermometry and compare the resulting palaeogeotherms obtained using *FITPLOT*. The suite of xenoliths from Somerset Island is again selected for this exercise due to the large dataset and large spread in P–T values.

While – as expected – there are differences in the individual xenolith P–T estimates obtained using harzburgite (NG09_NG85) or lherzolite (TA98_NG85) thermometry, there is no significant difference, outside of our estimated uncertainty, between the calculated palaeogeotherms (Table 2, Fig. 3). For instance, the thickness of lithosphere in each case is the same, 163 km, and the surface heat flow only varies by 0.2 mW m^{-2}. We therefore suggest that it might be feasible to combine P–T estimates from these two thermobarometer combinations without noticeable deterioration in the shape of the palaeogeotherm. Taking this approach would significantly increase the number of samples available for palaeogeotherm estimation at some locations (e.g. Sand et al., 2009).

We have not investigated whether combinations of other lherzolite geothermometers and barometers would show the same result with the harzburgite geothermobarometer combination of NG09_NG85.

Table 2
Output parameters from the palaeogeotherms shown in Figs. 2 and 3.

Thermobarometer	NT_NT	TA98_NG85	NG09_NG85	BK90_BK90
Lithosphere thickness	165 km	163 km	163 km	156 km
Diamond-in	168 ± 6 km	168 ± 6 km	168 ± 5 km	169 ± 7 km
Xenolith misfit	**102.7 °C**	**61.7 °C**	**49.9 °C**	**79.3 °C**

4.4. 'Disequilibrium' vs. 'equilibrium' samples

Nimis and Grütter (2009) define parameters with which to distinguish xenolith samples that are not in inter-mineral equilibrium, and are therefore unsuitable for P–T estimation using formulations based on equilibrium thermodynamics. We identified and removed the P–T data points from such xenoliths from the Somerset Island and Bultfontein xenolith P–T suites. Palaeogeotherms calculated from these filtered datasets were plotted using *FITPLOT* and compared to the palaeogeotherm obtained from the full (unfiltered) dataset, which includes both equilibrium and disequilibrium samples (Fig. 4, Table 3).

There is minimal difference between the resulting palaeogeotherms such that they are indistinguishable on Fig. 4, and resulting lithospheric properties are similar (Table 3). Their xenolith misfit envelopes overlap, but the misfit for the filtered dataset is smaller in both cases. This indicates that samples showing inter-mineral disequilibrium contribute to the scatter on a P–T array, and that removing these samples produces a more precise palaeogeotherm estimate, and therefore more precise estimates of lithosphere thickness. We will therefore use only equilibrated samples in all further discussions.

The Somerset Island and Bultfontein datasets both have their deepest, equilibrated xenolith at 140–150 km. It is about this depth where the *FITPLOT* palaeogeotherms begin to differ substantially from the other palaeogeotherm estimations (Fig. 1) and so we investigated whether a *FITPLOT* palaeogeotherm calculated from a deeper P–T array would show a similar increase in precision to that seen in the Somerset Island and Bultfontein datasets. To do this, we calculated palaeogeotherms for peridotite xenoliths from Finsch, in the Kaapvaal craton (Gibson et al., 2008; Lazarov et al., 2009). This suite contains xenoliths from >180 km, and has been cited as a deep and unperturbed P–T array (Bell et al., 2003) and can be compared to the well-constrained Bultfontein example.

The difference between the resulting "equilibrium" palaeogeotherm and the palaeogeotherm from the full dataset was larger than that for either Somerset Island or for Bultfontein (Fig. 5A). Samples that appear not to be in inter-mineral equilibrium yield systematically higher P–T than equilibrium samples at this location, and therefore excluding them from the 'equilibrium-only' dataset results in a slightly shallower palaeogeotherm (Fig. 5A). While the difference in lithosphere thickness and 'diamond-in' depth are within error in both cases, the result shows more clearly the potential effects of inter-mineral disequilibrium. Moreover, this analysis indicates that the suggestions that some Finsch peridotites may originate from

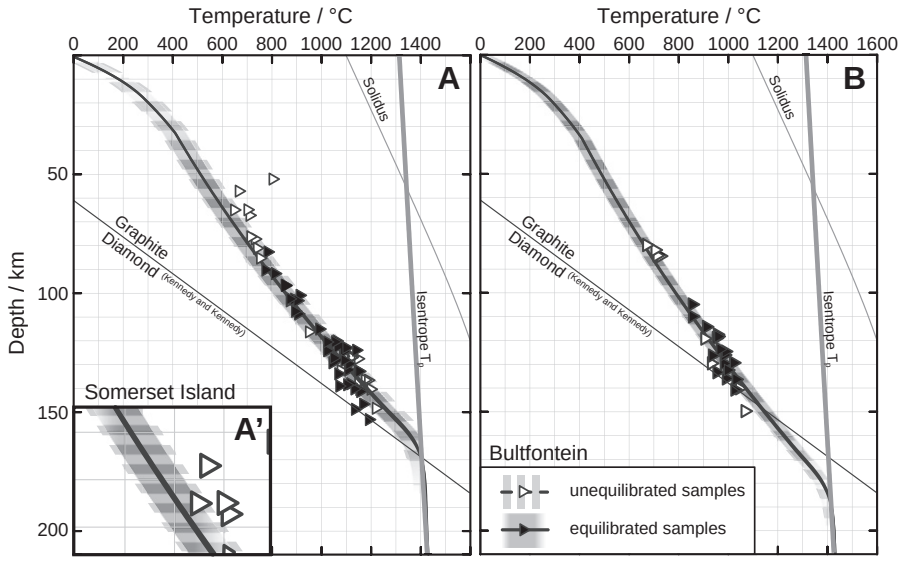

Fig. 4. (A) Plots of P–T data calculated for equilibrated (filled triangles) and unequilibrated (open triangles) mantle xenoliths from Somerset Island (mineral chemistry data from Schmidberger and Francis, 1999 and Schmidberger, 2001). (B) Plots of P–T data calculated for equilibrated (filled triangles) and unequilibrated (open triangles) mantle xenoliths from the Bultfontein kimberlite (mineral chemistry data from Boyd and Nixon, 1978 and Simon et al., 2007). Only one geotherm line is visible on both plots because the palaeogeotherms overlap. However, the xenolith misfit (error envelope) is larger for palaeogeotherms calculated using equilibrated plus unequilibrated samples.

depths close to 200 km (Finnerty and Boyd, 1984; Gibson et al., 2008) may be the result of inter-mineral disequilibrium.

Another obvious feature of the Finsch P–T array is that it lies at a high angle to the *FITPLOT* palaeogeotherm. Since this effect is not removed upon screening out samples showing disequilibrium, it implies that some other mechanism is responsible for the unusual nature of the P–T distribution, or that the Finsch P–T array does not approximate to a steady-state geotherm, as assumed by the *FITPLOT* program. Other palaeogeotherm formulations (e.g. Fig. 1) have steeper gradients than those calculated using the *FITPLOT* methodology, resulting partly from the assumption in the *FITPLOT* routine that the lithospheric mantle heat production = 0 μW m^{-3}. The steeper gradient of the Finsch array than the *FITPLOT* palaeogeotherm could thus reflect an underlying lithospheric mantle with a heat production greater than 0 μW m^{-3}. *FITPLOT* was modified to see if an increase in the heat production of the lithospheric mantle would yield a palaeogeotherm that better fits the Finsch P–T array.

We estimated the heat production beneath Finsch by averaging the K_2O contents of the clinopyroxenes that were above the quantification limit (0.04 wt.%), and that were shown to be in inter-mineral equilibrium. Core compositions were used, to minimise the effect of late-stage cryptic metasomatism. We obtained an average value of 0.05 wt.% K_2O for Finsch Diopside, to which we applied the approximation of Rudnick et al. (1998; their Fig. 1) to obtain a lithospheric heat production of 0.05 μW m^{-3}. This value is within the range of plausible heat production values for cratonic mantle used by Michaut et al. (2007) and Rudnick and Nyblade (1999), and was used this value as an input parameter in the *FITPLOT* palaeogeotherm fitting routine.

The newly calculated palaeogeotherm fit shows a decreased xenolith misfit in comparison to the fit where lithosphere heat production = 0 μW m^{-3} (Fig. 5B). The data lie along the model palaeogeotherm, instead of oblique to it. We therefore suggest that the high angle of the Finsch P–T array to the *FITPLOT* palaeogeotherm estimation might be due to locally higher mantle lithosphere heat

Table 3
Ouput parameters for the TA98_NG85 palaeogeotherms with screens applied to the data, as described in the text.

	All samples	Equilibrium only	Equilibrated, granular only	Equilibrated, porphyroclastic only
Somerset				
Lithosphere thickness	163 km	164 km	163 km	
Diamond-in	168 ± 6 km	168 ± 5 km	168 ± 4 km	
Xenolith misfit	61.7 °C	46.1 °C	39.5 °C	
Bultfontein				
Lithosphere Thickness	183 km	182 km	181 km	
Diamond-in	146 ± 7 km	147 ± 7 km	148 ± 6 km	
Xenolith misfit	36.4 °C	34.3 °C	32.0 °C	
Finsch				
Lithosphere Thickness	201 km	192 km	192 km	
Diamond-in	131 ± 10 km	138 ± 6 km	137 ± 7 km	
Xenolith misfit	64.4 °C	34.9 °C	39.1 °C	
Gibeon				
Lithosphere Thickness		167 km	161 km	186 km
Diamond-in		167 ± 11 km	168 ± 8 km	152 ± 5 km
Xenolith misfit		81.8 °C	84.2 km	34.8 °C

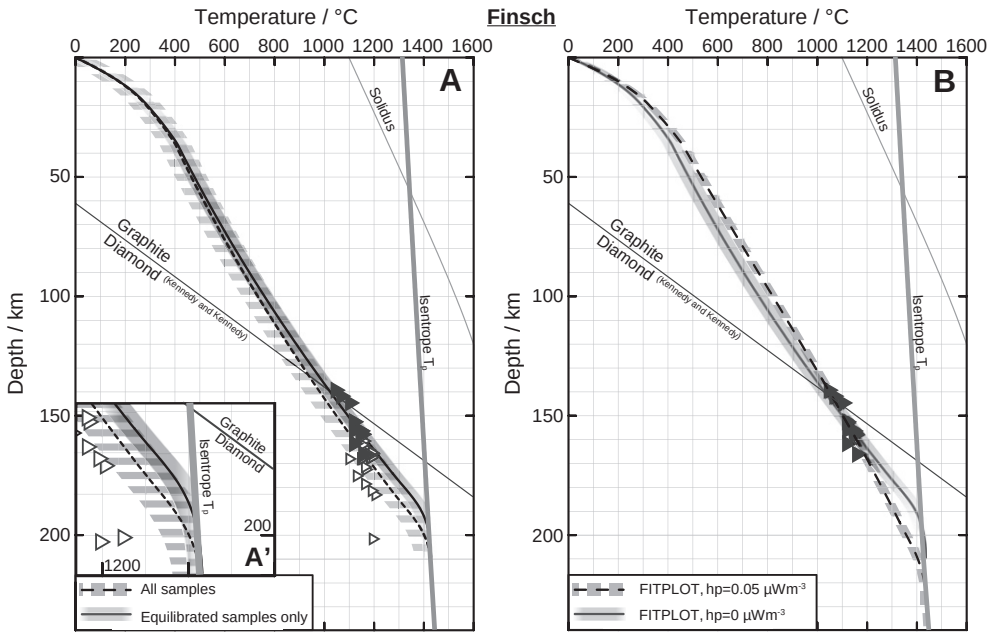

Fig. 5. (A). Plot of P–T data calculated for equilibrated (filled triangles) and unequilibrated (open triangles) mantle xenoliths from the Finsch kimberlite (mineral chemistry from: Gibson et al., 2008 and Lazarov et al., 2009), the palaeogeotherm calculated using all samples (dashed line) is slightly steeper (cooler) than the palaeogeotherm calculated using only equilibrated xenoliths (solid line). The enlarged area A' shows that the palaeogeotherm calculated using only the equilibrium samples lies just within the error envelope of that calculated using the full dataset. (B) Palaeogeotherms calculated using a modified version of the FITPLOT palaeogeotherm estimation method, to include varying heat production. The equilibrated xenolith array from Finsch is shown. The palaeogeotherm calculated with 0.05μWm^{-3}(dashed line and shading) yields a much more precise fit to the data than the 0μWm^{-3} (solid line and shading).

production. However, it is very important to note the limited depth range of the Finsch array, the limitations on the input values for the palaeogeotherm calculation, and the errors on the P–T estimates themselves. We cannot say for certain that this increased fit is due to higher heat production until samples of the shallower lithosphere become available for study. Nonetheless, there are other features of the Finsch kimberlite that support this tentative hypothesis.

Clinopyroxene from Finsch xenoliths indicate elevated K_2O (dependent on bulk composition, as well as pressure e.g., Harlow (1997)), relative to other suites, and this is consistent with a more metasomatised mantle that gives higher heat production in the lithosphere beneath. Furthermore, the Finsch kimberlite host rock is an orangeite (Mitchell, 1995) i.e. a Group II kimberlite (Smith, 1983). These magmas are systematically more enriched in incompatible trace elements than Group I kimberlites, consistent with an origin within enriched cratonic lithospheric mantle (Smith et al., 1983). Hence, the composition of the cpx and the nature of the host magma support the suggestion that the lithospheric mantle beneath Finsch was more enriched in HPE at the time of eruption, 120 Ma ago.

4.5. Effect of P–T array population size on the shape and precision of the palaeogeotherm

The datasets we are using to define the palaeogeotherms are small (generally <50 samples) and therefore filtering of datasets could potentially have significant effects on the resulting geotherm. To evaluate the sensitivity of the *FITPLOT* fitting method to sample population size, the P–T points in the Somerset Island array were given individual reference numbers. A random numbers table was used to select 20 samples for removal from the dataset (this being an average number of samples removed by any of the above data filtering tests). This process was repeated 10 times, and we examined the resulting palaeogeotherms and xenolith misfits for any systematic effect.

The lithospheric thickness estimates from all 10 tests vary by only 6 km. The xenolith misfit value obtained is quite variable, but shows no systematic effect as a result of the removal of P–T points. Therefore we conclude that the increased precision resulting from the removal of the 'disequilibrium' xenoliths is due to the properties of those xenoliths, rather than an artefact of decreasing the number of points in the P–T array.

Table 4
Output parameters from the palaeogeotherms in Fig. 6.

Somerset	Xenolith	Xenocryst	Filtered Xenocryst
Lithosphere thickness	163 km	191 km	165 km
Diamond-in	168 ± 4 km	137 ± 29 km	167 ± 8 km
Xenolith misfit	39.5 °C	166.6 °C	66.9 °C
Bultfontein	Xenolith	Xenocryst	Filtered xenocryst
Lithosphere thickness	181 km	198 km	196 km
Diamond-in	148 ± 6 km	133 ± 25 km	134 ± 16 km
Xenolith misfit	32.0 °C	157.0 °C	97.8 °C

4.6. Xenolith versus xenocryst palaeogeotherms

In diamond exploration, mantle xenolith data is sparse and an assessment of the thermal structure of the lithosphere beneath exploration targets is usually made using single-crystal mineral compositions from xenocrysts. Peridotite-derived xenocrysts have the advantage over xenolith data in that a significant number of P–T points can be obtained quickly and inexpensively from analysis of single-grain mounts (Grütter, 2009). It has been previously demonstrated in (4.2) and by Nimis and Grütter (2009) that the NT_NT single-cpx thermobarometer performs well in comparison to mineral-exchange formulations when used on xenolith clinopyroxene.

Xenocryst data tends to be more scattered in P–T space, and this makes it difficult to choose a best-fitting PC77 palaeogeotherm by eye. We apply quantitative palaeogeotherm fits to xenocryst data from Somerset Island and Bultfontein and compare this to the xenolith-derived, equilibrated, granular, TA98_NG85 *FITPLOT* palaeogeotherms from the same locality.

In general, the unfiltered xenocryst datasets produce much more scattered P–T arrays and palaeogeotherms with very large xenolith

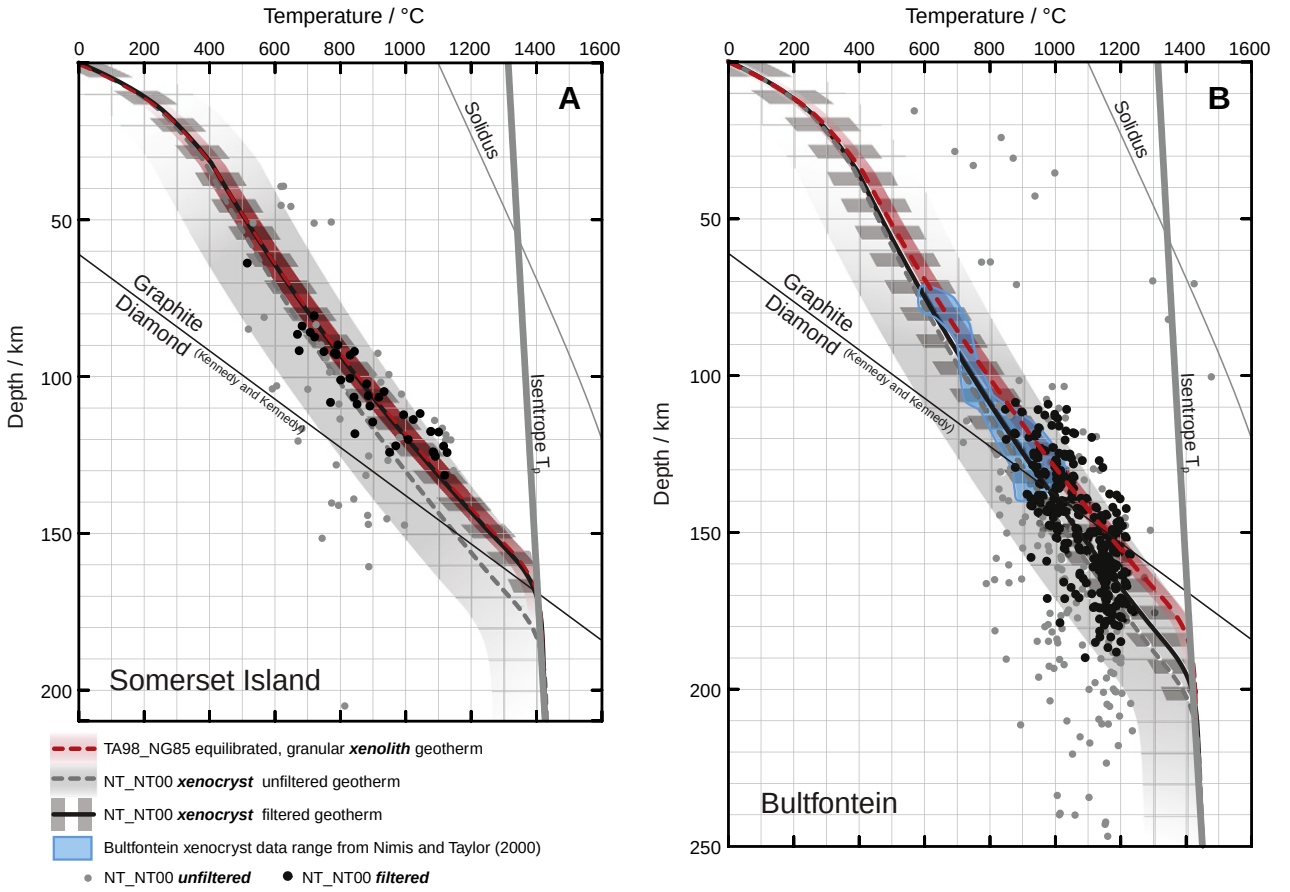

Fig. 6. Plots of P–T data calculated from filtered ('equilibrated') and unfiltered ('all') cpx xenocryst data from the Somerset Island (A) and Bultfontein (B) kimberlites. In each example, palaeogeotherms were calculated for filtered cpx xenocrysts (black solid line and dashed shading) and unfiltered (all) cpx xenocrysts (grey dashed line and solid shading) and compared to the equilibrated granular mantle xenolith palaeogeotherm (red dashed line and shading). The region of single-cpx P–T data from Bultfontein (Nimis and Taylor, 2000) is also shown as blue shaded region.

misfits: $\Delta T = 167$ °C for the Somerset Island array and 157 °C for the Bultfontein array (Table 4). Filtering these data (utilising the compositional screens of Nimis, 1998, and Grütter, 2009) significantly reduces the misfit, to 66.9 °C and 97.8 °C for Somerset Island and Bultfontein, respectively. The filtered xenocryst P–T array from Somerset Island yields a palaeogeotherm (solid black line, Fig. 6A) that is almost identical to that produced from the equilibrated, granular xenoliths (red dashed line, Fig. 6***A***). In the case of the much larger Bultfontein xenocryst dataset there is a distinct difference between the palaeogeotherm derived from the filtered xenocryst P–T data (196 km lithospheric thickness) and the equilibrated, granular xenolith P–T data (181 km), that is outside the xenolith misfit envelope of the xenolith data (red shaded region, Fig. 6B). This result would produce a potentially misleading estimate of the size of the "diamond-window" at Bultfontein if only the xenocryst data were used to estimate this parameter. However, these results may reflect the relatively short counting times used to obtain the large dataset in Fig. 5B. Other studies of Bultfontein xenocrysts that employed the same counting times as commonly-used for xenolith-based studies (e.g. Nimis and Taylor, 2000; their Fig. 8) produced a xenocryst array that is considerably less scattered in P–T space (see blue shaded region, Fig. 5B).

Considering only the Somerset Island results – where counting times for clinopyroxene microprobe analysis were the same for xenolith and xenocryst – would indicate that filtering clinopyroxene xenocryst compositions considerably increases the accuracy of the single-crystal geotherm estimation, to within error of the xenolith-derived geotherm, in agreement with Grütter (2009).

4.7. Quantitative petrological and seismic geotherm constraints on the evolution of the pericratonic lithosphere in southern Africa

4.7.1. Petrological evidence

On the basis of comparisons with PC77 geotherms, Boyd et al. (2004) argued that the geotherm beneath the pericratonic Rehoboth terrane in S.W. Namibia was the same as that beneath the Kaapvaal craton, and hence that the lithosphere thickness was the same in both regions at 70 Ma, the time of eruption of the Namibia kimberlites (Spriggs, 1988). This argument has recently been extended to include all lithosphere immediately surrounding the Kaapvaal craton (Janney et al., 2010). Franz et al. (1996b), Mitchell (1984) and Bell et al. (2003) all noted the distinct departure of the off-craton Gibeon porphyroclastic samples from the main array. We investigated the quantitative basis for these hypotheses using palaeogeotherms calculated by *FITPLOT*.

The exclusion of (equilibrated) porphyroclastic-textured samples from the off-craton Gibeon P–T array has a systematic and obvious effect (Fig. 7C). The Gibeon porphyroclastic xenoliths cluster at higher-temperatures than their granular, un-deformed counterparts, and removing them from the dataset causes the palaeogeotherm to steepen. A palaeogeotherm calculated using only Gibeon porphyroclastic P–T estimates (shown in Fig. 7C) lies just outside the error

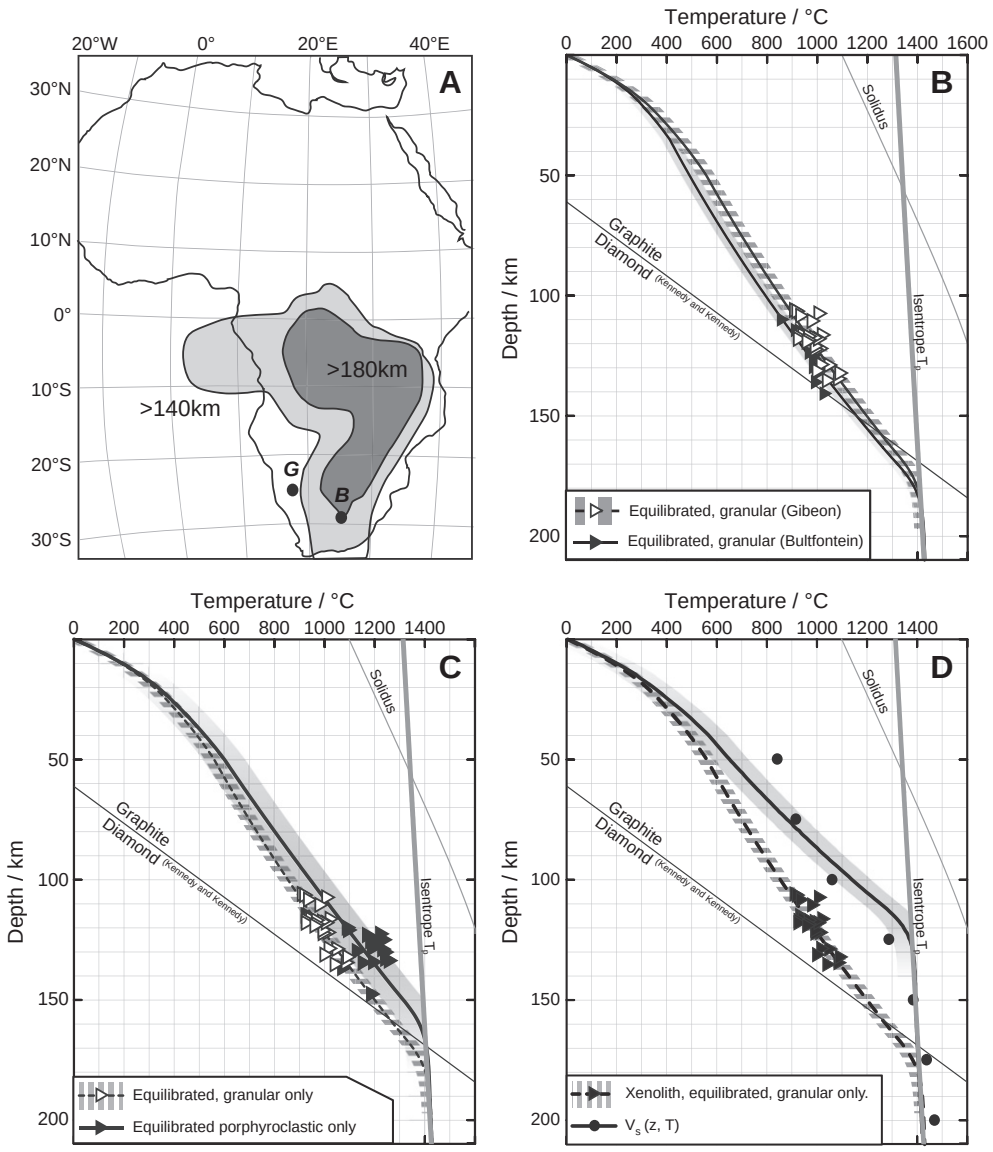

Fig. 7. (A) After Preistley and McKenzie (2006), map of the lithospheric thickness of Southern Africa from shear wave velocities, with the locations of Gibeon (G) and Bultfontien (B) indicated. (B) Palaeogeotherms calculated from P–T data for equilibrated, granular mantle xenoliths from Gibeon kimberlites (open triangles, dashed line and shading; Boyd et al., 2004; Franz et al., 1996a,b) and Bultfontein (filled triangles, solid line and shading; Boyd and Nixon, 1978; Simon et al., 2007). The lithospheric thickness calculated from these palaeogeotherms is the same, within error. (B) Palaeogeotherms calculated from P–T data for equilibrated granular mantle xenoliths (open triangles; dashed line and shading) and equilibrated porphyroclastic xenoliths (filled triangles; solid line and shading) from the Gibeon kimberlite field. The palaeogeotherm calculated from the porphyroclastic samples is shallower than that calculated from the granular samples. (D) The geotherm obtained from fitting seismic estimates of temperature and depth (solid circles) compared to the equilibrated, granular xenolith palaeogeotherm fit from the Gibeon kimberlite. The seismic geotherm is 50 km shallower than the xenolith palaeogeotherm, suggesting that the heating event indicated by the porphyroclastic xenoliths (4.7) resulted in lithospheric thinning.

envelope of the granular-only samples. This displacement indicates that the lithosphere beneath the Gibeon kimberlite field was not in steady state at the time of kimberlite eruption (Franz et al., 1996a; Mitchell, 1984).

To evaluate the claim that the palaeogeotherms were the same beneath the Kaapvaal craton and the Proterozoic Rehoboth terrane, we compare the equilibrated, granular P–T array from the Gibeon kimberlite field (Boyd et al., 2004; Franz et al., 1996a) with that calculated from equilibrated, granular Bultfontein peridotite P–T estimates (Fig. 7B). The palaeogeotherm fits yield very similar lithosphere thicknesses; 181 km vs.178 km, despite the slight elevation of the Gibeon palaeogeotherm at shallow temperatures. This is due to the increased crustal thickness in the Proterozoic terrane, and implies that while crustal structure and heat production are important when calculating palaeogeotherms – as emphasised by Rudnick and Nyblade (1999) – if the palaeogeotherms are calculated using the *FITPLOT* methodology, the effects of these crustal properties only affect the shallow lithospheric mantle.

From our quantitative palaeogeotherm analysis, we concur with Boyd et al. (2004) that there was a cratonic thermal regime and similar lithospheric thicknesses beneath the Rehoboth terrane and the Kaapvaal craton in the past. However, there has been some modification to this regime prior to the emplacement of the Gibeon kimberlites, shown by the clustering of the porphyroclastic samples at high temperature. This supports the conclusions of Franz et al. (1996b) who suggested that the decoupled P–T array indicates a heating event, associated with deformation of the lower lithosphere. Franz et al. (1996b) suggest that this might be caused by initiation of a failed rifting event, which was recorded in the xenolith suite. It is unlikely that such a transient is reflected in the surface heat flow; for this to occur, the thermal anomaly would have to remain in place for longer than 1 Ga to be recorded (Jaupart et al., 1998).

Equally, the systematic distribution of the equilibrated porphyroclastic samples derived from the Namibian lithosphere could be reflecting a changing thermal regime on the edge of cratonic regions, as proposed by Lenardic and Moresi (2000). They modelled the thermal structure of the lithosphere and upper asthenosphere, taking into account the effect of plate tectonics. They suggest that advection of heat into the thermal boundary layer beneath pericratonic regions, pulled by asthenospheric convection towards postulated downwellings beneath cratons, will counterbalance vertical heat conduction such that an inflected geotherm can be maintained. This effect could be reflected in a systematic displacement of porphyroclastic (sheared) xenoliths to higher pressures and temperatures than the extension of the conductive P–T array. The Gibeon porphyroclastic xenoliths are displaced to higher temperatures than the conductive array but are not displaced to higher pressures. This would indicate that they were not sourced from a boundary region that was distinct from the conductive lithosphere, as proposed by Lenardic and Moresi (2000), and were instead heated 'in situ', as proposed by Franz et al. (1996b) and Bell et al. (2003).

Franz et al. (1996b) also suggest that the Gibeon harzburgitic samples represent remnants of cratonic lithosphere, perhaps due to an extension of the Kaapvaal lithosphere beneath the Rehoboth terrane. From our palaeogeotherm data of the equilibrated peridotites, we can only conclude that a cratonic thermal regime once existed. We cannot constrain whether or not the lithosphere is an extension of the Kaapvaal craton, or simply a changing thermal regime beneath the Rehoboth terrane through time. However, we note that no indications of an Archean age have been obtained from available Re–Os isotopic data (Pearson et al., 2004).

4.7.2. Seismic estimates

Xenolith-derived palaeogeotherms and lithosphere thickness evaluations can be compared with estimates of lithospheric properties obtained using other methods, e.g. seismics. Southern Africa is well-defined seismically, having been the subject of the Kaapvaal Project (c.f, James et al., 2001). As a result, many estimates of the thickness of the lithosphere in this region have been published using a variety of methods including: receiver function analyses (e.g. Hansen et al., 2009; Niu et al., 2004), shear wave (V_s) inversions (e.g. Preistley and McKenzie, 2006), seismic tomography (e.g. Fouch et al., 2004) and seismic anisotropy (Yuan and Romanowicz, 2010). In many cases, lithospheric thicknesses obtained from these methods agree well with xenolith palaeogeotherm-derived values. However, seismic receiver function analyses consistently yield shallower estimates than those obtained from xenolith palaeogeotherm data, being on the order of 150–160 km versus ~200 km (Bell et al., 2003; Hansen et al., 2009; this study). Yuan and Romanowicz (2010) suggested that the shallow lithosphere thickness estimates produced by receiver function analyses could be identifying an anisotropic and depleted layer that lies within the lithosphere between 0 and 150 km, rather than defining the lithosphere–asthenosphere boundary, thus removing any major conflict between seismological and petrological estimates of lithosphere thickness beneath cratons.

Improved understanding of mineral physics now allows lithospheric geotherms to be calculated from seismic data using the parameterization of shear wave velocity (Vs) as a function of depth and temperature (z, T; Preistley and McKenzie, 2006). We calculated such a "seismic geotherm" for the Gibeon locality studied above in order to try to constrain modern-day lithospheric thickness. This geotherm was plotted using $V_s = f(z, T)$ estimates from the exact location of the Gibeon kimberlite pipes, and is shown in Fig. 7. Temperature was estimated at 25 km intervals, and input as P–T data into *FITPLOT*. It should be noted that the parameterization of $V_s = f(z, T)$ was constrained using xenolith P–T data, and the accuracy of lithospheric thicknesses estimated using this method is 20–30 km.

The xenolith data from the Gibeon locality indicate a significant thermal disturbance in the lithosphere at the time of kimberlite eruption, recorded in the porphyroclastic xenoliths, as discussed above. The seismic geotherm is a reflection of the lithosphere today and therefore should reflect any large-scale changes in the lithosphere beneath Gibeon since the eruption of the kimberlite.

A notable difference is observed between the seismic and xenolith geotherms, and the resulting lithosphere thickness estimates at Gibeon (Fig. 7D). The V_s geotherm is 55 km shallower, which is outside the error margin of both the xenolith palaeogeotherm (see Fig. 7B and D) and the seismic geotherm (20–30 km). The shallow nature of the present day lithospheric thickness under Namibia estimated from V_s data supports the hypothesis of a thermal event – recorded by the porphyroclastic samples – that caused lithospheric thinning in the peri-cratonic lithosphere to the West of the Kaapvaal craton between 70 Ma and today (Bell et al., 2003; Franz et al., 1996a; Mitchell, 1984). The mechanism behind such thinning cannot be resolved using P–T based xenolith palaeogeotherms, but may be due to the westward-migrating heating event proposed by Bell et al. (2003).

5. Conclusions

We have used a procedure that combines a numerical approach to modelling lithospheric heat flow with quantitative fitting of peridotite xenolith derived P–T data (McKenzie and Bickle, 1988; McKenzie et al., 2005) to generate palaeogeotherms for several well sampled kimberlites. The quantitative nature of the fitting procedure allows objective comparison of different palaeogeotherms, an aspect that is generally missing from typical xenolith-based thermobarometry studies. We demonstrate the potential of *FITPLOT* to produce accurate fits for discrete P–T arrays (4.1–4.7), including those derived from xenocrysts. We also show how it can be used to investigate and constrain problems related to lithosphere evolution, especially when combined with present-day seismic observations. Some of our conclusions amplify, and quantify those arrived at in earlier studies that used non-quantitative geotherm fitting techniques. We expect these conclusions to be generally applicable to other approaches if similar crust and mantle heat generation models are used.

Although different thermobarometer combinations yield differing absolute P–T estimates, for Somerset Island peridotites, the overall P–T array produced – and the subsequent palaeogeotherm calculated using *FITPLOT* – is the same regardless of these differences. This implies that P–T estimates from harzburgites (using the NG09_NG85), and lherzolites (using TA98_NG85), could be combined to increase the data density of a given xenolith P–T array and hence the accuracy of the palaeogeotherm fit. The precision of the *FITPLOT* palaeogeotherm fit can be improved by screening the xenolith P–T data for disequilibrium samples, as defined by Nimis and Grütter (2009).

For Bultfontein, comparison of geotherms calculated using peridotite xenoliths to those using clinopyroxene xenocrysts (single crystals from disaggregated peridotite) reveals significantly different geotherms and hence lithospheric thicknesses, even after careful data filtering. At Somerset Island; the xenolith and filtered xenocryst palaeogeotherms are similar, but the much greater imprecision of the xenocryst-derived palaeogeotherm makes the significance of this result difficult to assess.

Quantitative testing of previous suggestions that the lithospheric mantle beneath the Rehoboth crustal terrane of Namibia was of equivalent thickness and thermal structure to the main Kaapvaal craton (Bell et al., 2003; Boyd et al., 2004) shows that there are very subtle differences in the shape of the palaeogeotherms, but that the estimated maximum depth of lithosphere at the time of kimberlite eruption is indistinguishable, within the limits of thermobarometry.

We have shown that it is possible to obtain P–T estimates from inversions of seismic surface wave data, and use these to fit a

"present-day" geotherm for the Gibeon locality. The seismic geotherm supports the xenolith evidence for a thermal event, which is reflected at the present day by significantly thinner lithosphere. The temporal difference in geotherm constraints offered by kimberlite-derived xenoliths versus seismic observations opens up a powerful new way of studying lithospheric evolution beneath cratons.

Supplementary materials related to this article can be found online at doi:10.1016/j.lithos.2011.04.003.

Acknowledgements

The authors wish to thank DeBeers, for providing the xenocryst dataset from Bultfontein and Roberta Rudnick for providing her palaeogeotherm estimation spreadsheet. Thanks to the Geological Survey of Canada (GEM Minerals) and Durham University for funding this investigation. Nina Simon is thanked for a helpful review of an earlier version of this manuscript. Valuable suggestions were made by Thomas Stachel and an Anonymous reviewer, which significantly improved the paper.

KAM wishes to thank the Durham Volcanology Group for discussions regarding the figures.

References

Baier, B., Berckhemer, H., Gajewski, D., Green, R., Grimsel, C., Prodehl, C., Vees, R., 1983. Deep seismic sounding in the area of the Damara Orogen, Namibia, South West Africa. In: Martin, H., Eder, F. (Eds.), Intracontinental Fold Belts. Springer-Verlag, pp. 885–900.

Bank, C.G., Bostock, M.G., Ellis, R.M., Cassidy, J.F., 2000. A reconnaissance teleseismic study of the upper mantle and transition zone beneath the Archean Slave craton in NW Canada. Tectonophysics 319, 151–166.

Bell, D.R., Schmitz, M.D., Janney, E., 2003. Mesozoic thermal evolution of the southern African mantle lithosphere. Lithos 71, 273–287.

Birch, F., Roy, R.F., Decker, E.R., 1968. Heat flow and thermal history in New England and New York. In: An-Zen, E. (Ed.), Studies of Appalachian Geology. Wiley-Interscience, New York, pp. 437–451.

Boyd, F.R., 1973. A pyroxene geotherm. Geochimica et Cosmochimica Acta 37, 2533–2538.

Boyd, F.R., Nixon, H., 1978. Ultramafic nodules from the Kimberley pipes, South Africa. Geochimica et Cosmochimica Acta 42, 1367–1371.

Boyd, F.R., Pearson, D.G., Hoal, K.O., Hoal, B.G., Nixon, H., Kingston, M.J., Mertzman, S.A., 2004. Garnet lherzolites from Louwrensia, Namibia. Bulk composition and P/T relations. Lithos 77, 573–592.

Brey, G., Köhler, T., 1990. Geothermobarometry in four-phase Lherzolites II. New thermobarometers, and practical assessment of existing thermobarometers. Journal of Petrology 31, 1353–1378.

Canil, D., O'Neill, H.S.C., 1996. Distribution of ferric iron in some upper-mantle assemblages. Journal of Petrology 37, 609–635.

Cook, F.A., Van der Velden, A.J., Hall, K.W., Roberts, B.J., 1999. Frozen subduction in Canada's Northwest territories. Lithoprobe deep lithospheric reflection profiling of the western Canadian shield. Tectonics 18, 1–24.

Darbyshire, F.A., 2003. Crustal structure across the Canadian High Arctic region from teleseismic receiver function analysis. Geophysical Journal International 152, 372–391.

Durrheim, R.J., Green, R.W.E., 1992. A seismic refraction investigation of the Archaean Kaapvaal Craton, South Africa, using mine tremors as the energy source. Geophysical Journal International 108, 812–832.

Finnerty, A.A., Boyd, F.R., 1984. Evaluation of thermobarometers for garnet peridotites. Geochimica et Cosmochimica Acta 48, 15–27.

Fouch, M.J., James, D.E., VanDecar, J.C. Van, der Lee, S., 2004. Mantle seismic structure beneath the Kaapvaal and Zimbabwe Cratons. South African Journal of Geology 107, 33–44.

Franz, L., Brey, G., Okrusch, M., 1996a. Reequilibration of ultramafic xenoliths from Namibia by metasomatic processes at the mantle boundary. The Journal of Geology 104, 599–615.

Franz, L., Brey, G., Okrusch, M., 1996b. Steady state geotherm, thermal disturbances, and tectonic development of the lower lithosphere underneath the Gibeon Kimberlite Province, Namibia. Contributions to Mineralogy and Petrology 126, 181–198.

Gibson, S.A., Malarkey, J., Day, J.A., 2008. Melt depletion and enrichment beneath the Western Kaapvaal Craton. Evidence from Finsch peridotite xenoliths. Journal of Petrology 49, 1817–1852.

Green, R.W.E., Durrheim, R.J., 1990. A seismic refraction investigation of the Namaqualand Metamorphic Complex, South Africa. Journal of Geophysical Research 95, 19927–19932.

Grütter, H.S., 2009. Pyroxene xenocryst geotherms. Techniques and application. Lithos 112, 1167–1178.

Hansen, S.E., Nyblade, A.A., Julia, J., Dirks, H.G.M., Durrheim, R.J., 2009. Upper-mantle low-velocity zone structure beneath the Kaapvaal craton from S-wave receiver functions. Geophysical Journal International 178, 1021–1027.

Harlow, G.E., 1997. K in clinopyroxene at high pressure and temperature. An experimental study. American Mineralogist 82, 259–269.

Harte, B., 1977. Rock nomenclature with particular relation to deformation and recrystallisation textures in olivine-bearing xenoliths. The Journal of Geology 85, 279–288.

Hofmeister, A.M., 1999. Mantle values of thermal conductivity and the geotherm from phonon lifetimes. Science 283, 1699–1706.

James, D.E., Fouch, M.J., VanDecar, J.C., Van der Lee, S., Kaapvaal Seismic, G., 2001. Tectospheric structure beneath southern Africa. Geophysical Research Letters 28, 2485–2488.

Janney, P.E., Shirey, S.B., Carlson, R.W., Pearson, D.G., Bell, D.R., Le Roex, A.P., Ishikawa, A., Nixon, P.H., Boyd, F.R., 2010. Age, composition and thermal characteristics of South African off-craton mantle lithosphere: evidence for a multi-stage history. Journal of Petrology 51, 1849–1890.

Jaupart, C., Mareschal, J.C., 2007. Heat flow and thermal structure of the lithosphere. In: Gerald, S. (Ed.), Treatise on Geophysics 6: Crust and Lithosphere Dynamics. Elsevier, Amsterdam, pp. 217–251.

Jaupart, C., Mareschal, J.C., Guillou-Frottier, L., Davaille, A., 1998. Heat flow and thickness of the lithosphere in the Canadian Shield. Journal of Geophysical Research-Solid Earth 103, 15269–15286.

Katsura, T., Yoneda, A., Yamazaki, D., Yoshino, T., Ito, E., 2010. Adiabatic temperature profile in the mantle. Physics of the Earth and Planetary Interiors 183, 212–218.

Lazarov, M., Woodland, A.B., Brey, G., 2009. Thermal state and redox conditions of the Kaapvaal mantle. A study of xenoliths from the Finsch mine, South Africa. Lithos 112, 913–923.

Lenardic, A., Moresi, L., 2000. A new class of equilibrium geotherms in the deep thermal lithosphere of continents. Earth and Planetary Science Letters 176, 331–338.

McKenzie, D., Bickle, M.J., 1988. The volume and composition of melt generated by extension of the lithosphere. Journal of Petrology 29, 625–679.

McKenzie, D., Priestley, K., 2008. The influence of lithospheric thickness variations on continental evolution. Lithos 102, 1–11.

McKenzie, D., Jackson, J., Priestley, K., 2005. Thermal structure of oceanic and continental lithosphere. Earth and Planetary Science Letters 233, 337–349.

Michaut, C., Jaupart, C., 2007. Secular cooling and thermal structure of continental lithosphere. Earth and Planetary Science Letters 257, 83–96.

Michaut, C., Jaupart, C., Bell, D.R., 2007. Transient geotherms in Archean continental lithosphere. New constraints on thickness and heat production of the subcontinental lithospheric mantle. Journal of Geophysical Research — Solid Earth 112, B04408.

Michaut, C., Jaupart, C., Mareschal, J.-C., 2009. Thermal evolution of cratonic roots. Lithos 109, 47–60.

Mitchell, R.H., 1984. Garnet lherzolites from the Hanaus-I and Louwrensia kimberlites of Namibia. Contributions to Mineralogy and Petrology 86, 178–188.

Mitchell, R.H., 1995. Kimberlites, Orangeites and Related Rocks. Plenum, New York.

Nguuri, T.K., Gore, J., James, D.E., Webb, S.J., Wright, C., Zengeni, T.G., Gwavava, O., Snoke, J.A., Kaapvaal Seismic, G., 2001. Crustal structure beneath southern Africa and its implications for the formation and evolution of the Kaapvaal and Zimbabwe cratons. Geophysical Research Letters 28, 2501–2504.

Nickel, K.G., Green, D.H., 1985. Empirical geothermobarometry for garnet peridotites and implications for the nature of the lithosphere, kimberlites and diamonds. Earth and Planetary Science Letters 73, 158–170.

Nimis, P., 1998. Evaluation of diamond potential from the composition of peridotitic chromian diopside. European Journal of Mineralogy 10, 505–519.

Nimis, P., Grütter, H., 2009. Internally consistent geothermometers for garnet peridotites and pyroxenites. Contributions to Mineralogy and Petrology 159, 411–427.

Nimis, P., Taylor, W.R., 2000. Single clinopyroxene thermobarometery for garnet peridotites. Part 1, calibration and testing of a Cr-in-Cpx barometer and an enstatite-in-cpx thermometer. Contributions to Mineralogy and Petrology 139, 541–554.

Niu, F.L., Levander, A., Cooper, C.M., Lee, C.T.A., Lenardic, A., James, D.E., 2004. Seismic constraints on the depth keel beneath the and composition of the mantle Kaapvaal craton. Earth and Planetary Science Letters 224, 337–346.

Osako, M., Ito, E., Yoneda, A., 2004. Simultaneous measurements of thermal conductivity and thermal diffusivity for garnet and olivine under high pressure. Physics of the Earth and Planetary Interiors 143, 311–320.

Pearson, D.G., Irvine, G.J., Ionov, D.A., Boyd, F.R., Dreibus, G.E., 2004. Re–Os isotope systematics and platinum group element fractionation during mantle melt extraction: a study of massif and xenolith peridotite suites. Chemical Geology 208, 25–59.

Pollack, H.N., Chapman, D.S., 1977. Regional variation of heat flow, geotherms, and lithospheric thickness. Tectonophysics 38, 279–296.

Preistley, K., McKenzie, D., 2006. The thermal structure of the lithosphere from shear wave velocities. Earth and Planetary Science Letters 244, 285–301.

Rudnick, R.L., Fountain, D.M., 1995. Nature and composition of the continental crust. A lower crustal perspective. Reviews of Geophysics 33, 267–309.

Rudnick, R.L., Nyblade, A.A., 1999. The thickness and heat production of Archean lithosphere. contstraints from xenolith thermobarometry and surface heat flow, Mantle Petrology. Field Observations and High-Pressure Experimentation. A Tribute to Francis R. (Joe) Boyd. The Geochemical Society.

Rudnick, R.L., McDonough, W.F., O'Connell, R.J., 1998. Thermal structure, thickness and composition of continental lithosphere. Chemical Geology 145, 395–411.

Russell, J.K., Dipple, G.M., Kopylova, M.G., 2001. Heat production and heat flow in the mantle lithosphere, Slave Craton, Canada. Physics of the Earth and Planetary Interiors 123, 27–44.

Sand, K.K., Waight, T.E., Pearson, D.G., Nielsen, T.F.D., Makovicky, E., Hutchison, M.T., 2009. The lithospheric mantle below southern West Greenland. A geothermobarometric approach to diamond potential and mantle stratigraphy. Lithos 112, 1155–1166.

Schmidberger, S.S., 2001. Hf, Sr, Nd and Pb isotope systematics and major and trace element compositions of the Archean subcratonic lithosphere beneath Somerset Island, Arctic Canada, PhD Thesis, McGill University.
Schmidberger, S.S., Francis, D., 1999. Nature of the mantle roots beneath the north american craton. mantle xenolith evidence from Somerset Island Kimberlites. Lithos 48, 195–216.
Simon, N.S.C., Carlson, R.W., Pearson, D.G., Davies, G.R., 2007. The origin and evolution of the Kaapvaal cratonic lithospheric mantle. Journal of Petrology 48, 589–625.
Skinner, C., 1989. The petrology of peridotite xenoliths from the Finsch Kimberlite, South Africa. South African Journal of Geology 92, 197–206.
Sleep, N.H., 2003. Geodynamic implications of xenolith geotherms. Geochemistry, Geophysics, Geosystems 4, 1079.
Smith, C.B., 1983. Rubidium-strontium, Uranium-Lead, and Samarium-Neodymium isotopic studies of kimberlite and selected mantle-derived xenoliths, Ph.D. thesis. University of the Witwatersrand.
Snyder, D.B., 2008. Stacked uppermost mantle layers within the Slave craton of NW Canada as defined by anisotropic seismic discontinuities. Tectonics 27, TC4006.
Spriggs, A.J., 1988. An isotopic and geochemical study of kimberlites and associated alkaline rocks from Namibia. PhD thesis, University of Leeds, England.
Taylor, W.R., 1998. An experimental test of some geothermometer and geobarometer fomulations for upper mantle peridotites with application to the thermobarometery of fertile lherzolite and garnet websterite. Neues Jarhrbuch fur Mineralogie-Abhandlungen 172, 381–408.
Taylor, S.R., McLennan, S.M., 1985. The Continental Crust; Its Composition and Evolution. Blackwell.
Wittig, N., Pearson, D.G., Webb, M., Ottley, C.J., Irvine, G.J., Kopylova, M., Jensen, S.M., Nowell, G.M., 2008. Origin of cratonic lithospheric mantle roots. A geochemical study of peridotites from the North Atlantic Craton, West Greenland. Earth and Planetary Science Letters 274, 24–33.
Yuan, H.Y., Romanowicz, B., 2010. Lithospheric layering in the North American craton. Nature 466, 1063–1068.